

# FE Modelling and Model Updating of Laser Weld Joints

Thesis submitted in accordance with the requirements of  
the University of Liverpool for the degree of Doctor in Philosophy

by

Nurulakmar Abu Husain

September 2010

**PAGINATED  
BLANK PAGES  
ARE SCANNED AS  
FOUND IN  
ORIGINAL  
THESIS**

**NO  
INFORMATION  
MISSING**



# Abstract

Assembled structures are typically constructed by structural elements that are connected together by structural joints. For example, thousands of spot weld joints are used in a typical automotive structure in order to provide connections between layers of thin metal sheets used to form the structure. The spot weld joints also significantly contribute to the vehicles structural stiffness and dynamic characteristics; hence it is very important to have an acceptable FE model of the joints in order to evaluate the dynamic behaviour of such structures. It appears that most of the studies regarding spot weld joints have concentrated on spot welds made by the more conventional Resistance Spot Welding, while to the author's best knowledge, there is no reported works on modelling the dynamic behaviour of structures with laser welds, which is the main objective of this thesis.

Existing elements available in commercial FE software are researched and a suitable element is chosen to represent the laser weld joints for its dynamic predictions. A set of laser spot welded structures are manufactured and FE model representing the structures is developed systematically, starting from modelling and updating the substructures to the development of the FE model of the welded structures. Experimental modal analysis is conducted in order to obtain the modal parameters from the test structures, which are then employed in validating and improving the correlation between the developed FE models and their experimental counterparts.

Variability that exists in the test structures is also investigated and non-deterministic (or stochastic) model updating is carried out by using the perturbation method. Parameter selection for the stochastic model updating is studied first using two sets of very different structures: the first set consists of nominally identical (simple) flat plates, while the second set comprises of (more complicated) formed structures. The stochastic updating procedure is conducted with different combinations of parameters, and it is found that geometrical features (such as thickness) alone cannot converge the predicted outputs to the measured counterparts, hence material properties (for instance, Young's modulus and shear modulus) must be included in the updating process.

Then, the stochastic model updating is also conducted on the welded structures, using two approaches of parameter weighting matrix assignments. Results from one of the approaches demonstrate good correlation between the predicted mean natural



frequencies and their measured data, but poor correlation is obtained between the predicted and measured covariances of the outputs. In another approach, different parameter weighting matrices are assigned to the means and covariances updating equations. Results from this approach are in very good agreement with the experimental data and excellent correlation between the predicted and measured covariances of the outputs is achieved.

Finally, the developed deterministic FE model of the welded structures is used in damage identification exercise, consisting of two parts: (1) identification of defects, and (2) identification of real damage in the welded structure. In the first part, a defective structure is selected from the set of nominally identical structures and FE model updating procedure is performed in order to quantify the defects in the defective structure. In this exercise, only the natural frequencies are employed in the identification procedure and the identified defects are found to be reasonable and in agreement with the findings from visual inspection conducted prior to the identification work.

In identifying real damage in the welded structure, the identification procedure is conducted based on the natural frequencies and the mode shapes information of the damaged structure. The damage is characterised by the reductions in the Young's modulus of the weld patches to indicate the loss of material/stiffness at the damage region. Based on the updating results, it can be concluded that the identification procedure has successfully identified, localised and quantified the damage. The identification procedure also brings the predicted natural frequencies closer to their measured counterparts, with a very good correlation is achieved between the numerical and experimental modes.

# Acknowledgement

I would like to convey my sincerest gratitude to my primary supervisor, **Prof. Huang Ouyang**, for his invaluable supports, encouragements and supervision throughout the duration of this research. His continuous guidance has enabled me to complete my work successfully. I am also very grateful to have **Prof. John E. Mottershead** as my secondary supervisor. His valuable textbook and papers have helped me a lot to pave the path of the research.

I greatly appreciate the advice and expert opinions given by **Professor Michael I. Friswell** of Swansea University regarding my work.

Special thanks are due to the Principal Experimental Officer of the Dynamics and Control Group, **Dr. Simon James**, for his valuable advice in conducting my experimental work. I would also like to express my appreciation to **Mr. Andy Snaylam** from the Laser Engineering Group for his willingness in helping me produced the laser welded structures. Without their helps, the research would not be completed.

My greatest appreciation goes to **Dr. Hamed Haddad Khodaparast** for advice, help and guidance during the course of the work. Not to forget, thank you to all my other colleagues from **the Dynamics and Control Group** for their support and cooperations, especially to **Mr. Mohammad Yazdi Harmin** for helping me go through the stressful days at work by listening to my complaints.

Special appreciation for my husband, **Mr. Abd Razak Abd Hamid**, who endured this long process with me, sacrificed almost everything to enable me reaching my dreams while always offering support and love without fail. And to my lovely little girl, **Nurul Fathiah**, who is always my inspiration.

And finally, I would like to greatly acknowledge the support by the **Malaysian Ministry of Higher Education (MOHE)** and the **Universiti Teknologi Malaysia (UTM)** throughout the duration of this research.



# Contents

<b>Abstract</b>	<b>iii</b>
<b>Acknowledgement</b>	<b>v</b>
<b>Contents</b>	<b>ix</b>
<b>List of Figures</b>	<b>xiii</b>
<b>List of Tables</b>	<b>xvii</b>
<b>List of Symbols and Abbreviations</b>	<b>xix</b>
<b>1 Introduction</b>	<b>1</b>
1.1 Introduction . . . . .	1
1.1.1 Significance of laser weld joints in the research . . . . .	1
1.1.2 Structural dynamic analysis . . . . .	2
1.1.3 Experimental modal analysis . . . . .	3
1.1.4 Finite element modelling and model updating . . . . .	3
1.1.5 Uncertainties in structural dynamics . . . . .	5
1.1.6 Damage identification . . . . .	5
1.2 Summary of related research . . . . .	6
1.3 Overview of research . . . . .	7
1.3.1 Original contributions of the research . . . . .	9
1.3.2 List of publications . . . . .	9
1.4 Organisation of the thesis . . . . .	10
<b>2 Welding Technologies in Automotive Applications</b>	<b>13</b>
2.1 Introduction . . . . .	13
2.2 Resistance spot welding (RSW) . . . . .	13
2.2.1 The RSW process . . . . .	13
2.2.2 Application of RSW in automotive industry and its limitations	15
2.3 Laser Welding (LW) . . . . .	17

2.3.1	The laser welding process . . . . .	17
2.3.2	Application of laser welding in automotive industry and its advantages . . . . .	19
2.4	Other welding techniques . . . . .	20
2.4.1	Arc Welding . . . . .	20
2.4.2	Electron Beam Welding (EBW) . . . . .	20
2.5	Conclusions . . . . .	21
<b>3</b>	<b>Review of FE Modelling of Joints</b>	<b>23</b>
3.1	Introduction . . . . .	23
3.2	Modelling of bolted joints . . . . .	23
3.3	Modelling of weld joints . . . . .	25
3.3.1	Models for limit capacity analysis . . . . .	26
3.3.2	Models for dynamics analysis . . . . .	28
3.3.3	Modelling of laser weld joints . . . . .	33
3.4	Modelling of other joints . . . . .	34
3.5	Conclusions . . . . .	35
<b>4</b>	<b>Experimental Modal Analysis of Structures</b>	<b>37</b>
4.1	Introduction . . . . .	37
4.2	Experimental modal analysis . . . . .	37
4.2.1	Basic components of EMA . . . . .	39
4.3	Experimental modal analysis of substructures . . . . .	42
4.3.1	Experimental modal analysis of the flat plates . . . . .	44
4.3.2	Experimental modal analysis on the hat-shaped shells . . . . .	48
4.4	Experimental modal analysis of the welded structures . . . . .	48
4.5	Conclusions . . . . .	50
<b>5</b>	<b>FE modelling and model updating of the structure</b>	<b>59</b>
5.1	Introduction . . . . .	59
5.1.1	FE modelling and model updating . . . . .	60
5.1.2	FE model updating formulations . . . . .	64
5.1.3	Design sensitivity and optimization (SOL 200) of NASTRAN . . . . .	66
5.2	FE modelling and model updating of substructures . . . . .	67
5.2.1	FE modelling and model updating of the flat plates . . . . .	69
5.2.2	FE modelling and model updating of the hat-shaped shells . . . . .	73
5.3	FE modelling and model updating of the welded structures . . . . .	77
5.3.1	FE modelling of laser weld joints . . . . .	78
5.3.2	FE model updating of welded structures . . . . .	83
5.4	Conclusions . . . . .	87

<b>6</b>	<b>Stochastic model updating for variability in welded structures</b>	<b>91</b>
6.1	Introduction . . . . .	91
6.2	Uncertainty in structural dynamics . . . . .	92
6.2.1	Uncertainty classification . . . . .	92
6.2.2	Uncertainty representation . . . . .	92
6.2.3	Uncertainty propagation . . . . .	93
6.3	Stochastic model updating for uncertainty in structural dynamics . . .	97
6.3.1	Formulation of the perturbation method for stochastic uncertainty	98
6.3.2	Parameter selection for stochastic model updating . . . . .	102
6.4	Stochastic model updating of the welded structures . . . . .	118
6.5	Conclusions . . . . .	122
<b>7</b>	<b>Identification of defects/damage in a laser welded structure</b>	<b>127</b>
7.1	Introduction . . . . .	127
7.2	Damage identification methods . . . . .	128
7.2.1	Damage detection based on the change of natural frequency .	130
7.2.2	Damage detection based on the change of mode shapes . . . .	130
7.2.3	Damage detection based on the change of FRFs . . . . .	131
7.3	FE model updating for identification of defects . . . . .	132
7.3.1	Description of defective structures . . . . .	132
7.3.2	FE modelling and updating of benchmark structure . . . . .	134
7.3.3	Modelling of defective structure and identification of defects .	135
7.4	FE model updating for identification of damage . . . . .	137
7.4.1	Description of damaged structures . . . . .	138
7.4.2	Identification of damage in welded structure . . . . .	139
7.5	Conclusions . . . . .	146
<b>8</b>	<b>Conclusions and Future Work</b>	<b>149</b>
8.1	Conclusions of the thesis . . . . .	149
8.2	Recommendations for future work . . . . .	153
	<b>Appendix A: Welding Procedure Specification</b>	<b>157</b>
	<b>Appendix B: NASTRAN input files</b>	<b>160</b>
	<b>Appendix C: Example of calculation for covariance matrix of parameters</b>	<b>180</b>
	<b>References</b>	<b>193</b>



# List of Figures

2.1	Illustration of the RSW process . . . . .	14
2.2	Illustration of the spot weld made by RSW . . . . .	14
2.3	Illustration of the laser welding process . . . . .	18
2.4	Illustration of the spot weld made by laser welding . . . . .	18
3.1	FE models of bolted joint by Gaul and Lenz [40] . . . . .	24
3.2	The Jenkins-element model . . . . .	25
3.3	FE models of the weld-bonded joints by Chang et al. [51] . . . . .	26
3.4	FE models for a quarter geometry of spot weld joints by Deng et al. [32] and Chen et al. [46] . . . . .	27
3.5	FE model of spot weld by Radaj and Zhang [53] . . . . .	28
3.6	FE model of spot weld by Zhang and Richter [54] . . . . .	28
3.7	Single beam model . . . . .	29
3.8	Single brick model . . . . .	29
3.9	FE model by Salvini et al. [48] (a) geometrical representation of the model, and (b) detailed representation of the core . . . . .	30
3.10	Improved model by Vivio et al. [55] . . . . .	31
3.11	The ACM2 model by Heiserer et al. [47] . . . . .	31
3.12	The CWELD element available in NASTRAN . . . . .	31
3.13	CWELD element with 'ALIGN' format for point-to-point connectivity	32
3.14	CWELD element with 'ELEMID' and 'GRIDID' formats for point-to- patch connectivity . . . . .	33
3.15	CWELD element with (a) 'PARTPAT' and 'ELPAT' formats, and (b) 'ELEMID' and 'GRIDID' formats for patch-to-patch connectivity . .	34
4.1	Routes of vibration analysis . . . . .	38
4.2	General layout of EMA . . . . .	40
4.3	Impact hammer . . . . .	41
4.4	Accelerometer . . . . .	41
4.5	Floor of a typical automotive structure . . . . .	43
4.6	The laser welded structure . . . . .	43
4.7	The flat plate . . . . .	44



4.8	Illustration of the hat-shaped shell and its dimensions . . . . .	45
4.9	Experimental setup for the flat plates . . . . .	46
4.10	Apparatus used for modal testing . . . . .	46
4.11	Experimental model of the flat plate . . . . .	48
4.12	Experimental setup for the hat-shaped shells . . . . .	49
4.13	Experimental model of the hat-shaped shells . . . . .	50
4.14	The laser welding setup . . . . .	54
4.15	The welded structure produced by laser welding . . . . .	54
4.16	Experimental setup for the welded structures . . . . .	55
4.17	Experimental model of the welded structures . . . . .	55
4.18	The experimental mode shapes of the welded structures . . . . .	57
5.1	The FE modelling process . . . . .	61
5.2	Optimisation process in SOL 200 . . . . .	68
5.3	Iterative procedure of the Modified Method of Feasible Directions . . . . .	68
5.4	FE model of the flat plate . . . . .	69
5.5	The numerical mode shapes of the flat plates . . . . .	71
5.6	Parameters changes of the flat plates . . . . .	73
5.7	The FE model of the hat-shaped shell . . . . .	74
5.8	The first ten numerical mode shapes of the hat-shaped shells . . . . .	75
5.9	Parameters changes of the hat-shaped shells . . . . .	77
5.10	CBAR element in NASTRAN . . . . .	79
5.11	Refined mesh of the flat plates . . . . .	80
5.12	CHEXA element in NASTRAN . . . . .	80
5.13	The CWELD element with congruent and non-congruent mesh . . . . .	81
5.14	FE model of welded structure using CWELD elements with 'PART-PAT' format . . . . .	83
5.15	FE model of welded structure using CWELD elements with 'ALIGN' format . . . . .	85
5.16	Parameters changes of the welded structures . . . . .	88
5.17	Sixth to tenth numerical mode shapes of the welded structures . . . . .	89
6.1	Membership function of fuzzy set with interval representation . . . . .	94
6.2	Uncertainty propagation methods with their respective examples and relevant uncertainty representations . . . . .	95
6.3	Stochastic updating procedure . . . . .	101
6.4	Convergence achieved by the perturbation methods with increasing number of samples [99] . . . . .	103
6.5	The FP1 model . . . . .	104

6.6	Scatter plots of the FP1 model before and after the stochastic model updating . . . . .	105
6.7	The FP3 model . . . . .	106
6.8	Scatter plots of the FP3 model before and after the stochastic model updating . . . . .	107
6.9	The FP6 model . . . . .	108
6.10	Scatter plots of the FP6 model before and after the stochastic model updating . . . . .	109
6.11	Error after updating between the measured and predicted outputs covariances for the flat plates . . . . .	111
6.12	Scatter plots of the FPEG model before and after the stochastic model updating . . . . .	112
6.13	The HS4 model . . . . .	113
6.14	Scatter plots of the HS4 model before and after the stochastic model updating . . . . .	115
6.15	The HS2E model . . . . .	115
6.16	Error after updating between the measured and predicted outputs covariances for the hat-shaped shells . . . . .	117
6.17	Scatter plots of the HS2E model before and after the stochastic model updating . . . . .	117
6.18	Error after updating between the measured and predicted outputs covariances for the welded structures . . . . .	122
6.19	Initial and updated scatter plots for the first, second and third natural frequencies . . . . .	123
6.20	Initial and updated scatter plots for the first three natural frequencies . . . . .	124
7.1	Structure of the identification procedure . . . . .	132
7.2	Defective structure . . . . .	133
7.3	Parameters changes from the initial normalised values of unity for the defective structure . . . . .	137
7.4	Identification of damaged procedure . . . . .	138
7.5	Damaged structure . . . . .	139
7.6	Observation on the experimental mode shapes of the damaged structure to identify damage region . . . . .	141
7.7	FE model updating for damage identification . . . . .	142
7.8	Identified parameters . . . . .	145



# List of Tables

2.1	Comparison between carbon steels and aluminium alloys . . . . .	16
4.1	Nominal material properties of mild steel . . . . .	44
4.2	Information of the impact hammer and accelerometers used in testing the flat plates . . . . .	46
4.3	First ten measured natural frequencies for the flat plates . . . . .	47
4.4	Information of the impact hammer and accelerometers used in testing the hat-shapes shells . . . . .	49
4.5	First to fifth measured natural frequencies for the hat-shaped shells . .	51
4.6	Sixth to tenth measured natural frequencies for the hat-shaped shells .	52
4.7	First five measured natural frequencies for the flat plates used in welded structures . . . . .	53
4.8	First five measured natural frequencies for the hat-shaped shells used in welded structures . . . . .	53
4.9	Information of the impact hammer and accelerometers used in testing the welded structures . . . . .	53
4.10	First five measured natural frequencies for the welded structures . . .	56
4.11	Information of the apparatus used in roving hammer modal testing of the welded structures . . . . .	56
5.1	Measured natural frequencies and finite element predictions in Hz for the flat plates . . . . .	70
5.2	Flat plates: Natural frequency (NF) and mode shape (MS) sensitivities with respects to the normalised parameters . . . . .	71
5.3	Initial and updated natural frequencies (in Hz) for flat plates . . . . .	72
5.4	Parameter changes for the flat plate . . . . .	72
5.5	Flat plates: prediction of higher modes that are not included in the updating procedure . . . . .	73
5.6	Measured natural frequencies and finite element predictions in Hz for the hat-shaped shells . . . . .	74
5.7	Initial and updated natural frequencies (in Hz) for hat-shaped shell . .	76

5.8	Hat-shaped shells: Sensitivities of the natural frequencies to the selected normalised parameters in Hz . . . . .	76
5.9	Parameter changes for the hat-shaped shell . . . . .	76
5.10	Hat-shaped shells: prediction of higher modes that are not included in the updating procedure . . . . .	77
5.11	Comparison of initial natural frequencies (in Hz) using different elements	81
5.12	Comparison of mode shapes using different elements . . . . .	82
5.13	Comparisons of CBAR, CHEXA and CWELD by NASTRAN in modelling laser weld joints . . . . .	82
5.14	Measured natural frequencies and finite element predictions in Hz for the laser welded structures using CWELD elements with 'PARTPAT' format . . . . .	84
5.15	Laser welded structures (with 'PARTPAT' format): Sensitivities of the natural frequencies to the selected normalised parameters in Hz . . . . .	84
5.16	Parameter changes for the laser welded structures (with 'PARTPAT' format) . . . . .	84
5.17	Measured natural frequencies and finite element predictions in Hz for the laser welded structures using CWELD elements with 'ALIGN' format	86
5.18	Initial MAC values of the welded structures . . . . .	87
5.19	Laser welded structures: Sensitivities of the natural frequencies to the selected normalised parameters in Hz . . . . .	87
5.20	Parameter changes for the laser welded structures . . . . .	87
5.21	Updated MAC values of the welded structures . . . . .	88
5.22	Welded structures: prediction of higher natural frequencies that are not included in the updating procedure . . . . .	89
6.1	Deterministic model updating formulations . . . . .	98
6.2	Mean natural frequencies (in Hz) estimated using FP1 . . . . .	104
6.3	Identified mean parameter for FP1 . . . . .	104
6.4	Mean natural frequencies (in Hz) estimated using FP3 . . . . .	106
6.5	Identified mean parameter for FP3 . . . . .	106
6.6	Mean natural frequencies (in Hz) estimated using FP6 . . . . .	108
6.7	Identified mean parameter for FP6 . . . . .	109
6.8	Mean natural frequencies (in Hz) estimated using FPEG . . . . .	110
6.9	Identified mean parameter for FPEG . . . . .	110
6.10	Mean natural frequencies (in Hz) estimated using HS4 . . . . .	114
6.11	Identified mean parameter for HS4 . . . . .	114
6.12	Identified mean parameter for HS2E . . . . .	116
6.13	Mean natural frequencies (in Hz) estimated using HS2E . . . . .	116

6.14	Approximated values of material and geometrical properties of the laser weld joints . . . . .	118
6.15	Mean natural frequencies (in Hz) estimated for the welded structures . . . . .	121
6.16	Identified mean parameters estimated for the welded structures . . . . .	121
7.1	List of normal and problematic spot welds . . . . .	133
7.2	Experimental natural frequencies for the benchmark and defective structures . . . . .	134
7.3	Experimental and FE results (in Hz) of the benchmark structure . . . . .	135
7.4	Changes in parameters due to updating - benchmark . . . . .	135
7.5	Defective structure: Sensitivities of the natural frequencies to the selected normalised parameters in Hz . . . . .	136
7.6	Changes in parameters due to updating - defective . . . . .	137
7.7	Experimental and FE results (in Hz) of the defective structure . . . . .	138
7.8	Experimental natural frequencies for the undamaged and damaged structures . . . . .	139
7.9	Experimental mode shapes comparison between the undamaged and damaged structures . . . . .	140
7.10	Experimental and FE results (in Hz) of the damaged structure . . . . .	144
7.11	Initial MAC values of the damaged structures . . . . .	144
7.12	Damage coefficients for spot weld 11 to 15 . . . . .	144
7.13	Updated MAC values of the damaged structures . . . . .	145



# List of Symbols and Abbreviations

$d$	diameter
$n_x$	number of event occurrences
$n_t$	number of total occurrences
$t$	time
$w$	weighting coefficient
$z$	response variable
$f(t)$	vector of applied forces
$s$	search vector of the Steepest Descent Algorithm
$u$	vector of displacements
$\dot{u}$	vector of velocities
$\ddot{u}$	vector of accelerations
$z$	vector of response variables
$\underline{z}$	lower bound of response variable
$\bar{z}$	upper bound of response variable
$\hat{z}$	mean of response variables
$E$	Young's modulus
$G$	shear modulus
$H(\omega)$	frequency response function
$J$	objective function
$L$	length of weld
$P(x)$	probability
$T$	thickness
$\mathbf{B}$	damping matrix
$\mathbf{C}$	covariance matrix
$\mathbf{I}$	identity matrix
$\mathbf{K}$	stiffness matrix
$\mathbf{M}$	mass matrix
$\mathbf{N}$	shape function matrix
$\mathbf{S}$	sensitivity matrix
$\mathbf{T}$	transformation matrix
$\mathbf{W}_{\varepsilon\varepsilon}$	weighting matrix of measurements
$\mathbf{W}_{\theta\theta}$	weighting matrix of parameters



$\alpha$	damage coefficient
$\varepsilon$	error
$\lambda$	eigenvalue
$\lambda_r$	regularisation parameter
$\mu$	fuzzy membership function
$\nu$	Poisson's ratio
$\omega$	frequency in rad/sec
$\rho$	mass density
$\zeta_n$	modal damping
$\theta$	structural parameter variable
$\phi$	a vector of eigenvectors
$\theta$	a vector of structural parameters
$\underline{\theta}$	lower bound of parameter variables
$\overline{\theta}$	upper bound of parameter variables
$\hat{\theta}$	mean of structural parameters
ACM2	Area Contact Model 2
BIW	body-in-white
CO <sub>2</sub>	carbon dioxide
DOF	degree-of-freedom
EBW	electron beam welding
EMA	experimental modal analysis
FE	finite element
FFT	Fast Fourier Transform
FRF	frequency response function
GMAW	gas metal arc welding
GTAW	gas tungsten arc welding
HAZ	heat affected zone
IRF	impulse response function
LW	laser welding
MAC	modal assurance criteria
MCS	Monte Carlo simulation
MFD	Method of Feasible Directions
MMFD	Modified Method of Feasible Directions
MPC	multi-point constraint
NDT	non-destructive test
RSA	response surface approximation
RSW	resistance spot welding

# Chapter 1

## Introduction

### 1.1 Introduction

A general introduction of the research and motivation for the work are presented in Section 1.1.1. The research covers several areas, namely structural dynamic analysis (Section 1.1.2), experimental modal analysis (Section 1.1.3), finite element (FE) modelling and model updating (Section 1.1.4), uncertainty analysis in structural dynamics (Section 1.1.5) and damage identification (Section 1.1.6). A review of related research topics is included in Section 1.2 and an overview of this work is given in Section 1.3. Main contributions are explained and list of publications are included (Section 1.3.2). Section 1.4 shows the organisation of the thesis.

#### 1.1.1 Significance of laser weld joints in the research

The main motivation for this work is to explore the possibility of using existing elements from available commercial FE analysis packages for modelling spot weld joints made by laser welding (LW) process. The spot weld joints are normally employed in joining layers of thin metal sheets in the construction of structures (such as an automotive body-in-white (BIW)), providing significant contributions to the stiffness and dynamic characteristics of the structures. Thus, it is very important to have an acceptable FE model of the joints, so the dynamics of structures with these joints can be estimated accurately.

In automotive applications, resistance spot welding (RSW) is widely used for producing a typical automotive structures. However, owing to strong demands and regulations for better performance, improved fuel economy and more environmentally-efficient vehicles (that consequently lead to the use of new technologies in manufacturing (e.g., tailor welded blanks) and/or advanced lightweight materials such as aluminium and its alloys), the application of laser welding for producing spot welds is receiving increasing consideration by major automotive manufacturers (such as BMW, Mercedes and Audi, just to name a few) as a primary alternative to the conventional

resistance spot welding in the production of their car structures.

Laser welding can be employed efficiently and economically in various applications, with many advantages of the laser welding process over the conventional processes acknowledged. The main advantage of the laser welding process is its non-contact one-sided operation, which allows for simpler fixture and better access to hard-to-reach areas in the workpieces. This advantage is further enhanced by the flexibility of the operation that results in a faster and efficient process. The highly-flexible process also facilitates the possibility of different configuration of weld joints (e.g., continuous and stitched weld) to be achieved. In addition, due to the non-electrical nature of the laser output used in the laser welding process, a wide variety of metals and their alloys can be welded regardless of their materials properties. Because of these advantages, more welds can be produced in a single workstation, thus savings in terms of time, space and tooling costs can be achieved accordingly.

Due to the above-mentioned potentials of laser weld joints, it is necessary to investigate further on how these joints can be modelled accurately. Majority of reported works related to modelling of laser weld joints are mainly concerned in simulating the welding process itself, hence it is vital to develop an FE representation of these joints for the prediction of their dynamic behaviour. Nevertheless, modelling of joints is always a difficult task, and the need to bring the representations of numerical models to be closer to experimental model resulted in extensive research involving areas such as structural dynamic analysis, experimental modal analysis and FE modelling and model updating, as described in the followings.

### **1.1.2 Structural dynamic analysis**

Structural dynamics is one of the most important engineering disciplines, covering behaviour of structures subjected to dynamic loadings or excitations caused by human, wind, waves, traffic, earthquakes, etc.. Understanding the dynamics of structures has become increasingly important and structural analysts are constantly challenged to produce better designs to meet the economic, environmental and safety aspects imposed by governing bodies. As a result, modern structures have become more complicated. Structural dynamic analysis can be performed manually for simple structures, but for more complicated structures, however, the application of experimental modal analysis (EMA) and/or FE analysis by using commercially available FE packages such as NASTRAN and ABAQUS is necessary.

In the field of structural dynamics, much effort is given to developing accurate models that can be used to predict the response of the system due to various loadings or excitations. The analysis is normally limited to estimation of modal parameters (i.e., natural frequencies, modal damping, mode shapes, etc.) and the analytical estimates are frequently compared with experimental data. Correlation between the predicted

and measured data can be evaluated by applying a numerical correlation tool, such as the Modal Assurance Criteria (MAC) [1]. Subsequently, the analytical models can be improved by performing model updating to bring the model closer to the experimental counterpart.

### **1.1.3 Experimental modal analysis**

Modal analysis has become a very interesting domain for the past several decades. It has turned into an established technique to analyse the dynamical behaviour of structures (especially large and complicated ones), for instance, in the automotive and aerospace industry. Experimental modal analysis or modal testing [2, 3] is a field of measuring and analysing dynamic response of structures when excited by certain inputs (either by an instrumented hammer or a shaker), in order to produce a set of frequency response functions (FRFs) that contain inherent dynamic properties of a structure. Further analysis (such as curve fitting) can be carried out to estimate the modal parameters of the structures.

EMA plays an important role in design and analysis of engineering structures. It is normally conducted for validation of numerical models before they can be used for further detailed analysis. Modal parameters extracted from the EMA can be used in FE model updating procedure (as explained in Section 1.1.4) in order to bring the numerical models closer to the experimental models. The measured FRFs and modal parameters can also be utilised in damage identification procedures, as explained in Section 1.1.6.

### **1.1.4 Finite element modelling and model updating**

Structures with simple and standard geometrical shapes with well-established properties can be solved by using equations of motion describing their dynamics behaviour. For example, there are well-known solutions to the equations of motion for simple structures such as beams and plates. However, these analytical approaches are often not realisable to represent the dynamics behaviour of large and complicated structures such as an automotive BIW, hence FE analysis have to be carried out.

FE analysis has become the most popular technique in structural dynamic analysis, owing to recent advances in numerical methods and availability of powerful computing facilities. FE modelling enables prediction of structural behaviour under different types of loadings, so any deficiencies in the design of a structure can be detected from the early stage of design process. For example, an FE model can be used to predict vibration behaviour of a proposed design and modifications can be made to the design if any problems are found in the analysis, which can significantly reduce the number of expensive prototypes and experiments, as well as time-to-market.

Typically, extensive FE models are utilised in predicting the overall response of a real structure, which leads to highly expensive computational effort. In order to avoid the computational issue, it is acceptable for FE models to have reduced details by making certain assumptions and approximations, for instance by omitting certain local features. Unfortunately, this normally results in FE models that are susceptible to errors or inaccuracies, mainly due to inadequate modelling details, false or inaccurate assumptions used in the models, uncertainties in modelling, lack of information regarding the actual structures, and etc..

Obviously, it is always important to validate developed FE models with experimental data (as mentioned in Section 1.1.3) in order to ensure that appropriate models have been obtained. However, experimental and FE models are not always in perfect agreement, thus FE model updating has to be performed by minimising the difference between the FE and the experimental results, so that better correlation of the two models can be achieved. This results in reliable FE models that can be employed with full confidence in further analysis.

The FE model updating procedures can be performed either as one-step direct procedures or iteratively [4]. The former [5] directly reconstruct the global mass and stiffness matrices based on reference data in a single iteration, which consequently produces an updated model that replicates the measured data exactly. This removes the need for iteration, hence excessive computational effort can be avoided. However, the updated mass and stiffness matrices cannot always be related to physical changes of the FE model since there is no mechanism to control the parameter changes in the updating process, therefore the updated models are not physically meaningful. On the other hand, the latter methods (such as sensitivity-based methods [6, 7]) iteratively modify the structural parameters by minimising the differences between the model and reference data, thus the updated parameters are physically meaningful.

FE model updating can be also categorised into deterministic and non-deterministic model updating methods. Deterministic model updating methods [4] have already been well established, both in method development and applications to industrial-scale structures. In the deterministic methods, an FE model is updated by minimising the difference between its predicted data and a set of experimental data. The measured data is assumed to be deterministic, which is not always true in reality owing to the fact that structural properties are normally uncertain and thus uncertainties exist in the dynamic response. For instance, properties of an individual structure normally change with time due to environmental erosion and damage [8], and also when the structure is being reassembled. It is also unavoidable to have manufacturing variability [9–11] that exists among nominally identical structures, built in the same way from the same materials, such as in a mass production of automotive BIW. Therefore, numerical predictions based on the deterministically updated models cannot al-

ways ensure an accurate representation of the actual structure. Although deterministic methods could provide fairly good results, there is still a necessity to integrate some statistical information of the structures with algorithms of the deterministic model updating in order to incorporate the effect of uncertainties. Because of this, the use of non-deterministic model updating methods have recently become popular since they allow for manufacturing variability and modelling uncertainty to be incorporated. In non-deterministic model updating, numerical models with randomised parameters can be updated to match their experimental counterparts. As a result, robust and credible models are produced which in turn increase confidence in design and analysis of such structures. The non-deterministic model updating problems are computationally expensive, mainly due to the randomised parameters, so various assumptions and simplifications have to be made to ensure the efficiency of the methods.

### **1.1.5 Uncertainties in structural dynamics**

Uncertainties can be classified into *aleatory* and *epistemic* uncertainty, based on whether the source of uncertainties is reducible or not [12–14]. Aleatory uncertainty is derived as an irreducible uncertainty that arises from heterogeneity or diversity in a population (for example, intrinsic randomness in a set of structures) and frequently cannot be reduced through further study or measurement. This type of uncertainty is also referred to as irreducible, inherent, stochastic uncertainty or variability. For instance, different weight can be measured from different individual product, which will not change no matter how many times and/or how carefully the measurements are taken. Epistemic uncertainty, on the other hand, represents lack of knowledge, therefore can be reduced through further study or measurement. This type of uncertainty is referred to as reducible, subjective or cognitive uncertainty. For example, better information of products produced in the same production line can be obtained by taking more samples to increase the knowledge about the product.

The effects of uncertainties are of growing concern in the design of engineering structures, and issues concerning safety, reliability, performance, and so on have been raised. Problems in modelling engineering structures normally involve both types of uncertainties mentioned above. However, until now there is no clear division between them. For example, variability can also be a subject to lack of knowledge when information within its range is missing, which consequently becomes an epistemic uncertainty.

### **1.1.6 Damage identification**

Structural damage identification is a problem of interest in many engineering industries and the development of a methodology for accurate and reliable condition assessment

of structures has become very important. Furthermore, extensive research activities in damage identification have been driven by public demands and technological advancements (e.g., computing power, sensor technology) that results in development of various methods to detect damage at early stages [15–19]. These methods, in general, may be classified as local damage detection (that refers to non-destructive testing (NDT) such as CT scanning and ultrasonic) and global (or vibration-based) damage detection [15, 20]. Local damage detection methods utilise only information obtained from the damaged structure in order to determine the existence and location of damage. While they are proven to be very effective for small and regular structures, they are not as effective for large and complicated structures. Damage in such structures are better investigated by using the global vibration-based damage detection methods.

The main principle of the vibration-based damage detection methods rely on the fact that dynamical behaviour of structures can largely be influenced by damage, therefore the occurrence and evolution of damage can be detected by monitoring the changes in modal parameters and/or FRFs. These methods can be divided further into traditional and modern types. The former utilises the dynamic characteristics of the structures, such as the natural frequencies, modal damping and mode shapes, which requires the EMA to be conducted. Information from the EMA can be used to determine, identify, locate and quantify the damage. However, due to their dependency on the EMA (which can be costly and time-consuming) and other issues as outlined by Yan et al. [20], the modern type damage detection has become quite favourable. Examples of the modern damage detection methods include the Wavelet Analysis, Genetic algorithm and Artificial Neural Network.

## **1.2 Summary of related research**

Modelling of joints is always difficult, mainly due to complex characteristics of the joints (e.g., existence of local effects such as geometrical irregularities, material inhomogeneities and defects) that are not taken into account in the FE model, and a requirement of using a simple yet accurate FE model to represent the joints for real application such as in the automotive industry. There have been a number of joint models developed, ranging from very detailed models (that always lead to an overwhelming computational effort) to very coarse models (which may or may not accurately represent the particular joints), as extensively reviewed by Palmonella et al. [21–23]. A compromise must be reached in developing such models, hence extensive research effort can be seen in the topic as discussed in Chapter 3. The use of accurate coarse FE models of the joints would allow computational analysis to be performed on structures that contain thousands of joints (for instance, car structures, bridges, buildings, etc.).

With increasing reliance on computational analysis, the need to bring the represen-

tations of numerical models to be closer to experimental model resulted in extensive research and development of the FE model updating. This led to a generous amount of publications on the topic, as summarised by Mottershead and Friswell in Ref. [24]. Despite extensive research in the field, there still exists a fundamental problem of non-unique solutions. This shows that, although the topic is well maturing, the success seems to rely on the engineering understanding and the skill of the analyst in conducting the updating procedure.

As explained in Section 1.1.4, demand for improved computational methods that incorporate uncertainties in numerical computation is growing. When uncertainties are taken into account, a deterministic problem then changes to a non-deterministic (or stochastic) problem. In non-deterministic problems, response of a structure can no longer be precisely predicted. Therefore, the ability to numerically predict the behaviour of a structure with uncertainties is very useful and of great scientific value. Refs. [6, 9–11, 25] are amongst many published papers covering the stochastic model updating approach.

A substantial amount of research has also been made over the past decades in the damage identification of structures. Early detection of damage or defects will enable necessary actions to be taken, which in turn will avoid further problems. Originally, visual inspection has been the most commonly used method in observing structural damage. However, as structures become more complicated, the efficiency of the conventional visual inspection is reduced. Consequently, various methods have been developed to detect damage at early stages, as reported in Refs. [15, 17, 18, 26]. To date, a majority of research appears to focus on damage identification algorithms based on the modal properties. One of the most frequently used methods is the FE model updating [27], which has been applied successfully in many fields. The FE model updating method delivers an efficient, non-destructive, global damage identification technique, which is based on the fact that the modal parameters of the structure are affected by structural damage. Therefore, the FE model can be updated to match the measured modal parameters from the damaged structure in order to identify the structural damage, which is normally represented by a reduction in the stiffness properties of the elements in the model. However, damage algorithms based on measured FRFs have received increasing interest quite recently. Modern detection methods, as mentioned in Section 1.1.6, have also become quite popular in damage identification problems.

### **1.3 Overview of research**

Assembled structures such as automotive BIW, bridges and buildings, are typically constructed by structural elements (for instance, beams and plates) that are connected together by structural joints. In automotive industry, one of the most extensively used



type of joints to join panels to make the automotive BIW is spot weld joint [28], normally produced by traditional resistance spot welding (RSW). However, owing to a strong interest in the use of advanced and lightweight materials (e.g. aluminium alloy, which is very problematic if welded using the conventional RSW [29]) for BIW applications in recent years, the use of laser welding (LW) for producing spot welds is receiving increasing consideration.

A typical BIW, which is normally made of layers of thin metal sheets, can contain thousands of spot weld joints. Along with providing connections between sheets of metals, the properties and characteristics of these joints also significantly contribute to the vehicle's structural stiffness and dynamic characteristics. So, it is very important to have an acceptable FE model of the joints in order to evaluate the dynamic behaviour of such structures. It appears that most of the studies regarding spot weld joints have concentrated on spot welds made by the RSW [29–32], while modelling work related to welds made by LW have focused mainly on simulating the welding process itself [33–36]. To the author's best knowledge, there is no reported work on modelling the dynamic behaviour of structures with laser welds, which is the main objective of this thesis.

This thesis focuses on modelling of weld joints produced by laser welding. Existing elements available in commercial FE software are researched and a suitable element is chosen to represent the laser weld joints. Important issues related to laser weld joint modelling and its application to a structure are addressed and discussed. A previous work presented by Mottershead et al. [10] has been used as main reference in this thesis because of its relevance to the work conducted in this research. A set of laser spot welded structures are used (as explained in Chapter 4) and an FE model representing the structures is developed systematically starting from an initial FE modelling to deterministic FE model updating to improve the correlation between the initial FE and the experimental models. Variability that exists in the test structures is also investigated and non-deterministic (or stochastic) model updating is carried out by using the perturbation method [11,25]. Statistical properties of experimental data are considered and updating parameters are treated as random variables.

The developed FE model is also used in damage identification exercise. In this thesis, damage identification is presented in two parts: (1) identification of defects, and (2) identification of real damage in the welded structure. In the first part, a defective structure is selected from the set of nominally identical structures and FE model updating procedure is performed in order to quantify the defects in the defective structure. In the second part of damage identification, a damaged structure is investigated experimentally and its experimental data is employed in the identification process. Again, FE model updating is employed for the purpose.

### 1.3.1 Original contributions of the research

The main original contributions delivered by this research are listed as follows.

1. Most of the modelling works reported in the literature cover the spot weld joints made by the RSW process, while reported works related to the laser weld joints are mainly for simulating the welding process itself. To the author's best knowledge there is no reported work on modelling the dynamic behaviour of structures with laser welds, which has been successfully conducted in this thesis.
2. The FE model of the laser weld joints should be simple yet accurate enough to be used in real applications such as in the automotive industry. Hence, an existing element available in commercial FE package (i.e., CWELD in NASTRAN) is selected and a guideline on how it can be utilised for representing the laser weld joints is presented.
3. The developed deterministic FE model of the welded structures is reliable enough to be used in further analysis, namely the stochastic model updating and vibration-based damage identification, for verifying the feasibility of using the model in the dynamic predictions of laser welded structures. The results from both the stochastic and damage analysis are well correlated with their experimental counterparts.
4. The combined use of CWELD and NASTRAN's structural optimisation code (SOL 200) demonstrates the feasibility of implementing future analysis within a NASTRAN environment so that the developed method can be used for complicated structures by other researchers.

### 1.3.2 List of publications

- N. Abu Husain, H. Haddad Khodaparast, A. Snaylam, S. James, G. Dearden and H. Ouyang. Finite element modelling and updating of laser spot weld joints in a top-hat structure for dynamic analysis. *Proc. IMechE Part C: J. Mechanical Engineering Science*, 224:851-861, 2010.
- N. Abu Husain, H. Haddad Khodaparast and H. Ouyang. FE model updating of welded structures for identification of defects. Accepted for publication in the *International Journal of Vehicle Noise and Vibration*.
- N. Abu Husain, A. Snaylam, H. Haddad Khodaparast, S. James, G. Dearden and H. Ouyang. FE model updating for damage detection - application to a welded structure. *Key Engineering Materials*, 413-414:393-400, 2009.

- N. Abu Husain, H. Haddad Khodaparast, A. Snaylam, S. James, G. Dearden, M. Sharp and H. Ouyang. Modal testing and finite element model updating of laser spot welds. *Journal of Physics: Conference Series*, 181:012014 (8pp), 2009.
- N. Abu Husain, H. Haddad Khodaparast and H. Ouyang. Parameter selections for stochastic uncertainty in dynamic models of simple and complicated structures. *Proceeding of the 10th International Conference of Recent Advances in Structural Dynamics*, Southampton, UK, July 2010.
- N. Abu Husain, H. Haddad Khodaparast, J. E. Mottershead and H. Ouyang. Application of the perturbation method with parameter weighting matrix assignments for estimating variability in a set of nominally identical welded structures. *Proceeding of the 10th Biennial Conference on Engineering Systems Design and Analysis*, Istanbul, Turkey, July 2010.

## 1.4 Organisation of the thesis

**Chapter 2** reports welding technologies usually employed in the automotive industry. Traditional resistance spot welding is described and much recent laser welding is introduced. The use of the two welding technologies in the automotive applications is also discussed. Other welding technologies are mentioned.

**Chapter 3** presents a literature review of FE models developed for the most common types of joints (i.e., bolted joints, weld joints and some others). Attention is given to the weld joints, and several detailed and coarse models are included. An FE model of weld joints that is most suitable for the research is selected and discussed in detail.

**Chapter 4** explains the experimental modal analysis, including some explanation on the basic measurement system for vibration analysis. The chapter then describes the structures used in this research, which are a set of nominally identical laser spot welded structures, and details of the experimental modal analysis performed on the structures are also included. A brief explanation on the laser welding procedure conducted to join the structures is also presented.

**Chapter 5** describes the FE modelling and updating of the structures. Firstly, the development of FE models of substructures is given and FE model updating is conducted to minimise the errors between the FE results and their experimental counterparts. Having done this, the only errors when modelling the welded structures are assumed to be coming merely from the laser spot weld model. Then, several FE models of spot weld are investigated and the best option is selected to represent the laser weld joints.

Using this spot weld model and the FE models of the substructures, the laser welded structures are modelled and updated to the experimental data.

**Chapter 6** presents the non-deterministic (or stochastic) FE model updating of the welded structures, employing the FE models developed in Chapter 5. The perturbation method used for the stochastic analysis is explained and a guideline for parameter selection is detailed. The stochastic updating of the welded structures is conducted based on two different assumptions, which results are compared and discussed.

**Chapter 7** reports the work done on damage identification. Several identification methods are described and a vibration-based damage identification is employed. Methodology for identification of damage is given and the use of FE model updating in damage identification is also explained. This chapter is divided into two parts: firstly on identification of defects, and secondly for identification of damage.

**Chapter 8** outlines the main conclusions achieved in the research, as well as some recommendation for future work. Published journal papers and conference proceedings are also listed.



# Chapter 2

## Welding Technologies in Automotive Applications

### 2.1 Introduction

Resistance spot welding (RSW) is widely used for producing a typical BIW, which is normally made of thin metal sheets that are connected together by thousands of spot welds. However, owing to a strong interest in the use of advanced and lightweight materials (such as aluminium alloys) for BIW applications in recent years, the use of laser welding for producing spot welds is receiving increasing consideration. This chapter describes the two welding processes and discusses their applications in the automotive industry. The discerning features and attributes of the processes are identified and comparisons are made wherever relevant. Advantages and limitations of these welding technologies are also discussed. Other welding technologies are included at the end of the chapter.

### 2.2 Resistance spot welding (RSW)

RSW has been a dominant joining process since decades ago, used in a wide range of industries but notably for the production of vehicle body structures made of carbon steel sheets. The process is much preferred in mass production because of its simplicity and cost-effectiveness. The process has been frequently used for joining metal sheets of up to 3 mm thick [37]. Thicker sections can be joined with larger machines, but it is more practical and economical to use other types of welding for the purpose.

#### 2.2.1 The RSW process

RSW involves the application of heat and pressure when joining two or more metal sheets at a localised area. As the name implies, the heat for welding is generated within the material by resistance to the flow of electrical current passing through the

workpieces. Spot weld joints are normally made one at a time and the process is illustrated in Fig. 2.1. The workpieces are squeezed by a pair of copper alloy cylindrical electrodes to provide sufficient contact at the joint interface, and electrical current is then conveyed at the point of joining. The resistance to the current flow heats the faying surfaces to reach the melting point, thus forming a pool of molten metal that eventually solidifies into a weld nugget after cooling. Spot welds made by the RSW process are unique because they are formed internally with relation to the faying surfaces of the base metals, as depicted in Fig. 2.2.

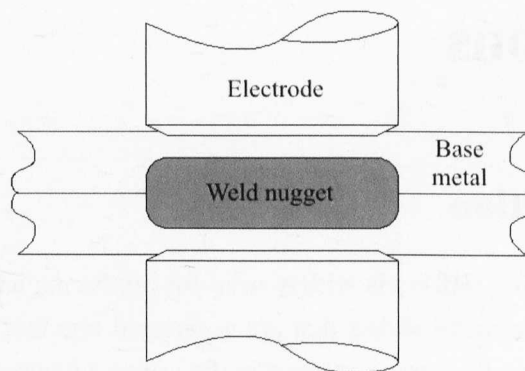


Figure 2.1: Illustration of the RSW process

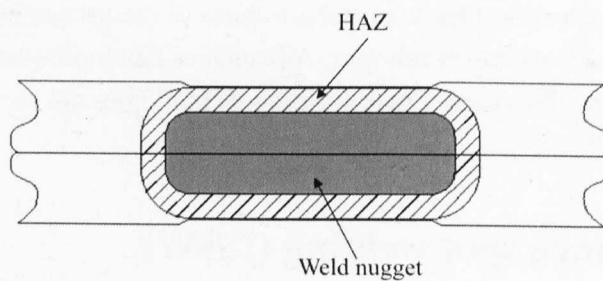


Figure 2.2: Illustration of the spot weld made by RSW

RSW relies on the amount of current flowing to produce the heat necessary to make the spot weld and the resistance in the welding process, which is composed of several main parts [37] as follows.

1. Resistance of the electrodes
2. Contact resistance between the electrodes and the workpieces
3. Body resistance of the workpieces
4. Contact resistance between the workpieces

These resistances are in series; therefore current flow from the electrodes will be retarded at each point of resistances. The contact resistance is significantly influenced by the conditions (such as the cleanliness, oxidations and smoothness) of the workpieces, and is proportional to the resistivities of the materials in contact (i.e., between the electrodes and the workpieces, or between the workpieces themselves). On the other hand, the resistance of the base metal is directly related to the resistivity of the material itself and the length of the current path (i.e., thickness of the workpiece). The body resistance is significantly important for materials with high resistivity, while the contact resistance is more important for high conductivity materials. By knowing the total resistance, the electrical current and duration of flow needed for producing a spot weld joint can be easily calculated.

## **2.2.2 Application of RSW in automotive industry and its limitations**

Since many decades ago, the RSW is used almost universally in the automotive manufacturing industry to weld layers of metal sheets to form a car structure, which typically contains thousands of spot welds. The process is normally fully-automated by employing industrial robots in the assembly lines in order to cope with the high-volume production. Despite being very popular, there are two key issues frequently associated with the conventional RSW process for automotive body assembly.

### The need for two-sided access, lack of flexibility

Because of the nature of a conventional RSW machine, metal sheets have to be inserted between the upper and lower electrodes. Hence, considering the size of a typical automotive BIW, a large spot welding gun is normally needed in order to make a weld on such structures. Furthermore, as the shape of structures becomes more complicated, many spot weld joints are usually located in areas that are inaccessible by the spot welding gun. Thus, the use of the spot welding gun highlights the lack of flexibility in the RSW process.

### Problematic when joining modern materials and their combinations

Carbon steels dominate the biggest percentage of material being welded with the RSW process. However, as the demand for automotive fuel efficiency increases, alternatives to carbon steel have been researched and aluminium alloys have been considered to be the most potential substitute for the application. The material is becoming vital to the automotive and aerospace industries, mainly because its inherently low density, high durability and superior corrosion resistance than carbon steels. Moreover, the material is ductile, more flexible in terms of manufacturing processes (i.e., can be easily machined, cast, drawn and extruded) and 100% recyclable.



Since weld nugget formation is greatly influenced by the properties of materials such as the melting temperature, density, resistivity, thermal conductivity and coefficient of thermal expansion, a big challenge is faced when joining aluminium using the RSW process due to its higher dynamic resistance and thermal conductivity than those of carbon steels (refer Table 2.1). Heat dissipates very quickly in materials with high thermal conductivity, causing problems in obtaining localised melting. The quick heat dissipation also results in cracking upon solidification process of the welds. Hence, additional heat must be given when welding such materials, which consequently results in the requirements of more powerful and expensive RSW machines, while extra measures must be taken during the cooling process. In addition to that, aluminium is very reactive and can be easily oxidised, creating a barrier on the welding surfaces. Furthermore, the contact of aluminium and copper during the welding process will form an alloy, which then accelerates the electrode wear [29]. Thus, the RSW process becomes more complicated, and requires careful, time-consuming and expensive preparations beforehand.

Table 2.1: Comparison between carbon steels and aluminium alloys

Properties	Carbon steel	Aluminium alloys
Young's modulus (GPa)	190 to 210	65 to 75
Density ( $\text{g/cm}^3$ )	7.75 to 8.05	2.60 to 2.80
Melting temperature ( $^{\circ}\text{C}$ )	1300-1500	630-650
Electrical resistivity at $20^{\circ}\text{C}$ ( $\Omega\text{m}$ )	1 to 10 ( $\times 10^{-7}$ )	28 to 67 ( $\times 10^{-7}$ )
Coefficient of thermal expansion (per $^{\circ}\text{C}$ )	11 to 15 ( $\times 10^{-6}$ )	22 to 23 ( $\times 10^{-6}$ )
Thermal conductivity at $20^{\circ}\text{C}$ (W/m.K)	44 to 52	120 to 210

Another problem of RSW is fronted when joining a combination of materials with different properties, as in the production of tailor welded blanks. The difference in properties between the upper and lower sheets will make it very problematic to be welded using the RSW process. This limitation reduces the applicability of the RSW for modern manufacturing technologies recently developed for the automotive and aerospace industries, promoting the use of other welding processes.

The first limitation can be avoided by employing modern RSW technology, as demonstrated by Cho et al. [38]. The new RSW process allows for a single-sided access with low electrode force. This improvement offers great potential in joining large panels, and in producing weld joints at locations that are normally inaccessible using the conventional RSW. In addition, the new system provides a simpler configuration; hence smaller facility can be achieved. Nevertheless, few issues (in addition to the second limitation described above) still exist with the new configuration. Because of the low electrode force, the thickness of the upper sheet should not be more than 1.4 mm,

and the lower sheet should have a certain amount of stiffness in order to support the electrode force. From all the issues, it can be concluded that the RSW process is lacking practicality for the assembly of modern automotive structures. Fortunately, there is a viable option that has the potential to overcome these limitations, i.e., the Laser Welding technology, explained in the next section.

## **2.3 Laser Welding (LW)**

Laser welding has been employed successfully to join a mixture of metals and alloys, including carbon steels, aluminium alloys, titanium, refractory metals, etc. Generally, there are two types of lasers used for welding, i.e., solid state lasers (e.g., neodymium in YAG (Nd-YAG) lasers) and gas lasers (e.g., carbon dioxide (CO<sub>2</sub>) lasers), that are normally employed for different applications. The high-speed welding process of laser welding makes it suitable for automation, but due to the expensive cost of setting up the equipments, the application of the technology for low-volume production is not always economical.

### **2.3.1 The laser welding process**

In the laser welding process (see Fig. 2.3), a focused high-powered laser beam is concentrated from a distance over a workpiece at a welding point, causing the base metal to melt. The welding process is achieved by the use of focusing optics with long focal length and a computer-controlled turning mirror, which converts the powerful laser beam from the laser source into a usable focused laser beam for melting the base metal. A pool of molten metal with deep penetration is created, which later solidifies into a weld nugget. Note that the construction of the weld nugget produced by laser welding (see Fig. 2.4) is completely dissimilar to the ones produced by the RSW process (Fig. 2.2). Interestingly, unlike many of the other joining processes, the overall dimensions of the weld nugget can be customised in laser welding by adjusting welding parameters such as the laser energy and focal point position.

Inert gas shielding is commonly applied in several welding processes including the laser welding to prevent oxidation or degradation of weld joints. In the laser welding process, this is achieved by using a shrouding system comprised of a gas jet aimed at the laser beam spot on the metal surface, as shown in Fig. 2.3. Pure Helium and Argon, or a mixture of both, are the most frequently used shielding gases in welding, mainly because of their cost-effectiveness and high ionisation potential.

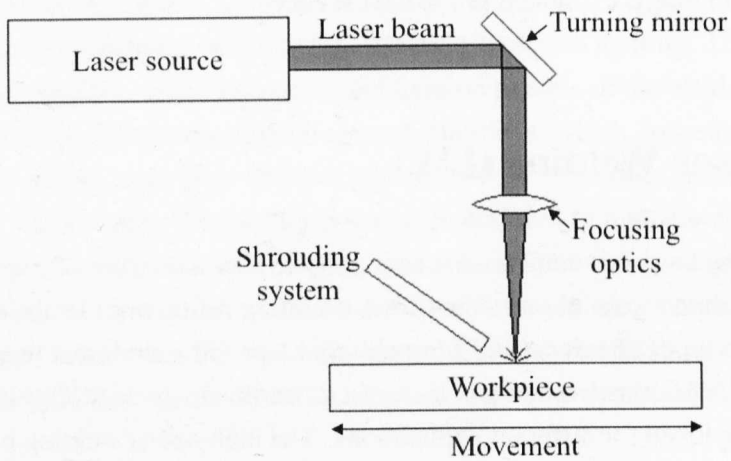


Figure 2.3: Illustration of the laser welding process

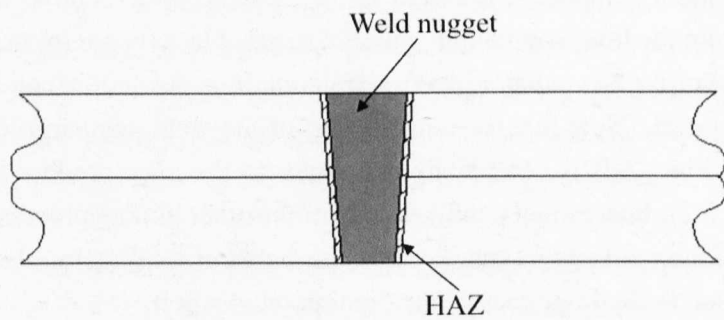


Figure 2.4: Illustration of the spot weld made by laser welding

### **2.3.2 Application of laser welding in automotive industry and its advantages**

Applications of laser welding in the automotive industry has increased steadily in recent years, with major automotive companies (such as BMW, Mercedes and Audi, just to name a few) employing the technology in the production of their car structures. The technology has received such a significant interest, it can now be considered as a primary alternative for the conventional joining processes such as the RSW. While the laser welding process offers many potentials in the automotive industry, the initial costs for setting up a laser welding system are considerably higher than that of a conventional RSW. Nevertheless, the process is ideal for high-volume production and the operational costs are expected to be lower as production volumes grow.

Laser welding can be employed efficiently and economically in place of many conventional joining processes in many different applications, with many advantages of the laser welding process over the conventional processes acknowledged. However, in order to obtain maximum benefit from laser welding, it is important to understand the fundamental advantages that the process has to offer. Some of the advantages of laser welding in comparison with RSW are as follows:

#### Non-contact operation, one-sided access

The laser welding process does not require physical contact with the workpieces. The non-contact operation of the laser welding promotes the use of simpler fixturing than the RSW and eliminates the issue of surface deformation from the clamping action of the spot welding gun, while the one-sided access improves weldability in otherwise hard-to-reach areas. In addition, the region of HAZ resulting from the laser welding process is very narrow (as illustrated in Fig. 2.4), hence better quality weld with minimum part distortion can be achieved and weld joints closer to sensitive components can be established.

#### Highly-flexible operation

The ability to manoeuvre the beam with the use of mirrors offers for more flexibility during the welding process, which is one of the main significant advantages of laser welding in comparison with the RSW. This allows for faster changeover from one weld location to another, which means applying more welds in a single station and consequently reduces the need of having too many welding stations as in the RSW. Accordingly, savings in terms of time, space and tooling costs can be achieved. Furthermore, the flexibility in welding also facilitates the possibility of different configuration of weld joints, including continuous, stitched, butt and fillet welds.

### Ability to weld a wide range of materials

Laser output used in the laser welding process is not electrical, therefore unlike the RSW the process of laser welding is not affected by the properties of the materials (e.g., resistivity and conductivity). Because of this, the laser welding technology has become an established joining method for a wide variety of metals and their alloys. Furthermore, the laser welding has more capability to weld dissimilar materials than the RSW.

### Applicability to new manufacturing technologies

Changes in the design of automotive structures contribute greatly to new manufacturing technologies in producing automotive subcomponents, in order to make cars safer, lighter, and more environmentally efficient. Tailor welded blanks is one of those new technologies, achieved by laser welding a combination of steel sheets with different geometrical and material properties into a single flat blank prior to forming to provide the optimal properties for specific applications. The technology allows fundamental significance in terms of weight savings by removing overlapping joints and unnecessary reinforcements, reduction in material waste through proper utilisation of materials, and improvement in structural stiffness/weight ratio, integrity and crash performance.

## **2.4 Other welding techniques**

### **2.4.1 Arc Welding**

Arc welding refers to a group of welding processes that use an electric arc as the heating source to melt and join metals. Gas Metal Arc Welding (GMAW) and Gas Tungsten Arc Welding (GTAW) are two commonly used arc welding in the automotive and aerospace industries. The GMAW (also referred as metal inert gas (MIG) welding) requires a continuous and consumable wire electrode to provide for filler materials during the welding process, while the GTAW (also known as tungsten inert gas (TIG) welding) uses a non-consumable tungsten electrode during welding. A shielding gas is supplied during welding in order to protect the arc and weld areas from the environment, and also to provide the desired arc characteristics.

### **2.4.2 Electron Beam Welding (EBW)**

Electron beam welding is accomplished by high velocity electrons that form into a concentrated beam to produce an intense local heating at a welding point over the workpieces, resulting with a deep and narrow weld joint [37]. As the laser welding process, EBW is well-suited to mass production as it is a non-contact joining technology, reducing the need for complex and large fixturing. Initial setting-up costs are

expensive, but similar to laser welding, the operational costs are expected to reduce with increasing volume of production. Examples of typical application in the automotive applications are in the assembly of gears and turbochargers.

## **2.5 Conclusions**

Automotive engineers are always on the look-out for methods to reduce vehicle weight in order to improve fuel efficiency and performance. These can be achieved by employing new technologies in manufacturing (e.g., tailor welded blanks) and also using advance lightweight materials such as aluminium and its alloys. The use of new materials and manufacturing technologies highlights the limitations of the conventional RSW in the application of modern automotive structures production. Consequently, laser welding has becoming a viable option for overcoming those RSW limitations.

Due to the increase of interest in the applications of laser welding for the automotive body production, it is important to understand the significance of the laser weld joints towards the dynamics of the vehicle. However, there are almost no reported works in the literature regarding the dynamics of laser welded structures, thus it is the aim of this research to investigate such structures for their dynamics prediction.



# Chapter 3

## Review of FE Modelling of Joints

### 3.1 Introduction

Structural systems are normally constructed by assemblies of components that are connected together by means of structural joints. There are many types of joints used in fastening components together, with bolted and welded joints being the most commonly used in structural design. These connecting elements bring significant contributions towards the dynamic characteristics of the structures. However, due to discontinuity in the structure surrounding the joints, they usually possess non-linear and complex behaviour. Furthermore, dynamic analysis of complicated structures with many joints is only practical with simplified joint models. Thus, constructing proper predictive models of structures with joints and interfaces has become more significant, which was discussed in a white paper by Dohner [39]. Some of published works available in modelling these joints are reviewed in this chapter, with attention given to modelling of weld joints due to its relevance to this research. Modelling of other types of joints (i.e., rivets and surface-to-surface joints) is included towards the end of this chapter.

### 3.2 Modelling of bolted joints

Bolted joints are one of the most dominant fastening mechanisms used in joining components together, largely because they can be easily disassembled, maintained and inspected. However, this type of joints has many complexities (such as nonlinear frictional behaviour, pretension effect, etc.) that are difficult to simulate in FE modelling. As the behaviour of the joints plays a significant role in the dynamic characteristics of structures, the need for developing accurate predictive models of the joints is very demanding. Modelling work associated with the bolted joints has been addressed by several authors, including Gaul and co-workers [40, 41], Oldfield et al. [42], Ibrahim and Pettit [43], and Kim et al. [44].

Gaul and Lenz [40] developed a detailed two-dimensional (2D) FE model of a lon-



itudinal resonator (a bolted lap joint under axial excitation) to provide understanding of different slip-stick mechanisms in the vicinity of the joints (Fig. 3.1(a)). The resonator was modelled with four-node plane stress elements and the bolted joint was modelled as illustrated in Fig. 3.1(b). Lumped mass was assigned for the longitudinal resonator, while the bolt hole and shaft were neglected. The authors also studied the dynamic behaviour of structures assembled by several bolted joints. For this purpose, a reduced model (known as Valanis model) was derived and used to represent the joints in subsequent finite element analysis, allowing the dynamic response of complicated structures with many bolted joints to be analysed at much reduced cost.

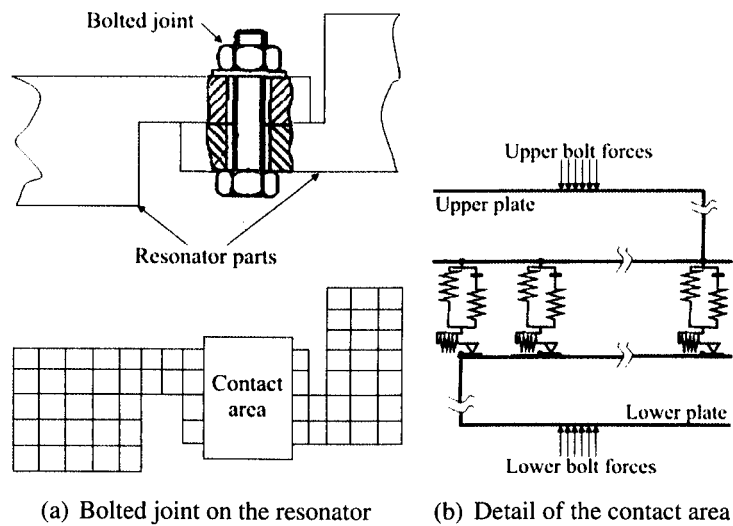


Figure 3.1: FE models of bolted joint by Gaul and Lenz [40]

The role of friction in bolted joint connections and modelling issues associated with the frictional behaviour of the joints was discussed thoroughly by Gaul and Nitsche [41], who cited 134 references. The paper addressed some approaches for modelling nonlinear behaviour of the bolted joint connections and classified the basic models of friction for bolted joints into two types, i.e., phenomenological and constitutive models. The former are based on experimental observation, while the latter are based on interface physics in the contact area. A generalised elasto-slip model (known as the Jenkins-element model (Fig. 3.2)) consisting of linear springs and Coulomb friction elements were used to represent the friction interface of the bolted joints. The model was able to simulate the friction force in a bolted joint very well [45]. The Jenkins-element model, alongside another simplified model known as the Bouc-Wen model, was also utilised by Oldfield et al. [42] to get necessary dynamic information when investigating a bolted joint under harmonic loading. Both simplified models were compared with a detailed 3D FE model and it was demonstrated that the dynamic properties of the joint were obtained successfully by the simplified models with a greatly reduced

computational effort.

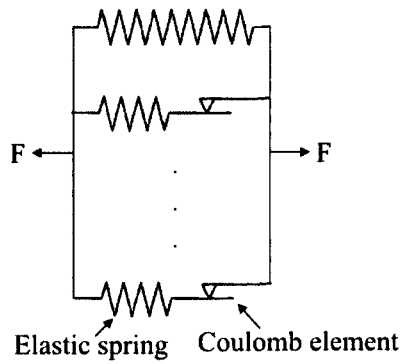


Figure 3.2: The Jenkins-element model

Another highly recommended review paper on bolted joints, presented by Ibrahim and Pettit [43], focused on problems relating to dynamic behaviour of structures with bolted joints, including 516 references. Joint uncertainties and relaxation were discussed and identification of (linear and non-linear) joint properties was a major topic of that paper. Design issues of fully and partially restrained joints, sensitivity analysis to variations of joint parameters and fatigue prediction for metallic and composite joints were also covered.

Kim et al. [44] studied modelling of a structure with bolted joints using four kinds of FE models: 1) a solid bolt model, 2) a coupled bolt model, 3) a spider bolt model, and 4) a no-bolt model, taking into consideration of pretension effect and contact behaviour between joined components. The most accurate model was found to be the solid bolt model; however the most effective model was the coupled bolt model, being approximately 50% faster and used roughly 20% of the memory compared with the solid bolt model.

### 3.3 Modelling of weld joints

In contrast to bolted joints, weld joints are permanent; and spot welds are very commonly used in joining metal sheet-like structures. However, like bolted joints, reliable evaluations of the behaviour of the welds are always a concern, since many factors such as geometrical irregularities, residual stresses, material inhomogeneity and defects in the welds, are difficult to be incorporated in the FE model [10]. Furthermore, a very detailed model of the welds would contribute to an expensive computational effort since there are thousands of such joints in real structures. Therefore, the only practical approach is to model the spot welds with a reasonably coarse model, without penalising the accuracy of the model.

A number of works on the modelling of spot welds have been published (e.g., [32, 46–49]) and most of these were discussed by Palmonella et al. [21]. FE models of the spot weld joints can be grouped into two categories: (i) models for limit capacity analysis, as in [32], and (ii) models for dynamics analysis, as in [49]. The former requires a very detailed mesh in order to work out a smooth stress field within and around a spot weld. On the other hand, models for dynamics analysis use a very coarse mesh, allowing for application of much simpler models with significantly fewer degrees-of-freedom (DOFs). This type of models simulates the stiffness (and mass) characteristics of the actual spot welds and their contributions towards the behaviour of the structure.

### 3.3.1 Models for limit capacity analysis

Models of spot weld for limit capacity analysis normally consist of brick (or solid) or plate/shell elements for modelling the welded regions (or areas surrounding the weld joints), and brick elements for modelling the weld nuggets [50]. For example, Chang et al. [51] modelled spot weld joints in the presence of adhesive, also known as weld-bonded joints, using eight-node brick elements with fine mesh surrounding the weld joints. The welded region was represented by three parts (i.e., the base metal, the spot weld and the adhesive layer (that can be removed to create a spot-weld-only model)), as shown in Fig. 3.3(a). The detail of the model was increased further [52] by incorporating indentation geometry due to the RSW process and detailed representation of the welded region was achieved by dividing the region into four zones (Fig. 3.3(b)) consisting of the base metal, the heat affected zone (HAZ), the weld nugget and the adhesive layer. The HAZ is divided further into five parts with different material properties.

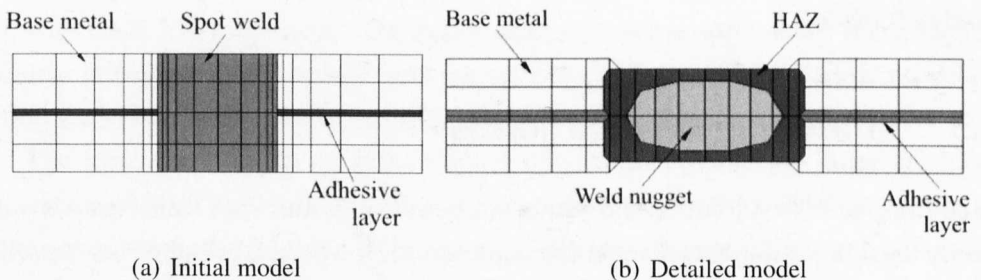


Figure 3.3: FE models of the weld-bonded joints by Chang et al. [51]

Deng et al. [32] addressed the underlying three dimensional (3D) features of the stress field in spot welds under shear and peel loading conditions. A very detailed FE representation of a quarter geometry for a spot weld and its surrounding area was made, with thousands of solid elements used in the modelling (Fig. 3.4(a)). A fine mesh

was employed within the weld nugget, while a coarse mesh was applied elsewhere. However, the material properties of the nugget and base metal were taken to be the same. One of the findings was that stress concentration appeared near the nugget boundary while the centre of the nugget was mostly stress-free, which indicates that the centre of the nugget does not contribute much to the load-bearing capability of the spot weld. A simplified version of this model was presented by Chen et al. [46], as illustrated in Fig. 3.4(b). The solid elements were replaced by shell elements and the weld nugget was assumed to be rigid, hence not modelled explicitly, unlike in the 3D solid model. Apart from the nugget, the rest of the model adopted the same mesh as the detailed model. It was demonstrated that the simplified model was able to estimate the stress field surrounding the spot weld regions. However, very refined mesh must be applied in order to achieve a very good approximation, which again is not always practical when there are thousands of welds.

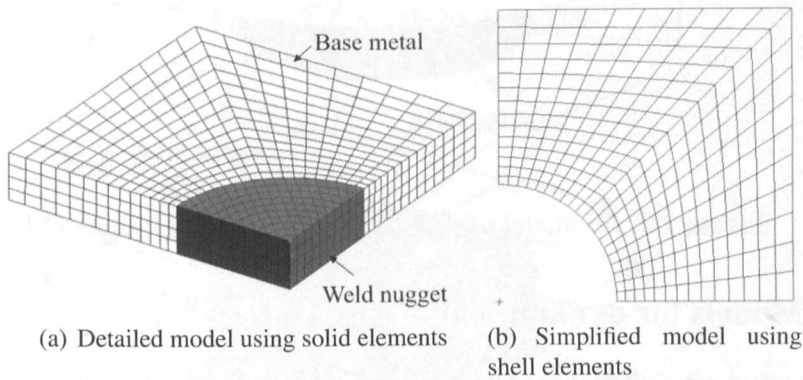


Figure 3.4: FE models for a quarter geometry of spot weld joints by Deng et al. [32] and Chen et al. [46]

Radaj and Zhang [53] studied geometrically non-linear behaviour of spot welded joints using FE model of spot weld as shown in Fig. 3.5. The model consists of plate/shell elements to represent the base metal and solid (i.e., brick) elements to constitute the nugget. The connection between the two element types is achieved by introducing pin-jointed rigid bars connected to the brick and shell elements, in order to link three translational DOFs of the brick elements to five (translational and rotational) DOFs of the shell elements [21].

A similar concept was proposed by Zhang and Richter [54] involving solid elements for the nugget connected to shell elements for the remaining structure by means of shell-to-solid element connector (i.e., RSSCON) available in NASTRAN. RSSCON functions similarly to the pin-jointed rigid bars used by Radaj and Zhang [53], i.e., to link the DOFs of the shell elements to the DOFs of the solid elements. The detail of the model is illustrated in Fig. 3.6.

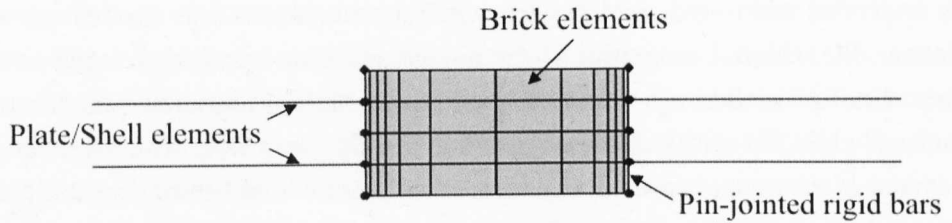


Figure 3.5: FE model of spot weld by Radaj and Zhang [53]

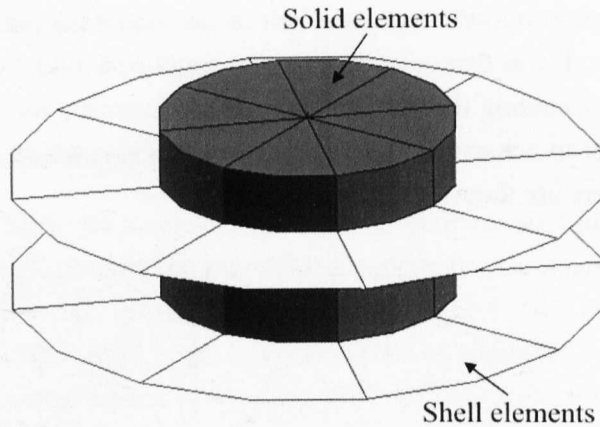


Figure 3.6: FE model of spot weld by Zhang and Richter [54]

### 3.3.2 Models for dynamics analysis

For many years, single beam models have been commonly employed in modelling spot weld joints in industries. In this type of models, an elastic or rigid beam element is connected to two surfaces with congruent meshes to allow a perpendicular node-to-node connection to the surfaces (see Fig. 3.7). According to Palmonella et al. [21], the application of the beam elements in modelling the spot weld joints is inadequate, owing to the fact that the spot weld nuggets are not precisely characterised by the beam elements resulting in underestimation of the spot weld's stiffness. Employing a single brick element can improve the stiffness estimation of the spot weld nugget. Similar to the single beam models, the brick element is connected to two congruently-meshed surfaces and the nodes of the brick elements are tied with coincident nodes of the surfaces in all DOFs, as depicted in Fig. 3.8.

Salvini et al. [48] developed an FE model (Fig. 3.9) that is composed of two circular sheets to represent the welded plates, and a rigid core to represent the spot weld. An FE representation of the rigid core is illustrated in Fig. 3.9(b), where a vertical beam element (with six DOFs at each node) is connected to two sets of beam elements and rigid connectors oriented in radial direction to link the core to the circular plates. Some modification was made on the model, as reported by Vivio et al. [55] and illustrated in

Fig. 3.10. The new model comprises of three main parts: (1) a primary beam that links the upper and lower parts of the model via two secondary links, (2) two sets of internal radiating beams that are attached to the sheets by translational and rotational links, and (3) two sets of external radiating beams that are pinned to the upper and lower sheets. By introducing the external and internal radial beams, vertical displacements are decoupled from in-plane rotations, which is an issue of the previous model [21].

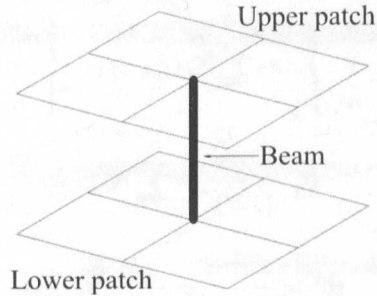


Figure 3.7: Single beam model

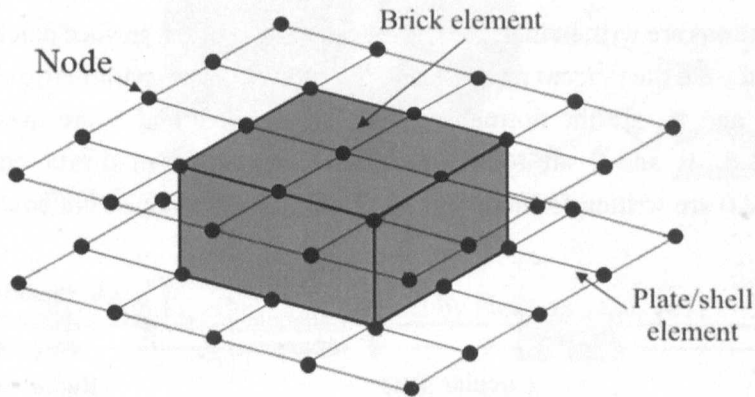


Figure 3.8: Single brick model

Another spot weld model known as Area Contact Model 2 (ACM2) was proposed by Heiserer et al. [47]. The model (shown in Fig. 3.11) was developed using a brick element and the connections to the upper and lower surfaces were established via weighted multi-point constraint (MPC) elements known as RBE3, also available in NASTRAN. The ACM2 is a coarse spot weld model that can be employed for both limit capacity and dynamics analysis. The model allows non-congruent meshes to be employed, thus spot weld joints can be modelled without having to be on the nodes. The ACM2 model requires for the physical properties of the spot weld joints to be considered, which make them suitable as parameters in the FE model updating procedure.

Alternatively, CWELD element (Fig. 3.12) available in the NASTRAN element library can be employed for the dynamics prediction of the spot weld joints. The



element, explained in detail in NASTRAN documentations [56] and Ref. [49], consists of a two-node special shear flexible beam type element with 12 DOFs (six for each node) and each node is connected to a set of nodes from its corresponding patch (i.e., a shell element or a group of shell elements connected to the CWELD element) with constraints from the Kirchhoff shell theory. All six DOFs from each node GA are connected to three translational DOFs of nodes  $GA_i$ , as follows.

$$\begin{Bmatrix} u \\ v \\ w \end{Bmatrix}_A = \sum \mathbf{N}_i(\xi_A, \eta_A) \cdot \begin{Bmatrix} u \\ v \\ w \end{Bmatrix}_i \quad (3.1)$$

$$\theta_x^A = \frac{\partial w}{\partial y} = \sum \mathbf{N}_{i,y} \cdot w_i \quad (3.2)$$

$$\theta_y^A = -\frac{\partial w}{\partial x} = -\sum \mathbf{N}_{i,x} \cdot w_i \quad (3.3)$$

$$\theta_z^A = \frac{1}{2} \left( \frac{\partial v}{\partial x} - \frac{\partial u}{\partial y} \right) = \frac{1}{2} (\sum \mathbf{N}_{i,x} \cdot v_i - \sum \mathbf{N}_{i,y} \cdot u_i) \quad (3.4)$$

These equations are written in the local tangent system of the surface patch at point GA, where  $x$  and  $y$  are the tangent coordinates,  $\mathbf{N}_{i,i}$  represents the parametric shape function matrix,  $\xi_A$  and  $\eta_A$  are the normalised coordinates,  $u$ ,  $v$  and  $w$  are the displacement DOFs, and  $\theta_x$ ,  $\theta_y$  and  $\theta_z$  are rotational DOFs. Another set of similar equations (Eqs. (3.1) to (3.4)) are written for node GB resulting in twelve constraint equations.

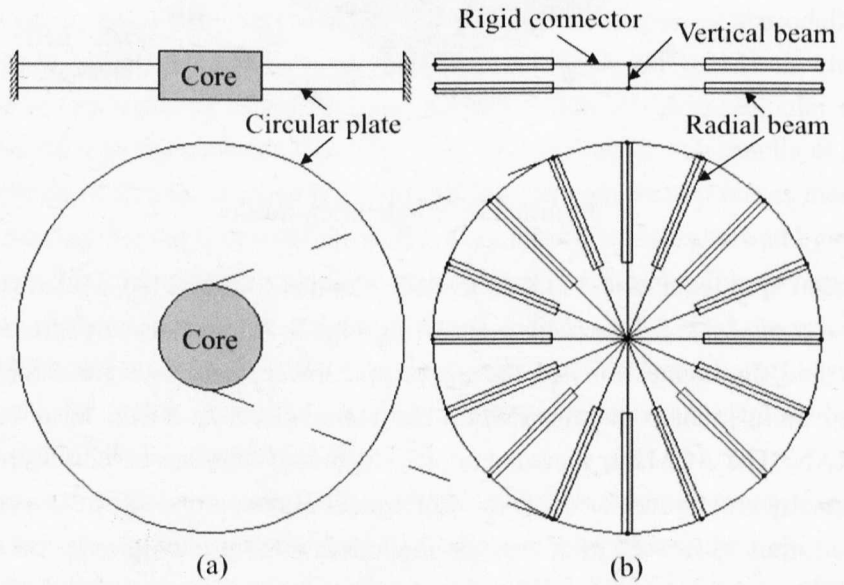


Figure 3.9: FE model by Salvini et al. [48] (a) geometrical representation of the model, and (b) detailed representation of the core

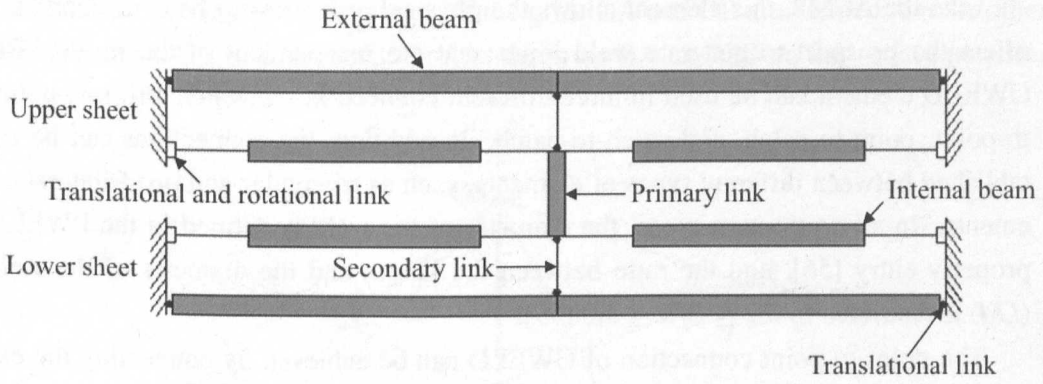


Figure 3.10: Improved model by Vivio et al. [55]

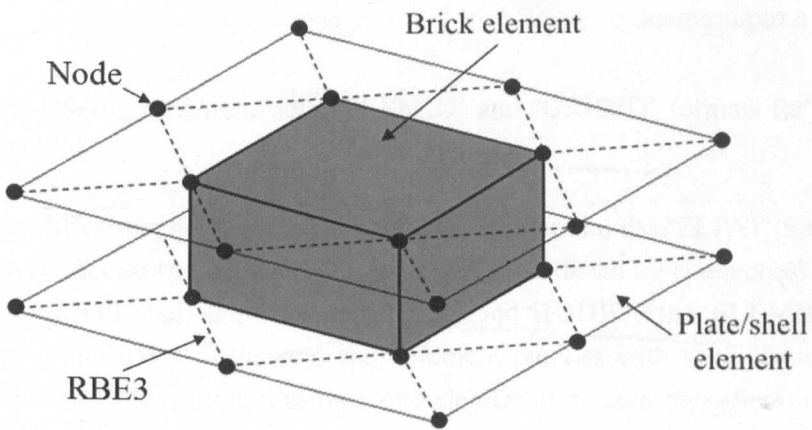


Figure 3.11: The ACM2 model by Heiserer et al. [47]

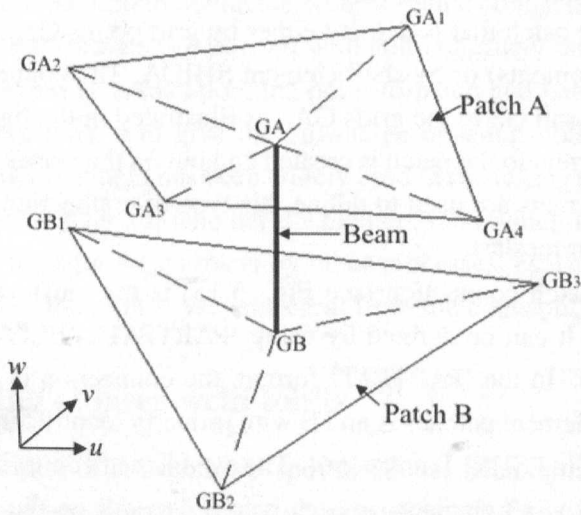


Figure 3.12: The CWELD element available in NASTRAN



Like the ACM2, this element allows the physical properties to be considered and offers the prospect to generate weld joints that are independent of the mesh. The CWELD element can be used in three different connection types [49, 56], i.e., point-to-point, point-to-patch, and patch-to-patch. In addition, the connections can be established between different types of elements, such as triangular and quadrilateral elements. In all connection types, the diameter of the weld is defined in the PWELD property entry [56], and the ratio between the length and the diameter of the weld ( $L/d$ ) is restricted to  $0.2 \leq L/d \leq 5.0$  [49].

The point-to-point connection of CWELD can be achieved by connecting the existing upper and lower vertex grids, GA and GB, see Fig. 3.13. Two shell normals in the direction of GA-GB are automatically generated and their resulting vector gives the weld axis. This type of connection is defined in 'ALIGN' format and congruent mesh is a requirement.

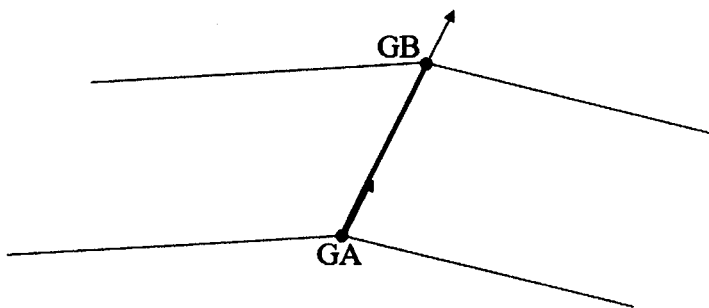


Figure 3.13: CWELD element with 'ALIGN' format for point-to-point connectivity

A point-to-patch connection (Fig. 3.14) is obtained when a vertex grid GS is connected to a surface patch that is defined either by grid points  $GA_i$  (that do not have to belong to shells elements) or by shell element SHIDA. The connection is established by connecting the grid GS to the grids  $GA_i$ , as illustrated in the figure. A shell normal in the direction normal to the patch is created and put on the vertex grid GS. 'GRIDID' and 'ELEMID' formats are used to define this type of connection, and it can be used with non-congruent meshes.

The patch-to-patch connection (see Fig. 3.15) is the most versatile of the three connection types. It can be defined by using 'PARTPAT', 'ELPAT', 'ELEMID' and 'GRIDID' formats. In the 'PARTPAT' format, the connection is established by connecting two shell element patches A and B with property identification PIDA and PIDB that can be defined in PSHELL entry [56]. The established connection (which can connect between 1x1 to 3x3 elements in each patch) depends on the location of GA and GB, and also the size of the weld diameter. Note that, GS is generated from a normal projection on each of the two surface patches, as illustrated in the figure. In this type

of connection, the grid GS is ignored if the grids GA and GB are defined. On the other hand, the grid GS will be used to project the grids GA and GB on the surface patches.

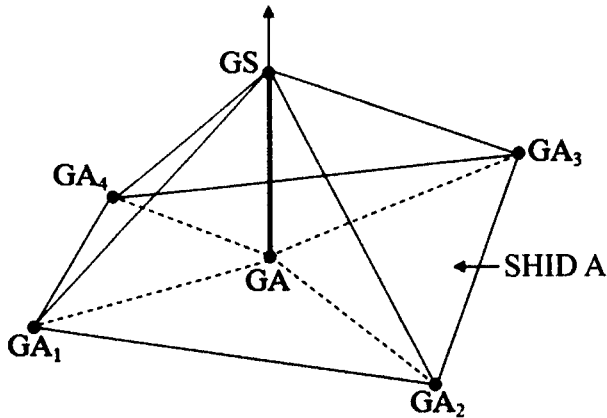


Figure 3.14: CWELD element with 'ELEMID' and 'GRIDID' formats for point-to-patch connectivity

The only difference between the 'PARTPAT' format and the 'ELPAT' format is in terms of the connection of 'ELPAT' format that is established by connecting two shell element patches with shell identifications SHIDA and SHIDB. If the 'ELEMID' format is used, the connectivity of the two shell element patches with shell identifications SHIDA and SHIDB is restricted to only one element per patch regardless of the size of the weld. If SHIDB is not defined, the 'ELEMID' format defines the point-to-patch connection. The format 'GRIDID' is used when connecting the two surface patches with a sequence grid points  $GA_i$  and  $GB_i$ . Similarly to the 'ELEMID' format, the 'GRIDID' format can be used to define the point-to-patch connection when all  $GB_i$  are not given. All of these formats can be used with non-congruent meshes.

From all three types of connection, the point-to-patch and patch-to-patch give the most general connectivity, and give the advantage of using non-congruent meshes. Although the CWELD element has been widely used in modelling spot welds produced by the RSW, it is still uncertain whether the element (and which type of connections) can well represent the spot welds made by other processes, especially Laser Welding as the construction of the joint is very different from the conventional RSW.

### 3.3.3 Modelling of laser weld joints

Although FE modelling of conventional spot welds has been carried out by a number of researchers, there has been no work of modelling the laser spot weld joints for structural dynamic analysis, to the author's best knowledge. Existing modelling works related to the laser weld joints focus mainly on simulating the welding process itself,

as presented by Dong and Wei [34], De et al. [33], Tsirkas et al. [35], Cho et al. [36], and Montalvo-Urquiza et al. [57], to name a few. This highlights the need to find a proper solution in modelling the laser weld joints as they have recently received quite a significant interest, especially in the automotive applications.

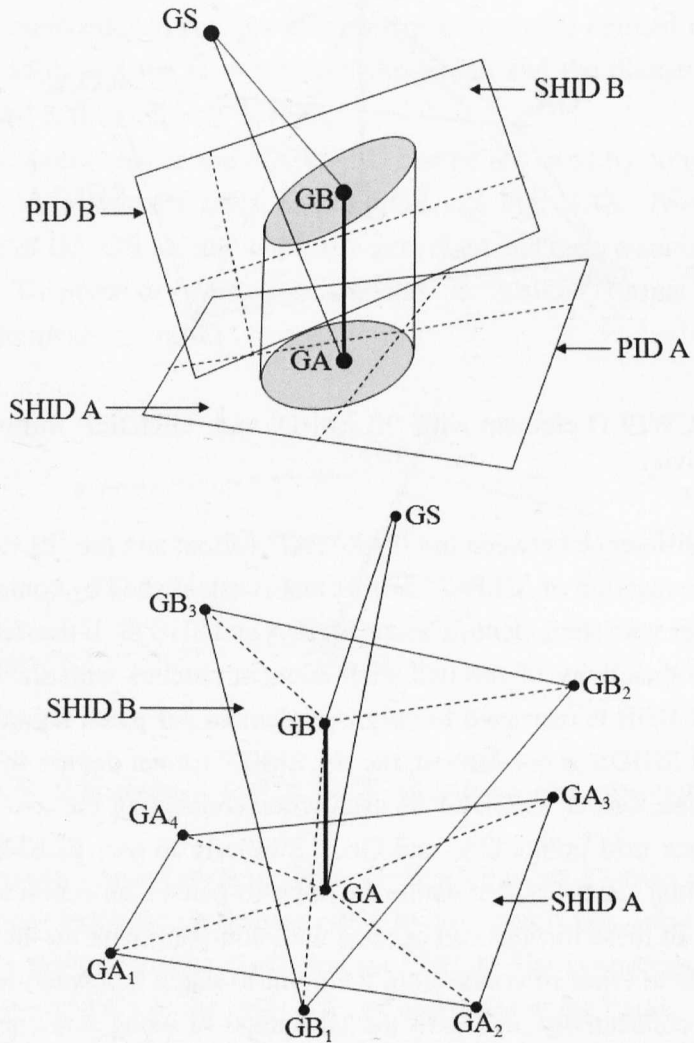


Figure 3.15: CWELD element with (a) 'PARTPAT' and 'ELPAT' formats, and (b) 'ELEMID' and 'GRIDID' formats for patch-to-patch connectivity

### 3.4 Modelling of other joints

Development of FE models for rivet joints has been reported by Christian [58], Langrand et al. [59], Kelly and Costello [60] and Iyer et al. [61], while modelling of surface-to-surface contact regions has been presented by Beer [62], Ahmadian and co-workers [63, 64], and Mayer and Gaul [65], just to name a few. Brown and Suegling

[66], and He and Zhu [67] developed FE models to represent fillets in thin-walled structures.

### **3.5 Conclusions**

FE models of bolted and spot weld joints are presented in this chapter. Various solutions have been reported, from detailed 3D models to simplified models using basic elements (such as springs and beams) available in FE packages. The type of FE models to be used depends upon the information that is being sought after from a particular analysis. For example, a detailed solid model would accurately simulate the stress and strain in the vicinity of joints, but may produce unnecessary expensive computational effort when predicting dynamic behaviour of structures with many joints.

FE modelling of conventional (RSW) spot weld joints has been carried out by a number of researchers; however, to the author's best knowledge, there has been no work of modelling spot welds made by Laser Welding for structural dynamic analysis. Although the CWELD element has been used extensively over the years, the feasibility of using this element for dynamics prediction of spot welds made by Laser Welding is still uncertain due to dissimilar constructions of the laser spot welds to the conventional spot welds.

Amongst all of the models presented in this chapter, the CWELD element is the most appealing spot weld model to be used in modelling the laser weld joints, due to the advantage of flexibility in the type of mesh and the potential to update the element in the FE model updating. Furthermore, there are three different connections that can be chosen in finding the best way to develop the model. The application and accuracy of some of the spot weld models in representing the laser spot weld joints are investigated further in Chapter 5 and comparisons are made in order to find the best solution for modelling the laser weld joints.



# Chapter 4

## Experimental Modal Analysis of Structures

### 4.1 Introduction

Experimental study of structural dynamics plays an important role in design and analysis of engineering structures. In the past several decades, it has turned into an established technique to analyse the dynamical behaviour of structures, for instance, in the automotive and aerospace industry. Measured data can be used not only for better understanding of the dynamics of structures, but also for validation of numerical models before they can be used for further detailed analysis.

In this chapter, an introductory overview of experimental modal analysis is provided. Brief explanation on the basic system of vibration measurement is also included. It is important to comprehend this background information before modal testing can be conducted on any test structures, as also presented in this chapter. With the aim to understand the dynamics of laser weld joints, a set of nominally identical structures are produced with some laser weld joints. The welded structures (comprising of two substructures connected by laser weld joints) are described, and a brief explanation on the laser welding process involved in joining the components is included. Moreover, experimental work carried out on the structures is also explained in the chapter.

### 4.2 Experimental modal analysis

Experimental observations are vital in the field of structural dynamics, especially for major objectives of [2, 68]:

- determining the nature and extent of vibration response levels in operation
- verifying theoretical models and predictions of various dynamic phenomena
- measurement of essential material properties under dynamic loading

The second objective indicated above can be achieved by the experimental modal analysis (EMA), which is a process of measuring (often out of normal service environment) and analysing dynamic properties of structures under a known vibrational excitation. This complete process of data acquisition and its subsequent analysis is also known as Modal Testing [2].

Essentially, modal testing is conducted in order to construct a mathematical model of a physical structure based entirely on measured vibration data, by measuring not only the response levels but also the excitations given to the structure thus permitting a relationship to be defined between them. These measured responses and excitations are usually presented in time-history domain before being transformed into frequency domain to reveal frequency response functions (FRFs) or impulse response functions (IRFs). The response model can also be obtained theoretically by direct analysis, as explained in the following.

The theoretical route to vibration analysis is shown in Fig. 4.1, which includes three stages through which the theoretical vibration analysis progresses [2, 68]: (1) spatial model, (2) modal model, and (3) response model. Generally, a mathematical model is constructed to describe the structure's physical characteristics, usually in terms of mass, damping and stiffness properties. This stage is referred to as spatial model. The spatial model is then used to define the modal model; i.e., a description of structure's behaviour as a set of vibration modes in the form of its modal properties (i.e., natural frequencies, mode shapes, etc.). The modal model always describes the normal modes of the structure, in which the structure vibrates naturally without any external excitations. The third stage (response model) is then performed in order to describe how the structure will respond under given excitation conditions by constructing a set of FRFs within a specified range of frequency.

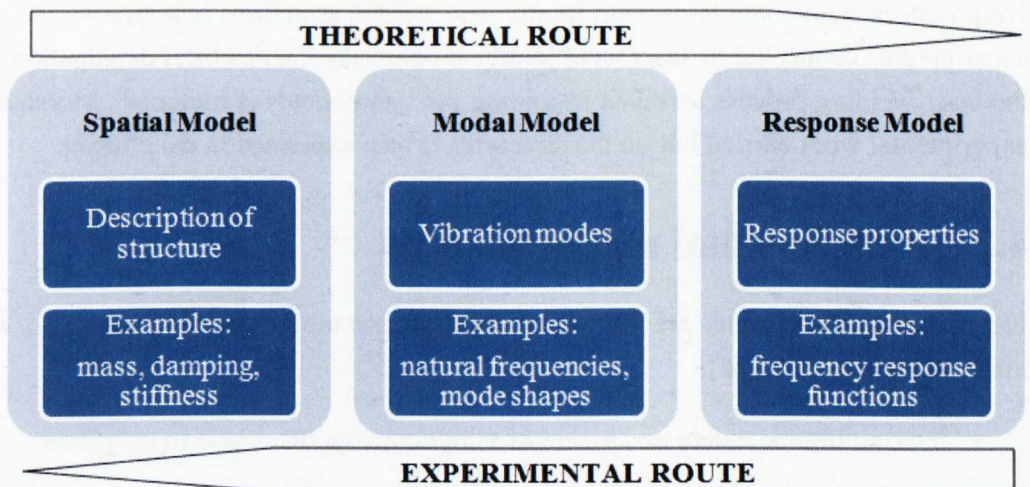


Figure 4.1: Routes of vibration analysis

The experimental route to vibration analysis is undertaken in the reverse direction of the theoretical route, where the FRFs are measured to construct the response model, and the modal model consisting of natural frequencies, modal damping and mode shapes can then be defined. Lastly, the spatial model can be obtained providing enough measurements are attained in order to characterise the physical structure. It is therefore very important to include enough DOFs in the measurement and also to cover most of the vibration modes within a specified frequency range. Relationships between the response model ( $H(\omega)$ ) to the spatial and modal models can be constituted by the following two relationships [2, 68]:

$$H(\omega) = [\mathbf{K} + i\omega\mathbf{B} - \omega^2\mathbf{M}]^{-1} \quad (4.1)$$

$$H(\omega) = \phi[\omega^2 - \omega_n^2 + 2i\omega_n\zeta_n]^{-1}\phi^T \quad (4.2)$$

in which  $\mathbf{M}$ ,  $\mathbf{B}$  and  $\mathbf{K}$  represent the spatial model of mass, damping and stiffness properties, while  $\omega_n$ ,  $\phi$  and  $\zeta_n$  represent the natural frequency, mode shapes vector and modal damping to construct the modal model.  $\omega$  is the excitation frequency of the system.

The mathematical model of the structure obtained from the EMA may be utilised in many application areas, such as: (1) for obtaining the vibration properties for validating corresponding vibration data predicted by FE models, and (2) for adjusting or correcting FE models in order to bring their modal properties closer to the measured data (i.e., FE model updating). Both of these areas are attempted in this research, as presented in the next chapters.

### 4.2.1 Basic components of EMA

Basic components of EMA are described in this section. A typical layout for measurement system used for single-point excitation is illustrated in Fig. 4.2, which includes three main elements of EMA as briefly explained next [2, 3].

#### Excitation of structure

There are various types of mechanisms available for excitation of a structure, which can be generally classified into contacting and non-contacting types. The first type of excitation mechanisms involve connecting an exciter (such as electromagnetic or electrohydraulic shakers) that remains attached to the structure throughout the modal test. The need to have the mechanism connected to the test structure causes some constraining and mass loading effects of the structure, which are the main disadvantages of such a system.



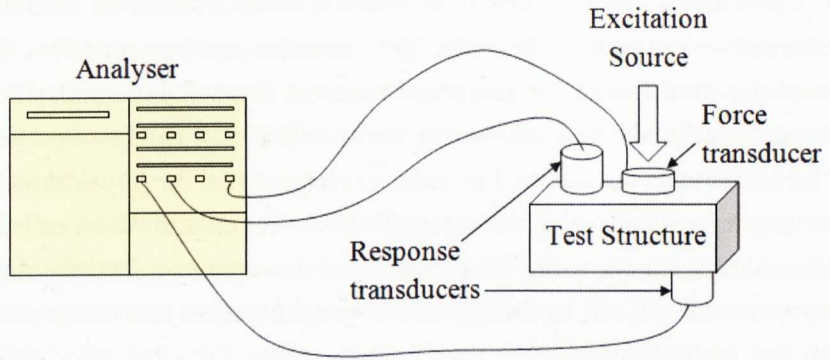


Figure 4.2: General layout of EMA

The connecting excitation mechanism, also known as the shaker, is established by a system that applies the excitation, generally in the form of a driving force  $f(t)$ , at a given coordinate of the test structure. The excitation signals can be any of a wide variety of signal forms (including harmonic, impulsive, random, transient, periodic, etc.), which must be chosen to match the requirements of the test. Moreover, a signal generator and a power amplifier are required in order to provide large enough input for the measurement. The excitation is commonly measured by a force transducer located at the connection between the shaker and the structure under investigation.

The second type of excitation mechanisms includes excitation devices that are either in contact for a short period (for example, an impact hammer) or have no contact whatsoever (such as an electromagnetic device) with the test structure while the excitation is being applied. The impact hammer by itself is a complete excitation mechanism, with a force transducer attached to its head. Therefore, there is no need for a connection between the excitation device and the test structure, hence the mass loading effects can be avoided. Furthermore, the device does not require a signal generator and a power amplifier, which are essential for the shakers.

The impact hammer (Fig. 4.3) is used to hit the structure in order to excite a broad range of frequencies, which depends on the properties of the hammer head and hammer tip. The magnitude of impact is determined by the mass of the hammer head and the velocity of the impact that is introduced by the operator, while the frequency range is defined by the stiffness of the contacting surfaces and the mass of the hammer head. Therefore, the stiffer the materials, the higher the effective frequency range. Similarly, the lighter the mass of the hammer head, the higher the frequency range covered by the impact. Thus, impact hammer normally accompanies with a set of different tips and heads that are interchangeable to attain appropriate impact magnitudes and frequency ranges.

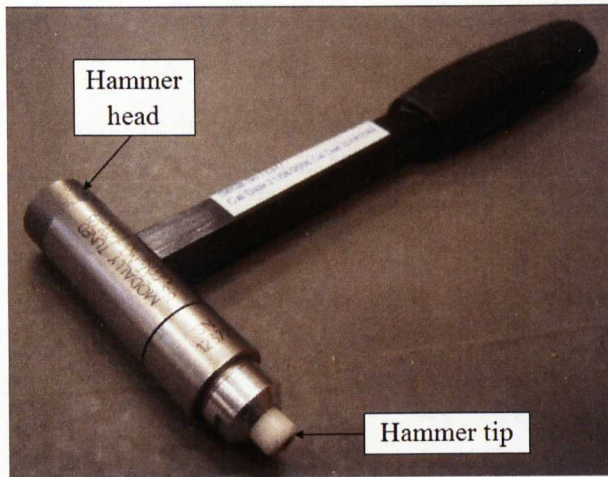


Figure 4.3: Impact hammer

### Sensing mechanisms

Sensing mechanism (or transducer) is used for measurement of force excitation (by means of force transducers) or acceleration response (by means of accelerometers - Fig. 4.4) in modal testing. Electric signals proportional to the physical parameters to be measured (such as force or accelerations) are generated by these transducers; if the signals are weak, then conditioning amplifiers may be needed to boost the signals into a signal strong enough to be measured by the analyser.



Figure 4.4: Accelerometer

There are two main factors to be considered when attaching and locating the transducers on the test structure. Firstly, there are various means of attaching the accelerometers to the surface of the structure under investigation; these include using a stud, magnet, a layer of wax, and even hand-held during the test. The use of wax provides the simplest and easiest means of attachment, thus is applied widely in modal testing. Next, it is also important to correctly position the accelerometers so they are not located too close to a node of vibration modes. Furthermore, the location of the measurement points must be selected properly in order to capture the actual mode shapes of the test structure.

## **Data acquisition and processing mechanisms**

The fundamental objective of the data acquisition and processing system is to measure the excitation and response signals transmitted by the excitation and sensing mechanisms using sophisticated devices called analysers. A spectrum analyser (also known as Fast Fourier Transform (FFT) analyser) is commonly used in modal testing, as it can provide direct measurement of the FRFs. This is done by converting the analogue time domain signals developed by the transducers into digital frequency domain information that can afterwards be processed by digital computers.

Data acquisition and processing mechanisms provide all the tools and functions required for experimental modal analysis, including tools to create FRF sets, perform modal parameter estimation, validate the modal model using different methods and compare the original FRFs with synthesized ones.

## **4.3 Experimental modal analysis of substructures**

A typical automotive body-in-white (BIW) is normally constructed by substructures that play an essential role in the strength and stiffness of the car body. For the purpose of this work, the automotive substructures (as shown in Fig. 4.5) are replicated and simplified (see Fig. 4.6), with two substructures (i.e., a flat plate and a hat-shaped shell) connected together by a group of laser spot welds. Overall dimension of the welded structure is 564 mm in length, 110 mm in width and 40 mm in height, and a set of nine identical structures were manufactured following a general guideline from Mottershead et al. [10] in order to minimise the manufacturing variability of the structures. The guideline is given as follows.

1. Standard rolled metal sheets of nominal thickness of 1.5 mm should be used
2. All plates should be cut from the same batch of metal sheet
3. Material within 30 mm from the edge of the sheet should not be used
4. All plates must be aligned lengthways in parallel to rolling direction of the metal sheet
5. All hat-shaped shells must be made by the same person, using the same bending equipment
6. All the plates and hat-shaped shells must be numbered as pairs

Following the guideline, each of the substructures was fabricated from a batch of cold-rolled mild steel sheets with nominal thickness of 1.5 mm and material properties



as given in Table 4.1. From these metal sheets, 33 pairs of flat plates and hat-shaped shells were manufactured. The flat plates were cut with dimensions as depicted in Fig. 4.7, while rectangular plates with specific dimensions (in relation to the overall dimension of the hat-shaped shell) were cut from the metal sheets and then bent using a bending machine to form the hat-shaped shells (Fig. 4.8). Every individual substructure was weighed and mean values of 0.7 kg and 1.0 kg were obtained for the flat plates and the hat-shaped shells, respectively.

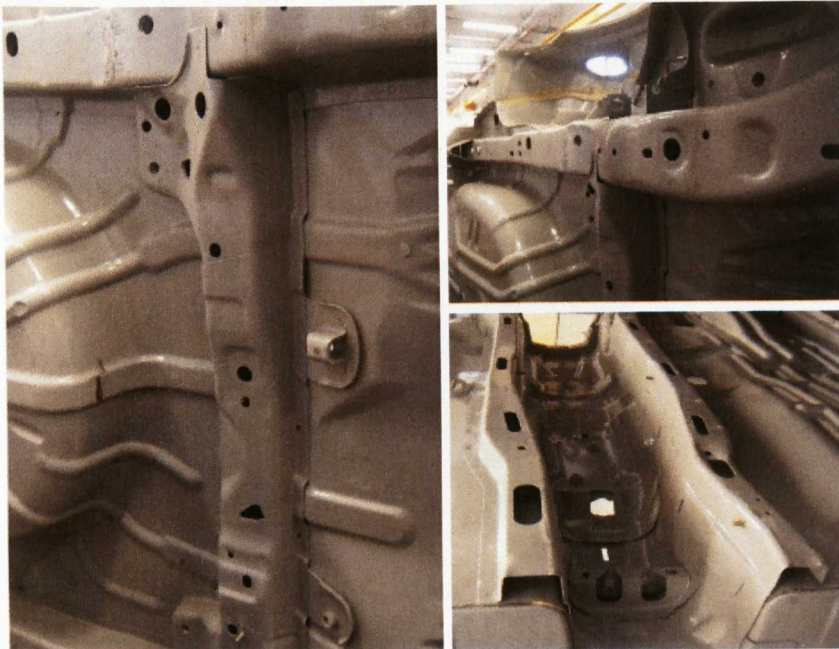


Figure 4.5: Floor of a typical automotive structure

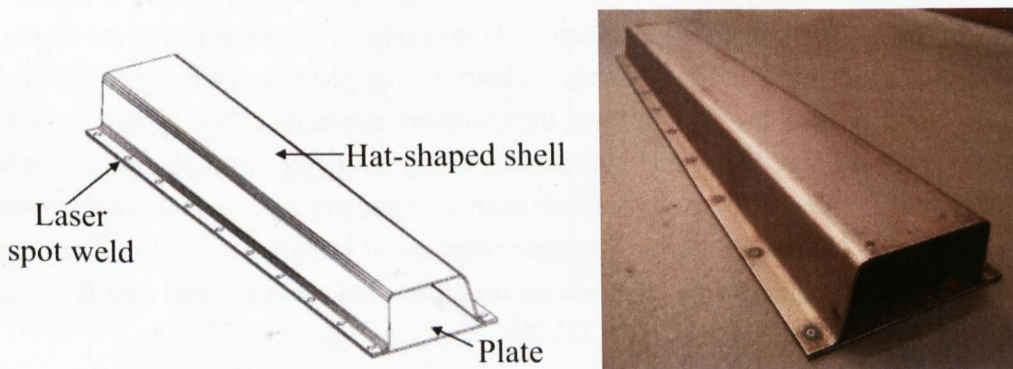


Figure 4.6: The laser welded structure

Closer inspections were made on each individual substructure and some discrepancies in terms of geometrical dimensions were determined. Measurements were conducted on each of the flat plates and the average thickness from all the plates was found

to be slightly smaller (i.e., 1.45 mm) than the nominal thickness of 1.5 mm. Moreover, the fold radii of the hat-shaped shells were found to be 1 mm smaller than the nominal design of 5 mm, while the flanges were 2 mm shorter than expected (i.e., 10 mm instead of 12 mm). These discrepancies are taken into consideration when modelling both substructures, as described in Chapter 5.

Table 4.1: Nominal material properties of mild steel

Properties	Values
Mass density ( $\rho$ )	7850 kg/m <sup>3</sup>
Poisson's ratio ( $\nu$ )	0.3
Young's modulus ( $E$ )	210 GPa
Shear modulus ( $G$ )	81 GPa

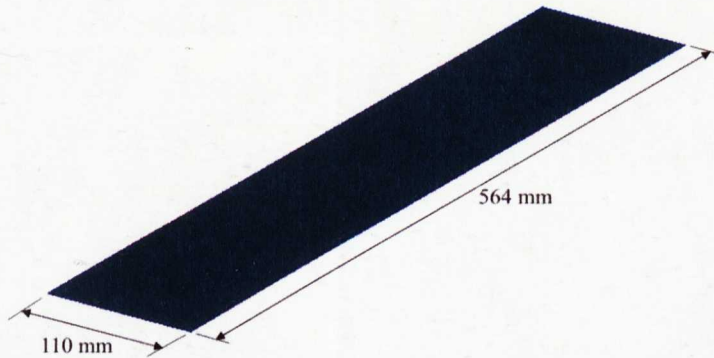


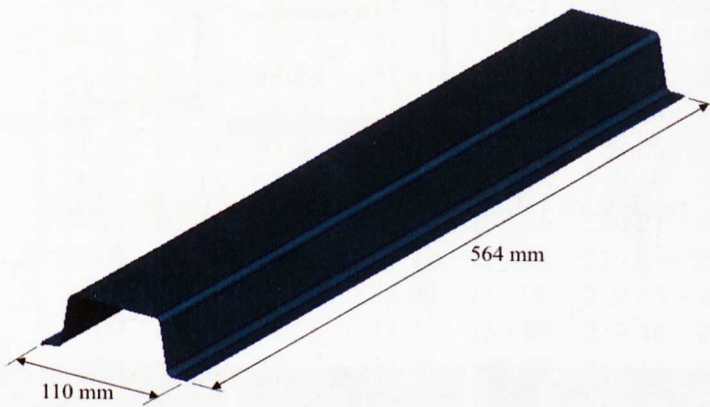
Figure 4.7: The flat plate

Modal testing was performed by conducting the main aspects of experimental modal analysis [2], including excitation of the structure, measurement of the response, and data acquisition and processing, on both the flat plates and hat-shaped shells before being welded together to form the complete structures. The experiments were carried out on each individual substructure using the LMS Test.Lab package, where an impact hammer was used to excite each substructure and several accelerometers were employed to measure the vibration response at multiple locations. The experimental setups for both substructures are described and the measured data is given in the following subsections.

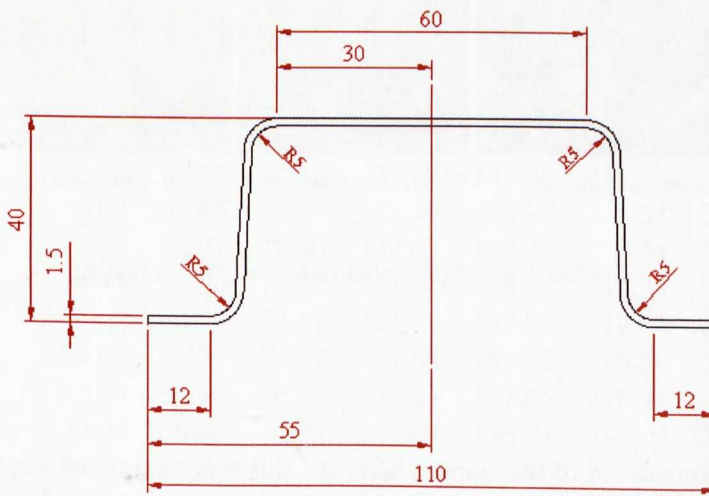
### 4.3.1 Experimental modal analysis of the flat plates

Modal testing with free-free boundary condition was conducted for the flat plates, with experimental setup as illustrated in Fig. 4.9. The free-free boundary condition was achieved by using a pair of strings for hanging the flat plates during testing. A PCB

impact hammer (Fig. 4.10(a)) and two Kistler accelerometers (Fig. 4.10(b)) were used in the test, with specifications given in Table 4.2. The plates were tested using one hammer point and two measurement points as depicted in Fig. 4.9, and the locations of the hammer and measurement points were chosen with care so that they are not near any nodal points. The responses were measured using a 12-channel LMS system (Fig. 4.10(c)) and extracted using the LMS PolyMAX curve-fitting procedure. The first seven measured natural frequencies of the flat plates, together with their means and standard deviations, are given in Table 4.3.



(a) The hat-shaped shell



(b) Cross-section of the hat

Figure 4.8: Illustration of the hat-shaped shell and its dimensions



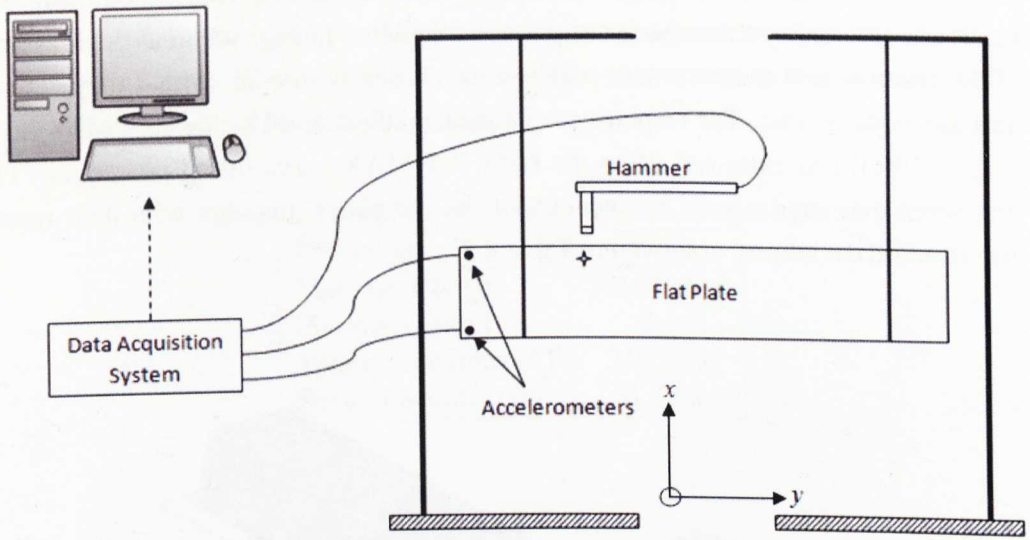


Figure 4.9: Experimental setup for the flat plates

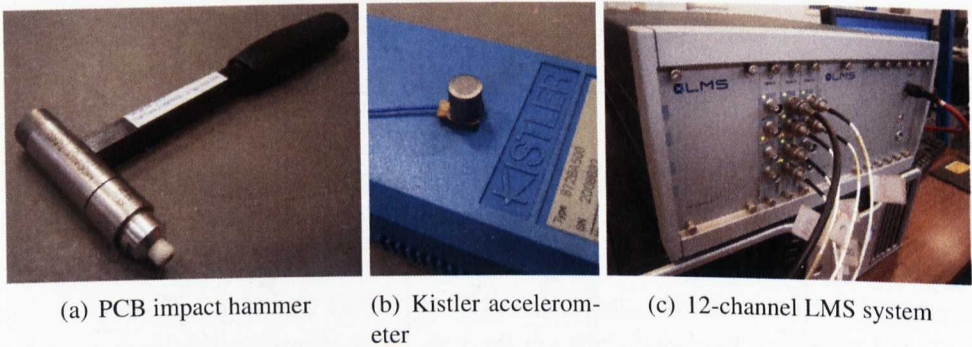


Figure 4.10: Apparatus used for modal testing

Table 4.2: Information of the impact hammer and accelerometers used in testing the flat plates

Apparatus	Manufacturer	Serial number	Location (see Fig. 4.11)	Direction
Hammer	PCB	12377	Node 112	z-direction
Accelerometers	Kistler	2008894	Node 101	z-direction
	Kistler	2008895	Node 103	z-direction

Table 4.3: First ten measured natural frequencies for the flat plates

Sample	Frequencies (Hz)						
	1	2	3	4	5	6	7
1	24.21	67.15	78.03	132.27	159.41	220.02	246.81
2	24.12	66.93	77.98	132.11	159.34	219.80	247.10
3	24.40	67.53	78.91	133.03	160.94	220.98	249.46
4	24.12	66.88	77.80	131.88	158.94	219.48	246.51
5	24.21	67.09	77.94	132.22	159.21	220.06	246.69
6	24.32	67.44	78.57	132.78	160.51	220.64	248.71
7	24.11	66.81	77.97	131.68	159.39	219.13	246.70
8	24.11	66.88	77.74	131.81	158.85	219.46	245.94
9	24.20	67.15	78.24	132.27	159.88	220.13	247.45
10	24.20	67.08	77.86	132.23	159.25	220.05	246.56
11	24.21	67.16	77.80	132.36	159.29	220.29	246.92
12	24.24	67.16	77.91	132.36	159.56	220.21	247.40
13	24.06	66.76	77.07	131.77	157.83	219.33	244.96
14	24.07	66.86	77.07	132.00	158.06	219.65	245.58
15	24.09	66.88	77.56	131.90	158.69	219.48	246.18
16	24.04	66.81	77.27	131.86	158.37	219.13	245.80
17	24.01	66.69	77.39	131.65	158.46	218.98	246.13
18	23.96	66.60	76.24	131.43	156.49	218.74	243.18
19	24.17	67.00	77.65	132.13	158.65	219.91	246.25
20	24.23	67.17	78.20	132.46	159.78	220.32	247.81
21	24.24	67.20	78.09	132.49	159.64	220.48	247.47
22	24.26	67.23	77.78	132.57	159.10	220.52	246.73
23	23.98	66.63	77.23	131.51	158.24	218.87	245.85
24	23.96	66.62	77.16	131.47	158.26	218.90	245.53
25	24.07	66.65	77.99	131.37	158.98	218.51	246.39
26	24.22	66.97	78.30	132.05	159.48	219.41	247.14
27	24.11	66.86	77.72	131.91	158.68	219.31	246.28
28	24.02	66.73	77.17	131.73	157.95	219.11	245.04
29	24.01	66.71	77.57	131.68	158.95	219.10	246.66
30	23.94	66.50	76.95	131.31	157.45	218.41	244.46
31	24.09	66.85	76.28	131.83	156.31	219.14	243.53
32	24.00	66.72	77.39	131.64	158.46	218.83	245.54
33	24.03	66.61	77.51	131.39	158.06	218.61	245.52
Mean	24.12	66.92	77.65	131.97	158.80	219.55	246.31
Std.	0.11	0.25	0.57	0.42	0.97	0.68	1.27



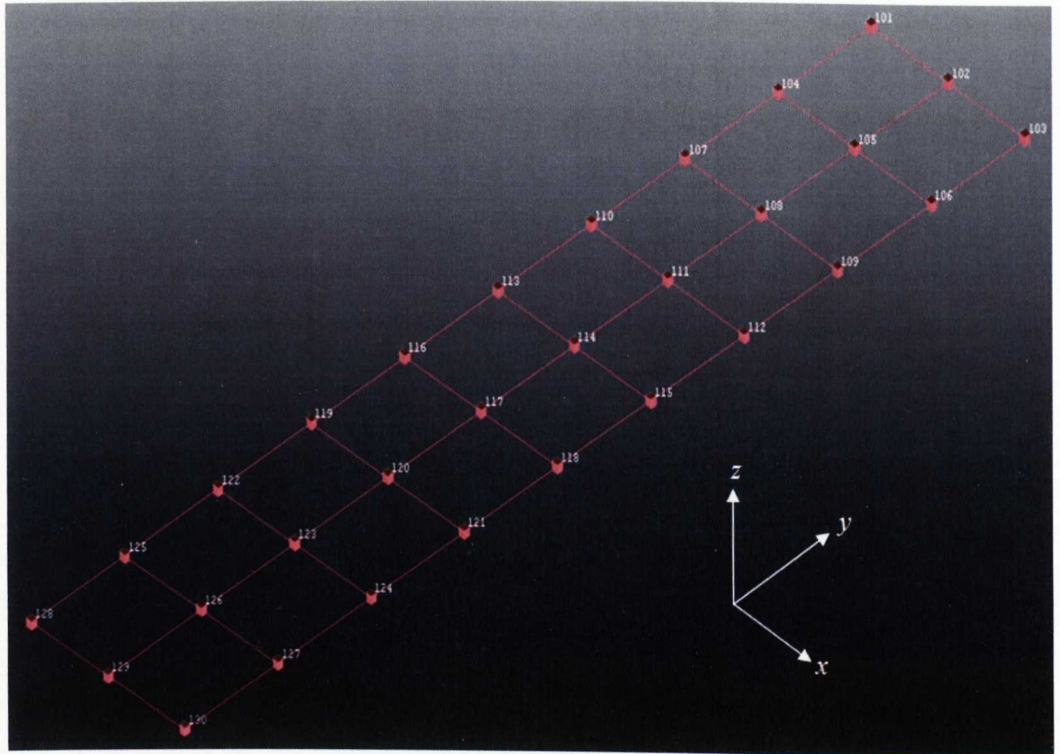


Figure 4.11: Experimental model of the flat plate

### 4.3.2 Experimental modal analysis on the hat-shaped shells

The hat-shaped shells were tested similarly to the flat plates, i.e., by impact hammer modal testing with free-free boundary condition. However, the test for the hat-shaped shells was conducted using one hammer point and five measurement points (as illustrated in Fig. 4.12), and the information of the apparatus is given in Table 4.4. Again, the responses were measured by using the 12-channel LMS system and extracted using the LMS PolyMAX curve-fitting procedure. Tables 4.5 and 4.6 tabulates the first ten measured natural frequencies for the hat-shaped shells.

## 4.4 Experimental modal analysis of the welded structures

The substructures were sent for laser welding after being tested. The laser welding process was conducted in-house at the Laser Lab, part of the School of Engineering at the University of Liverpool. Nine pairs of the flat plates and hat-shaped shells with variability as tabulated in Tables 4.7 and 4.8 were selected and laser welded following a laser welding specification as given in Appendix A. The laser weld joints were produced by using an 8 kW CO<sub>2</sub> laser machine (Ferranti Photonics). The substructures

were placed in a fixture (Fig. 4.14(a)) and the laser beam was focused onto the surface of the workpieces by using a Zinc Selenide (ZnSe) beam focusing system with 190 mm focal length lens. Helium was used as shielding gas with a flow rate of 30 liter/min. The laser welding arrangement is shown in Fig. 4.14(b). The laser spot weld joints, which were made at the flanges of the structure, are 5 mm in diameter and 60 mm apart in the longitudinal direction (as shown in Fig. 4.15).

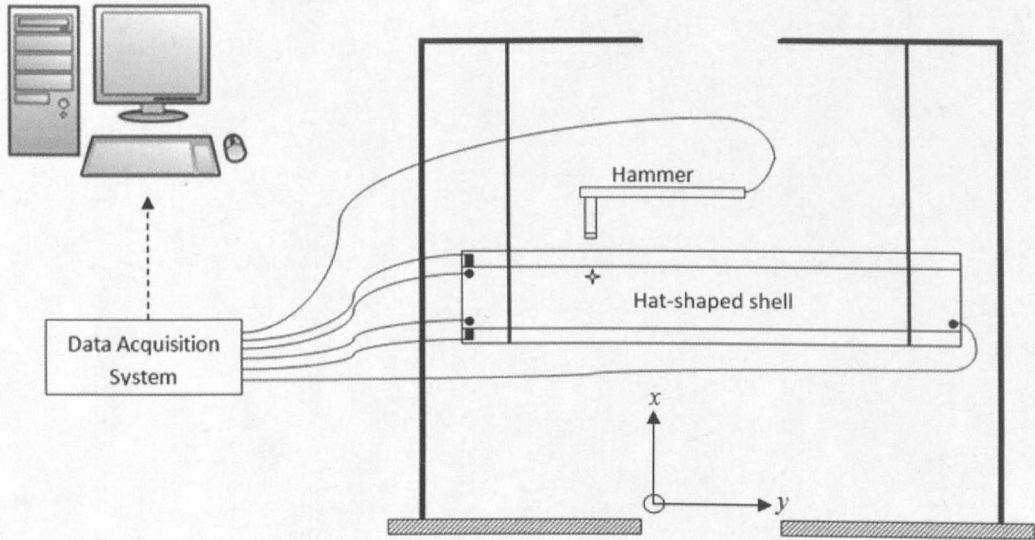


Figure 4.12: Experimental setup for the hat-shaped shells

Table 4.4: Information of the impact hammer and accelerometers used in testing the hat-shapes shells

Apparatus	Manufacturer	Serial number	Location (see Fig. 4.13)	Direction
Hammer	PCB	12377	Node 219	z-direction
Accelerometers	Kistler	2008894	Node 201	x-direction
	Kistler	2008895	Node 202	z-direction
	Kistler	2008896	Node 204	z-direction
	Kistler	2008897	Node 205	x-direction
	Kistler	2001588	Node 247	z-direction

The welded structures were tested with free-free hammer test using two hammer points and seven measurement points (as depicted in Fig. 4.16) to determine the first five natural frequencies. Hammer point 1 was hit in two directions (i.e., the x- and z-directions), while hammer point 2 was hit only in the z-direction, as described in Table 4.9. Multiple hammer points were chosen to excite certain modes that apparently could not be excited when a single hammer point was employed. Seven Kistler accelerometers were used, with six of them placed on the flat plate where most deformations occur

and only one was placed on the sidewall of the hat-shaped shell. The measured natural frequencies for the first five modes of the nine structures are tabulated in Table 4.10.

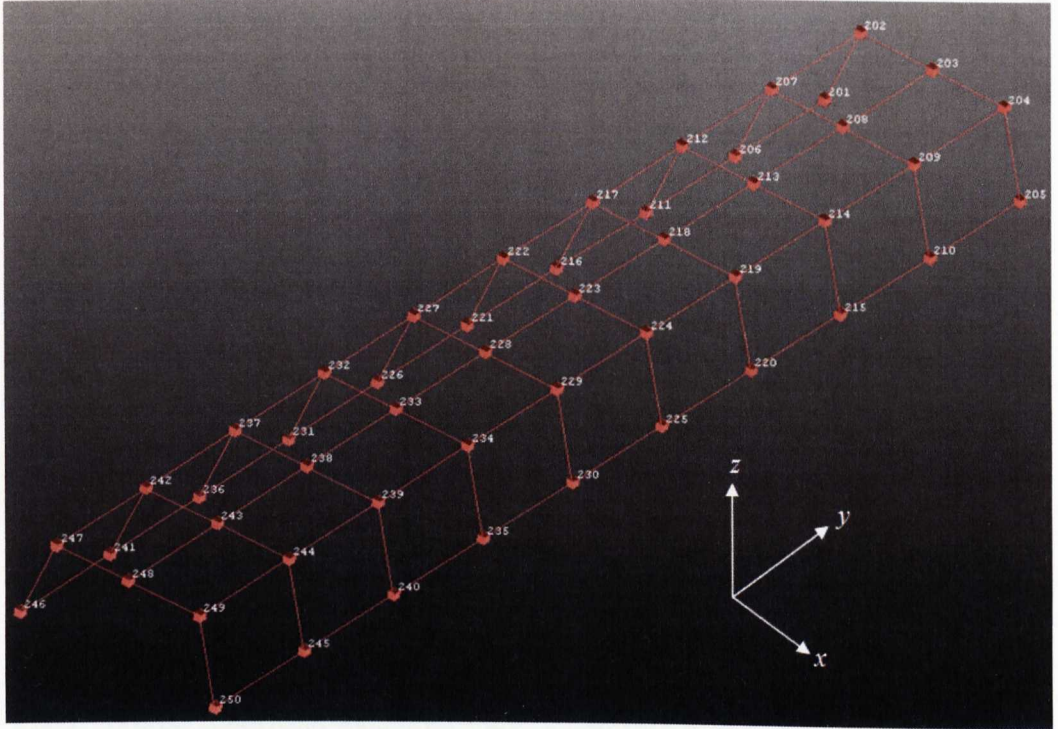


Figure 4.13: Experimental model of the hat-shaped shells

An additional test (i.e. 80-point roving hammer test with four measurement points, shown in Table 4.11) was conducted on one of the welded structures in order to capture the actual mode shapes of the experimental model, which were then used to verify the mode shapes obtained from the earlier tests. This particular multi-impact roving hammer test was not performed on each individual welded structure to avoid high time consumption for carrying out the whole test. The first five mode shapes from the roving hammer test are given in Fig. 4.18.

## 4.5 Conclusions

In this chapter, experimental modal analysis has been explained, and the theoretical and experimental routes of vibration analysis are described. Brief explanations of the three main aspects of the basic measurement system used in vibration analysis (i.e., excitation, transduction and data analysers) have also been included. It is important to have a good understanding of the concept of EMA before performing the modal test, as presented in the remainder of the chapter.



Table 4.5: First to fifth measured natural frequencies for the hat-shaped shells

Sample	Frequencies (Hz)				
	1	2	3	4	5
1	69.96	271.99	286.05	333.40	393.68
2	70.43	273.79	289.01	333.93	394.85
3	70.39	273.20	287.46	334.12	393.73
4	70.49	275.59	289.46	334.44	397.46
5	70.69	270.25	287.83	335.23	399.11
6	69.02	270.34	284.12	333.04	392.57
7	69.99	273.84	288.29	333.21	394.71
8	70.21	270.27	284.62	333.39	393.76
9	70.37	274.14	286.82	334.01	395.29
10	68.97	273.78	284.47	332.40	393.46
11	69.89	272.70	285.23	332.25	393.74
12	69.41	277.18	290.48	333.83	392.97
13	70.59	274.16	287.36	334.53	397.40
14	70.21	275.16	288.40	334.92	395.95
15	70.37	275.22	289.39	334.71	396.41
16	70.62	275.67	289.83	334.92	396.72
17	69.49	275.54	288.52	335.95	394.73
18	70.65	272.88	289.26	336.59	396.71
19	70.24	273.09	285.96	335.13	397.19
20	70.53	277.06	292.79	336.09	396.92
21	70.49	274.45	288.59	335.54	398.29
22	70.26	271.75	285.52	335.24	396.26
23	69.34	273.18	286.74	335.21	395.50
24	70.48	273.10	290.39	336.28	394.07
25	69.31	274.18	287.35	334.76	392.89
26	69.92	273.44	288.19	334.40	395.93
27	70.39	274.12	289.78	334.85	397.40
28	70.59	274.69	287.01	335.33	395.99
29	70.30	275.86	292.10	336.10	396.52
30	70.14	274.44	289.09	335.26	394.36
31	69.30	272.35	286.29	335.43	393.86
32	70.11	270.31	285.63	336.24	394.18
33	70.64	274.52	289.25	335.45	396.73
Mean	70.11	273.70	287.92	334.73	395.43
Std.	0.50	1.81	2.11	1.11	1.70

Table 4.6: Sixth to tenth measured natural frequencies for the hat-shaped shells

Sample	Frequencies (Hz)				
	6	7	8	9	10
1	632.10	639.94	720.21	759.26	780.78
2	634.34	642.27	722.99	754.36	783.29
3	634.75	641.75	717.20	759.24	783.46
4	637.31	646.03	733.99	769.01	784.71
5	637.12	646.35	737.40	767.77	784.53
6	633.09	641.03	723.13	755.35	781.66
7	634.65	642.26	719.73	754.71	779.04
8	632.35	640.78	721.70	752.64	783.23
9	636.63	643.98	726.24	759.92	782.65
10	633.66	642.23	724.39	756.45	781.45
11	632.38	640.85	728.08	761.97	758.14
12	634.62	641.66	721.13	756.48	782.80
13	640.37	648.35	727.15	762.77	783.03
14	637.03	644.87	726.02	755.77	783.25
15	640.27	647.05	723.38	758.68	779.58
16	638.56	645.46	721.55	763.31	784.29
17	633.91	640.49	726.41	752.16	777.95
18	636.49	643.88	725.39	763.27	778.52
19	637.33	645.47	725.59	766.59	779.15
20	639.13	647.07	721.15	760.18	778.90
21	638.92	648.67	728.86	767.07	778.59
22	635.01	643.36	725.47	760.88	777.96
23	631.57	638.65	731.15	768.97	778.83
24	630.40	637.57	719.35	749.97	783.03
25	631.18	639.12	725.22	751.89	779.74
26	635.98	643.15	731.86	764.26	780.39
27	634.84	643.24	726.62	770.71	781.94
28	632.61	640.63	726.70	759.98	784.41
29	634.22	641.73	730.76	760.42	781.81
30	630.66	639.53	724.83	757.96	780.12
31	631.79	639.55	726.93	751.97	777.03
32	631.70	639.13	724.06	751.78	779.00
33	633.96	642.14	734.73	764.66	784.21
Mean	634.82	642.67	725.74	759.71	780.53
Std.	2.80	2.92	4.61	5.72	4.62

Table 4.7: First five measured natural frequencies for the flat plates used in welded structures

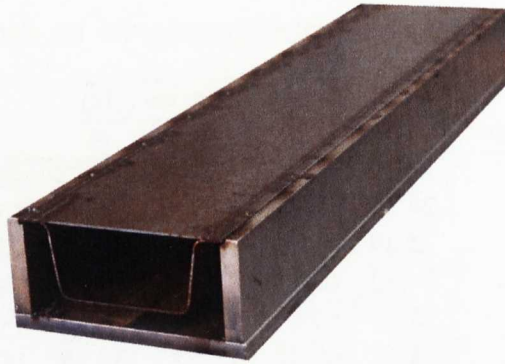
Sample	Frequencies (Hz)				
	1	2	3	4	5
1	24.21	67.15	78.03	132.27	159.41
2	24.12	66.93	77.98	132.11	159.34
3	24.40	67.53	78.91	133.03	160.94
4	24.12	66.88	77.80	131.88	158.94
5	24.21	67.09	77.94	132.22	159.21
6	24.32	67.44	78.57	132.78	160.51
7	24.11	66.81	77.97	131.68	159.39
8	24.11	66.88	77.74	131.81	158.85
9	24.20	67.15	78.24	132.27	159.88
Mean	24.20	67.09	78.13	132.23	159.61
Std.	0.10	0.25	0.38	0.44	0.71

Table 4.8: First five measured natural frequencies for the hat-shaped shells used in welded structures

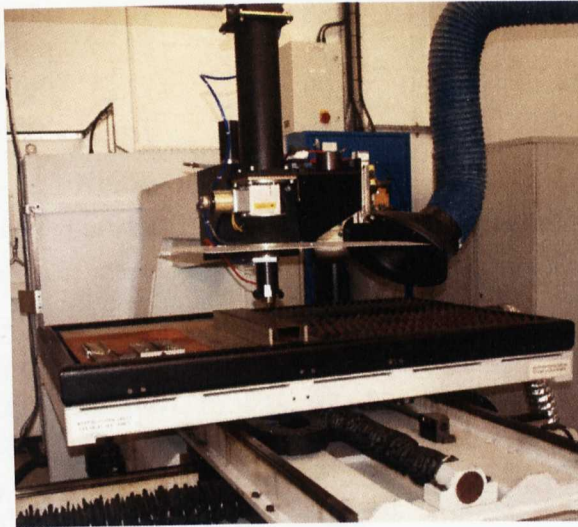
Sample	Frequencies (Hz)				
	1	2	3	4	5
1	69.96	271.99	286.05	333.40	393.68
2	70.43	273.79	289.01	333.93	394.85
3	70.39	273.20	287.46	334.12	393.73
4	70.49	275.59	289.46	334.44	397.46
5	70.69	270.25	287.83	335.23	399.11
6	69.02	270.34	284.12	333.04	392.57
7	69.99	273.84	288.29	333.21	394.71
8	70.21	270.27	284.62	333.39	393.76
9	70.37	274.14	286.82	334.01	395.29
Mean	70.17	272.60	287.07	333.86	395.02
Std.	0.49	1.97	1.86	0.69	2.06

Table 4.9: Information of the impact hammer and accelerometers used in testing the welded structures

Apparatus	Manufacturer	Serial number	Location (see Fig. 4.17)	Direction
Hammer	PCB	12377	Node 209	x- and z-direction
			Node 224	z-direction
Accelerometers	Kistler	2008881	Node 101	z-direction
	Kistler	2008882	Node 102	z-direction
	Kistler	2008883	Node 103	z-direction
	Kistler	2008884	Node 111	z-direction
	Kistler	2008885	Node 222	x-direction
	Kistler	2008887	Node 128	z-direction
	Kistler	2008888	Node 129	z-direction



(a) Fixture for the workpieces



(b) Laser welding arrangement

Figure 4.14: The laser welding setup

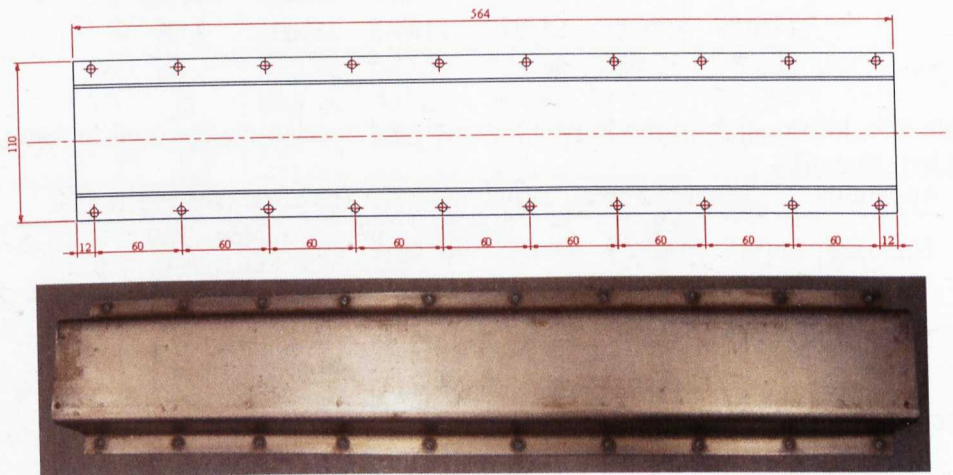


Figure 4.15: The welded structure produced by laser welding

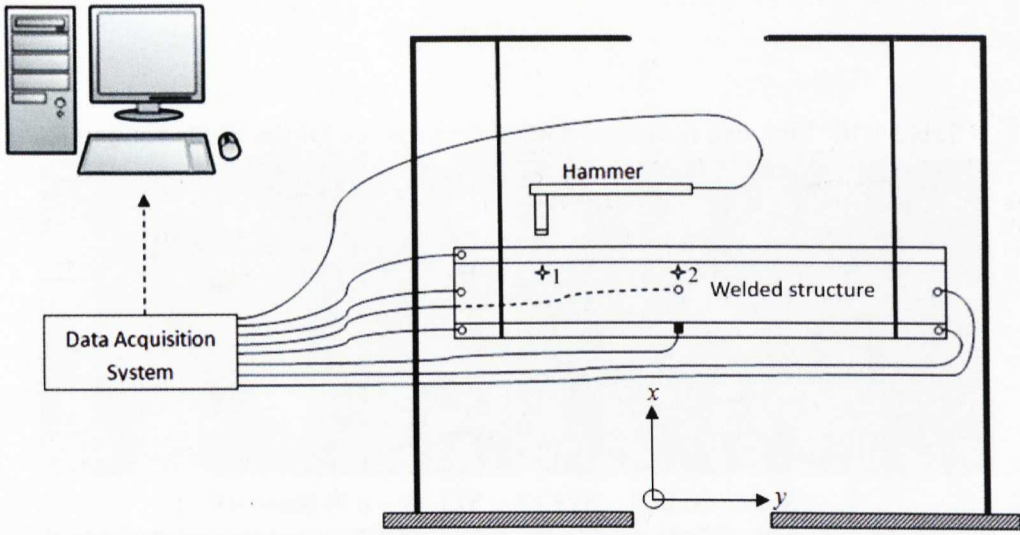


Figure 4.16: Experimental setup for the welded structures

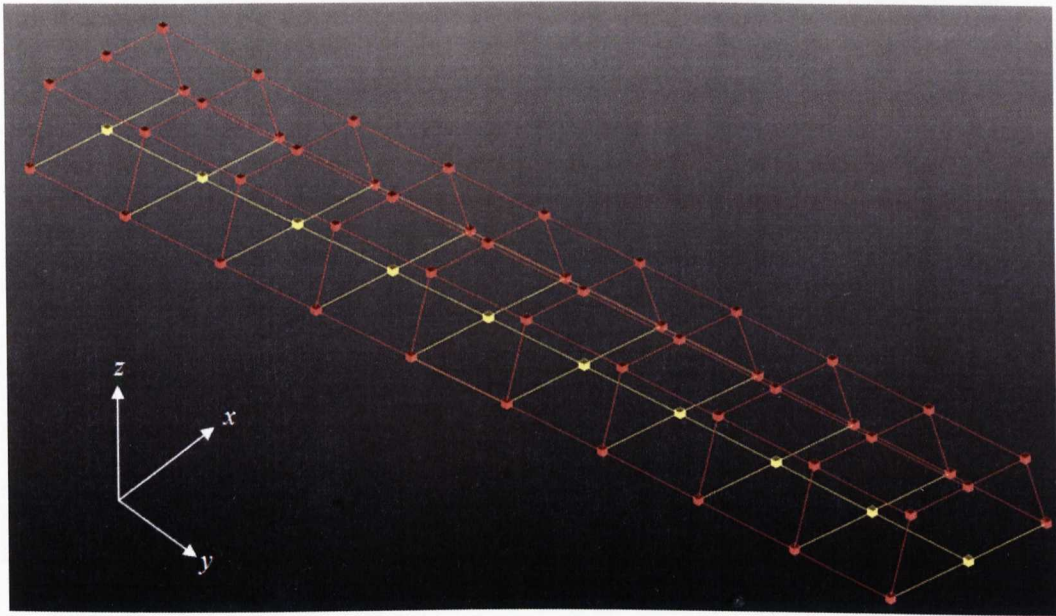


Figure 4.17: Experimental model of the welded structures



Table 4.10: First five measured natural frequencies for the welded structures

Sample	Frequencies (Hz)				
	1	2	3	4	5
1	509.33	557.16	578.25	634.42	646.65
2	511.08	554.14	577.00	626.59	640.17
3	508.67	554.53	575.92	626.59	645.54
4	509.03	555.26	577.79	628.64	644.45
5	512.18	558.39	580.89	630.84	646.44
6	509.32	552.90	578.38	627.65	646.08
7	507.04	550.40	572.83	625.47	643.49
8	508.03	558.13	573.71	630.04	645.74
9	506.15	556.29	573.74	628.78	644.40
Mean	508.12	553.69	575.39	627.45	643.66
Std.	3.15	5.33	3.87	4.88	4.00

Table 4.11: Information of the apparatus used in roving hammer modal testing of the welded structures

Apparatus	Manufacturer	Serial number	Location	Direction
Hammer	PCB	12377	All 80 nodes	x- & z-direction
Accelerometers	Kistler	2007226	Node 201	x-direction
	Kistler	2008879	Node 220	z-direction
	Kistler	2008881	Node 226	z-direction
	Kistler	2008882	Node 249	x-direction

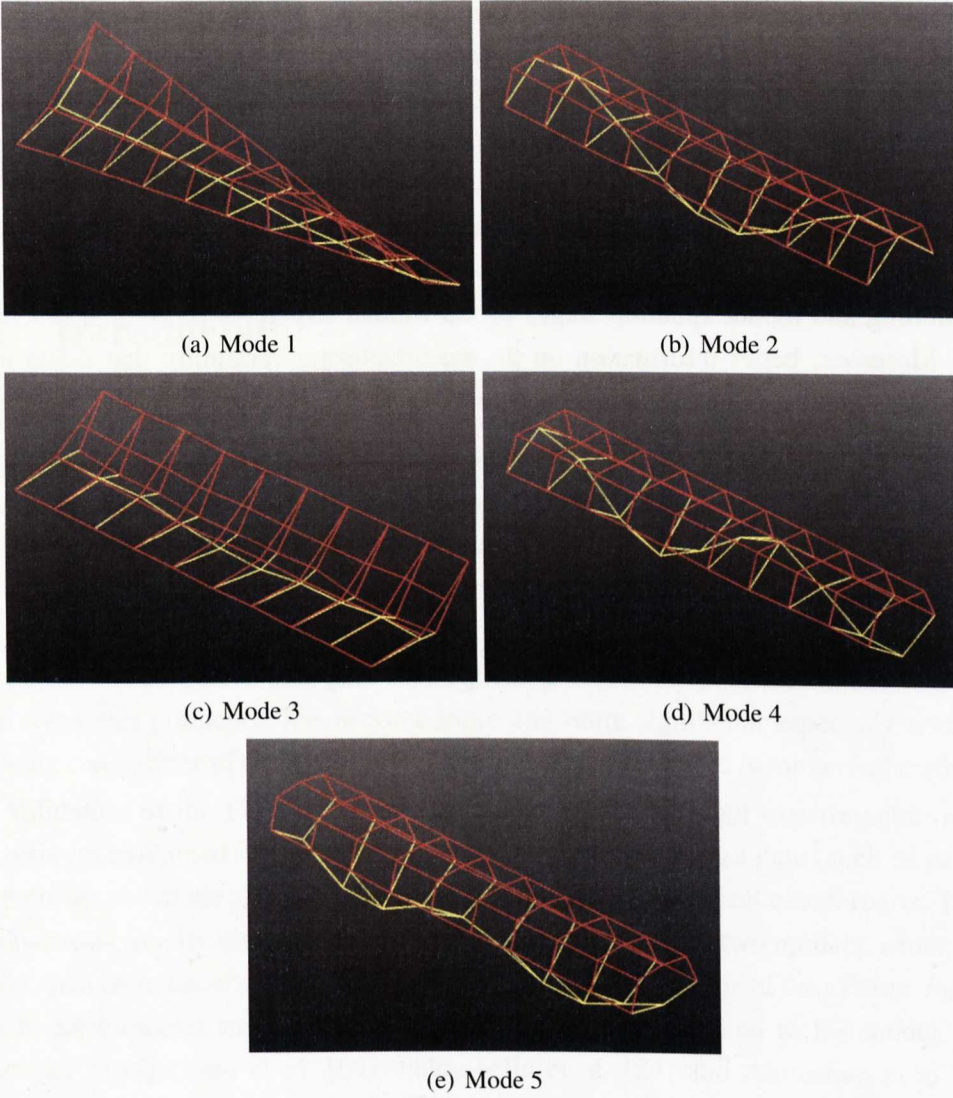


Figure 4.18: The experimental mode shapes of the welded structures

A number of nominally identical structures (each consisting of two substructures: a flat plate and a hat-shaped shell) have been manufactured to be investigated in this research, and their descriptions have been included in this chapter. Modal testing has been conducted on each of the substructures in order to determine the natural frequencies and the mode shapes of the flat plates and the hat-shaped shells. The experimental procedures for both substructures are briefly reported. The experimental data from both substructures will be employed in the next chapter to validate and update their FE models closer to their experimental counterparts.

Then, the substructures are sent to the Laser Engineering Lab to be laser welded. The procedure of laser welding is given and a welding specification is attached in Appendix A. These laser welded structures are also described and explanation of the experimental modal analysis performed on these structures is included. Similarly to the substructures, the experimental data obtained from the experiment are used in the FE modelling and model updating stages of the welded structures (presented in Chapter 5). Moreover, better information on the manufacturing variability that exists in the structures can be obtained, and non-deterministic (or stochastic) model updating is performed as reported in Chapter 6.

# Chapter 5

## FE modelling and model updating of the structure

### 5.1 Introduction

Traditional design phases that include building and testing product prototypes are no longer practical and economical to be employed today due to demands of a reduced time-to-market among product manufacturers. In order to meet the demands, increasing use of the FE analysis especially in the field of structural analysis has been accomplished. Therefore, much effort is given to the development of accurate analytical models for the prediction of the system's response to various excitations, boundary conditions and parameter changes. Consequently, development of FE models for structural dynamics prediction has become more and more significant especially with the growing capabilities of computing facilities and recent advances in numerical methods.

Validation of the FE models are performed by carrying out experimental modal analysis (as explained in Chapter 4) in order to obtain measured data (such as natural frequencies and mode shapes) to be compared with their numerical counterparts. These comparisons usually disclose some discrepancies between the two models, which normally stem from uncertainties regarding the governing equations of the system, mainly due to assumptions and inaccurate boundary conditions applied to the model. For example, Mottershead et al. [69], Palmonella et al. [23] and Ahmadian et al. [64] found significant differences between the initial numerical natural frequencies and their experimental counterparts when investigating different types of joints. These cases demonstrate that the FE models have to be modified in order to reduce the discrepancies by performing the FE model updating procedure [4].

The FE model updating problem has been well-investigated for the past decades and many approaches have been researched and reported. Most of the updating approaches use the experimental modal data as an exact reference for updating the selected parameters in order to minimise the differences between the experimental and

numerical natural frequencies and mode shapes. However, the data obtained from the experiments are always partial (or incomplete) since it is almost impossible to measure all the DOFs or vibration modes during the experiments, especially in large and complicated structures [2, 4, 24, 70]. Amongst the measured quantities, the natural frequencies are normally identified quite accurately, though this is frequently not the case for the mode shapes. There are also some other works (for example, Fritzen and Zhu [71]) that employ measured FRFs instead of the modal data as their reference in the updating procedure. Moreover, anti-resonance information obtained from the FRFs is also suggested as an alternative to the mode shapes, as it can be measured with less error [72, 73]. A paper by Mottershead and Friswell [24] gives an extensive description of the FE model updating methods, with 243 references cited.

This chapter firstly explains the FE modelling and model updating procedure, including formulation used in model updating, followed by a description of the Design Sensitivity and Optimization (SOL 200) capability of NASTRAN. Next, the development of an FE model of the laser welded structures that comprises of two main stages (as depicted in Fig. 5.1): (1) the FE modelling and model updating of the substructures, and (2) the FE modelling and model updating of the welded structures, is described. The substructures are tested and updated before being welded together in order to isolate the error in the weld joints from those in the substructures, thus the uncertainties in the welded structures should arise mainly from the spot weld models. The main focus of this chapter is on modelling of the laser spot weld joints using existing elements available in commercial software packages, therefore the selection of elements to represent the laser weld joints is also explained in detail. The experimental results obtained in Chapter 4 are used as references when validating and updating the developed FE models.

### 5.1.1 FE modelling and model updating

The FE method is a well-established technique for analysing the behaviour of structures subjected to a variety of loads. In the FE analysis, complicated structures are discretised into a finite number of standard elements (such as beams and shells) that are defined by supposedly known material properties and boundary conditions. Therefore, global mass and stiffness matrices of a model can be easily computed, irrespective of the complexity of the structure, by assembling the mass and stiffness matrices of each individual element [4, 74]. These matrices can then be used to construct a set of second order differential equations in matrix form (Eq. (5.1)), which may be solved for estimating dynamic response of the structure.

$$\mathbf{M}\ddot{\mathbf{u}} + \mathbf{B}\dot{\mathbf{u}} + \mathbf{K}\mathbf{u} = \mathbf{f}(t) \quad (5.1)$$

with  $\mathbf{M}$ ,  $\mathbf{B}$  and  $\mathbf{K}$  represent the assembled  $n \times n$  mass, damping and stiffness matrices of the structure, while  $\mathbf{u}$ ,  $\dot{\mathbf{u}}$  and  $\ddot{\mathbf{u}}$  are the  $n \times 1$  displacements, velocities and accelerations vectors, respectively, due to the  $n \times 1$  input force vector  $\mathbf{f}(t)$ .  $n$  stands for the number of DOFs of the whole structure.

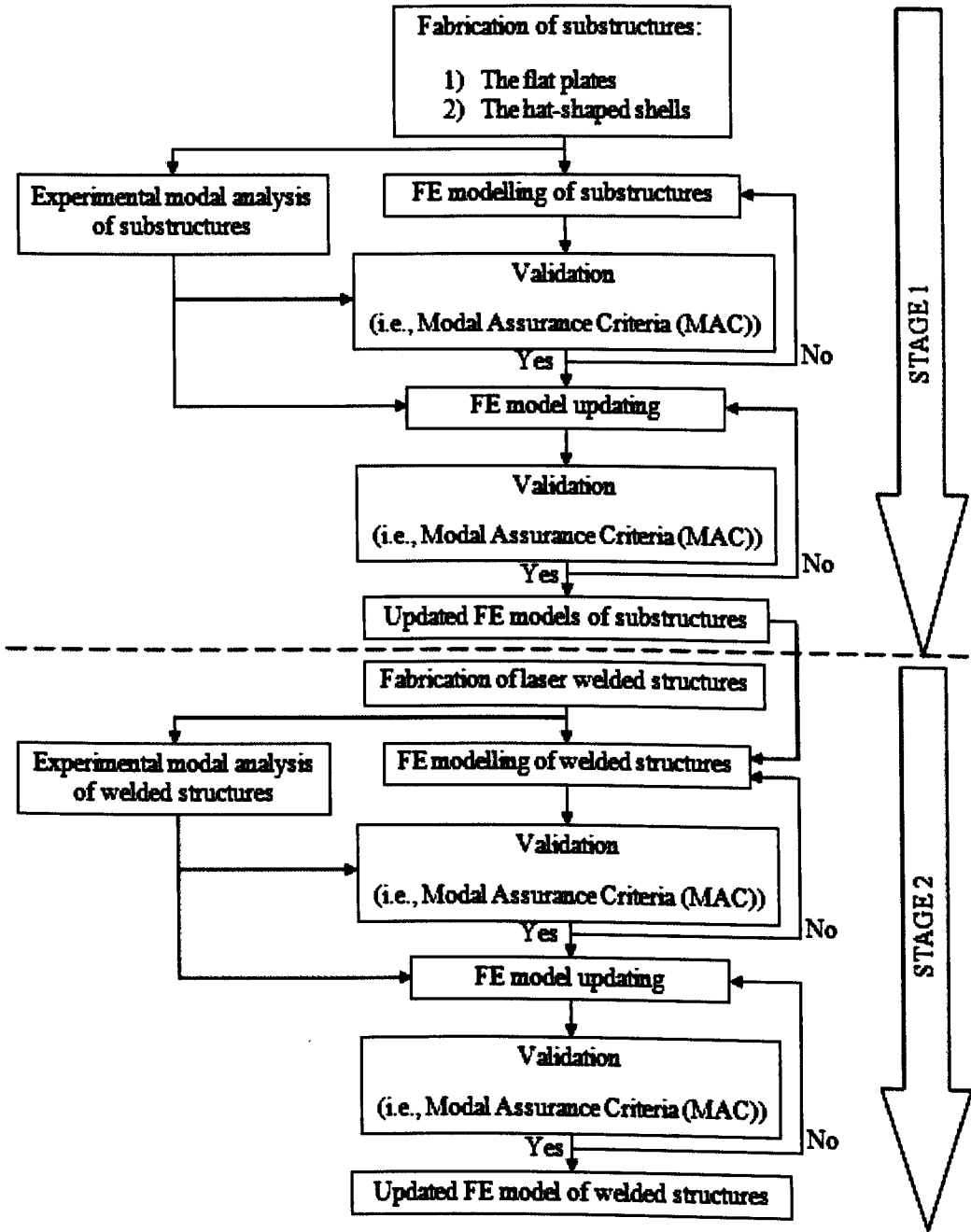


Figure 5.1: The FE modelling process

For an undamped free vibration system, Eq. (5.1) reduces to

$$\mathbf{M}\ddot{\mathbf{u}} + \mathbf{K}\mathbf{u} = 0 \quad (5.2)$$

which may be solved by assuming a harmonic solution of the form

$$\mathbf{u} = \phi \sin \omega t \quad (5.3)$$

where  $\phi$  is the eigenvector or mode shape,  $\omega$  is the natural frequency of the structure in rad/sec, while  $t$  represents the time. Eq. (5.3) can be differentiated twice into

$$\ddot{\mathbf{u}} = -\omega^2 \phi \sin \omega t \quad (5.4)$$

which can then be substituted into Eq. (5.2) to derive a simplified form of eigenequation, as follows.

$$(-\lambda \mathbf{M} + \mathbf{K})\phi \sin \omega t = 0 \quad (5.5)$$

where  $\lambda = \omega^2$  is the eigenvalue of the system. Since  $\sin \omega t$  cannot equal to zero, the equation reduces to the following,

$$(-\lambda \mathbf{M} + \mathbf{K})\phi = 0 \quad (5.6)$$

for which the only non-trivial solutions are those which satisfy  $\det |-\lambda \mathbf{M} + \mathbf{K}| = 0$ .

The computation of the natural frequencies and the mode shapes is performed by solving Eq. (5.6), which can be easily achieved by employing widely available FE solvers. In this work, for example, the computation of undamped natural frequencies and mode shapes is conducted using the Normal Modes analysis (SOL 103) of NAS-TRAN [75]. The outputs from SOL 103 are then compared with their experimental counterparts for validation purposes. Discrepancies between the numerical and measured natural frequencies can be directly assessed, however further analysis is needed to validate the mode shapes.

The degree of correlation between mode shape vectors originating from different sources can be provided by the MAC values [1,2,4], which is widely used to pair mode shapes derived from analytical models with those obtained experimentally. The MAC value is a scalar constant that ranges between 0 and 1, with a value of 0 meaning no correlation at all and a value of 1 indicating perfect correlation between the two sets of vectors. The values are presented in a matrix form, so well-correlated models should have values of close to 1 diagonally and values close to 0 off-diagonally. The MAC between experimentally-measured mode shapes ( $\phi_m$ ) and numerically-predicted mode shapes ( $\phi_a$ ) can be calculated as follows.

$$\text{MAC}_{jk} = \frac{|\phi_{mj}^T \phi_{ak}|^2}{(\phi_{ak}^T \phi_{ak})(\phi_{mj}^T \phi_{mj})} \quad (5.7)$$

The comparisons between the numerical modal properties (i.e., the natural frequencies and mode shapes) and their measured counterparts will normally reveal some discrepancies between the two approaches, thus the FE model updating method [4] should be performed to minimise the errors. The method aims to correct the geometrical and/or physical parameters and/or boundary conditions of the FE models, and has been well-accepted as a viable approach to improve the correlation between the FE models and the experimental data. The method has been applied widely in many applications especially for mechanical and civil structures.

Many researchers have performed FE model updating on structural joints in mechanical structures. For example, Kim and Wu [76], and Arruda and Santos [77] conducted the FE model updating to structures with mechanical joints for identification of the joint properties (i.e., stiffness and damping). Mottershead et al. [10] applied the model updating technique to converge a set of analytical models upon a set of nominally identical physical structures welded with spot weld joints. Another paper by the same authors [69] investigated a three-storey aluminium space frame, using five model updating experiments with different sets of updating parameters in order to obtain a physical improvement to the modelling of the joints provided by standard Meroform aluminium nodes. Palmonella et al. [23] updated three different FE models of spot weld joints to improve the accuracy of these models by searching for the optimum values of the parameters characterising the spot weld models using experimental data. There are also many other reported works on FE model updating applications in different types of structures.

In FE model updating, the system matrices (i.e., mass and stiffness) that describe the FE model are modified, either directly or iteratively, with respect to the reference modal parameters such as the measured natural frequencies and mode shapes. Direct methods directly solve the global mass and stiffness matrices in order to match the predicted and measured modal parameters. While these methods could reproduce the measured data exactly, however, the updated mass and stiffness matrices cannot always be related to the physical changes of the original model [4]. The iterative methods, on the other hand, require an iterative process to be performed in order to minimise an objective function that is generally a nonlinear function of the updating parameters, so that the difference between the predicted modal parameters and their measured counterparts could be reduced. Due to their iterative nature, the iterative methods require higher computational effort than the direct methods. Although exact solutions could



not be obtained, the physical meaning of the updated parameters is guaranteed. The iterative FE model updating is employed in this research.

In practice, the FE model updating procedure is usually ill-conditioned and the solutions are always non-unique; which is further complicated by measurement noise, thus leads to inaccurate solution and divergence in iteration [78]. Since the success of FE model updating method relies primarily on the experience and skill of the analyst, it is very important to understand the formulation and methodology of the FE model updating technique. Therefore, the following subsections describe the FE model updating formulations and the Design Sensitivity and Optimization solution (SOL 200) used in this research.

### 5.1.2 FE model updating formulations

The iterative FE model updating methods are generally based on sensitivity analysis. The updating formulation can be expressed as a function of analytical responses, structural parameters and a sensitivity matrix in terms of truncated Taylor Series expansion as follows [4].

$$\mathbf{z}_m = \mathbf{z}_j + \mathbf{S}_j(\boldsymbol{\theta}_{j+1} - \boldsymbol{\theta}_j) \quad (5.8)$$

In the formulation,  $\mathbf{z}_m$  is the vector of the measurement (or reference) data that may include both eigenvalues and eigenvectors of the system, while  $\mathbf{z}_j$  is the vector of analytical output at  $j^{\text{th}}$  iteration and  $\boldsymbol{\theta}$  is the vector of system parameters such as Young's modulus, thickness, etc..

In Eq. (5.8),  $\mathbf{S}_j$  is an  $m \times n$  sensitivity matrix at  $j^{\text{th}}$  iteration, which contains the first derivatives of the eigenvalues and eigenvectors with respect to the parameters. The sensitivity coefficient denotes the rates of change of the  $j^{\text{th}}$  eigenvalues ( $\lambda_j$ ) and/or eigenvectors ( $\phi_j$ ) due to changes in the structural parameters ( $\boldsymbol{\theta}$ ). The derivatives of both eigenvalues and eigenvectors can be expressed as [2, 4, 79],

$$\mathbf{S}_j = \frac{\partial \lambda_j}{\partial \boldsymbol{\theta}} = \phi_j^T \left[ \frac{\partial \mathbf{K}}{\partial \boldsymbol{\theta}} - \lambda_j \frac{\partial \mathbf{M}}{\partial \boldsymbol{\theta}} \right] \phi_j \quad (5.9)$$

$$\frac{\partial \phi_j}{\partial \boldsymbol{\theta}} = \sum_{s=1}^n - \left( \frac{\phi_s^T \left[ \frac{\partial \mathbf{K}}{\partial \boldsymbol{\theta}} - \lambda_j \frac{\partial \mathbf{M}}{\partial \boldsymbol{\theta}} \right] \phi_j}{\lambda_s - \lambda_j} \right) \phi_s \quad (5.10)$$

Rearranging Eq. (5.8) and introducing a weighting matrix of measurements ( $\mathbf{W}_{\epsilon\epsilon}$ ) and a weighting matrix of parameters ( $\mathbf{W}_{\theta\theta}$ ) into the equation gives a deterministic model updating equation,

$$\boldsymbol{\theta}_{j+1} = \boldsymbol{\theta}_j + \mathbf{T}_j(\mathbf{z}_m - \mathbf{z}_j) \quad (5.11)$$

where  $\mathbf{T}_j$  is a transformation matrix, which can be written as

$$\mathbf{T}_j = (\mathbf{S}_j^T \mathbf{W}_{\varepsilon\varepsilon} \mathbf{S}_j + \mathbf{W}_{\theta\theta})^{-1} \mathbf{S}_j^T \mathbf{W}_{\varepsilon\varepsilon} \quad (5.12)$$

while  $\mathbf{W}_{\varepsilon\varepsilon}$  and  $\mathbf{W}_{\theta\theta}$  are positive definite weighting matrices.  $\mathbf{W}_{\varepsilon\varepsilon}$  is usually given by the reciprocals of the measurements variance, while  $\mathbf{W}_{\theta\theta}$  must be chosen so that only uncertain parameters will change more during the updating procedure than the other parameters. The choice of  $\mathbf{W}_{\varepsilon\varepsilon} = \mathbf{I}$  and  $\mathbf{W}_{\theta\theta} = \mathbf{0}$  would result in pseudo-inverse [4]. For an ill-conditioned model updating problem,  $\mathbf{W}_{\theta\theta} = \lambda_r * \mathbf{I}$  where  $\lambda_r$  is a regularisation parameter found by plotting an L-curve [80].

The Design Sensitivity and Optimization code (SOL 200) of NASTRAN is used for updating, and an objective function based on residuals between measurement data (e.g., natural frequencies, mode shapes, FRFs, etc.) and their predictions are set for minimisation in the updating procedure. The procedure continues until convergence is accomplished when the difference between values of the objective function ( $J$ ) from consecutive iterations is sufficiently small. In this work, the objective function is constructed based on eigenvalue residuals, given by

$$J = \sum_{i=1}^n w_i \left( \frac{\lambda_i}{\lambda_i^{\text{exp}}} - 1 \right)^2 \quad (5.13)$$

where  $\lambda_i^{\text{exp}}$  is the  $i^{\text{th}}$  experimental eigenvalue and  $\lambda_i$  is the  $i^{\text{th}}$  eigenvalue predicted by the FE model. Appropriate weighting coefficients ( $w_i$ ) are assigned to the objective function (Eq. (5.13)) to give more weight to certain modes that may need more attention than the others. Nevertheless,  $w_i = 1$  is used in this work to give all the modes the same level of attention.

It is important to note that Eq. (5.13) only holds if the measured and its predicted counterpart are paired correctly, and therefore it is vital to ensure that the experimental and numerical data relate to the same mode. In addition, it is generally preferable to use a larger number of experimental modal properties in the updating process. Obviously, this would be more difficult but the updated model should be more predictive than using only a few modal data. Nevertheless, only the eigenvalue information is used for updating in this work, while the mode shapes data is only utilised to check the pairing of the experimental and analytical modes. The mode shapes are not considered in the updating procedure since they normally contain more measurement errors and are rather insensitive to parameters changes than the eigenvalues [81].

It should be noted that any modifications made to the system parameters could affect the modal properties of the system, as shown in Eq. (5.8). Therefore, the parameters and modal properties involved in the updating process must be selected properly. While the mathematical formulations of model updating are very well established, the

selection of parameters for updating remains a difficult problem for analysts. Selecting the updating parameters is an important aspect of the FE model updating process [4, 69, 82] and any parameters for material and geometric properties (such as area, inertia, thickness, diameter, density, Young's modulus, etc.) can be considered. However, the parameters selected should be justified by engineering understanding of the structure [69, 83–85] and the number of parameters should be kept smaller than the modal properties to avoid ill-conditioning problems [4, 82]. Moreover, it is vital for the responses to be sensitive to the updating parameters; hence it is necessary to compute the sensitivities beforehand so that only the most influential parameters are chosen.

Sensitivity analysis can be performed by using existing FE codes (such as NASTRAN) to compute the sensitivity coefficients (Eqs. (5.9) and (5.10)) of possible system parameters. At the end, only sensitive parameters should be selected amongst the trialled parameters. In this work, the sensitivity analysis is conducted by using SOL 200 of NASTRAN [86]. Furthermore, SOL 200 is also employed in the FE model updating procedure by casting the updating procedure as an optimisation problem, which is explained further in the following sections.

### 5.1.3 Design sensitivity and optimization (SOL 200) of NASTRAN

SOL 200 of NASTRAN [86] is employed for model updating through steps illustrated in Fig. 5.2. This comprehensive multidisciplinary optimisation algorithm uses partial derivatives (or gradient) of a function (e.g., Eq. (5.13) in this work) to assist in the numerical search for an optimum in the optimisation procedure. The partial derivatives of the objective function are determined by the forward finite difference method, as explained in the followings.

Approximation functions used in NASTRAN are based on Taylor Series expansions. So, if  $J = z(\theta)$ ,

$$z(\theta + \Delta\theta) = z(\theta) + \left. \frac{dz}{d\theta} \right|_{\theta} \Delta\theta + \left. \frac{d^2z}{d\theta^2} \right|_{\theta} \frac{\Delta\theta^2}{2!} + \left. \frac{d^3z}{d\theta^3} \right|_{\theta} \frac{\Delta\theta^3}{3!} + \dots \quad (5.14)$$

which is usually truncated only up to the first derivative term in the series, so a linear approximation of the function can be obtained as follows.

$$z(\theta + \Delta\theta) = z(\theta) + \left. \frac{dz}{d\theta} \right|_{\theta} \Delta\theta \quad (5.15)$$

Then, the sensitivity coefficient of the function with respect to the variable can be computed by the finite difference approximation

$$\frac{dz(\theta)}{d\theta} \approx \frac{z(\theta + \Delta\theta) - z(\theta)}{\Delta\theta} \quad (5.16)$$

where  $(\theta + \Delta\theta)$  is the estimated design variable,  $\theta$  is the prior estimate of the variable and  $\Delta\theta$  represents the small perturbation given to the variable. If more than one variable is of concern (as always in most practical applications), Eqs. (5.15) and (5.16) can be expressed as

$$z(\theta + \Delta\theta) = z(\theta) + \nabla z(\theta) \cdot \Delta\theta \quad (5.17)$$

$$\nabla z(\theta) = \frac{z(\theta + \Delta\theta) - z(\theta)}{\Delta\theta} \quad (5.18)$$

with  $\nabla z(\theta)$  representing the resultant vector of partial derivatives (or gradient) of the function. The search direction ( $s$ ) is defined by the opposite direction of the gradient vector, as follows.

$$s = -\nabla z(\theta) \quad (5.19)$$

It should be noted that the optimisation algorithms in NASTRAN generally belong to the gradient-based methods [86]. The Steepest Descent algorithm is used to determine an initial search direction until it reaches a constraint boundary. At this point, a finite move in the direction of the steepest descent would not be allowed as the constraint would be violated. A default optimiser used in NASTRAN (i.e., the Modified Method of Feasible Directions (MMFD)) is then employed to establish a new search direction that satisfy all the constraints. The iterative procedure of the method is shown graphically in Fig. 5.3. Let  $x^0$  be the starting point while  $s^0$  gives the initial (i.e., the steepest gradient) search direction. The procedure obeys the initial direction until a constraint boundary (e.g.  $g_1$  in the figure) is encountered. The optimiser then effectively follows the active constraint boundary  $g_1$  by establishing a finite move in a new search direction tangent to the constraint ( $s^1$ ). Note that one or more constraints may be slightly violated in the interim, which is a characteristic of the MMFD optimiser. This characteristic distinguishes the MMFD optimiser from the original Method of Feasible Direction (MFD) that would not allow any violations to occur [87]. It is the MMFD optimiser's task to return to the feasible region by stepping back towards the constraint boundary along the current search direction. The optimiser then proceeds to find the optimum in the objective function. Further information on the optimiser can be found in NASTRAN Design Sensitivity and Optimization User's Guide [86].

## 5.2 FE modelling and model updating of substructures

Development of the FE models of both substructures (i.e., the flat plates and the hat-shaped shells) are explained in the following sections.

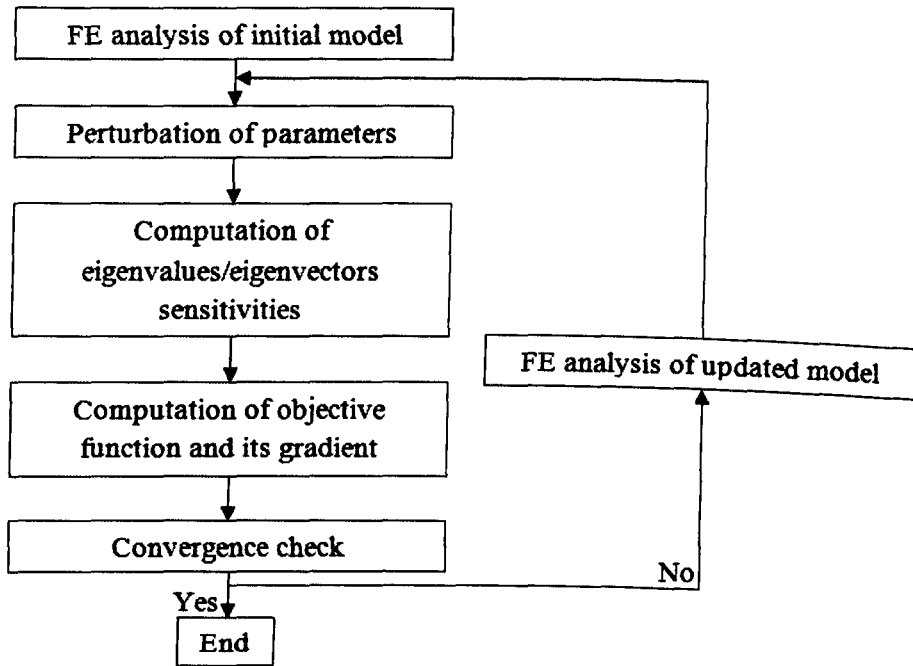


Figure 5.2: Optimisation process in SOL 200

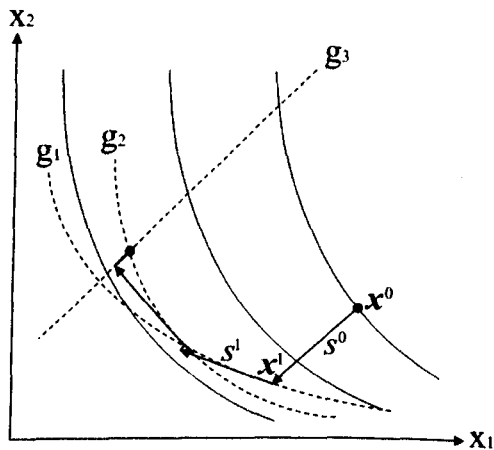


Figure 5.3: Iterative procedure of the Modified Method of Feasible Directions

### 5.2.1 FE modelling and model updating of the flat plates

The flat plates are initially modelled by using NASTRAN's four-node quadrilateral plate elements (i.e., CQUAD4 [56]), which are formulated based on the Mindlin-Reissner plate theory. There are five DOFs at each node of the elements, with zero stiffness for the rotational DOF about the surface normal of the elements. The CQUAD4 elements can model in-plane, bending, and transverse shear behavior. The FE modelling of the flat plates consisting of 300 elements is shown in Fig. 5.4, while the NASTRAN code for the flat plate model is presented in Appendix B1. The material properties of mild steel are used in the FE model with nominal values as tabulated in Table 4.1, and uniform thickness is assumed across the plates.

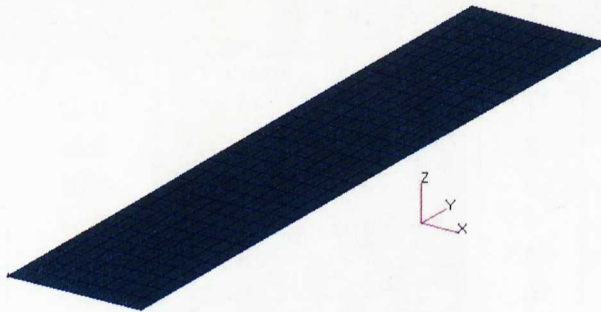


Figure 5.4: FE model of the flat plate

As explained in the previous chapter, a closer inspection on the flat plates reveals a discrepancy in terms of the actual thickness of the plates to the nominal thickness originally required. It is essential to highlight that the FE model must be geometrically well-defined before the FE model updating can be performed as the FE model updating can only correct the errors that originated from the uncertainties of modelling parameters. Therefore, the discrepancy of thickness must be taken into account and the mean thickness of 1.45 mm is used in the FE model instead of the nominal value of 1.5 mm.

Solution 103 of NASTRAN [75] is used to compute the first seven natural frequencies and mode shapes of the initial FE model, as shown in Table 5.1 and Fig. 5.5 respectively. The natural frequencies obtained from the FE analysis are compared with the experimental natural frequencies and, as can be seen from the table, all bending modes are found to be in good agreement with the experimental data while errors of up to 3% are found from the torsional modes. In order to reduce the discrepancies between the two sets of data, FE model updating has to be conducted. In the updating procedure, only the first five modes are included while the remaining modes are used later to assess the quality of the updated model.

There are a number of ways in which the flat plate can be parameterised for updating. Several parameters (i.e., the thickness, Young's modulus, shear modulus, density

and Poisson's ratio) have been considered and the sensitivity analysis has been performed using SOL 200. In the sensitivity analysis, the parameters are normalised in the form of  $\theta/\theta_0$ , hence the sensitivities become  $(\delta\lambda/\delta\theta)\theta_0$ , where  $\delta$  denotes a small increment. The sensitivities of the first five natural frequencies and the mode shapes of the first three modes at three locations are tabulated in Table 5.2, and comparisons are made to choose the most suitable parameters for the updating procedure. From the table, it can be summarised that the natural frequencies are sensitive to the changes of four parameters: the thickness, Young's modulus, shear modulus and density, while the sensitivity values of the mode shapes are very small. Thus, the mode shapes are not considered for sensitivity analysis in the updating work presented in this chapter.

Table 5.1: Measured natural frequencies and finite element predictions in Hz for the flat plates

Mode	Experiment	Initial FE	Error (%)
1	24.12	24.27	0.62
2	66.92	67.24	0.48
3	77.65	75.31	3.01
4	131.97	132.51	0.41
5	158.80	154.31	2.83
6	219.55	223.30	1.71
7	246.31	240.87	2.21

Based on the sensitivity data, the thickness is the most sensitive amongst all four parameters; however, it is not chosen as updating parameter since the correction of the thickness has already been made to the FE model. Hence, the thickness is assumed to have already been corrected. The Poisson's ratio proves to be not sensitive enough, while the Young's modulus and the density provide the same level of sensitivities. However, only one of these two parameters is selected for updating due to their direct relation in the calculation of the natural frequency, and the Young's modulus is selected as it may contain more uncertainties than the density. The shear modulus, despite not being sensitive enough for bending modes (i.e., 1, 2 and 4), is selected for its contribution for the torsional modes (i.e, 3 and 5). Thus, in conclusion only two parameters are selected for the flat plates as follows:

- The Young's modulus of the flat plates ( $E_{\text{flatplate}}$ )
- The shear modulus of the flat plates ( $G_{\text{flatplate}}$ )

The initial values of the Young's modulus and shear modulus of the flat plates are set to 210 GPa and 81 GPa, respectively. The Young's modulus is allowed to vary from 185 GPa to 220 GPa, while the shear modulus is given only a small variation from 80 GPa to 84 GPa.



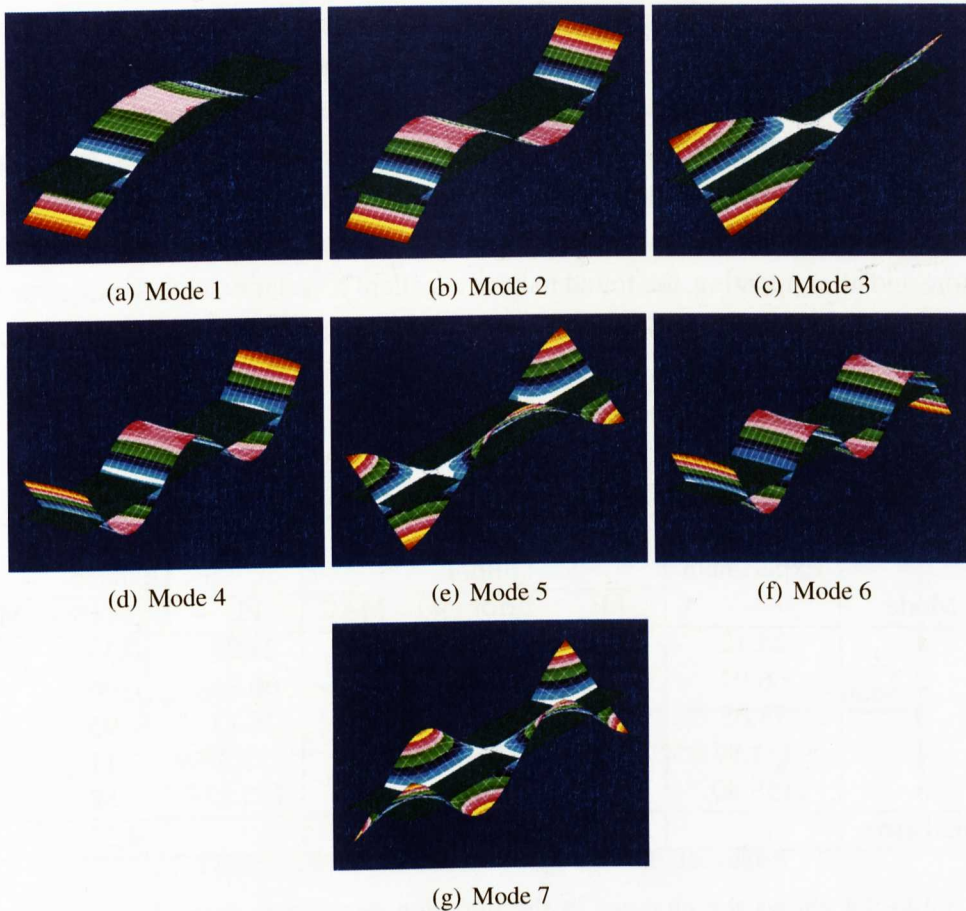


Figure 5.5: The numerical mode shapes of the flat plates

Table 5.2: Flat plates: Natural frequency (NF) and mode shape (MS) sensitivities with respects to the normalised parameters

Output type	Thickness ( $T$ )	Young's modulus ( $E_{\text{plate}}$ )	Shear modulus ( $G_{\text{plate}}$ )	Density ( $\rho$ )	Poisson's ratio ( $\nu$ )
NF 1	24.30	12.15	0.72	-12.15	0.10
NF 2	67.49	33.74	6.37	-33.75	0.88
NF 3	74.91	37.44	137.56	-37.59	-8.29
NF 4	133.59	66.79	22.89	-66.81	3.03
NF 5	153.59	76.76	290.19	-77.08	-1.55
MS 1 (point 1)	0.012	0.000	0.000	0.012	-0.002
MS 1 (point 2)	-0.714	0.000	0.000	-0.714	-0.020
MS 1 (point 3)	0.012	0.000	0.000	0.012	-0.002
MS 2 (point 1)	-0.012	0.000	0.000	-0.012	-0.007
MS 2 (point 2)	0.000	0.000	0.000	0.000	0.000
MS 2 (point 3)	-0.012	0.000	0.000	-0.012	-0.007
MS 3 (point 1)	-0.015	0.000	0.000	-0.015	-0.021
MS 3 (point 2)	0.000	0.000	0.000	0.000	0.000
MS 3 (point 3)	-0.015	0.000	0.000	-0.015	-0.021



Updating is done by minimising the objective function (Eq. (5.13)) and performed on the basis of the first five measured frequencies (see Table 5.3 and Appendix B2). In addition, MAC analysis is performed based on the measured points (explained in Chapter 4) in order to validate the developed FE model of the flat plate. As the mode shapes of the flat plate are well known a priori, two DOFs are believed to be sufficient to identify the measured mode shapes. The mode shapes of the numerical models, before and after updating, are found to have excellent correlation with the experimental data, which can be observed from the MAC values presented in the table. Obviously using more measured points will produce more reliable MAC values and this is done for the complete welded structure (see Section 5.3).

Table 5.3: Initial and updated natural frequencies (in Hz) for flat plates

Mode	I Experiment	II			III		
		Initial			Updated		
		FE	Error (%)	MAC	FE	Error (%)	MAC
1	24.12	24.27	0.62	1	24.20	0.33	1
2	66.92	67.24	0.48	1	66.96	0.06	1
3	77.65	75.31	3.01	1	76.13	1.95	1
4	131.97	132.51	0.41	1	131.83	0.11	1
5	158.80	154.31	2.83	1	155.82	1.88	1
Total error			7.35			4.33	

Table 5.4 shows the changes in the updating parameters from the initial values, while Fig. 5.6 depicts the changes of the updating parameters from the initial normalised values of unity to convergence. Convergence is obtained immediately and the updated natural frequencies are significantly better with errors of less than 2% are achieved. All the natural frequencies of the flat plate are improved and the errors for the torsional modes are reduced by approximately 1%.

Table 5.4: Parameter changes for the flat plate

Parameter	Initial value	Updated value
$E_{\text{plate}}$ (GPa)	210.00	208.86
$G_{\text{plate}}$ (GPa)	81.00	82.60

The updated FE model of the flat plates is now used for predicting the remaining modes not included in the updating procedure (i.e., modes 6 and 7), so the quality of the updated model can be assessed. As tabulated in Table 5.5, the two natural frequencies have improved slightly with maximum error of approximately 1.5%. The results demonstrate that the updated FE model represents the experimental model quite well, which indicate that the chosen parameters in the updating procedure are appropriate for improving the correlation between the experimental and numerical models. In particular, the Young's modulus value is reduced slightly after updating, which results in a

slightly lower flexural rigidity in the FE model and consequently reduces the frequencies of the bending modes. On the other hand, modification of the shear modulus (i.e., by increasing the value) provides a significant improvement in the torsional modes (i.e., increases the natural frequencies of the torsional modes). This shows that the initial FE model was a bit stiffer in bending while slightly flexible in torsion than it should be in the actual structure.

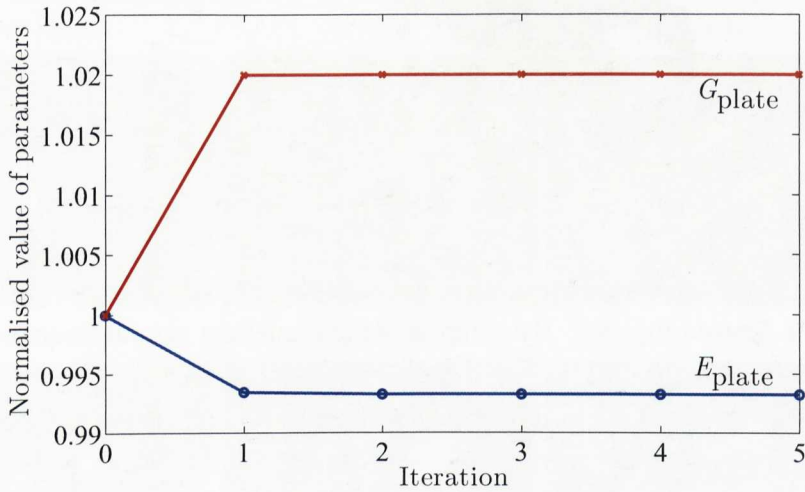


Figure 5.6: Parameters changes of the flat plates

Table 5.5: Flat plates: prediction of higher modes that are not included in the updating procedure

Mode	I	II		III	
	Experiment	FE	Error (%)	FE	Error (%)
6	219.55	223.30	1.71	222.00	1.12
7	246.31	240.87	2.21	242.51	1.54

### 5.2.2 FE modelling and model updating of the hat-shaped shells

The hat-shaped shells are modelled using approximately 3000 CQUAD4 elements, as shown in Fig. 5.7 and coded as in Appendix B3. Similarly to the flat plates, the nominal properties as in Table 4.1 are assigned to the FE model, and the discrepancies between the actual hat-shaped shells in comparison with the nominal design, as explained in Chapter 4, are incorporated. These findings are vital to the development of the FE model as the outcome of the numerical model is found to be very sensitive to the fold radii of the hat-shaped shells.

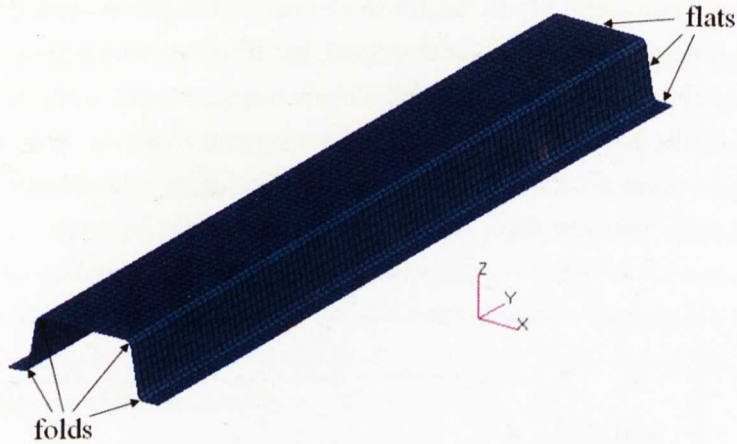


Figure 5.7: The FE model of the hat-shaped shell

The first ten natural frequencies and mode shapes of the initial FE model are shown in Table 5.6 and Fig. 5.8. By comparing the numerical natural frequencies with their experimental counterparts, it can be seen that errors of up to 6% exist. FE model updating is performed based on the first five modes (tabulated in Table 5.7) in order to reduce these errors between the two sets of natural frequencies, while the remaining modes (i.e., modes 6 to 10) are used later for assessing the quality of the updated model.

Table 5.6: Measured natural frequencies and finite element predictions in Hz for the hat-shaped shells

Mode	Experiment	Initial FE	Error (%)
1	70.11	67.28	4.04
2	273.70	256.98	6.11
3	287.92	273.47	5.02
4	334.73	334.41	0.10
5	395.43	386.35	2.30
6	634.82	627.80	1.11
7	642.67	637.58	0.79
8	725.74	707.99	2.45
9	759.71	720.74	5.13
10	780.53	774.82	0.73

From Table 5.7, errors of up to approximately 6% can be observed while very good MAC values of more than 0.95 are obtained for all the modes. The updating procedure is performed by means of three parameters (see Appendix B4): (1) the thickness of fold regions of the hat-shaped shells, (2) the thickness of flat regions of the hat-shaped shells, and (3) the Young's modulus of the hat-shaped shells. Sensitivities of natural frequencies to changes in these parameters are shown in Table 5.8, while their initial



values for updating are summarised in Table 5.9.

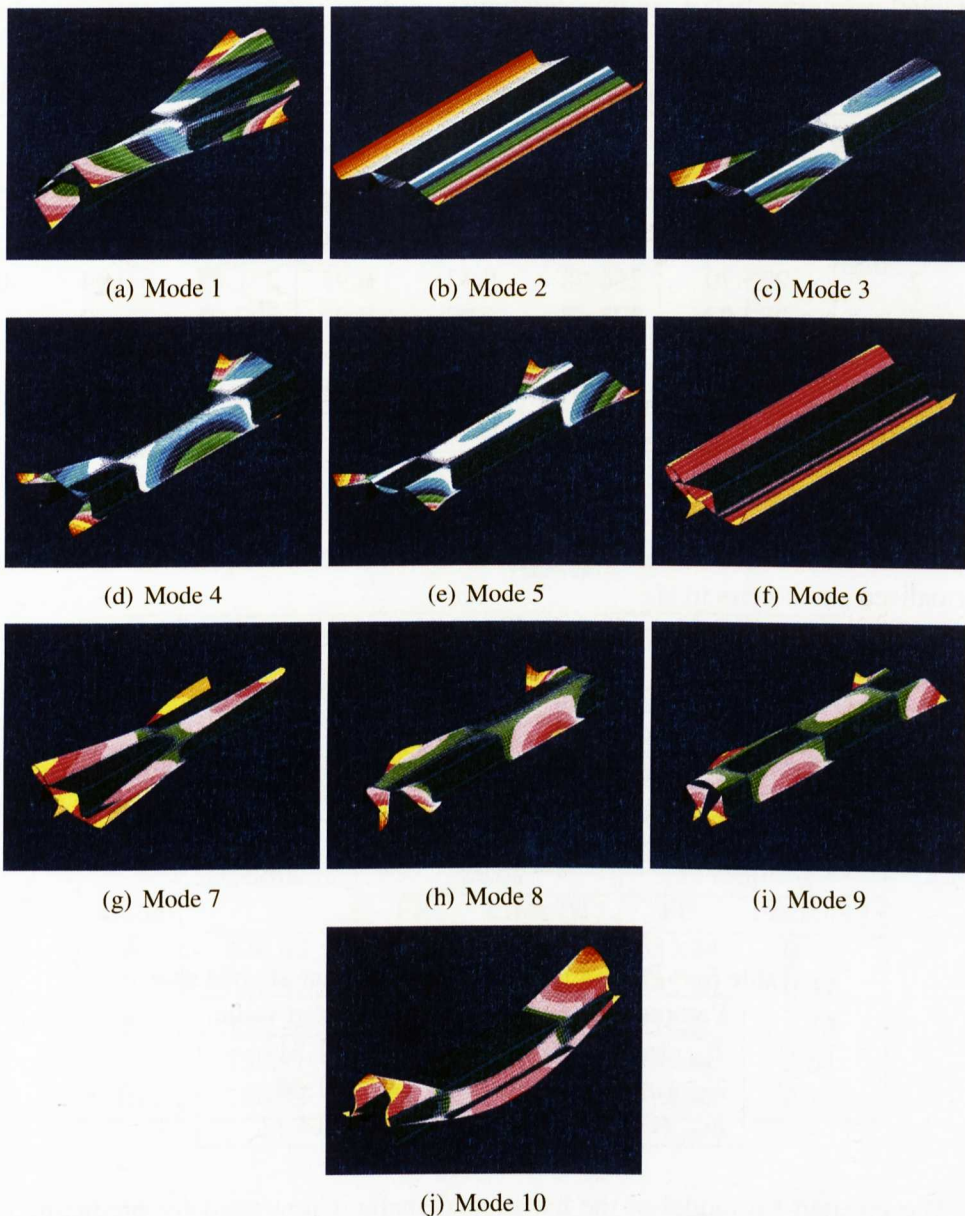


Figure 5.8: The first ten numerical mode shapes of the hat-shaped shells

Table 5.7 (Column III) gives the updated natural frequencies, while the final values of the updating parameters are tabulated in Table 5.9. The discrepancies of the natural frequencies for all five modes are reduced significantly, with the maximum of less than 1.1%. Some changes can also be observed from the two thickness parameters, i.e., the final value of the fold thickness appears to be smaller than the initial, while the updated thickness of the flat regions is found to be bigger than the initial value. Moreover, the Young's modulus of the hat-shaped shells is found to change only slightly within reasonable range. The changes of the updating parameters from the initial normalised

values of unity are shown in Fig. 5.9. Similarly to the flat plates, the convergence is obtained very quickly (i.e., in two iterations).

Table 5.7: Initial and updated natural frequencies (in Hz) for hat-shaped shell

Mode	I Experiment	II Initial			III Updated		
		FE	Error (%)	MAC	FE	Error (%)	MAC
1	70.11	67.28	4.04	0.96	70.24	0.19	0.96
2	273.70	256.98	6.11	0.95	271.12	0.94	0.95
3	287.92	273.47	5.02	0.97	287.64	0.10	0.97
4	334.73	334.41	0.10	0.99	336.51	0.53	0.99
5	395.43	386.35	2.30	0.98	399.67	1.07	0.99
Total error			17.56			2.83	

Table 5.8: Hat-shaped shells: Sensitivities of the natural frequencies to the selected normalised parameters in Hz

Mode	Fold thickness ( $T_{fold}$ )	Flat thickness ( $T_{flat}$ )	Young's modulus ( $E_{hat}$ )
1	7.70	58.06	1.89
2	188.00	237.70	231.82
3	239.10	247.76	211.94
4	43.46	68.80	158.91
5	252.30	222.55	210.76

Table 5.9: Parameter changes for the hat-shaped shell

Parameter	Initial value	Updated value
$T_{fold}$ (mm)	1.45	1.31
$T_{flat}$ (mm)	1.45	1.53
$E_{hat}$ (GPa)	210.00	214.22

The updated FE model of the hat-shaped shells is now used for prediction of the remaining modes not included in the updating procedure (i.e., modes 6 to 10). As can be seen from Table 5.10, the natural frequencies of all the modes used in the prediction improved significantly from the initial predictions with maximum error of 2.64%. However, due to the complexity of the vibration modes (as shown in Fig. 5.8) of the hat-shaped shells, it is very difficult to relate the influence of the updating parameters to each mode directly. Nevertheless, the updating results demonstrate that the parameters used in the updating procedure are appropriate.

Since the FE models of both substructures (i.e., the flat plates and the hat-shaped shells) have been updated successfully, they can now be employed in modelling the welded structures. By ignoring the uncertainties due to manufacturing when welding

the structures, the uncertainties in the developed FE model are attributed only to the weld modelling.

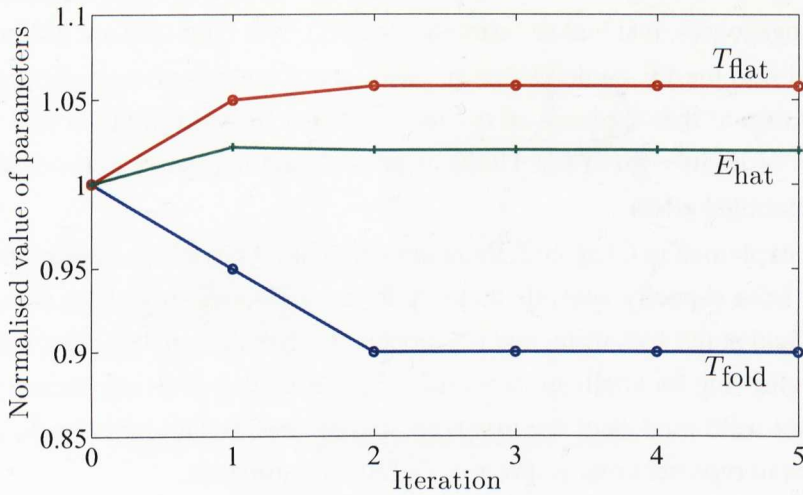


Figure 5.9: Parameters changes of the hat-shaped shells

Table 5.10: Hat-shaped shells: prediction of higher modes that are not included in the updating procedure

Mode	I		II		III	
	Experiment	Initial		Predicted		
		FE	Error (%)	FE	Error (%)	
6	634.82	627.80	1.11	635.24	0.07	
7	642.67	637.58	0.79	645.70	0.47	
8	725.74	707.99	2.45	716.10	1.33	
9	759.71	720.74	5.13	739.66	2.64	
10	780.53	774.82	0.73	782.83	0.29	

### 5.3 FE modelling and model updating of the welded structures

This subsection details the modelling work of the welded structures, and explains the selection of elements to represent the laser weld joints. The updated FE models of the flat plates and the hat-shaped shells are utilised here, and the success in updating both models of the substructures indicates that the uncertainties incorporated in the complete model are largely due to the modelling of the laser weld joints. It is therefore vital to use an appropriate model that is able to represent the dynamic characteristics of the joints very well.

### 5.3.1 FE modelling of laser weld joints

Modelling weld joints is always difficult, owing to the existence of many local effects induced during the welding process (such as geometrical irregularities, material inhomogeneities, residual stresses and defects). Not only they are difficult to be incorporated into the FE model, there are also lots of uncertainties regarding these effects. In addition to that, because of the large number of weld joints in real structures, FE models of joints with as few DOFs as possible are necessary in order to minimise the computational effort.

As explained in Chapter 2, there are two main types of spot weld models: (1) models for limit capacity analysis that require very detailed models to compute a smooth stress field at the spot weld, and (2) models for dynamic analysis that use a very coarse mesh, allowing for application of much simpler models with significantly fewer DOFs. The spot weld models of the first type are not considered in this work, as they are too detailed to represent many spot weld joints in a structure.

The spot weld models for dynamic analysis can be categorised into two categories, i.e., models that require congruent mesh and models that do not. The former necessitates surface re-meshing for any changes in the models in order to ensure coincident nodes for the spot weld connections. In contrast, spot weld connections of the second category can be established at any locations using the existing mesh, so it is possible to assemble components with different meshes. The advantage of having non-congruent mesh is so important, hence it is now becoming so favourable in the industries.

The feasibility of using some of the most common spot weld models for modelling the laser weld joints is investigated, as presented in the following paragraphs. The type of elements that best represents the laser weld joints and has the potential for model updating is selected for modelling the welded structures.

#### Single beam models

Structural joints like the spot welds and bolts are usually represented by simple (elastic or rigid) two-node beam elements to establish the mass and stiffness properties of the real joints. These models require a node-to-node connection, thus a congruent mesh must be employed. The single beam models (see Fig. 3.7) are investigated by using elastic beam elements (i.e., CBAR) available in NASTRAN [56]. The CBAR element is a simple general purpose one-dimensional beam element that supports tension and compression, torsion, bending and shear behaviours. As depicted in Fig. 5.10, the element consists of two grid points (GA and GB) with six DOFs (i.e., three translations and three rotations) at each point. In addition, the beam properties must be constant along the length of the element, while the shear center and neutral axis must coincide. The element is formulated based on the classical beam theory that assumes no

shear deformation across the section of the beam. In other words, any deformation due to shear is not accounted for, hence the plane cross sections remain plane during deformation.

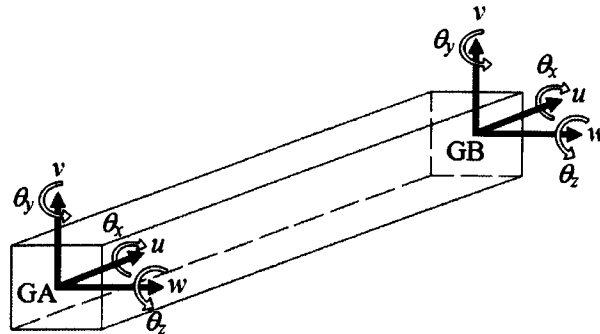


Figure 5.10: CBAR element in NASTRAN

Due to the requirement of congruent mesh, the FE model of the flat plates are re-meshed with approximately 2000 CQUAD4 elements (as shown in Fig. 5.11 and Appendix B5) to match the mesh of the FE model of the hat-shaped shells. The refined FE model is also used in modelling the welded structures using brick elements and CWELD with 'ALIGN' format (explained later in this chapter). These substructures' FE models are connected together by twenty CBAR elements with circular cross section at the specified locations illustrated in Fig. 4.15 to form the FE model of the welded structures. The input NASTRAN code for the model is given in Appendix B6. The natural frequencies and mode shapes produced from the FE model are shown in Tables 5.11 (Column II) and 5.12 (Column II), respectively, and they are compared with the experimental natural frequencies and mode shapes. The natural frequencies are found to be significantly underestimated by the model with a total error of more than 55%, which indicates that this type of connection generally tends to underestimate the stiffness of the joints [21]. Furthermore, there is also a mode swapping issue with the third and fourth numerical mode shapes, as can be seen from Table 5.12.

### Single brick models

A six-sided brick element (i.e., CHEXA in NASTRAN [56]) is used to characterise the spot weld joint in the welded structures. The CHEXA element has eight corner grid points and up to twenty grid points if the twelve optional midside grid points are included; each with three translational DOFs as illustrated in Fig. 5.12. The nodes of the brick element must be coincident with the nodes of the lower and upper surfaces (as depicted in Fig. 3.8), hence similarly to the single beam models, a congruent mesh is necessary. The input NASTRAN code is presented in Appendix B7, while



the results from using these brick elements in modelling the laser spot weld joints are given in Tables 5.11 (Column III) and 5.12 (Column III), respectively. Comparing these results with the measured data demonstrates that the brick elements are able to represent the stiffness of the weld joints quite well, with significant reduction in the error of natural frequencies in comparison with the results produced using the beam elements. Moreover, the issue of mode swapping does not exist when using the brick elements.



Figure 5.11: Refined mesh of the flat plates

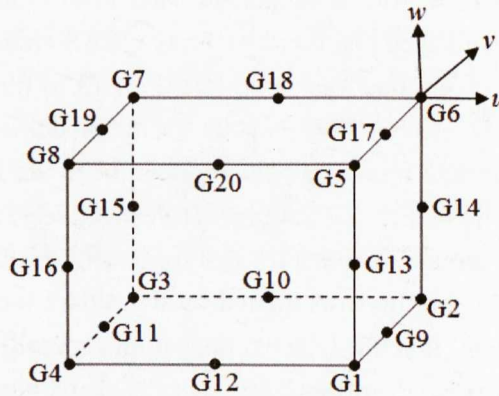


Figure 5.12: CHEXA element in NASTRAN

Heiserer et al. [47] developed an improved version of the brick model (illustrated in Fig. 3.11) known as the ACM2 model or CHEXA in LMS VirtualLab, consisting of a brick element with weighted average constraint elements (i.e., RBE3) in NASTRAN [56]. The RBE3 elements are employed to distribute applied loads onto a set of nodes, which removes the problem of increased local stiffness when rigid link is used [28]. In addition, the ACM2 removes the need for congruent mesh, thus the spot weld joints can be located anywhere in the model. Nevertheless, the ACM2 model is not investigated in this work as it is not available in NASTRAN.

## CWELD element

The CWELD element (see Fig. 3.12) developed by Fang et al. [49] has been implemented in NASTRAN [56]. As explained in Section 3.3.2, the CWELD element can be established with congruent or non-congruent meshes as illustrated in Fig. 5.13. In this section, twenty CWELD elements with patch-to-patch connection type (i.e., 'PARTPAT' format) are employed in modelling the welded structures (see Appendix B8), hence non-congruent mesh can be used in the model. The natural frequencies from this model are tabulated in Table 5.11 (Column IV) and the mode shapes are depicted in Table 5.12 (Column IV). From the findings, it can be seen that the natural frequencies are underestimated with maximum error of approximately 10%. The mode shapes, however, are in very good agreement with the measured data.

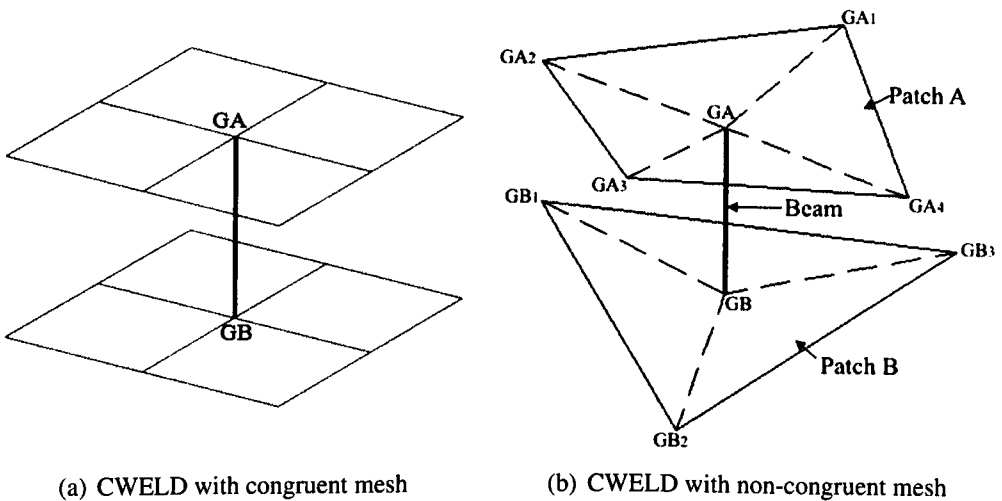


Figure 5.13: The CWELD element with congruent and non-congruent mesh

Table 5.11: Comparison of initial natural frequencies (in Hz) using different elements

Mode	[I]	[II]		[III]		[IV]	
	Experiment	CBAR	Error (%)	CHEXA	Error (%)	CWELD	Error (%)
1	508.12	473.50	6.81	488.34	3.89	480.27	5.48
2	553.69	482.45	12.87	557.83	0.75	515.58	6.88
3	575.39	537.05	6.66	559.19	2.82	550.88	4.26
4	627.45	536.18	14.55	621.04	1.02	567.36	9.58
5	643.66	544.55	15.40	624.17	3.03	579.79	9.92
Total error		56.30		11.51		36.12	

## Comparisons and selection of elements for representing laser weld joints

The three types of spot weld models are compared in order to choose the most suitable model to represent the laser spot weld joints. As summarised in Tables 5.11 and

5.13, the beam model fails to predict the natural frequencies accurately. On the other hand, while also suffering with underestimation of natural frequencies, the use of the CWELD element manages to bring the error down. This is further improved when the brick model is employed. In terms of the mode shapes prediction (Table 5.12), mode swapping problem occurs when utilising the beam model. In contrast, the mode shapes are successfully predicted by the brick and CWELD elements.

Table 5.12: Comparison of mode shapes using different elements

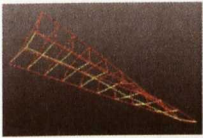

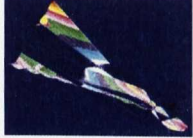

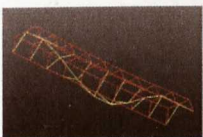

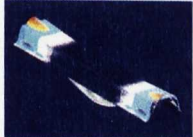

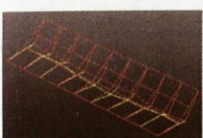







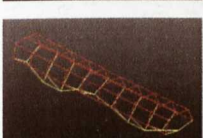
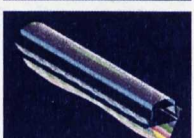


Mode	[I] Experiment	[II] CBAR	[III] CHEXA	[IV] CWELD
1				
2				
3				
4				
5				

Table 5.13: Comparisons of CBAR, CHEXA and CWELD by NASTRAN in modelling laser weld joints

	CBAR	CHEXA	CWELD
Prediction of natural frequencies	Poor	Good	Satisfactory
Prediction of mode shapes	Poor	Good	Good
Non-congruent mesh	No	No	Yes/No (based on connection type)

On the matter of modelling convenience, the beam and brick models (unless ACM2 by Heiserer et al. [47] is employed) requires coincident meshed surfaces while the CWELD model can be used with both congruent and non-congruent mesh depending



on the type of connection used when defining the CWELD element. Furthermore, the CWELD element poses a big potential for model updating, as both geometrical and material properties of the weld model can be updated. From these comparisons, it is found that the characteristics of the CWELD element is much more appealing than the other two models, so the CWELD element is selected for representing the laser weld joint.

### 5.3.2 FE model updating of welded structures

#### FE model of welded structures using CWELD elements with ‘PARTPAT’ format

The laser spot weld joints are modelled using twenty CWELD elements with patch-to-patch connection (as presented in the previous section), as shown in Fig. 5.14. It is known that the use of the CWELD elements in modelling the joints result in underestimation of the natural frequencies (see Table 5.11 (Column IV) or Table 5.14 (Column II)); thus, FE model updating needs to be conducted in order to bring the predicted natural frequencies closer to their measured counterparts.

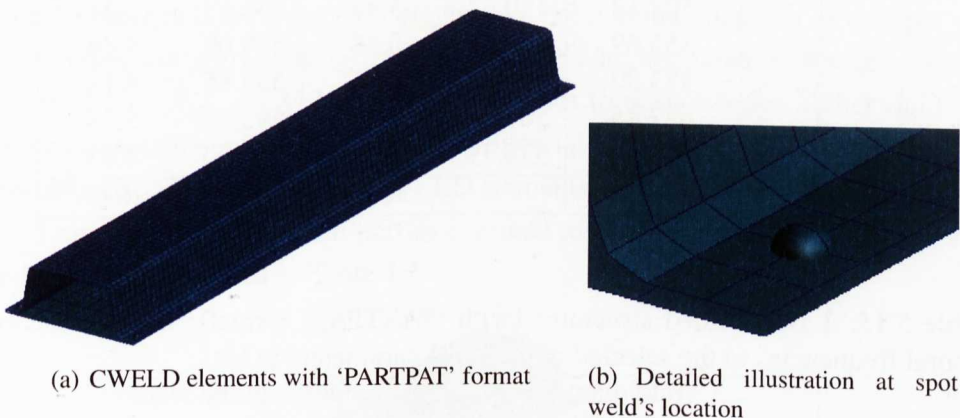


Figure 5.14: FE model of welded structure using CWELD elements with ‘PARTPAT’ format

The updating procedure outlined in Section 5.1.2 is applied to the FE model of the welded structure and SOL 200 is run to update the model until the computed natural frequencies match those from the experiment (refer to Appendix B9 for optimisation code). Prior to updating, sensitivity analysis is performed with respect to the properties of the CWELD element (i.e., diameter, Young’s modulus, shear modulus, density and Poisson’s ratio), so that the most sensitive parameters can be selected for the procedure. From the sensitivity values (Table 5.15), it is found that the natural frequencies are only sensitive to the changes of the diameter and Young’s modulus of the spot welds. Hence, these two parameters are used in the updating procedure.

The initial values of the diameter and Young's modulus of the weld are set to 5 mm and 210 GPa, respectively. The former is allowed to vary between 3.5 to 5.5 mm, while the latter has a range of 185 to 220 GPa. The updated natural frequencies are tabulated in Table 5.14 (Column III), while changes in updating parameters are shown in Table 5.16. Although the updated values for both parameters reach the maximum allowable values, the total error of natural frequencies is only reduced to approximately 21%. The results show that the natural frequencies are still underestimated by the numerical model, which demonstrates the lack of stiffness in the CWELD modelling. Furthermore, based on the updating results, it is concluded that the two CWELD parameters alone cannot successfully improve the results of the initial model; hence the FE model of the laser weld joints needs to be modified in order to improve the correlation between the experimental and numerical models.

Table 5.14: Measured natural frequencies and finite element predictions in Hz for the laser welded structures using CWELD elements with 'PARTPAT' format

Mode	I Experiment	II Initial		III Updated	
		FE	Error (%)	FE	Error (%)
1	508.12	480.27	5.48	506.03	0.41
2	553.69	515.58	6.88	529.09	4.44
3	575.39	550.88	4.26	539.85	6.18
4	627.45	567.36	9.58	592.43	5.58
5	643.66	579.79	9.92	617.70	4.03
Total error			36.12		20.65

Table 5.15: Laser welded structures (with 'PARTPAT' format): Sensitivities of the natural frequencies to the selected normalised parameters in Hz

Mode	Weld diameter ( $d_{weld}$ )	Young's modulus of the weld ( $E_{weld}$ )
1	7.13	12.27
2	10.50	15.64
3	34.40	58.79
4	42.84	62.00
5	36.18	53.17

Table 5.16: Parameter changes for the laser welded structures (with 'PARTPAT' format)

Parameter	Initial value	Updated value
$d_{weld}$ (mm)	5.0	5.5
$E_{weld}$ (GPa)	210	220

### Improved FE model of welded structures using CWELD elements with ‘ALIGN’ format

Based on the findings presented in the previous section, it is decided that the FE model of the laser weld joints is insufficient to represent the actual stiffness of the joints. It is also established that the properties of the CWELD element alone cannot bring the numerical data closer to the measured data. Hence, patches surrounding the CWELD elements must be manipulated in order to deal with the lack of stiffness encountered by the previous model. In order to do so, the patch-to-patch CWELD connection is replaced with point-to-point connection (i.e., ‘ALIGN’ format - see Section 3.3.2 for more details). The ‘ALIGN’ format has been chosen so a better control of patch size surrounding each weld can be obtained by defining the size of the FE mesh.

By using the ‘ALIGN’ format, congruent mesh must be used hence refined FE model of the flat plates (as in Fig. 5.11) is employed in the FE model of the welded structures, as depicted in Fig. 5.15. According to Fang et al. [49], the CWELD element simulates the force transfer between the two patches accurately for  $d_{\text{weld}}/S \leq 1$ , where  $S$  is the mesh size. The stiffness of the connection may be underestimated by the CWELD element if the diameter is larger than the surface patch. In this work, the size of the patches is set to be 20% bigger than the nominal diameter of the spot weld joints (consequently gives  $d_{\text{weld}}/S = 0.83$ ), while a higher value of Young’s modulus is assigned (i.e.,  $E_{\text{patch}} = 350$  GPa) to the patches to acknowledge higher rigidity of the weld connection than the adjacent bulk material. The initial values for the material properties and the diameter of the CWELD elements are also defined, with the diameter being 5 mm and the material properties assumed to be the same as the nominal values of mild steel, as tabulated in Table 4.1.

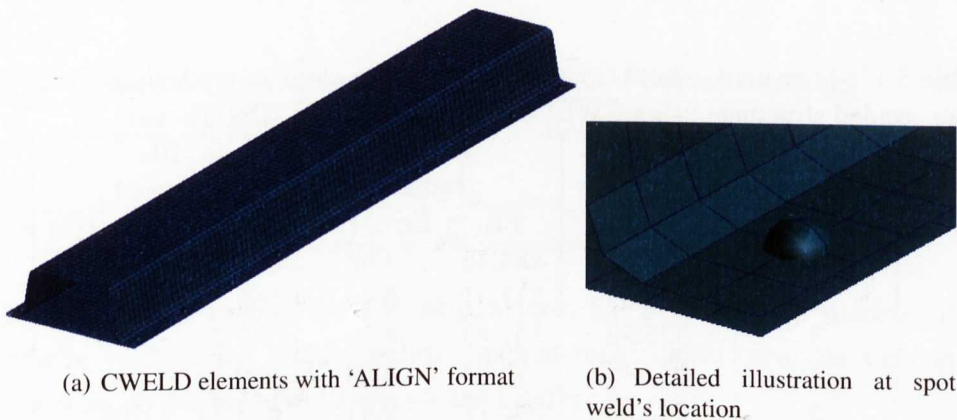


Figure 5.15: FE model of welded structure using CWELD elements with ‘ALIGN’ format

These modifications slightly improve the initial natural frequencies of the FE model, as given in Table 5.17 (Column II), demonstrating that the properties of the patches are

critical when modelling the weld joints. In order to quantify the correlation between the initial FE and experimental models, MAC values are computed as given in Table 5.18. While the MAC values are already reasonably good, the natural frequencies of all the experimental modes are still underestimated by the numerical model with frequency errors being more than 4%. These errors show the critical need for removing the uncertainties from the weld modelling, therefore the FE model updating procedure has to be carried out.

The updating procedure is performed using the diameter ( $d_{weld}$ ), Young's modulus of the weld ( $E_{weld}$ ) and Young's modulus of the patch ( $E_{patch}$ ) as parameters. The sensitivity coefficients for these parameters are tabulated in Table 5.19, and the initial values of these updating parameters are summarised in Table 5.20. The values of the weld parameters are allowed to vary in a limited reasonable range only, while the Young's modulus of the patch is allowed to have a very big variation due to the uncertainties of the patch properties.

Updating is carried out on the basis of the first five measured frequencies from the welded structures. The updating procedure converges after five iterations, as depicted in Fig. 5.16, and the updated natural frequencies and parameters are presented in Tables 5.17 (Column III) and 5.20 respectively. From Table 5.17, it can be concluded that the natural frequencies are improved significantly and the MAC values for all the modes are more or less similar to the initial values (see Tables 5.18 and 5.21). The results achieved also show that the CWELD parameters (i.e.,  $d_{weld}$  and  $E_{weld}$ ) reach the maximum allowable values, as in the previous model. Attention is given to the Young's modulus of the patch (i.e.,  $E_{patch}$ ) which is considered as the parameter that most affects the behaviour of the model. Based on the updating results, it is found that the  $E_{patch}$  is approximately three times the Young's modulus of the weld.

Table 5.17: Measured natural frequencies and finite element predictions in Hz for the laser welded structures using CWELD elements with 'ALIGN' format

Mode	I Experiment	II Initial		III Updated	
		FE	Error (%)	FE	Error (%)
1	508.12	484.46	4.66	497.19	2.15
2	553.69	517.91	6.46	565.24	2.09
3	575.39	551.43	4.16	569.26	1.07
4	627.45	575.81	8.23	629.54	0.33
5	643.66	583.11	9.41	633.24	1.62
Total error			32.92		7.26

Prediction of higher modes that are not included in the updating procedure (i.e., modes 6 to 10) is conducted and the results are presented in Table 5.22 and Fig. 5.17. By using the initial FE model (before updating), big errors of up to almost 9% can be

observed on bending modes (i.e., modes 6, 7, 8 and 10) while very small error (0.13%) is obtained for the torsional mode (i.e., mode 9). However, the natural frequencies of these bending modes improve significantly when predicted using the updated FE model, which indicates that the updated model represents the measured model well. It demonstrates that the bending stiffness of the FE model has improved by the modification to  $E_{patch}$  after updating, which consequently improves the frequencies of all bending modes.

Table 5.18: Initial MAC values of the welded structures

FE modes	Experimental modes				
	1	2	3	4	5
1	<b>0.95</b>	0.00	0.00	0.00	0.00
2	0.00	<b>0.87</b>	0.00	0.00	0.01
3	0.00	0.00	<b>0.98</b>	0.00	0.00
4	0.00	0.00	0.00	<b>0.75</b>	0.00
5	0.00	0.01	0.00	0.03	<b>0.97</b>

Table 5.19: Laser welded structures: Sensitivities of the natural frequencies to the selected normalised parameters in Hz

Mode	Weld diameter ( $d_{weld}$ )	Young's modulus of the weld ( $E_{weld}$ )	Young's modulus of the patch ( $E_{patch}$ )
1	2.55	7.78	16.56
2	9.48	25.07	58.42
3	3.44	8.73	22.65
4	10.51	26.60	65.59
5	10.37	26.03	62.89

Table 5.20: Parameter changes for the laser welded structures

Parameter	Initial value	Updated value
$d_{weld}$ (mm)	5.0	5.5
$E_{weld}$ (GPa)	210	220
$E_{patch}$ (GPa)	350	659

Since the FE models of the welded structures has been updated successfully, it can now be employed in further analysis, such as for stochastic analysis and damage identification, as presented in Chapter 6 and Chapter 7.

## 5.4 Conclusions

In this chapter, FE modelling and model updating procedure have been explained and stages involved when modelling the welded structures (i.e., (1) the FE modelling and



model updating of the substructures, and (2) the FE modelling and model updating of the welded structures) are described. Three different types of most commonly used spot weld models (i.e., beam, brick and CWELD elements) have been investigated for representing the laser weld joints, and their advantages and disadvantages are briefly discussed. When single beam elements are employed, the results show that the natural frequencies are significantly underestimated and the mode shapes are not predicted so accurately. The problem in the prediction of the natural frequencies and the mode shapes are solved when using the brick elements. However, the computational penalty due to the use of solid brick elements and congruent mesh is so significant, thus it is decided that they should not be employed in the FE model. In the end, the CWELD element is chosen and applied in modelling the laser welded structures.

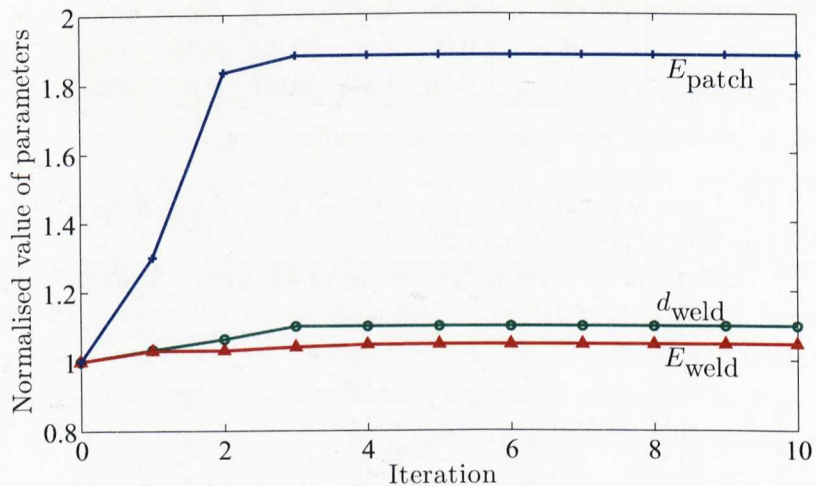


Figure 5.16: Parameters changes of the welded structures

Table 5.21: Updated MAC values of the welded structures

FE modes	Experimental modes				
	1	2	3	4	5
1	<b>0.96</b>	0.00	0.00	0.00	0.00
2	0.00	<b>0.86</b>	0.01	0.00	0.01
3	0.00	0.00	<b>0.99</b>	0.00	0.00
4	0.00	0.01	0.00	<b>0.79</b>	0.00
5	0.00	0.02	0.00	0.03	<b>0.97</b>

Initially, the capability of the CWELD elements to represent the laser spot welds is uncertain and their potential in producing reasonably accurate values of natural frequencies is questionable. Numerical results show that the initial frequencies are very low in comparison with the experimental data when CWELD is used and it is also

found that the CWELD parameters alone cannot improve the results of the initial model even after updating. Further investigation reveals that when a patch parameter is included in the updating, the results improve significantly. The approach indicates that the right selection and combination of updating parameters is important in minimising the errors in the FE model. However, the procedure itself does not guarantee that the updated parameters will have physical meanings; hence, proper selections of parameters and their values must be made to ensure that a realistic model is obtained in the process. The combined use of CWELD and SOL 200 by NASTRAN in modelling the laser welded structures allows wider applications of the approach developed in this research.

Table 5.22: Welded structures: prediction of higher natural frequencies that are not included in the updating procedure

Mode	I Experiment	II		III	
		Initial		Predicted	
		FE	Error (%)	FE	Error (%)
6	664.89	605.85	8.88	645.31	2.94
7	676.52	648.55	4.13	691.73	2.25
8	745.48	728.78	2.51	731.28	1.90
9	815.20	816.22	0.13	818.33	0.38
10	868.58	849.54	2.19	861.63	0.80

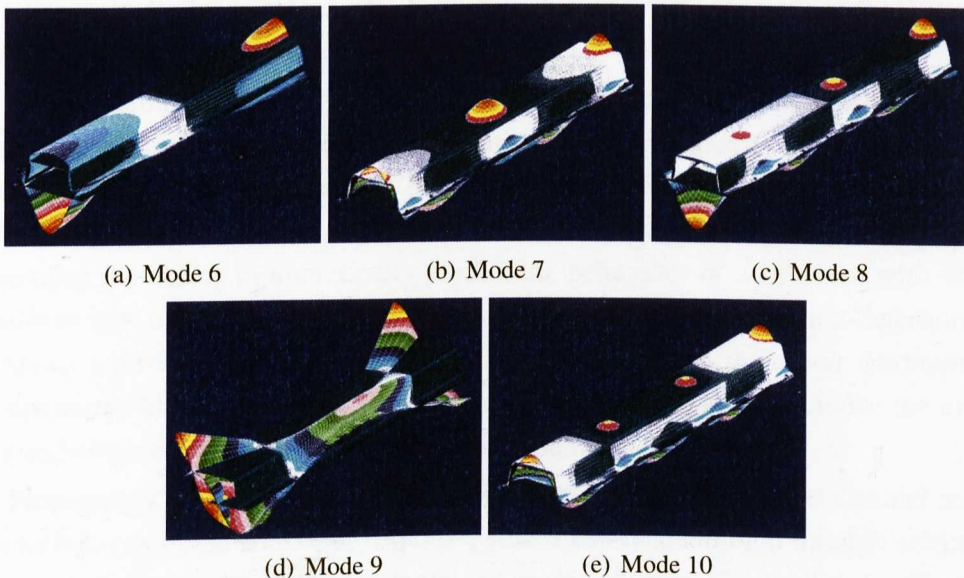


Figure 5.17: Sixth to tenth numerical mode shapes of the welded structures

Most importantly, it is essential to have an appropriate mesh in the FE model since it will influence the size of the patch used in the FE model. The CWELD element simulates the force transfer between the two patches accurately for  $d_{\text{weld}}/S \leq 1$ . The

stiffness of the connection may be underestimated by the CWELD element if the diameter is larger than the surface patch. In this work, the size of the patches is set to be 20% bigger than the nominal diameter of the spot weld joints (consequently gives  $d_{\text{weld}}/S = 0.83$ ), while the Young's modulus of the patch should be approximately three times the value of the Young's modulus of the weld. These values are recommended as starting points for dynamic analysis of structures of similar constructions with many laser spot welds when the CWELD element is used. Nevertheless, users may need to make appropriate modifications to fit the requirements of their structures. It should be noted that the FE model updating presented in this chapter does not consider the uncertainties due to manufacturing variability of the structures. The next chapter discusses the matter and non-deterministic (or stochastic) model updating is explained.

# Chapter 6

## Stochastic model updating for variability in welded structures

### 6.1 Introduction

Interest in uncertainty in engineering structures is growing, owing to the fact that structural properties are normally uncertain and therefore uncertainty exists in the dynamic response. Properties of an individual structure normally change with time due to environmental erosion and damage [8, 88], and also when the structure is being reassembled. It is also unavoidable to have manufacturing variability [9–11, 88] that exists among nominally identical structures, built in the same way from the same materials, such as in a mass production of automotive BIW.

Issues relating to uncertainty and variability, such as safety and reliability, lead to increasing demands for improved computational methods that incorporate uncertainties in the structural properties. When these uncertainties are taken into account, a deterministic problem then changes to a non-deterministic problem. It is highly appreciated that the ability to numerically predict the behaviour of a structure with uncertainties is very useful and of great scientific value. Nevertheless, the non-deterministic problems are more complex and computationally expensive than their deterministic counterparts. Moreover, little knowledge may be available to characterise the uncertainties, which could result in inaccurate information of the outputs.

Propagation of uncertain structural parameters through the system's model results in uncertainties in the structural response, which can be quantified through selections of propagation methods as briefly explained in this chapter. Firstly, the classification, representation and propagation methods for uncertainty are discussed. Relevant works regarding uncertainty by other researchers are included and thorough investigations on parameter selections for stochastic updating are performed. The uncertainty problem in the laser welded structures is investigated and two approaches are studied to efficiently represent and propagate uncertainty due to manufacturing variability in the

welded structures. The non-deterministic (or stochastic) model updating formulation is included and the results are discussed.

## 6.2 Uncertainty in structural dynamics

### 6.2.1 Uncertainty classification

Uncertainty can originate from many sources, such as the lack of knowledge, physical randomness of structures, inaccurate information, etc.. It may be distinguished into two categories [12–14, 89], i.e., epistemic and aleatory uncertainty, based on whether the source of uncertainties is reducible or not.

*Epistemic uncertainty* is derived from some level of ignorance, lack of knowledge or incomplete information of the system or the surrounding environment, and can be reducible through further research or measurement. Hence, this type of uncertainty is also referred to as reducible uncertainty, subjective uncertainty or model form uncertainty.

*Aleatory uncertainty*, on the other hand, arises from heterogeneity or diversity in a population (for example, intrinsic randomness associated with the physical system or the environment under consideration) and frequently cannot be reduced through further study or measurement. This type of uncertainty is also referred to as irreducible uncertainty, inherent uncertainty, stochastic uncertainty or variability.

However, aleatory uncertainty could also be due to lack of knowledge when information within its range is missing that consequently becomes epistemic uncertainty.

### 6.2.2 Uncertainty representation

Uncertainty can be represented by various mathematical tools, including the probability theory, interval arithmetic and fuzzy set theory, just to name a few [88, 90]. These three approaches are briefly explained in the following.

**The probability theory** is concerned with analysis of random events (such as random variables and stochastic processes) of a large set of data. In the probabilistic approach, uncertainty is characterised by the probabilities associated with the events, which can be defined as the ratio of the number of occurrences of that particular event ( $n_x$ ) over the total number of occurrences ( $n_t$ ), as expressed in Eq. (6.1). Examples of random events in structural dynamics include experimental measurements of a large set of test

structures, and a large number of mathematical simulations of structures with randomly varying parameters.

$$P(x) = \lim_{n_t \rightarrow \infty} \frac{n_x}{n_t} \quad (6.1)$$

**The interval arithmetic** is employed to represent uncertainty where uncertain parameters  $\theta$  and response variables  $z$  are bounded within their upper and lower limits (as expressed in Eq. (6.2)) in order to avoid the possibility of extreme events. This representation does not require information about the type of uncertainty in the variables, hence it is very useful for uncertainty estimation especially in cases where probabilities cannot be obtained or unknown.

$$\theta \in [\underline{\theta}, \bar{\theta}] \quad \text{and} \quad z \in [\underline{z}, \bar{z}] \quad (6.2)$$

**The Fuzzy sets theory** facilitates uncertainty analysis through vague or ‘fuzzy’ definition of variables. The theory is more suitable for qualitative reasoning and classification of variables into a fuzzy set, rather than for quantitative estimation of uncertainty. In fuzzy sets approach, the uncertainty is described in terms of membership functions ( $\mu$ ) as a replacement for probabilistic information. The values of the membership functions correspond to the ‘degrees of truth’ within a range of [0, 1], as illustrated in Fig. 6.1 and described in the following.

$$\mu(\theta) = \begin{cases} 1 & \text{if } \theta \in A \\ 0 & \text{if } \theta \notin A \\ p; 0 < p < 1 & \text{if } \theta \text{ partially belongs to } A \end{cases} \quad (6.3)$$

### 6.2.3 Uncertainty propagation

Quantification of uncertainty in the outputs of a model with uncertain inputs is generally referred to as uncertainty propagation, which can be distinguished into three main categories: sampling methods [91, 92], response surface approximation (RSA) methods [93], and convex methods [94, 95]. The Monte Carlo simulation (MCS) method and its variants are examples of the sampling methods, while the perturbation and the interval methods belong to the RSA and convex approaches, respectively.

Selection of the propagation method is mostly dependent on the representation of the uncertainty, with examples as summarised in Fig. 6.2. The choice of methods has been reported by many people; for instance, the MCS and perturbation methods were

considered by Fonseca et al. [90] when estimating uncertainties in model parameters based on the probability in experimental response variables. Excellent results were obtained by both methods, but the MCS was proven to be much more computationally expensive than the perturbation method. These two methods are explained further in this chapter due to their popularity in uncertainty propagation.

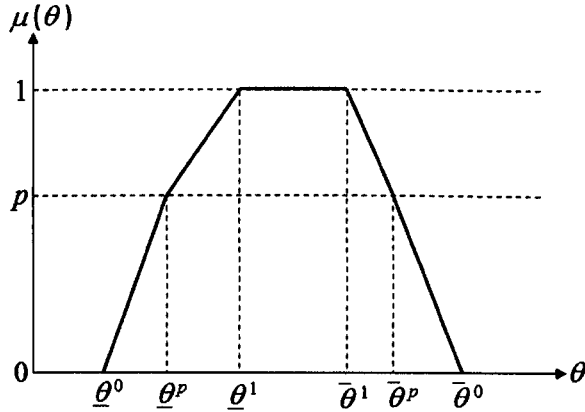


Figure 6.1: Membership function of fuzzy set with interval representation

### The Monte Carlo Simulation method

The MCS method is one of the most popular methods for analysing the propagation of uncertainty in deterministic mathematical models. The method employs a set of random input variables ( $\theta$ ) that are generated according to their probability distributions in order to evaluate the behaviour of a system or process by iteratively analysing the simulated model to bring out the probability of one or more outputs ( $z$ ). The response statistical properties (i.e., mean and variance) can then be computed from the simulated responses as expressed below.

$$\begin{aligned}
 \text{Response} & : z = f(\theta) \\
 \text{Mean} & : \hat{z} = \int P(z) \cdot z \, dz \\
 \text{Variance} & : \text{cov}(z, z) = \int P(z) \cdot (z - \hat{z})^2 \, dz
 \end{aligned} \tag{6.4}$$

The MCS is a general and straightforward method, and can be used for both stochastic (that requires probability information) and deterministic (without probability information) problems. It provides approximate solutions to many mathematical problems and is frequently employed to validate other methods. However, a large number of samples need to be generated that usually results in considerably time consuming procedure before estimates of parameters of interest are obtained.



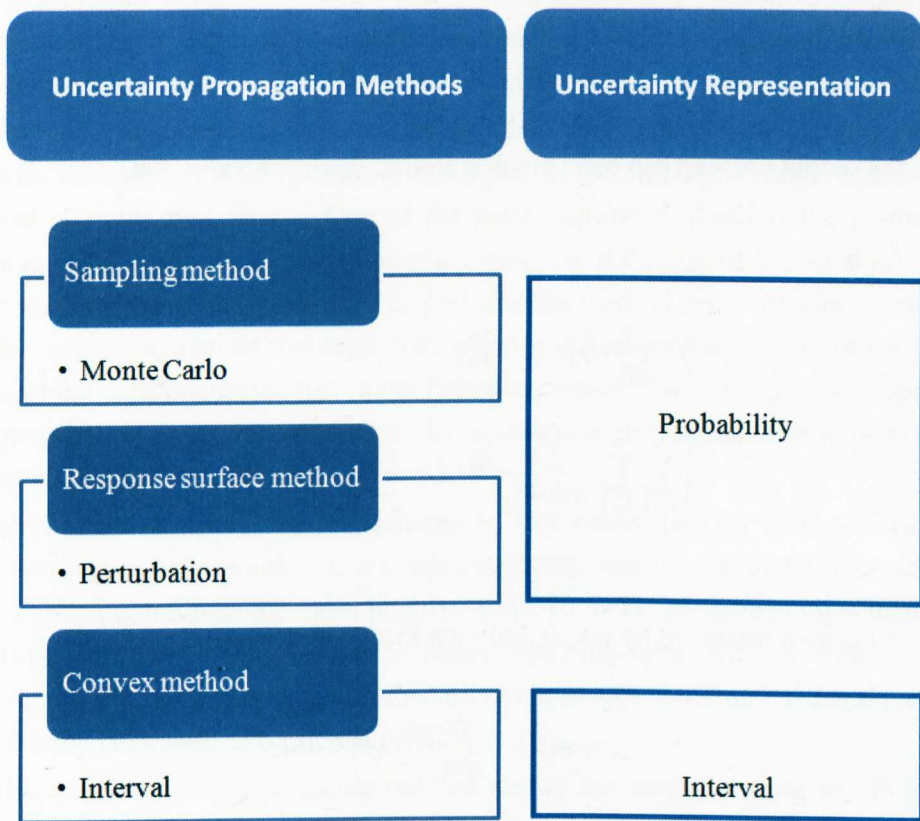


Figure 6.2: Uncertainty propagation methods with their respective examples and relevant uncertainty representations



## The perturbation method

The perturbation method, based on a truncated Taylor series expansion, has been a popular alternative to the MCS method in uncertainty propagation mainly due to its flexibility and lower computational effort [90]. Nevertheless, it should be noted that the method can only perform well when the uncertainties are small and parameter distribution is Gaussian [96]. In this method, the uncertain parameters ( $\theta$ ) are assumed to follow a multivariate normal distribution with mean vector and covariance matrix as follows,

$$\theta \sim N_n(\hat{\theta}, \text{cov}(\theta, \theta)) \quad (6.5)$$

while the output vector  $z$  can be estimated around the mean value  $z(\hat{\theta})$  as,

$$\begin{aligned} z &= z(\hat{\theta}) \\ &+ \sum_{i=1}^n \frac{\partial z}{\partial \theta_i}(\hat{\theta}) \cdot (\theta_i - \hat{\theta}_i) \\ &+ \frac{1}{2} \sum_{i=1}^n \sum_{j=1}^n \frac{\partial^2 z}{\partial \theta_i \partial \theta_j}(\hat{\theta}) \cdot (\theta_i - \hat{\theta}_i) \cdot (\theta_j - \hat{\theta}_j) + \dots \end{aligned} \quad (6.6)$$

Eq. (6.6) is then truncated by taking only the first order term into

$$z = z(\hat{\theta}) + \frac{\partial z}{\partial \theta_i}(\hat{\theta}) \cdot (\theta_i - \hat{\theta}_i) \quad (6.7)$$

or

$$\Delta z = \hat{S} \Delta \theta \quad (6.8)$$

to form the first-order perturbation equation.  $\hat{S} = \frac{\partial z}{\partial \theta}$  is the sensitivity matrix of  $z$  evaluated at  $\hat{\theta}$ . Therefore, the covariance matrices can be written as,

$$\text{cov}(\Delta z, \Delta z) = \hat{S} \times \text{cov}(\Delta \theta, \Delta \theta) \times \hat{S}^T \quad (6.9)$$

$$\text{cov}(\Delta \theta, \Delta z) = \text{cov}(\Delta \theta, \Delta \theta) \times \hat{S}^T \quad (6.10)$$

## 6.3 Stochastic model updating for uncertainty in structural dynamics

Structural parameters are normally assumed to be known in forward problems, but unknown in inverse problems such as in model updating [4]. It is often easier to measure the variability in structural dynamics (such as modal properties and frequency response functions (FRFs)) than measuring the uncertainty in structural parameters. The statistical estimates from the response measurements may then be used to deduce the statistical estimates of the parameters. This inverse problem of estimating the parameter distribution from the measured response distribution is called uncertainty identification or quantification [90].

Statistical methods have been widely used in model updating and methods for dealing with the estimation of parameter variability in the stochastic model updating has evolved over the past years. One of the most popular methods is the perturbation method, which uses the sensitivities expressing the influence of the stochastic input parameters on the output quantity. The perturbation method generally aims at calculating the first two statistical moments (i.e., mean and standard deviations) of the parameters, which is further explained in the following subsection. Driven by its popularity, the perturbation approach remains under continuous development despite extensive research since the past decades.

Application of the FE model updating is well established for deterministic problems, but due to uncertainties in real test structures, non-deterministic (or stochastic) model updating has become more popular. Refs. [6, 9–11, 25] are amongst many published papers covering the stochastic model updating approach. A review of past, present and future developments in the stochastic model updating has been presented by Stefanou [97], with 196 references cited.

The stochastic model updating method allows for manufacturing variability and modelling uncertainty to be incorporated so that numerical models with randomised parameters can be updated to match their experimental counterparts [9]. In addition, variability in measurements due to noise can also be considered, as presented by [6, 98]. As a result, robust and credible models are produced which in turn increase confidence in design and analysis of such structures.

However, the stochastic model updating problems are computationally expensive, mainly due to the randomised parameters, hence various assumptions and simplifications have to be made to ensure the efficiency of the methods, as investigated by Haddad Khodaparast and Mottershead [99]. In their work, two efficient methods in stochastic model updating: 1) a perturbation method, and 2) a method based upon the minimisation of an objective function, were investigated. The first method was shown to be viable and the need to compute second order sensitivities (as reported by Hua

et al. [25]) was removed leading to considerable reduction in computational effort in practical engineering applications. A perturbation method reported by Hua et al. [25] is developed for estimating the statistical properties (i.e., means and covariances) of structural parameters on the basis of the measured modal parameters with uncertainty. Nevertheless, the method requires the determination of second-order sensitivities in order to converge the predicted mean values and covariances upon the measured values. Another study using the perturbation method is presented by Govers and Link [100]. This work demonstrates a method to adjust parameter means and covariance matrix from multiple sets of experimental modal data. The method is performed by updating mean parameters to minimise the difference between the measured and predicted outputs, followed by updating of parameter covariance matrix, where the difference between the measured and analytical output covariance matrices is minimised. The perturbation method presented by Haddad Khodaparast et al. [11, 99] is employed in this research for the stochastic model updating, as explained further in the following sections.

### 6.3.1 Formulation of the perturbation method for stochastic uncertainty

Conventional, deterministic model updating formulations are derived in Chapter 5 with main equations summarised in Table 6.1.

Table 6.1: Deterministic model updating formulations

Description	Equation	Equation number
Truncated Taylor series expansion	$\mathbf{z}_m = \mathbf{z}_j + \mathbf{S}_j(\boldsymbol{\theta}_{j+1} - \boldsymbol{\theta}_j)$	Eq. (5.8)
Eigenvalue sensitivity	$\mathbf{S}_j = \frac{\partial \lambda_j}{\partial \boldsymbol{\theta}} = \boldsymbol{\phi}_j^T \left[ \frac{\partial \mathbf{K}}{\partial \boldsymbol{\theta}} - \lambda_j \frac{\partial \mathbf{M}}{\partial \boldsymbol{\theta}} \right] \boldsymbol{\phi}_j$	Eq. (5.9)
Deterministic model updating	$\boldsymbol{\theta}_{j+1} = \boldsymbol{\theta}_j + \mathbf{T}_j(\mathbf{z}_m - \mathbf{z}_j)$	Eq. (5.11)
Transformation matrix	$\mathbf{T}_j = (\mathbf{S}_j^T \mathbf{W}_{\epsilon\epsilon} \mathbf{S}_j + \mathbf{W}_{\theta\theta})^{-1} \mathbf{S}_j^T \mathbf{W}_{\epsilon\epsilon}$	Eq. (5.12)

Including the variability in measurements,

$$\mathbf{z}_m = \widehat{\mathbf{z}}_m + \Delta \mathbf{z}_m \quad \text{and} \quad \mathbf{z}_j = \widehat{\mathbf{z}}_j + \Delta \mathbf{z}_j \quad (6.11)$$

where  $\widehat{\mathbf{z}}$  denotes the mean values of the measurements and  $\Delta \mathbf{z}$  represents the vectors of random variables.

Similarly, the variability of the structural parameters at  $j^{\text{th}}$  iteration is defined as,

$$\theta_j = \hat{\theta}_j + \Delta\theta \quad (6.12)$$

where  $\hat{\theta}$  denotes the mean values of the parameters and  $\Delta\theta$  represents the vector of random variables.

The transformation matrix is now represented by

$$\mathbf{T}_j = \hat{\mathbf{T}}_j + \Delta\mathbf{T}_j \quad (6.13)$$

where

$$\hat{\mathbf{T}}_j = (\hat{\mathbf{S}}_j^T \mathbf{W}_{\varepsilon\varepsilon} \hat{\mathbf{S}}_j + \mathbf{W}_{\theta\theta})^{-1} \hat{\mathbf{S}}_j^T \mathbf{W}_{\varepsilon\varepsilon} \quad (6.14)$$

$$\Delta\mathbf{T}_j = \sum_{k=1}^n \frac{\partial \mathbf{T}_j}{\partial z_{m_k}} \Delta z_{m_k} \quad (6.15)$$

$\hat{\mathbf{S}}_j$  denotes the sensitivity matrix at the parameter means ( $\hat{\mathbf{S}}_j = \mathbf{S}(\theta)$ ) and  $\Delta z_{m_k}$  represents the  $k^{\text{th}}$  element of  $\Delta z_m$ . Substituting Eqs. (6.11) to (6.13) into the deterministic problem (Eq. (5.11)) produces the stochastic model updating equation, as follows.

$$\hat{\theta}_{j+1} + \Delta\theta_{j+1} = \hat{\theta}_j + \Delta\theta_j + (\hat{\mathbf{T}}_j + \Delta\mathbf{T}_j) (\hat{z}_m + \Delta z_m - \hat{z}_j - \Delta z_j) \quad (6.16)$$

Separating the zeroth-order and first-order terms from Eq. (6.16) gives,

$$\Delta^0: \hat{\theta}_{j+1} = \hat{\theta}_j + \hat{\mathbf{T}}_j (\hat{z}_m - \hat{z}_j) \quad (6.17)$$

and

$$\Delta^1: \Delta\theta_{j+1} = \Delta\theta_j + \hat{\mathbf{T}}_j (\Delta z_m - \Delta z_j) + \Delta\mathbf{T}_j (\hat{z}_m - \hat{z}_j) \quad (6.18)$$

Eqs. (6.17) and (6.18) are used to determine the parameter means and the parameter covariance matrix, respectively, in the perturbation method [11]. The parameter covariance matrix equation can then be written as,

$$\mathbf{C}_{\theta\theta_{j+1}} = \mathbf{C}_{\theta\theta_j} - \mathbf{C}_{\theta z_j} \hat{\mathbf{T}}_j^T + \hat{\mathbf{T}}_j \mathbf{C}_{EE} \hat{\mathbf{T}}_j^T - \hat{\mathbf{T}}_j \mathbf{C}_{Z\theta_j} + \hat{\mathbf{T}}_j \mathbf{C}_{ZZ_j} \hat{\mathbf{T}}_j^T \quad (6.19)$$

with the parameters covariance matrix,

$$\mathbf{C}_{\theta\theta} = \text{cov}(\Delta\theta, \Delta\theta)$$

the covariance matrix of the measured outputs,

$$\mathbf{C}_{EE} = \text{cov}(\Delta \mathbf{z}_m, \Delta \mathbf{z}_m)$$

the covariance matrix of the predicted outputs,

$$\mathbf{C}_{ZZ} = \text{cov}(\Delta \mathbf{z}, \Delta \mathbf{z}) = \widehat{\mathbf{S}} \times \text{cov}(\Delta \boldsymbol{\theta}, \Delta \boldsymbol{\theta}) \times \widehat{\mathbf{S}}^T$$

the covariance matrix of the parameters and the predicted outputs,

$$\mathbf{C}_{\theta Z} = \text{cov}(\Delta \boldsymbol{\theta}, \Delta \mathbf{z}) = \text{cov}(\Delta \boldsymbol{\theta}, \Delta \boldsymbol{\theta}) \times \widehat{\mathbf{S}}^T$$

and the covariance matrix of the predicted outputs and the parameters,

$$\mathbf{C}_{Z\theta} = \text{cov}(\Delta \mathbf{z}, \Delta \boldsymbol{\theta}) = \widehat{\mathbf{S}} \times \text{cov}(\Delta \boldsymbol{\theta}, \Delta \boldsymbol{\theta})$$

where ‘cov’ represents the covariance between two random variables, which is computed using the mean-centred first order perturbation method. The measured outputs covariance matrix ( $\mathbf{C}_{EE}$ ) is determined from the measured data, while the assignment of the initial parameters covariance matrix ( $\mathbf{C}_{\theta\theta}$ ) relies on the engineering insight of the analyst.

These covariance matrices give a measure of interdependency between the quantities and contain all individual variances and covariances, which can be written in the form of

$$\text{cov}(X_i, X_j) = \begin{bmatrix} \text{var}(X_1) & \text{cov}(X_1, X_2) & \cdots & \text{cov}(X_1, X_n) \\ \text{cov}(X_2, X_1) & \text{var}(X_2) & \cdots & \text{cov}(X_2, X_n) \\ \vdots & \vdots & \vdots & \vdots \\ \text{cov}(X_n, X_1) & \text{cov}(X_n, X_2) & \cdots & \text{var}(X_n) \end{bmatrix} \quad (6.20)$$

Please note that if  $i = j$ , the covariance of  $\text{cov}(X_i, X_j) = \text{cov}(X_i, X_i) = \text{cov}(X_j, X_j) = \text{var}(X_i) = \text{var}(X_j)$ . So, the diagonal elements of the covariance matrix represent the variances of each random variable, while the off-diagonal elements represent the covariances between two random variables. If no correlation exists between the two random variables, zero off-diagonal terms are obtained in the matrix (for example, the initial  $\mathbf{C}_{\theta\theta}$  as shown in Appendix C).

The covariance can also be mathematically represented by

$$\begin{aligned} \text{cov}(X_i, X_j) &= E[(X_i - \widehat{X}_i)(X_j - \widehat{X}_j)] \\ &= \int \int P(X_i, X_j) \cdot (X_i - \widehat{X}_i)(X_j - \widehat{X}_j) dX_i dX_j \end{aligned} \quad (6.21)$$

An example of calculation for Eq. (6.19) is given in Appendix C.

A procedure outlined by Haddad Khodaparast et al. [11] is followed to determine the statistical data (i.e., means and standard deviations) of the structural parameters that converge: (1) the mean predicted modal data ( $\widehat{z}$ ) on the mean measured modal data ( $\widehat{z}_m$ ), and (2) the covariance matrix of the predicted modal data ( $C_{ZZ}$ ) on the covariance matrix of the measured modal data ( $C_{EE}$ ). For the sake of completeness and to aid understanding, this procedure is detailed in Fig. 6.3.

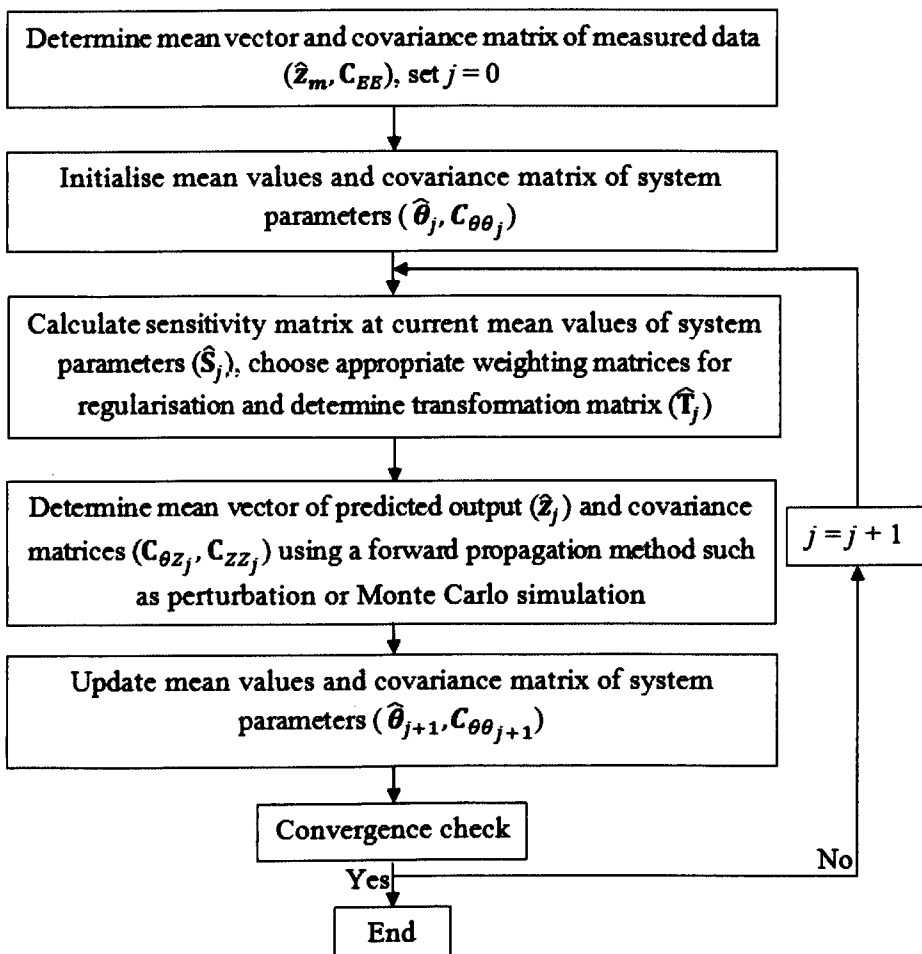


Figure 6.3: Stochastic updating procedure

As mentioned earlier, a significant advantage of the perturbation method [11, 99] used here over another similar perturbation method by Hua et al. [25] is that only the first-order sensitivity matrix is needed in Eq. (6.19), hence a big reduction in terms of computational effort is achieved. The MCS method with multivariate normal distribution is used to generate scatter plots of analytical and experimental data, before and after updating is performed.

### 6.3.2 Parameter selection for stochastic model updating

This section explains how parameter selections can be sufficiently made for the stochastic problems. Two case studies of stochastic uncertainty in (simple) flat plates and (more complicated) formed hat-shaped shells, introduced earlier in Section 4.3, are performed to investigate how updating can be adequately conducted with different combinations of parameters. The existing experimental data from the flat plates and the hat-shaped shells presented in Chapter 4 are utilised and the stochastic model updating approach (i.e., the perturbation method presented in Ref. [11]) is used for the work. Different combinations of (geometrical and material properties) parameters are tested, and important findings are then used as a guideline when selecting the parameters for the actual stochastic model updating of the welded structures (Section 6.4).

#### Case 1: Parameter selection for stochastic model updating in simple flat plates

Selection of parameters in the stochastic updating is investigated first by using simple structures such as the flat plates used in this work. The exercise is performed by using the geometrical and material properties as parameters to determine the best combination for carrying out the stochastic model updating of such simple structures. The existing measurement data tabulated in Table 4.3 is utilised and the covariance matrix of the measured outputs for the first five natural frequencies of the flat plates is determined as follows.

$$\mathbf{C}_{EE\text{plate}} = \begin{bmatrix} 0.01 & 0.03 & 0.05 & 0.05 & 0.09 \\ & 0.06 & 0.11 & 0.11 & 0.19 \\ & & 0.32 & 0.17 & 0.54 \\ & \text{sym.} & & 0.18 & 0.31 \\ & & & & 0.95 \end{bmatrix}$$

Firstly, only the geometrical features of the structures, i.e., the thickness of the plates are studied. The FE model of the flat plates is modified into:

1. FE model of flat plates with one thickness (i.e., existing model) (FP1)
2. FE model of flat plates with three thicknesses (FP3)

### 3. FE model of flat plates with six thicknesses (FP6)

Initial values of 1.45 mm and standard deviations of  $1.45 \times 10^{-2}$  mm are assigned for the thickness of each region in all three models. It should be noted that the initial standard deviations are deliberately set at 1% of the initial parameter values. Next, the material properties of the flat plates are included as the updating parameters to see the effect of the parameter selections. The stochastic model updating is then conducted for each model and their results are discussed in the followings. Scatter clouds of measured and predicted outputs are generated by the Monte Carlo simulation following the Gaussian distribution to show convergence of the stochastic updating procedure. The number of samples used in plotting the scatter clouds is chosen based on the findings by Haddad Khodaparast and Mottershead [99], as illustrated in Fig. 6.4. From the figure, five hundred samples are clearly enough to give an accurate estimate of the parameter variability using the perturbation method.

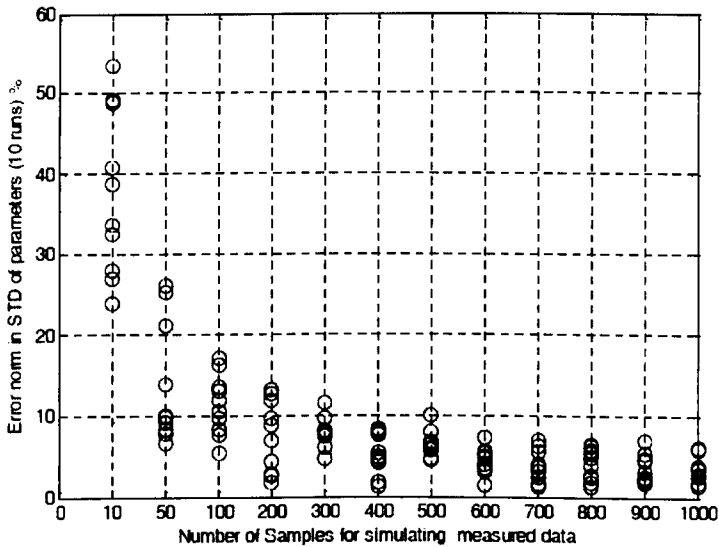


Figure 6.4: Convergence achieved by the perturbation methods with increasing number of samples [99]

#### *Stochastic model updating using FP1*

The stochastic updating is conducted on the existing model of the flat plates (as depicted in Fig. 6.5), and the updated mean natural frequencies and parameters upon convergence are tabulated in Tables 6.2 and 6.3 against their initial values. It can be seen from Table 6.2 that the updated mean natural frequencies obtained using the FP1 model deviate from the mean measured natural frequencies by almost 9% in total. On the other hand, the updated parameter is very close to the initial value, while the estimated standard deviation is one order smaller than the initial.



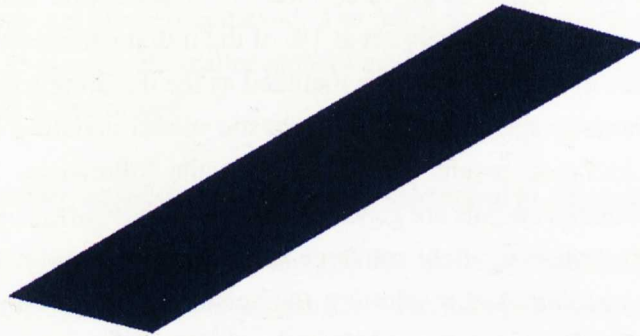


Figure 6.5: The FP1 model

Table 6.2: Mean natural frequencies (in Hz) estimated using FP1

Mode	I Experiment	II Initial		III Updated	
		FE	Error (%)	FE	Error (%)
1	24.12	24.27	0.62	24.63	2.13
2	66.92	67.24	0.48	68.24	1.97
3	77.65	75.31	3.01	76.42	1.58
4	131.97	132.51	0.41	134.47	1.89
5	158.80	154.31	2.83	156.59	1.39
Total error			7.35		8.96

Table 6.3: Identified mean parameter for FP1

Parameter	Initial value	Identified value
$T$	1.450 mm	1.472 mm
std. ( $T$ )	$1.45 \times 10^{-2}$ mm	$7.18 \times 10^{-3}$ mm

Using the identified parameters, the covariance matrix of the predicted outputs ( $\mathbf{C}_{ZZ_{FP1}}$ ) is computed as follows,

$$\mathbf{C}_{ZZ_{FP1}} = \begin{bmatrix} 0.01 & 0.04 & 0.04 & 0.08 & 0.09 \\ & 0.11 & 0.12 & 0.21 & 0.25 \\ & & 0.13 & 0.24 & 0.27 \\ & sym. & & 0.42 & 0.48 \\ & & & & 0.56 \end{bmatrix}$$

with the percentage of errors to the measured data illustrated in Fig. 6.11(a), while Fig. 6.6 shows the scatter plots of the measured and predicted outputs before and after the stochastic model updating process. Generally, the errors between the outputs covariances are very big (up to about 130%) when using the FP1 model, hence it can be concluded that the approach fails to produce a good estimate of the  $\mathbf{C}_{ZZ}$ . Furthermore, the scatter plots illustrate that the updating procedure fails to converge the predicted outputs to the measured data, although the size of the updated scatter cloud is better estimated than the initial.

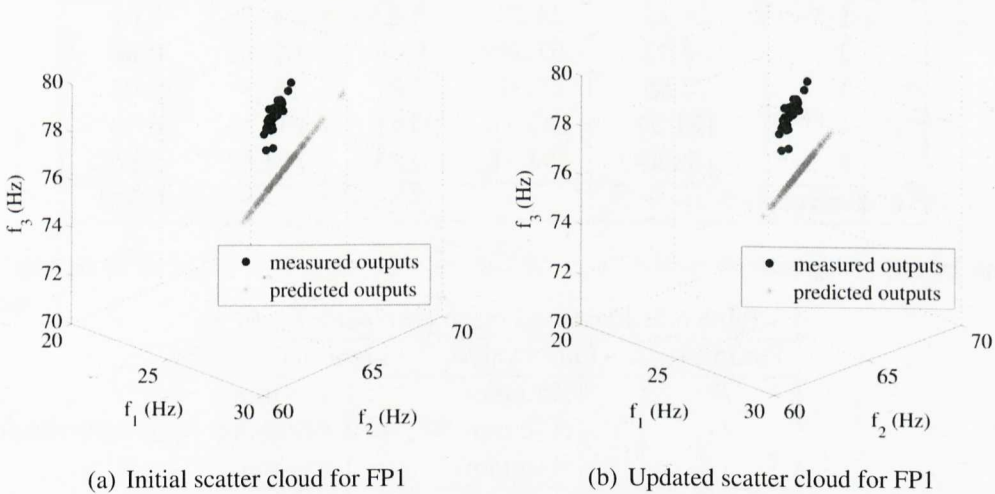


Figure 6.6: Scatter plots of the FP1 model before and after the stochastic model updating

### Stochastic model updating using FP3

For this exercise, the FE model of the flat plates is divided into three regions (Fig. 6.7), with initial mean natural frequencies and parameters as tabulated in Tables 6.4 and 6.5. Upon convergence, the total error of the mean natural frequencies is reduced to 7.43% as compared to about 9% when using only one thickness as updating parameter. Moreover, the identified parameters and their corresponding standard deviations are

included in Table 6.5, with all updated estimates identified close to their corresponding initial values apart from the standard deviations of  $T_2$  which is one order smaller than the initial.



Figure 6.7: The FP3 model

Table 6.4: Mean natural frequencies (in Hz) estimated using FP3

Mode	I Experiment	II Initial		III Updated	
		FE	Error (%)	FE	Error (%)
	1	24.12	24.27	0.62	24.27
2	66.92	67.24	0.48	67.32	0.60
3	77.65	75.31	3.01	75.29	3.03
4	131.97	132.51	0.41	132.68	0.53
5	158.80	154.31	2.83	154.57	2.66
Total error			7.35		7.43

Table 6.5: Identified mean parameter for FP3

Parameter	Initial value	Identified value
$T_1$	1.450 mm	1.453 mm
$T_2$	1.450 mm	1.449 mm
$T_3$	1.450 mm	1.453 mm
std. ( $T_1$ )	$1.45 \times 10^{-2}$ mm	$1.13 \times 10^{-2}$ mm
std. ( $T_2$ )	$1.45 \times 10^{-2}$ mm	$7.31 \times 10^{-3}$ mm
std. ( $T_3$ )	$1.45 \times 10^{-2}$ mm	$1.13 \times 10^{-2}$ mm

Using the identified parameters, the covariance matrix of the predicted outputs ( $C_{ZZFP3}$ ) is given as,

$$C_{ZZFP3} = \begin{bmatrix} 0.01 & 0.03 & 0.04 & 0.06 & 0.06 \\ & 0.06 & 0.09 & 0.13 & 0.13 \\ & & 0.13 & 0.17 & 0.18 \\ & sym. & & 0.24 & 0.26 \\ & & & & 0.58 \end{bmatrix}$$

and the percentage of errors to the measured data is shown in Fig. 6.11(b). It can be observed that having more thickness parameters reduces the overall error of the output covariance matrix, however the maximum error of the covariance for the FP3 model is still very big (i.e., up to 60%). In addition to that, the scatter plots of the measured and predicted outputs before and after the stochastic model updating process also fail to converge, as depicted in Fig. 6.8.

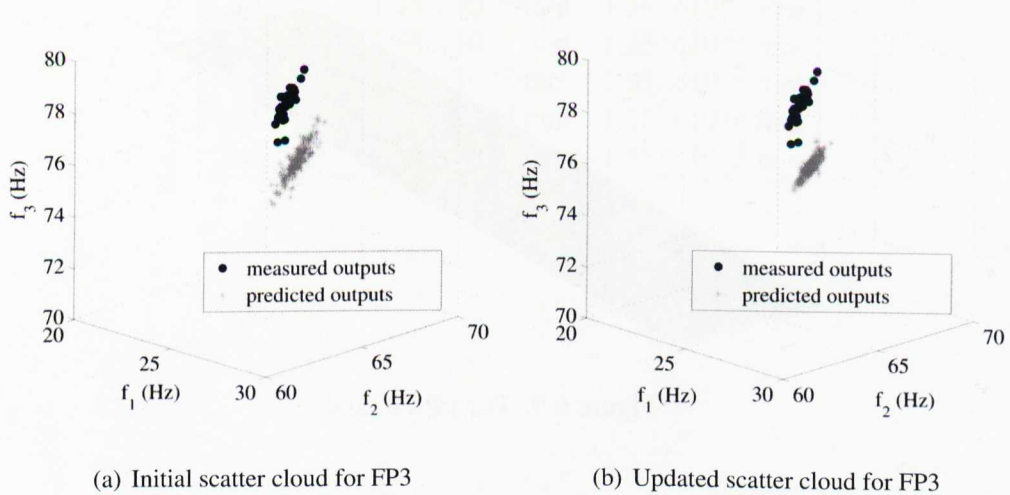


Figure 6.8: Scatter plots of the FP3 model before and after the stochastic model updating

### Stochastic model updating using FP6

The FE model of the flat plates is divided into six regions (see Fig. 6.9) to investigate if having more parameters would improve the predicted results. The initial and updated values of the mean natural frequencies and parameters are presented in Tables 6.6 and 6.7, which do not show much improvement from the FP3 results. The mean natural frequencies and the identified mean parameters are exactly the same as predicted by the FP3 model, while their corresponding standard deviations are quite close to their corresponding initial values.

Using the identified parameters, the covariance matrix of the predicted outputs ( $C_{ZZFP6}$ ) is



$$C_{ZZFP6} = \begin{bmatrix} 0.01 & 0.03 & 0.04 & 0.06 & 0.06 \\ & 0.06 & 0.09 & 0.12 & 0.13 \\ & & 0.13 & 0.17 & 0.18 \\ & sym. & & 0.24 & 0.26 \\ & & & & 0.28 \end{bmatrix}$$

and the percentage of errors to the measured data is shown in Fig. 6.11(c), while the scatter clouds are illustrated in Fig. 6.10. From the results, it may be concluded that having more thickness parameters would not improve the stochastic updating results at all. Hence, different sets of parameters are explored by including the material properties in the stochastic updating procedure as explained next.

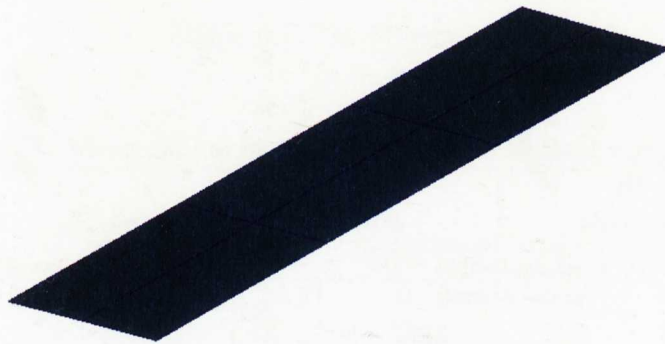


Figure 6.9: The FP6 model

Table 6.6: Mean natural frequencies (in Hz) estimated using FP6

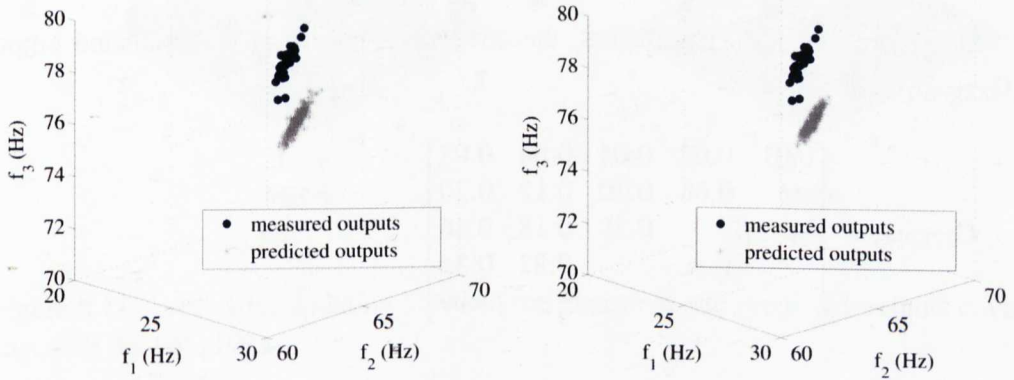
Mode	I Experiment	II Initial		III Updated	
		FE	Error (%)	FE	Error (%)
	1	24.12	24.27	0.62	24.27
2	66.92	67.24	0.48	67.32	0.60
3	77.65	75.31	3.01	75.29	3.03
4	131.97	132.51	0.41	132.68	0.53
5	158.80	154.31	2.83	154.57	2.66
Total error			7.35		7.43

#### *Stochastic model updating using material properties*

In this exercise, the material properties (i.e., the Young's modulus ( $E$ ) and shear modulus ( $G$ )) are used for the stochastic updating. The FE model of the flat plates is assumed to have uniform thickness of 1.45 mm with uniform material properties across the plate, as in the FP1 model. The initial mean values of 210 GPa and 81 GPa are assigned for the Young's modulus and shear modulus respectively, with initial standard

Table 6.7: Identified mean parameter for FP6

Parameter	Initial value	Identified value
$T_1$	1.450 mm	1.453 mm
$T_2$	1.450 mm	1.449 mm
$T_3$	1.450 mm	1.453 mm
$T_4$	1.450 mm	1.453 mm
$T_5$	1.450 mm	1.449 mm
$T_6$	1.450 mm	1.453 mm
std. ( $T_1$ )	$1.45 \times 10^{-2}$ mm	$1.35 \times 10^{-2}$ mm
std. ( $T_2$ )	$1.45 \times 10^{-2}$ mm	$1.26 \times 10^{-3}$ mm
std. ( $T_3$ )	$1.45 \times 10^{-2}$ mm	$1.35 \times 10^{-2}$ mm
std. ( $T_4$ )	$1.45 \times 10^{-2}$ mm	$1.35 \times 10^{-2}$ mm
std. ( $T_5$ )	$1.45 \times 10^{-2}$ mm	$1.26 \times 10^{-3}$ mm
std. ( $T_6$ )	$1.45 \times 10^{-2}$ mm	$1.35 \times 10^{-2}$ mm



(a) Initial scatter cloud for FP6

(b) Updated scatter cloud for FP6

Figure 6.10: Scatter plots of the FP6 model before and after the stochastic model updating

deviations of 1% of their initial mean values. The updated results upon convergence are given in Tables 6.8 and 6.9, which present significant improvement in terms of the natural frequencies with the total error of only 3.17%. The identified parameters are compared with the updated parameters from the deterministic updating and they are found to be quite close, indicating that the stochastic updating for the flat plates has been conducted well.

Table 6.8: Mean natural frequencies (in Hz) estimated using FPEG

Mode	I Experiment	II Initial		III Updated	
		FE	Error (%)	FE	Error (%)
1	24.12	24.27	0.62	24.23	0.47
2	66.92	67.24	0.48	67.04	0.18
3	77.65	75.31	3.01	76.67	1.25
4	131.97	132.51	0.41	131.93	0.03
5	158.80	154.31	2.83	156.86	1.22
Total error			7.35		3.17

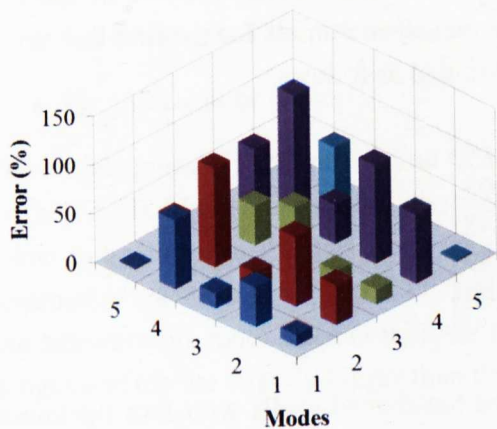
Table 6.9: Identified mean parameter for FPEG

Parameter	Initial value	Identified value
$E$	210.0 GPa	209.6 GPa
$G$	81.0 GPa	83.8 GPa
std. ( $E$ )	2.10 GPa	1.60 GPa
std. ( $G$ )	0.81 GPa	1.23 GPa

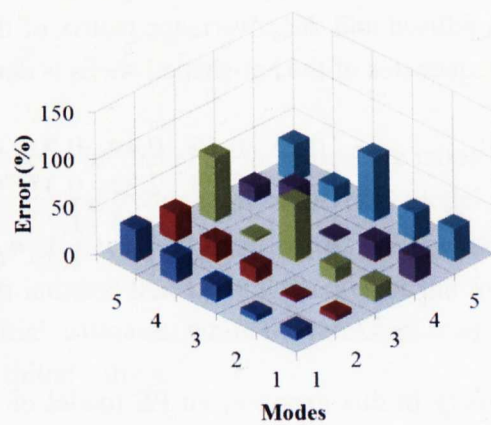
Using the identified parameters, the covariance matrix of the predicted outputs ( $C_{ZZFPEG}$ ) is

$$C_{ZZFPEG} = \begin{bmatrix} 0.01 & 0.02 & 0.04 & 0.04 & 0.08 \\ & 0.06 & 0.10 & 0.12 & 0.20 \\ & & 0.28 & 0.18 & 0.56 \\ & sym. & & 0.22 & 0.36 \\ & & & & 1.09 \end{bmatrix}$$

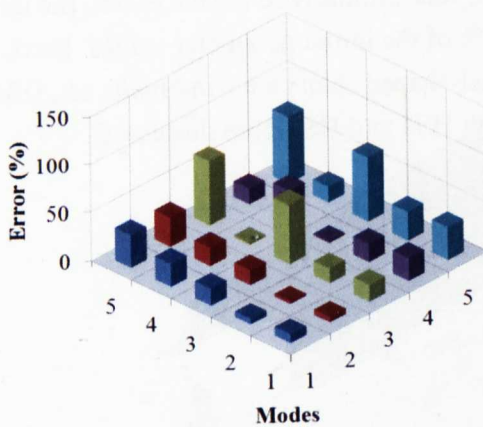
and the percentage of errors to the measured data is shown in Fig. 6.11(d), which is considerably low than the errors produced using the thicknesses as parameters. In addition to that, Fig. 6.12 presents the convergence of the predicted outputs over the measured outputs. As demonstrated by the results, using the material properties as the updating parameters produces reasonable parameter estimates that consequently converges the outputs successfully. Although the results seem promising, they need to be confirmed in the next case using the more complicated formed hat-shaped shells.



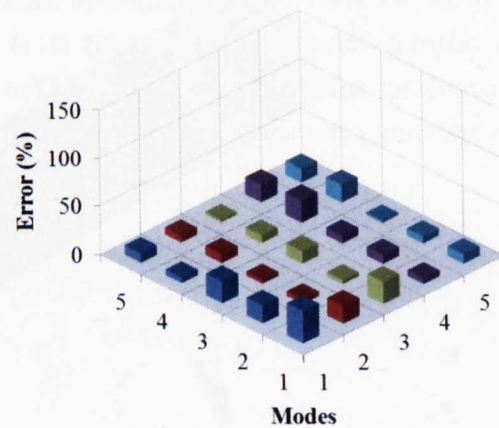
(a) FP1



(b) FP3



(c) FP6



(d) FPEG

Figure 6.11: Error after updating between the measured and predicted outputs covariances for the flat plates



## Case 2: Parameter selection for stochastic model updating in complicated formed shells

The findings obtained from the stochastic model updating of simple plates are tested using more complicated structures, i.e., the formed hat-shaped shells. The formed shells are updated firstly by using only the thicknesses as the updating parameters and secondly by using a combination of thickness and the material properties as the parameters. The existing measurement data of the hat-shaped shells tabulated in Table 4.5 is utilised and the covariance matrix of the measured outputs for the first five natural frequencies of the hat-shaped shells is determined as follows.

$$C_{EEhat} = \begin{bmatrix} 0.25 & 0.12 & 0.49 & 0.23 & 0.60 \\ & 3.28 & 2.83 & 0.37 & 0.65 \\ & & 4.45 & 1.23 & 1.48 \\ & sym. & & 1.23 & 0.89 \\ & & & & 2.88 \end{bmatrix}$$

Firstly in this exercise, an FE model of the hat-shaped shells with four thicknesses (HS4) is employed. Initial values of 1.45 mm and standard deviations of  $1.45 \times 10^{-2}$  mm are assigned for the thickness of each region. Similarly to the flat plates, the initial standard deviations are deliberately set at 1% of the initial parameter values. Next, the thicknesses and material properties of the hat-shaped shells are combined (i.e., HS2E) as updating parameters and results from both HS4 and HS2E are discussed.

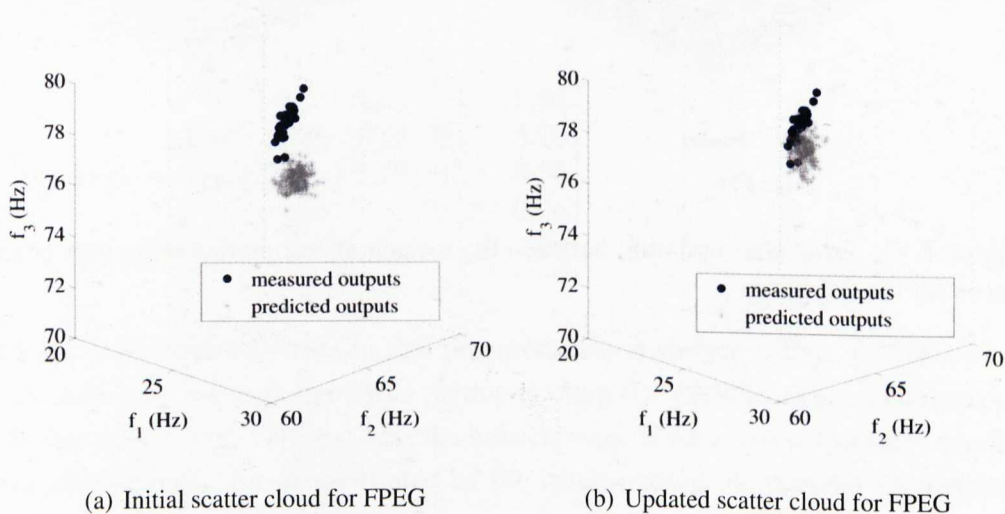


Figure 6.12: Scatter plots of the FPEG model before and after the stochastic model updating

### Stochastic model updating using HS4

The FE model of the hat-shaped shells is divided into four regions as illustrated in Fig. 6.13, with

- $T_1$  : thickness of the folds
- $T_2$  : thickness of the flanges
- $T_3$  : thickness of the sidewalls
- $T_4$  : thickness of the top

The initial values of the mean natural frequencies predicted by the model are tabulated in Table 6.10. Upon convergence, the mean natural frequencies of the HS4 model are found to be closer to the measured values with a total error of 5.44%. The updated parameters are shown in Table 6.11, which indicate that the thicknesses of the folds and sidewalls are much smaller than the initial estimates, while the thicknesses of the flanges and top are slightly bigger than the initial values.

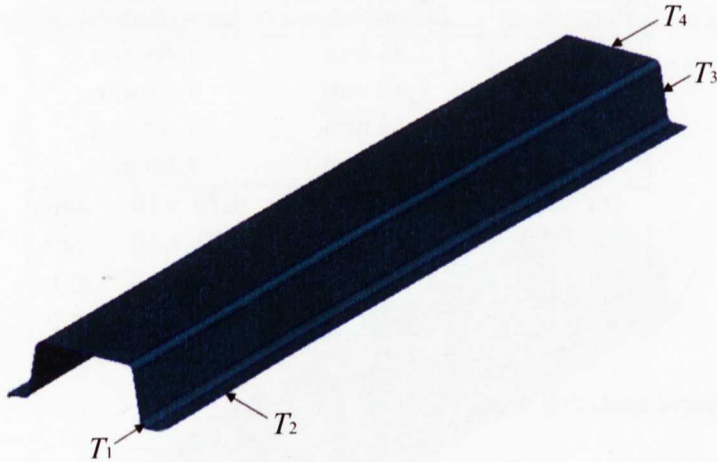


Figure 6.13: The HS4 model

Using these updated mean parameters, the covariance matrix of the predicted outputs  $\mathbf{C}_{ZZHS4}$  is computed as

$$\mathbf{C}_{ZZHS4} = \begin{bmatrix} 0.23 & 0.21 & 0.38 & 0.22 & 0.63 \\ & 3.37 & 2.83 & 0.56 & 1.19 \\ & & 2.62 & 0.79 & 1.68 \\ & sym. & & 1.15 & 1.09 \\ & & & & 2.34 \end{bmatrix}$$

and the difference between the predicted outputs covariance over the measured outputs covariance is illustrated in Fig. 6.16(a). Despite considerable errors of up to approximately 85% in the predicted outputs covariance, the updated scatter cloud of the natural frequencies seems to converge successfully to the measured outputs as can be seen in Fig. 6.14.

Table 6.10: Mean natural frequencies (in Hz) estimated using HS4

Mode	I Experiment	II Initial		III Updated	
		FE	Error (%)	FE	Error (%)
	1	70.11	67.28	4.03	69.12
2	273.70	256.98	6.11	268.11	2.04
3	287.92	273.47	5.02	283.29	1.61
4	334.73	334.41	0.10	333.44	0.38
5	395.43	386.35	2.30	391.66	0.95
Total error			15.26		5.44

Table 6.11: Identified mean parameter for HS4

Parameter	Initial value	Identified value
$T_1$	1.45 mm	1.40 mm
$T_2$	1.45 mm	1.48 mm
$T_3$	1.45 mm	1.32 mm
$T_4$	1.45 mm	1.56 mm
std. ( $T_1$ )	$1.45 \times 10^{-2}$ mm	$4.76 \times 10^{-2}$ mm
std. ( $T_2$ )	$1.45 \times 10^{-2}$ mm	$4.81 \times 10^{-2}$ mm
std. ( $T_3$ )	$1.45 \times 10^{-2}$ mm	$5.24 \times 10^{-2}$ mm
std. ( $T_4$ )	$1.45 \times 10^{-2}$ mm	$1.81 \times 10^{-2}$ mm

#### Stochastic model updating using HS2E

In this exercise, the FE model of the hat-shaped shells is updated by using the combination of thicknesses and material properties, as follows

- $T_1$  : thickness of the fold regions
- $T_2$  : thickness of the flat regions
- $E$  : Young's modulus

with the regions as shown in Fig. 6.15. The initial mean parameters and their standard deviations are tabulated in Table 6.12, while the initial mean natural frequencies are given in Table 6.13. Upon convergence, the total error of the mean natural frequencies

against the measured data reduces significantly to 2%. The thickness of the fold regions appears to be smaller, while the flat regions are thicker than the initial estimates. The standard deviations estimated by the stochastic model updating are in the same order as the initial estimates.

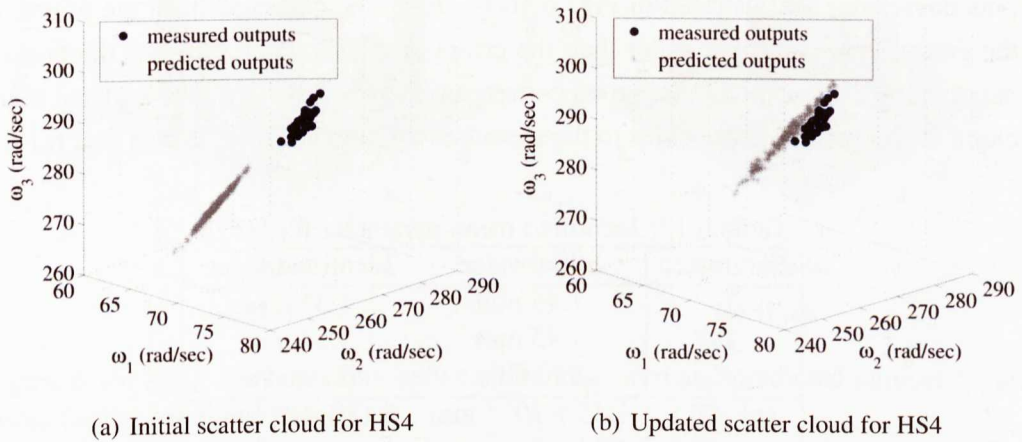


Figure 6.14: Scatter plots of the HS4 model before and after the stochastic model updating

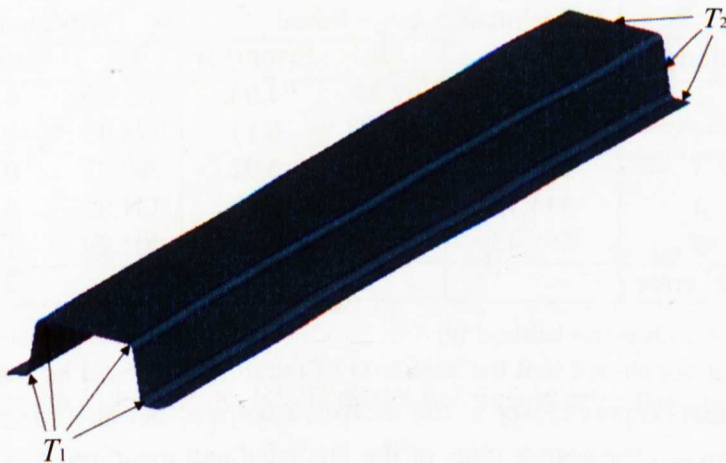


Figure 6.15: The HS2E model

The covariance matrix of the predicted outputs  $C_{ZZHS2E}$  predicted using these updated mean parameters is

$$C_{ZZHS2E} = \begin{bmatrix} 0.26 & 0.17 & 0.52 & 0.24 & 0.58 \\ & 3.18 & 2.17 & 0.30 & 0.50 \\ & & 2.68 & 0.99 & 1.05 \\ & sym. & & 1.24 & 0.68 \\ & & & & 2.34 \end{bmatrix}$$

and the difference between the predicted outputs covariance over the measured outputs covariance is illustrated in Fig. 6.16(b). It can be observed from the figure that the errors are generally smaller than the errors produced using only the thickness as parameters. Furthermore, very good convergence is obtained from the updated scatter cloud of the natural frequencies to the measured outputs, as illustrated in Fig. 6.17.

Table 6.12: Identified mean parameter for HS2E

Parameter	Initial value	Identified value
$T_1$	1.45 mm	1.31 mm
$T_2$	1.45 mm	1.54 mm
$E$	210 GPa	216 GPa
std. ( $T_1$ )	$1.45 \times 10^{-2}$ mm	$6.12 \times 10^{-2}$ mm
std. ( $T_2$ )	$1.45 \times 10^{-2}$ mm	$1.14 \times 10^{-2}$ mm
std. ( $E$ )	2.10 GPa	2.65 GPa

Table 6.13: Mean natural frequencies (in Hz) estimated using HS2E

Mode	I Experiment	II		III	
		Initial		Updated	
	FE	Error (%)	FE	Error (%)	
1	70.11	67.28	4.03	70.34	0.32
2	273.70	256.98	6.11	273.40	0.11
3	287.92	273.47	5.02	289.77	0.64
4	334.73	334.41	0.10	337.82	0.92
5	395.43	386.35	2.30	401.70	1.59
Total error			15.26		2.00

It may be concluded that the selection of parameters should be made not only to bring the mean outputs closer to the measured outputs, but also to reach good convergence between the scatter plots of the predicted and measured data. The findings presented in this section indicate that selecting some of the material properties as the updating parameters provides better convergence than those updated by using only the thickness parameters. Furthermore, the error between the covariance matrix of the predicted and measured outputs is also improved when including both geometrical and material properties in the updating procedure, rather than choosing a number of the geometrical properties alone, as has been demonstrated in this section. The findings



are followed as guidelines when selecting the updating parameters in the main work, i.e., the stochastic model updating of the welded structures.

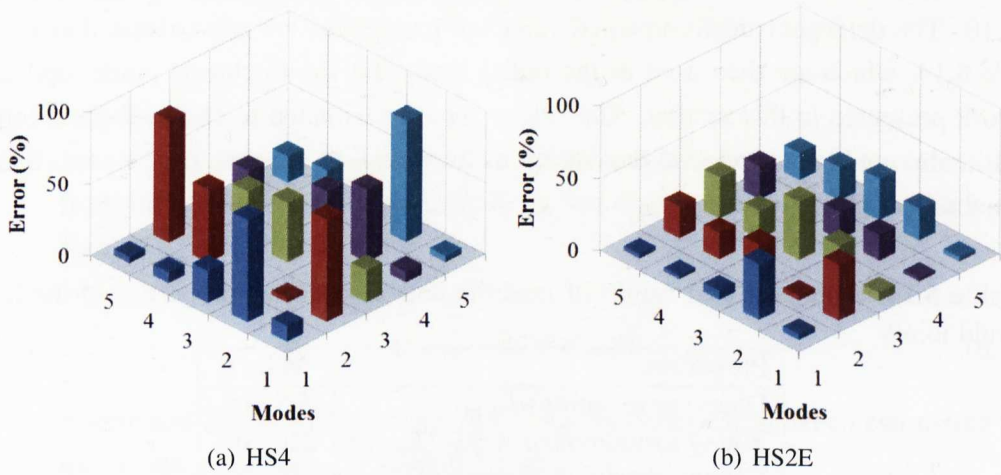


Figure 6.16: Error after updating between the measured and predicted outputs covariances for the hat-shaped shells

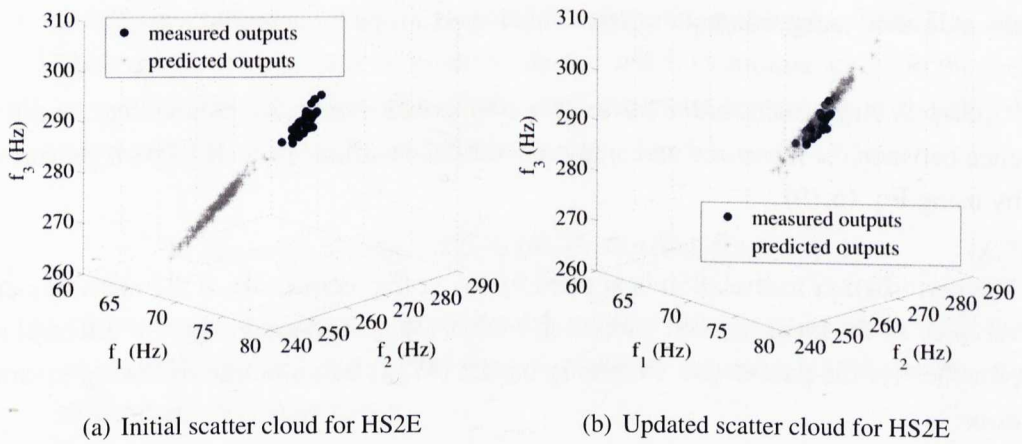


Figure 6.17: Scatter plots of the HS2E model before and after the stochastic model updating

## 6.4 Stochastic model updating of the welded structures

The stochastic model updating is performed on the FE model of the laser welded structures (as presented in Section 5.3) based on the measurement data tabulated in Table 4.10. The deterministically-updated values of parameters are approximated as in Table 6.14, which are then used as the initial inputs for the stochastic model updating work presented in this section. The values are approximated to ensure that the initial estimates are close enough to the deterministic values, as required by the perturbation method.

Table 6.14: Approximated values of material and geometrical properties of the laser weld joints

Properties	Values
Diameter of welds ( $d_{\text{weld}}$ )	5.5 mm
Young's modulus of welds ( $E_{\text{weld}}$ )	220 GPa
Young's modulus of patch ( $E_{\text{patch}}$ )	650 GPa

Variability that exists in the experimental data of the welded structures is investigated by carrying out the following steps simultaneously.

*Step 1: Adjustment of the mean parameters*, by minimising the difference between the measured and predicted outputs. This is performed by using Eq. (6.17).

*Step 2: Adjustment of the parameter covariance matrix*, by minimising the difference between the measured and analytical output covariance matrix. This is performed by using Eq. (6.19).

The perturbation formulation is applied by using the reciprocals of the measurements variance as the measurement weighting matrix ( $\mathbf{W}_{\epsilon\epsilon}$ ) and assigning two different approaches for the parameters weighting matrix ( $\mathbf{W}_{\theta\theta}$ ) based on the following assumptions.

*Assumption 1:* The substructures are assumed to remain exactly the same after the welding process, i.e., no deformations on the flat plate and the hat-shaped shell due to welding. Thus, the only source of variability in the measurements comes from the laser spot weld joints.

*Assumption 2:* The substructures are assumed to experience some deformations during the welding process. Therefore, the variability in the measurements could be due to the deformation of the substructures and also the uncertainties associated with

the laser spot weld joints.

The first assumption is adopted in Approach 1, while the second assumption is applied in Approach 2. Both approaches are explained as follows.

- **Approach 1**

In this approach, the variability of the measured data is assumed to come solely from the weld parameters (i.e.,  $d$ ,  $E_{\text{weld}}$  and  $E_{\text{patch}}$ ). A weighting matrix in the form of

$$\mathbf{W}_{\theta\theta 1} = \lambda_r * \text{diag}(1, 1, 1) \quad (6.22)$$

is assigned for both steps of the stochastic model updating when estimating the means and covariances of the parameters.

- **Approach 2**

In contrast to Approach 1, Approach 2 includes eight parameters: five from the substructures (i.e.,  $E$  and  $G$  of the flat plates, and  $T_1$ ,  $T_2$  and  $E$  of the hat-shaped shells) and three from the spot weld joints (i.e.,  $d$ ,  $E_{\text{weld}}$  and  $E_{\text{patch}}$ ). As explained earlier, the parameters of the substructures are included to incorporate some uncertainties in the substructures following the welding process. However, these parameters are not expected to change much in comparison with the weld parameters, hence different weighting coefficients are applied when updating the mean parameters (step 1), as follows

$$\mathbf{W}_{\theta\theta 21} = \lambda_r * \text{diag}(1000, 1000, 1000, 1000, 1000, 1, 1, 1) \quad (6.23)$$

where bigger weighting is given to the substructures parameters to limit their changes during updating. The weld parameters are not weighted as much to allow them to change more.

On the other hand, the variances of these eight parameters are highly uncertain; hence smaller weighting (i.e., similar weighting as in Approach 1) is used to allow for the parameter covariances to change freely in the second updating step (i.e., to update the parameter covariance matrix).

$$\mathbf{W}_{\theta\theta 22} = \lambda_r * \text{diag}(1, 1, 1, 1, 1, 1, 1, 1) \quad (6.24)$$

The covariances of the parameters are taken to possess more uncertainties than the mean values as there are no prior information in the distribution of these



parameters due to difficulties in measuring the actual parameters values from the physical structures. Assigning different weighting matrices for each updating step (i.e., Eq. (6.23) for step 1, and Eq. (6.24) for step 2) will ensure that the mean parameter values reflect the physical parameters of the structures after the welding process, while allowing for uncertainties in the distribution of parameter values to be considered. A regularisation parameter ( $\lambda_r$ ) of 400 is selected and employed in both approaches.

Stochastic model updating using Approach 1 is discussed first, followed by the second approach. The updating procedure is conducted based on the measured mean natural frequencies of the welded structures obtained from the modal testing as explained in Chapter 4. From the measured data, the covariance matrix of the measured outputs ( $\mathbf{C}_{EE}$ ) is given as,

$$\mathbf{C}_{EE} = \begin{bmatrix} 9.95 & 13.31 & 11.53 & 11.51 & 8.70 \\ & 28.42 & 15.71 & 24.32 & 18.47 \\ & & 15.01 & 14.75 & 11.52 \\ & sym. & & 23.85 & 17.30 \\ & & & & 16.00 \end{bmatrix}$$

It can be seen from Table 6.15 that the updated mean natural frequencies obtained using the first approach are close to the mean measured frequencies, and the total error is improved from the initial value.

The initial means and standard deviations of all weld parameters are shown in Table 6.16. As mentioned earlier, the initial mean values are approximated from the deterministically-updated values, while the initial standard deviations are deliberately set at 1% of the mean values. As can be observed from the table, the results of the updated means and standard deviations using Approach 1 are not in good agreement with the initial values. Considerable changes can be seen on the mean parameters, while the estimated standard deviations are generally bigger than the initial estimates.

Using these identified estimates, the covariance matrix of the predicted outputs ( $\mathbf{C}_{ZZI}$ ) is computed as follows,

$$\mathbf{C}_{ZZI} = \begin{bmatrix} 0.91 & 3.16 & 0.56 & 3.54 & 3.23 \\ & 12.92 & 4.11 & 14.35 & 12.58 \\ & & 6.78 & 2.49 & 4.69 \\ & sym. & & 18.09 & 14.19 \\ & & & & 14.10 \end{bmatrix}$$

and the percentage of error between  $\mathbf{C}_{EE}$  and  $\mathbf{C}_{ZZI}$  is shown in Fig. 6.18(a). Generally, the errors are very big (i.e., up to approximately 90%) when using the first approach,

hence it can be concluded that the approach fails to produce a good estimate of the  $C_{ZZ}$ .

The updated mean natural frequencies using the second approach is also tabulated in Table 6.15. It can be seen from the table that the identified and measured natural frequencies achieved by using the second approach are in good agreement, although the total error produced by Approach 2 is slightly bigger than the total error of Approach 1. The identified means and standard deviations using the second approach are given in Table 6.16. As can be observed from the table, the changes in the identified means and standard deviations of the parameters with respect to the initial estimates are reasonable.

Table 6.15: Mean natural frequencies (in Hz) estimated for the welded structures

Mode	I Experiment	II		III		IV	
		Initial		Approach 1		Approach 2	
		FE	Error (%)	FE	Error (%)	FE	Error (%)
1	508.12	494.01	2.78	500.68	1.46	498.10	1.97
2	553.69	552.87	0.15	567.61	2.51	568.14	2.61
3	575.39	564.72	1.85	573.42	0.34	570.35	0.88
4	627.45	615.33	1.93	631.56	0.66	632.85	0.86
5	643.66	620.32	3.63	635.44	1.28	636.40	1.13
Total error			10.34		6.25		7.43

Table 6.16: Identified mean parameters estimated for the welded structures

Parameter	Initial	Approach 1	Approach 2
$d_{weld}$	5.5 mm	6.0 mm	5.6 mm
$E_{weld}$	220 GPa	230 GPa	222 GPa
$E_{patch}$	650 GPa	1595 GPa	737 GPa
std. ( $d_{weld}$ )	0.055 mm	0.16 mm	0.06 mm
std. ( $E_{weld}$ )	2.20 GPa	5.57 GPa	2.65 GPa
std. ( $E_{patch}$ )	6.50 GPa	10.49 GPa	3.17 GPa

The identified estimates using Approach 2 give a  $C_{ZZ2}$  as follows,

$$C_{ZZ2} = \begin{bmatrix} 10.65 & 13.30 & 11.60 & 11.84 & 9.99 \\ & 25.39 & 13.78 & 22.39 & 18.57 \\ & & 13.37 & 13.22 & 11.32 \\ & sym. & & 22.35 & 18.36 \\ & & & & 16.84 \end{bmatrix}$$

and the error as shown in Fig. 6.18(b). The error of each element appears significantly smaller than the one produced by the first approach. This shows that the estimated

means and standard deviations of the second approach are reasonable and the modification made to the weighting matrices are valid.

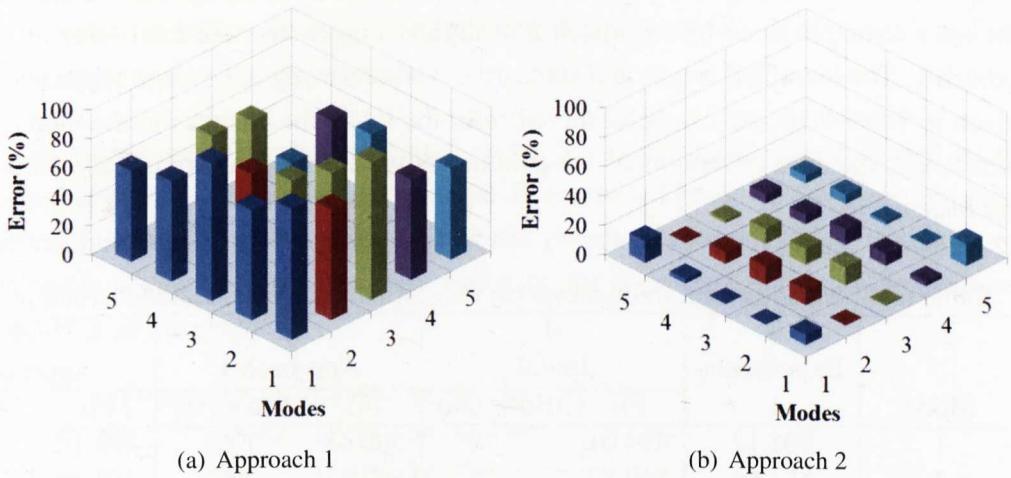
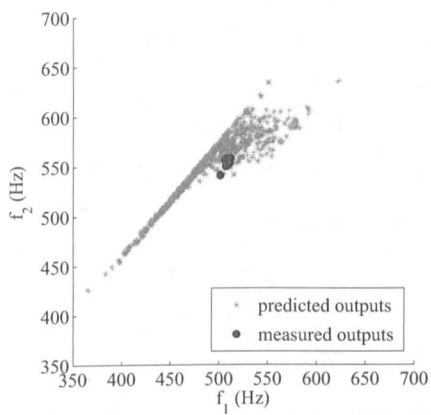


Figure 6.18: Error after updating between the measured and predicted outputs covariances for the welded structures

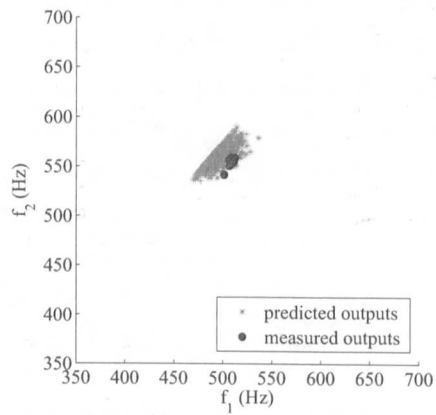
Fig. 6.19 and 6.20 show the convergence of the predictions upon the experimental data in the space of the first three natural frequencies using the second approach. In these scatter clouds, five hundred samples are generated by the Monte Carlo simulation following the Gaussian distribution. It can be seen from the figure that the general trends of the updated results are similar to that of the initial results. The findings demonstrate that modification to the weighting assignment is capable of bringing the numerical results to convergence. This could be due to the inclusion of uncertainties in the substructures following the welding process in the stochastic analysis.

## 6.5 Conclusions

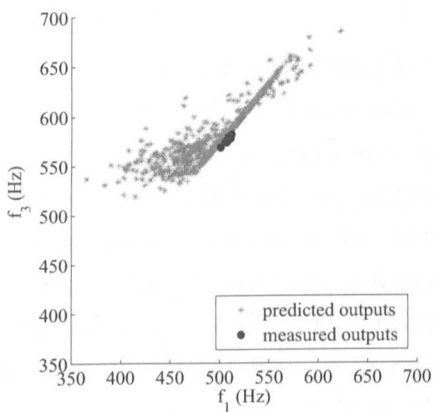
This chapter has included some necessary information of uncertainty in structural dynamics, including its classifications, representations and propagations methods. Then, stochastic model updating is explained and case studies using two very different sets of structures (i.e., simple plates and complicated hat-shaped shells) are provided for parameter selection in the stochastic model updating procedure. Different sets of parameters (i.e., geometrical and material properties) are investigated and the findings in the case studies are used as a guideline in selecting the updating parameters for quantifying variability in the dynamics of the laser welded structures.



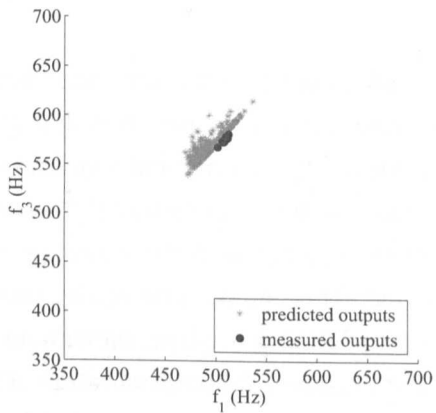
(a) Initial scatter plot for the first and second natural frequencies



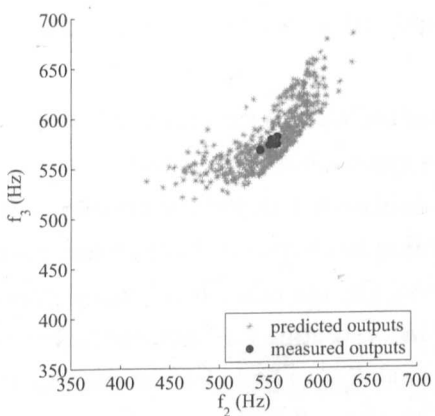
(b) Updated scatter plot for the first and second natural frequencies



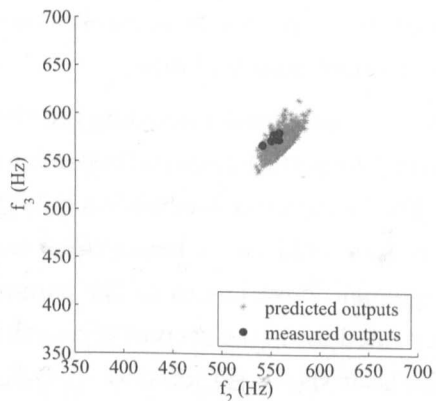
(c) Initial scatter plot for the first and third natural frequencies



(d) Updated scatter plot for the first and third natural frequencies

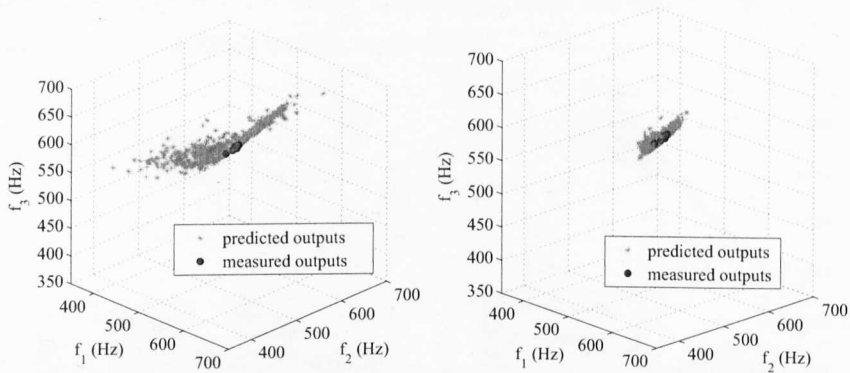


(e) Initial scatter plot for the second and third natural frequencies



(f) Updated scatter plot for the second and third natural frequencies

Figure 6.19: Initial and updated scatter plots for the first, second and third natural frequencies



(a) Initial scatter plot for the first three natural frequencies (b) Updated scatter plot for the first three natural frequencies

Figure 6.20: Initial and updated scatter plots for the first three natural frequencies

As some general guidelines, the selection of parameters should be made by choosing the most sensitive parameters that affect the outputs of the system. This can be easily achieved by carrying out a simple sensitivity analysis. The selection of parameters should also be made so that the mean outputs are closer to the measured outputs, and convergence between the scatter plots of the predicted and measured outputs can be obtained. This can be achieved by including both geometrical and material properties in the updating procedure, rather than choosing a number of geometrical properties alone. For example, although variation of thickness across the plate is incorporated into the FE model, good convergence could not be reached; indicating that certain modes (for example, torsional modes) could not be improved by solely having the thickness variation. When using material properties as updating parameters, the problematic modes are better represented. For instance, updated shear modulus value improves the torsional modes representation.

The stochastic model updating problem for the welded structures are performed by employing the perturbation method using two approaches of parameters weighting matrices. The first approach considers only the main uncertain parameters that come from the laser spot weld joints, hence equal weighting has been employed when estimating the means and covariances of the parameters. On the other hand, more parameters are accounted for in the second approach by incorporating the uncertainties associated with the laser spot weld joints (i.e.,  $d$ ,  $E_{\text{weld}}$  and  $E_{\text{patch}}$ ) and also the uncertainties associated with the substructures (i.e.,  $E$  and  $G$  of the flat plates, and  $T_1$ ,  $T_2$  and  $E$  of the hat-shaped shells) due to the deformation following the welding process. Therefore, two different weightings have to be introduced, one for each step of updating. It is found that the second approach has significantly improved the results over the first approach. Scatter clouds of the measured and predicted outputs are generated by the

Monte Carlo simulation following the Gaussian distribution to show convergence of the stochastic updating procedure, and as demonstrated in this chapter, the predicted space has converged upon the measured space very well. Additionally, the number of samples (i.e., five hundred) used in plotting the scatter clouds are clearly enough to give an accurate estimate of the parameter variability using the perturbation method.





# Chapter 7

## Identification of defects/damage in a laser welded structure

### 7.1 Introduction

Damage detection of aerospace, civil, and mechanical engineering structures are essential in determining their safety, reliability, and operational life. For example, a typical automotive body-in-white (BIW) could contain thousands of spot weld joints that are not only required for connections between layers of metal sheets but also contributing significantly to the vehicle's structural stiffness and dynamic characteristics. However, some of these joints may be imperfect or even absent during the manufacturing process and they are also highly susceptible to damage due to operational and environmental conditions during the vehicle lifetime. So, because of their significance to the dynamics of vehicles, early detection and estimation of damage are important so necessary actions (such as structural repair and/or part replacement) can be made to avoid further problems.

Damage identification procedure consists of obtaining information about the existence, location, and extent of damage in structures using non-destructive methods. The damage identification methods using dynamic properties information are closely related to the updating of a mathematical model using test data, hence can be classified as an inverse minimisation problem [26, 101]. Therefore, FE model updating has been considered as one of the most frequently used methods in damage identifications, as reported by Fritzen et al. [27] and Pascual et al. [102], just to name a few. Existence of damage or a defect often leads to alteration of vibration modes in a structure, which can be manifested by changes in the vibration data. For instance, loss of stiffness due to damage would result in lower natural frequencies; thus demonstrating the dependency between the vibration characteristics and the physical properties of structures. Therefore, an adequate FE model that is able to detect changes in the structural properties should be used in order for the damage to be identified accurately.

In damage identification, the FE model updating procedure is normally conducted in two stages: (1) the initial FE model is updated to match the measured data of the undamaged structure (which is used as a reference model), and (2) the reference FE model is updated to reproduce the experimental modal data of the damaged structure and damage can then be identified by examining the changes in the stiffness property of the updated model. Nonetheless, uncertainties in the FE model along with errors in the measured vibration data could limit the success of the method [103]. For instance, less pronounced damages may not be detected owing to the presence of measurement noise, and healthy structural elements could be identified as damaged instead [104].

A general summary of vibration-based structural damage detection methods are presented in this chapter, which is followed by thorough explanation regarding the work conducted on the identification of defects/damage in a laser welded structure. In this research, the identification procedure is carried out in two parts: one using only the natural frequencies information and another using both the natural frequencies and mode shapes data, both are performed with the FE model updating method. The first part of the investigation concerns of detecting manufacturing defects in a laser welded structure (Section 7.3), while the second part reports the identification of actual damage in a welded structure (Section 7.4).

## 7.2 Damage identification methods

Various methods for damage identification of structures has been developed in the last few decades, mainly for health monitoring purposes [105]. The methods can be generally classified as *local damage detection* [106] and *global damage detection* [107,108], as explained in the following:

**Local damage detection techniques** refer to non-destructive testing, where existence and location of local damage can be detected. Originally, visual inspection has been the most commonly used method in observing structural damage; however as structures become more complicated, the efficiency of the conventional visual inspection is reduced. Furthermore, it is also impossible to identify damage that is hidden or invisible to human eyes, hence other local methods such as CT scanning, ultrasonic, acoustic and X-ray inspections are employed as better alternatives. One of the main advantages of these methods is that they only require data obtained from the damaged structure, so there is no need for information from the intact/healthy structures. Nevertheless, these methods are effective only on small and regular structures. For large complicated structures (especially in closed and invisible environments), these approaches require some knowledge of damage location in order to avoid a costly and time-consuming procedure.

**Global damage detection techniques** (or vibration-based damage detection) has been employed to detect damage across the whole structure (regardless of the size and shapes) using dynamic characteristics (notably natural frequencies, mode shapes, modal damping and FRFs) of the structure. It is known that structural parameters will change once damage emerges in the structure, which consequently alters the dynamic properties of the structure. Therefore, these methods are more appropriate as the structural state can be assessed globally by monitoring the changes in the dynamic properties of the structure. These dynamic-based identification methods have received significant interest [20, 109, 110] (especially by civil, mechanical and aerospace communities) that consequently results in literature being extensively published, as summarised by Doebling et al. [15, 16] and Sohn et al. [111].

The vibration-based damage detection can be divided into: (1) traditional, and (2) modern type [20]. The former utilises the dynamic characteristics of the structures, which requires the experimental modal analysis in order to measure the natural frequencies, mode shapes, modal damping, FRFs, etc.. This type of damage identification is applied in this research using the FE model updating technique. The modern-type (e.g., Wavelet analysis, Genetic algorithm and Artificial Neural Network), on the other hand, is based on online measured response signal of structures in service. One main advantage of this type of vibration-based damage detection is that it can monitor the dynamic response signals of the structure in operation, hence structural shutdown or production halt can be avoided. Furthermore, it is possible to establish universal methodology for detection of damage, regardless of the shape of the structure. Nevertheless, there are still some issues to be resolved in the modern-type method, including possible contamination of measured signals by noise that may hinder the detection of tiny damages. The modern type damage identification is not employed in this research, hence it is not explained further in the thesis.

The eigenvalue problem in existence of damage can be expressed as follows,

$$(-\tilde{\lambda}\tilde{\mathbf{M}} + \tilde{\mathbf{K}})\tilde{\phi} = 0 \quad (7.1)$$

where  $\tilde{\phi}$  indicates the properties in the damaged state. Assuming that the mass remains unchanged (i.e.,  $\tilde{\mathbf{M}} = \mathbf{M}$ ), therefore

$$\begin{aligned} \tilde{\mathbf{K}} &= \mathbf{K} + \Delta\mathbf{K} \\ \tilde{\lambda} &= \lambda + \Delta\lambda \end{aligned} \quad (7.2)$$

$$\tilde{\phi} = \phi + \Delta\phi$$

where  $\Delta\lambda$  and  $\Delta\phi$  are the changes in modal data due to the changes in stiffness ( $\Delta\mathbf{K}$ )

that is caused by the changes in structural parameters. It is shown by the above two equations that the damaged structural parameters can be identified by knowing the measured eigenvalues and eigenvectors in the damaged state. In addition to that, the changes in the modal characteristics may be different for each mode because the changes depend on the nature, location and severity of the damage. Therefore, the information of the changes in the vibration characteristics is very useful in: (1) detecting the occurrence of damage, (2) localising the damage zones, and (3) quantifying the extent of damage in the structure.

The dependency of the vibration characteristics on the physical properties of structures offers the possibility to indicate the state of health or quality of structures that leads to increasing interest in the traditional-type vibration-based damage detection methods. Consequently, many techniques have been researched to include the measured vibration data for detecting damage in structures; for example, using natural frequencies [112, 113], mode shapes [114–116] and mode shape curvatures [117], and many more [118–120]. Some of these traditional-type vibration-based damage detection methods are briefly summarised in the following sections. A thorough review has been reported extensively by Doebling et al. [15].

### **7.2.1 Damage detection based on the change of natural frequency**

The most common dynamic parameter used in damage detection is the natural frequency, which has been used by many researchers to indicate the structural damage. For example, Cawley and Adams [113] and Lee and Chung [121] demonstrated that a state of damage can be detected from the changes in natural frequencies. In a practical structure, the natural frequency is easy to measure and the measurement accuracy of natural frequency is generally higher than that of the mode shapes or modal damping. However, the natural frequency is often not sensitive enough to small damages in the structure. Furthermore, the measurement of natural frequency cannot provide enough information for structural damage detection, as it only provides the information on the global behaviour of the structure. Therefore, the method may not be able to correctly predict the damage location because the structural damage in different location may cause the same frequency change. Hence, it can be generally said that the existence of structural damage can be detected through the natural frequency change, while the determination of damage location and extent is difficult using only the natural frequency unless the information of the mode shapes is included [122].

### **7.2.2 Damage detection based on the change of mode shapes**

The mode shape is also commonly used in damage identification as it contains more damage information than the natural frequency, as has been investigated by many re-

searchers [114–116]. The mode shapes have the advantage of being spatially specific, so it is possible to ascertain the location and extent of structural damage. However, the measurement of mode shapes is more complex and the measurement error is distinctly larger than that of the natural frequency. Furthermore, it is observed that higher frequency modes are considerably sensitive to localised damage, but they are more difficult to measure accurately and are often difficult to interpret for complex structures.

Pandey et al. [117] introduced the use of mode shape curvatures (i.e., derivatives of mode shapes) as an alternative to the mode shape information, which is applied for damage identification in a cantilever and a simply supported analytical beam model. It was found that the greatest difference between the curvature mode shapes of intact and damaged structures are localised in the region of damage, while the changes in the curvature mode shapes can be used to indicate the extent of damage as they increase with increasing size of damage. Whilst the mode shape curvatures offer spatial specificity along with high sensitivity to damage, unfortunately it can still be subjected to numerical estimation difficulties resulting from the need for differentiation. Moreover, their estimation from experimental data are also very difficult [123].

### **7.2.3 Damage detection based on the change of FRFs**

Another critical issue of using the modal data in detecting damage is the fact that the natural frequencies and mode shapes are indirectly-measured, hence usually contain accumulative errors due to modal parameter extraction procedure [119]. Furthermore, the modal properties give less information than directly-measured FRFs [124]; thus it is more sensible to employ the FRFs for structural damage detection and system identification.

Wang et al. [125] used measured FRF data obtained before and after damage in order to construct their damage identification algorithm. Lee and Shin [124] proposed an FRF-based damage identification method that uses a damage distribution function with non-zero values at damage locations. So, undamaged regions (with zero damage distribution function) can be eliminated from the identification algorithm derived from dynamic equations of motion for the damaged structures. Sampaio et al. [126] proposed the FRF Curvature Method that is based on the changes in the curvature of the FRFs of the damaged and undamaged structure for damage detection, localisation and quantification.

Despite the interest in the FRF-based damage detection method, there are still some problems that need to be addressed including main issues such as contamination of noise in the FRF measurements and data incompleteness, which greatly influenced the accuracy of the structural damage detection procedure. Furthermore, this method requires a large amount of measured data and computational effort, which is not advantageous if fast detection is needed. Because of these difficulties, the method is not

investigated further in this research. Therefore, identifying damage or defects from natural frequencies without having to use the mode shape information is attempted first in this work, followed by a further investigation using both the natural frequencies and mode shapes.

### 7.3 FE model updating for identification of defects

The procedure for detection of defects in a welded structure is illustrated in Fig. 7.1. It is important to conduct the defect detection procedure using an FE model that is well-correlated with a benchmark structure [127]. Hence, an identical structure to the ones presented in Chapter 4 was specially produced with smaller manufacturing tolerance to provide a benchmark structure closest to the nominal design. Modal testing was then conducted on the benchmark structure and the experimental results are used as a point of reference in the identification work. Next, the developed FE model of the welded structure (as explained in Chapter 5) is used and updated to match the benchmark experimental data. Identified benchmark parameters from the updating procedure are then employed in modelling a defective structure. The FE model of the defective structure also incorporates the findings from visual inspection that has been carried out prior to the modelling stage. The model is then updated based on the experimental data from the defective structure to reproduce the measured modal properties of the defective structure.

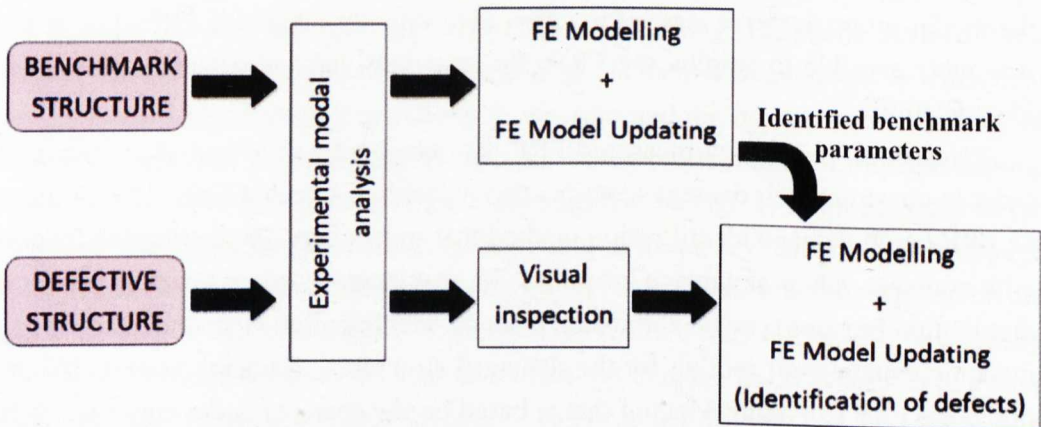


Figure 7.1: Structure of the identification procedure

#### 7.3.1 Description of defective structures

A defective structure is identified from the nine identical structures produced initially (as presented in Chapter 4), by comparing the measured natural frequencies of each individual structure with the measured natural frequencies of the benchmark structure. A



structure (i.e., sample number 7 in Table 4.10) with the biggest variation to the benchmark measured data is identified, and visual inspection is carried out. The spot welds are grouped into three groups (Table 7.1): 1) ‘normal’ welds, 2) ‘oversized’ welds, and 3) ‘undersized’ welds, as illustrated in Fig. 7.2. The ‘oversized’ and ‘undersized’ welds are considered as defects. These discrepancies in size are incorporated in the FE model of the defective structure, as described in Section 7.3.3.

Table 7.1: List of normal and problematic spot welds

Group	Number of welds	Spot weld ID *(see Fig. 7.2)
Oversized	8	1, 11-14, 17-19
Normal	7	2-4, 10, 15-16, 20
Undersized	5	5-9

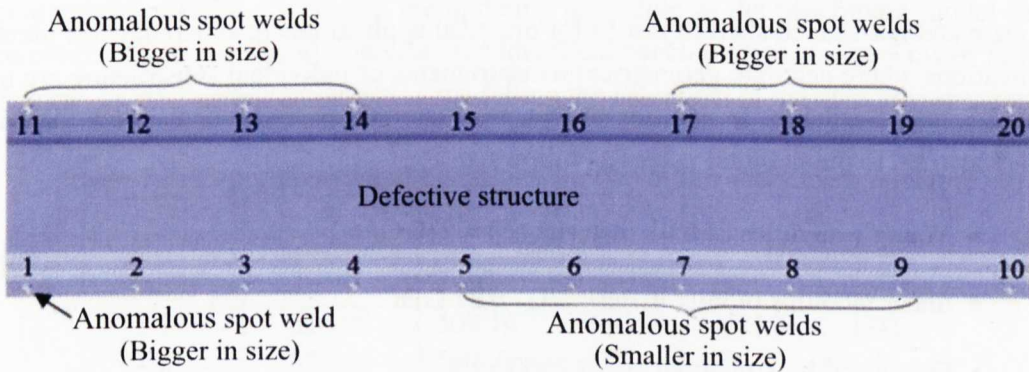


Figure 7.2: Defective structure

The identification procedure requires vibration responses of both benchmark and defective structures to be acquired first, hence 80-point roving hammer test with four measurement points was performed on both structures following the setup presented in Section 4.4. The measured natural frequencies of the benchmark and defective structures are given in Table 7.2, so the significance of defects in terms of the natural frequencies can be observed. It can be seen that the existence of defects does not affect all the resonant modes equally, with some modes are more influenced by the presence of defects compared with others. It is also worth mentioning that the deviations of the frequencies from the benchmark data are very small, especially for modes 2, 4 and 5. This is because frequencies alone often may not be sensitive enough to significantly distinguish damage or defects in a structure [105]. Therefore, it is advisable to include more structural information (such as mode shapes) in damage detection if local behaviour of damage is the main focus, which is presented in Section 7.4, since regions located at or near the damage would deform differently [128]. The experimental vibration measurements of both structures are employed in the next sections for model

verification and identification work.

Table 7.2: Experimental natural frequencies for the benchmark and defective structures

Mode	Benchmark	Defective	Difference (%)
1	513.95	507.04	1.35
2	550.46	550.40	0.01
3	578.69	572.83	1.01
4	624.86	625.47	0.10
5	639.07	643.49	0.69

### 7.3.2 FE modelling and updating of benchmark structure

A numerical investigation on the benchmark structure is performed using the FE model as shown in Fig. 5.15, with nominal value of 1.5 mm for the thicknesses of the flat plate and hat-shaped shell to justify for practical applications in actual damage identifications where accurate geometrical measurements of individual substructure are not necessarily available. In addition to that, the material properties of the bulk material are also set to the nominal values as follows,

- Young's modulus of bulk material ( $E$ ) = 210 GPa
- Shear modulus of bulk material ( $G$ ) = 81 GPa
- Density of bulk material ( $\rho$ ) = 7860 kgm<sup>-3</sup>

while the approximated values of the spot weld parameters (as shown in Tables 6.14 and 7.4) are assigned to the weld and patch parameters, as follows.

- Diameter of welds ( $d_{\text{weld}}$ ) = 5.5 mm
- Young's modulus of welds ( $E_{\text{weld}}$ ) = 220 GPa
- Young's modulus of patch ( $E_{\text{patch}}$ ) = 650 GPa

The natural frequencies of the initial FE model of the benchmark structure are compared with the benchmark experimental results, as tabulated in Table 7.3. As shown in the table, the maximum error is no larger than 1.8% and in most cases less than 1%; which demonstrates a very good correlation between the initial FE and the experimental model, therefore confirms the findings of the updating work reported in Chapter 5. However, FE model updating is still being performed on the benchmark model to isolate any uncertainties from the model for the identification procedure.

Earlier findings presented in Chapter 5 suggest that the two parameters of the CWELD element (i.e.,  $d_{\text{weld}}$  and  $E_{\text{weld}}$ ) could not bring the numerical results of the



welded structure near to their experimental counterparts, thus  $E_{\text{patch}}$  must be included for the updating procedure. Each of these three parameters has an initial value as given in Table 7.4 and they are allowed to have some variations depending on the uncertainty level associated with the parameters.  $d_{\text{weld}}$  and  $E_{\text{weld}}$  are allowed to vary within a limited reasonable range only (approximately 15% variation), while  $E_{\text{patch}}$  is allowed to have a very big variation (i.e., 50%) due to high uncertainties in the properties of the patch.

The deterministic model updating formulation (Eq. (5.8)) is used for updating the benchmark structure, with results presented in Tables 7.3 and 7.4. From Table 7.3, it can be seen that the errors of the first and fifth modes are increased, but the maximum error drops to less than 1.5% while the total error is smaller than the initial. This demonstrates that changes in the physical properties affect each mode differently, which highlights the complex interaction between the physical properties and dynamic characteristics [128]. Generally, the updating procedure of the benchmark model can be concluded as successful; therefore the identified benchmark parameters (as in Table 7.4) can be confidently employed in modelling the FE model of the defective structure.

Table 7.3: Experimental and FE results (in Hz) of the benchmark structure

Mode	I Experiment	II Initial		III Updated	
		FE	Error (%)	FE	Error (%)
1	513.95	509.16	0.93	508.39	1.08
2	550.46	560.29	1.79	557.71	1.32
3	578.69	581.96	0.57	580.89	0.38
4	624.86	627.46	0.42	624.47	0.06
5	639.07	634.39	0.73	631.63	1.16
Total error			4.43		4.01

Table 7.4: Changes in parameters due to updating - benchmark

Parameter		Initial value	Updated value	Change [%]
Weld Diameter, $d_{\text{weld}}$	(mm)	5.5	5.41	0.94
Weld Young's Modulus, $E_{\text{weld}}$	(GPa)	220	219	0.35
Patch Young's Modulus, $E_{\text{patch}}$	(GPa)	650	622	4.27

### 7.3.3 Modelling of defective structure and identification of defects

Applying the findings from Tables 7.1 and 7.4, the initial FE model of the defective structure is established. Sensitivity analysis is conducted to identify suitable updating parameters and four updating parameters are selected as follows.

- the diameter of the 'oversized' welds ( $d_{\text{big}}$ )

- the diameter of the ‘undersized’ welds ( $d_{\text{small}}$ )
- the Young’s modulus of the ‘oversized’ weld patch ( $E_{\text{bigpatch}}$ )
- the Young’s modulus of the ‘undersized’ weld patch ( $E_{\text{smallpatch}}$ )

The sensitivities of the natural frequencies with respect to the selected parameters are shown in Table 7.5, while the initial values of the four parameters are tabulated in Table 7.6. The weld diameters (i.e.,  $d_{\text{big}}$  and  $d_{\text{small}}$ ) are allowed to vary in a limited reasonable range, while the Young’s moduli of the patches (i.e.,  $E_{\text{bigpatch}}$  and  $E_{\text{smallpatch}}$ ) are allowed to have very big variations due to high uncertainties of the patch properties.

Table 7.5: Defective structure: Sensitivities of the natural frequencies to the selected normalised parameters in Hz

Mode	$d_{\text{big}}$	$d_{\text{small}}$	$E_{\text{bigpatch}}$	$E_{\text{smallpatch}}$
1	1.23	8.30	9.88	2.89
2	2.87	17.35	5.91	16.27
3	1.40	9.36	2.21	6.52
4	4.88	29.86	6.94	19.49
5	4.23	25.65	5.04	13.59

In the updating procedure for the identification of defects, appropriate weighting coefficients are assigned to the objective function (Eq. (5.13)) based on the errors tabulated in Table 7.2. The weighting coefficients are then calculated as follows,

$$w_i^{\text{damage}} = \left| \frac{\varepsilon_i - \varepsilon_{\text{min}}}{\varepsilon_{\text{min}}} \right| \quad (7.3)$$

with  $\varepsilon_i$  represents the natural frequency deviation between the benchmark and defective structures at  $i^{\text{th}}$  mode, and  $\varepsilon_{\text{min}}$  represents the minimum frequency difference between the two structures. Eq. (5.13) can now be rewritten as,

$$J = \sum_{i=1}^n w_i^{\text{damage}} \left( \frac{\lambda_i^{\text{damage}}}{\lambda_i^{\text{damageexp}}} - 1 \right)^2 \quad (7.4)$$

The updating procedure converges after seven iterations, as depicted in Fig. 7.3, and the identified defect parameters are listed in Table 7.6. The natural frequencies from the initial and updated FE model of the defective structure are given in Table 7.7. By updating the initial FE model to the experimental data, the total error reduces by more than 70% of the initial total error. The diameter of the ‘oversized’ welds ( $d_{\text{big}}$ ) is

increased by approximately 9% from the initial value and the ‘undersized’ weld ( $d_{\text{small}}$ ) is reduced by approximately 25%. It should also be noted that the mesh size used in the model is fixed to 20% of the nominal diameter. Hence, increased value of  $E_{\text{bigpatch}}$  indicates not only increased rigidity at the patch area, but may also demonstrates affected area that is bigger than the size of the mesh used for the patch. Conversely, reduced value of  $E_{\text{smallpatch}}$  demonstrates reduced rigidity that consequently indicates smaller patch area. If the updated values are believed to reflect the reality, both sets of welds may be classified as defects, hence support the findings from the earlier visual inspection made to detect physical inconsistencies in the welds.

Table 7.6: Changes in parameters due to updating - defective

Parameter	Initial value	Updated value	Change [%]
Big Weld Diameter, $d_{\text{big}}$ (mm)	5.50	5.98	8.73
Small Weld Diameter, $d_{\text{small}}$ (mm)	4.50	3.38	24.89
Big Weld Patch, $E_{\text{bigpatch}}$ (GPa)	622	1159	86.27
Small Weld Patch, $E_{\text{smallpatch}}$ (GPa)	622	285	54.18

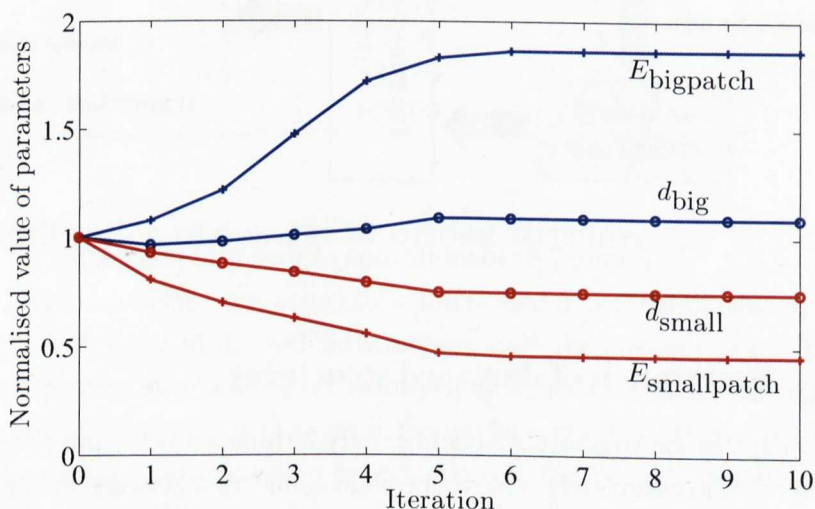


Figure 7.3: Parameters changes from the initial normalised values of unity for the defective structure

## 7.4 FE model updating for identification of damage

The procedure for identification of damage in a welded structure is illustrated in Fig. 7.4. The benchmark structure used in the previous section is employed here and the measured data of the benchmark is utilised as reference data of undamaged structure.

Then, damage was introduced to the benchmark structure and modal testing was performed. Next, the developed FE model of the benchmark structure is updated to match the measured data of the damaged structure to localise and quantify the damage.

Table 7.7: Experimental and FE results (in Hz) of the defective structure

Mode	I Experiment	II Initial		III Updated	
		FE	Error (%)	Updated FE	Error (%)
	1	507.04	508.81	0.35	509.41
2	550.40	560.50	1.83	550.38	0.00
3	572.83	581.38	1.49	576.97	0.72
4	625.47	628.84	0.54	625.54	0.01
5	643.49	635.83	1.19	641.66	0.28
Total error			5.41		1.49

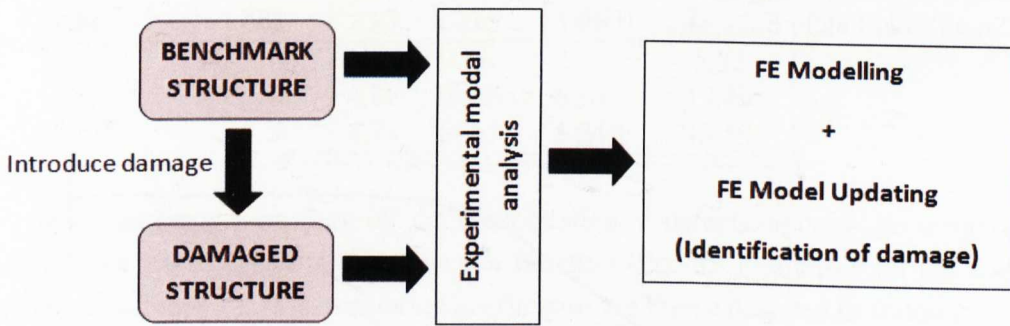


Figure 7.4: Identification of damaged procedure

### 7.4.1 Description of damaged structures

The damage in the structure was deliberately introduced by drilling out spot weld 13 (see Fig. 7.5) to completely remove the weld connection between the flat plate and the hat-shaped shell. Modal parameters of the damaged structure (i.e., the natural frequencies and mode shapes) were identified by conducting 80-point roving hammer test with a similar procedure performed on the benchmark structure (explained in Section 4.4). The first five natural frequencies and the mode shapes of the damaged structure are compared with the benchmark, as shown in Tables 7.8 and 7.9 respectively. It can be seen from the table that the existence of damage does not really affect the fundamental mode, with a very small difference of 0.69% between the undamaged and damaged structure. However, the deviations of the natural frequencies for the fourth and fifth modes are very noticeable (with almost 15% for the fourth mode). In addition, the second and third modes appear to have small deviations from the benchmark data, but it



should be noted that these modes (plus the fourth modes) are swapped - see Table 7.9. Furthermore, the mode shapes are no longer symmetrical in the longitudinal direction due to the existence of damage.

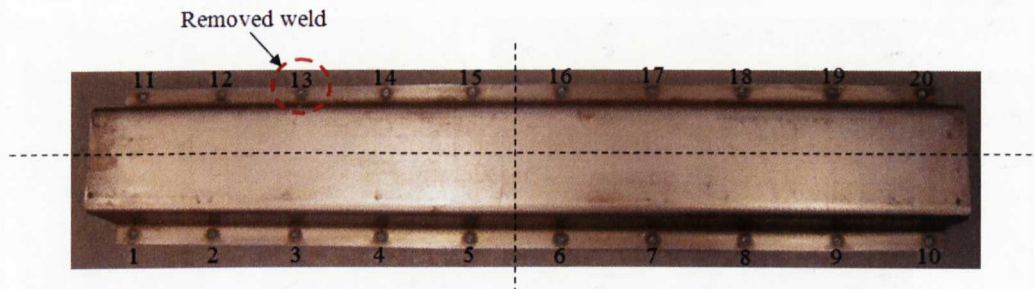


Figure 7.5: Damaged structure

Table 7.8: Experimental natural frequencies for the undamaged and damaged structures

Mode	Benchmark	Damaged	Difference (%)
1	513.95	510.40	0.69
2	550.46	545.70	0.86
3	578.69	572.6	1.05
4	624.86	532.10	14.84
5	639.07	609.00	4.71

### 7.4.2 Identification of damage in welded structure

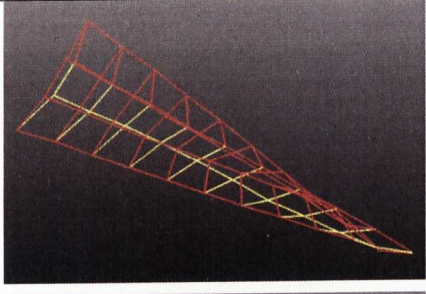
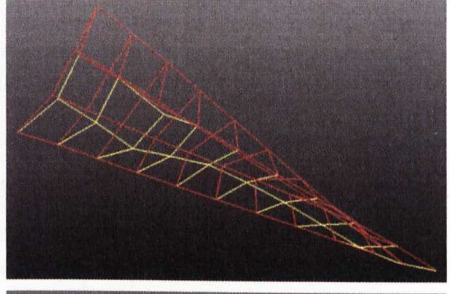
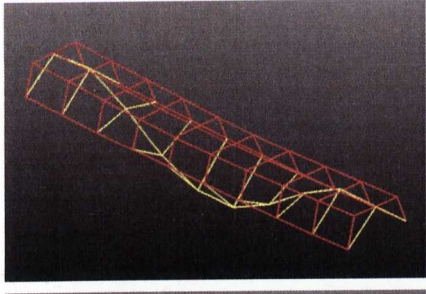
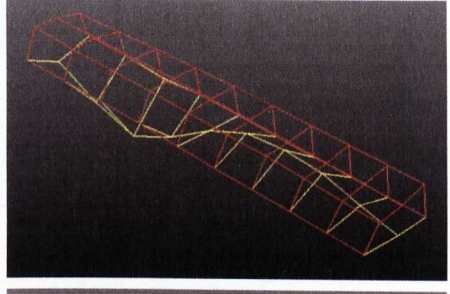
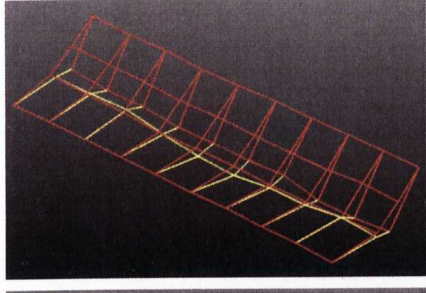
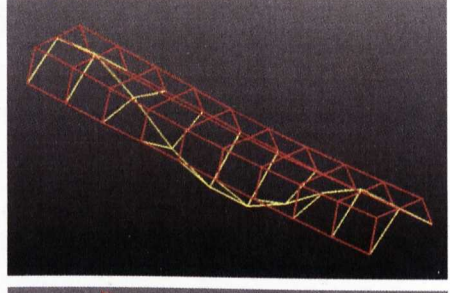
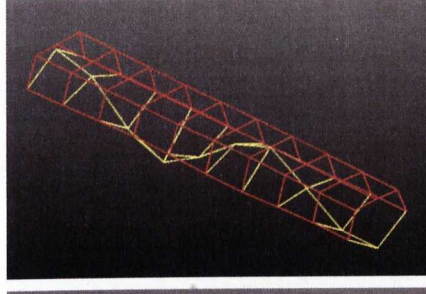
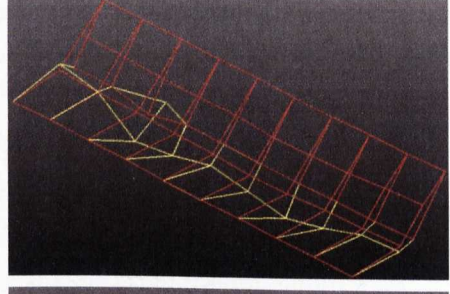
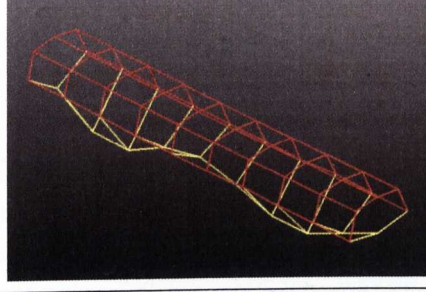
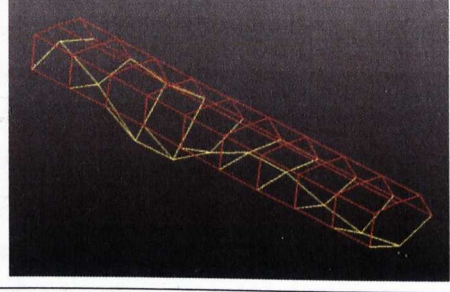
The updated FE model of the undamaged structure is used in the identification process. When identifying damage in the welded structure, only the changes in the Young's modulus of the patches surrounding the twenty spot welds are considered since they are proven to be quite sensitive to changes in the modal properties. Therefore, damage in the welded structure is characterised by reductions in the Young's modulus to indicate the loss of material/stiffness at the damaged patches.

The Young's modulus is expressed as

$$E_k^d = \alpha_k E_k^h \quad (k = 1, 2, \dots, 20) \quad (7.5)$$

where  $E_k^d$  denotes the Young's modulus in damaged state,  $E_k^h$  represents the Young's modulus in healthy (or undamaged) state, and  $\alpha_k$  is a coefficient whose value ranges from 0 to 1, with a value of 0 meaning 100% damage and a value of 1 indicating no damage at all. If there is no prior knowledge of the integrity of the structure, then  $\alpha_k = 1$  is set at the start of the identification work, which is the case in this work.

Table 7.9: Experimental mode shapes comparison between the undamaged and damaged structures

Mode	Undamaged	Damaged
1		
2		
3		
4		
5		



Because of the symmetrical nature of the welded structure, more information is required to assist the identification process. The experimental mode shapes of the damaged structure are observed and it is acknowledged that the damage occurs only at one quarter of the welded structure, as highlighted in Fig. 7.6. Based on this information, it is decided that only one quarter of the structure would be considered as damage region, thus reducing the number of possible damage locations. In this work, spot welds 11 to 15 are regarded as possible damaged spot welds in the damage region.

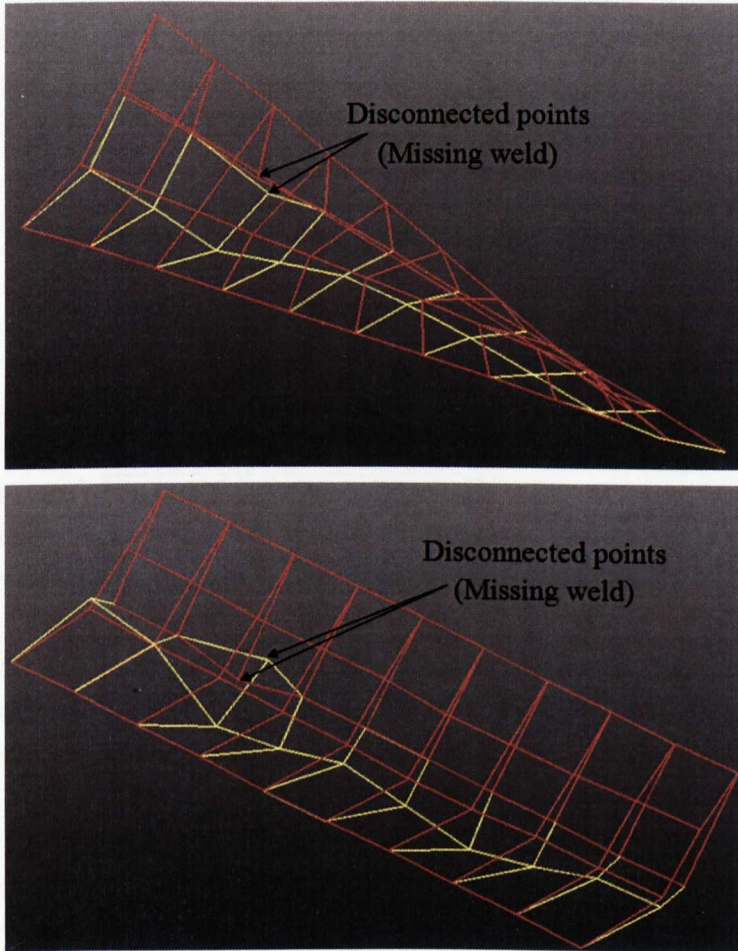


Figure 7.6: Observation on the experimental mode shapes of the damaged structure to identify damage region

The damaged coefficients can then be assigned as,

$$\underline{\alpha}_k^h \leq \alpha_k^h \leq \bar{\alpha}_k^h \quad \text{and} \quad \underline{\alpha}_k^d \leq \alpha_k^d \leq \bar{\alpha}_k^d \quad (7.6)$$

where  $\alpha_k^h$  represents the coefficient for the healthy regions, while  $\alpha_k^d$  denotes the coefficient for the effected region. In this work,  $0.8 \leq \alpha_k^h \leq 1$  is used for the healthy regions whereas  $0.001 \leq \alpha_k^d \leq 1$  is assigned for the damage area. Note that a very



small value is used for  $\underline{\alpha}_k^d$  instead of 0 in order to avoid poor geometrical and/or material properties (hence potential numerical difficulties) at the spot weld connections in the FE model. It should also be pointed out that an overlap in terms of the value of coefficients for both damage and healthy areas exists. The overlap region is required since the actual damaged spot weld is not known, and there may be healthy spot welds in the specified damage area.

Inverse algorithm for the identification of damage used in this work is shown in Fig. 7.7. Note that an initial value of 1 is set for all the coefficients in the updating procedure. However, the coefficients are bounded to:

$$\alpha_k = \begin{cases} 1 & \text{if } \alpha_k > 1 \\ \underline{\alpha}_k^h & \text{if } \alpha_k^h < \underline{\alpha}_k^h \\ \underline{\alpha}_k^d & \text{if } \alpha_k^d < \underline{\alpha}_k^d \end{cases} \quad (7.7)$$

after each iteration.

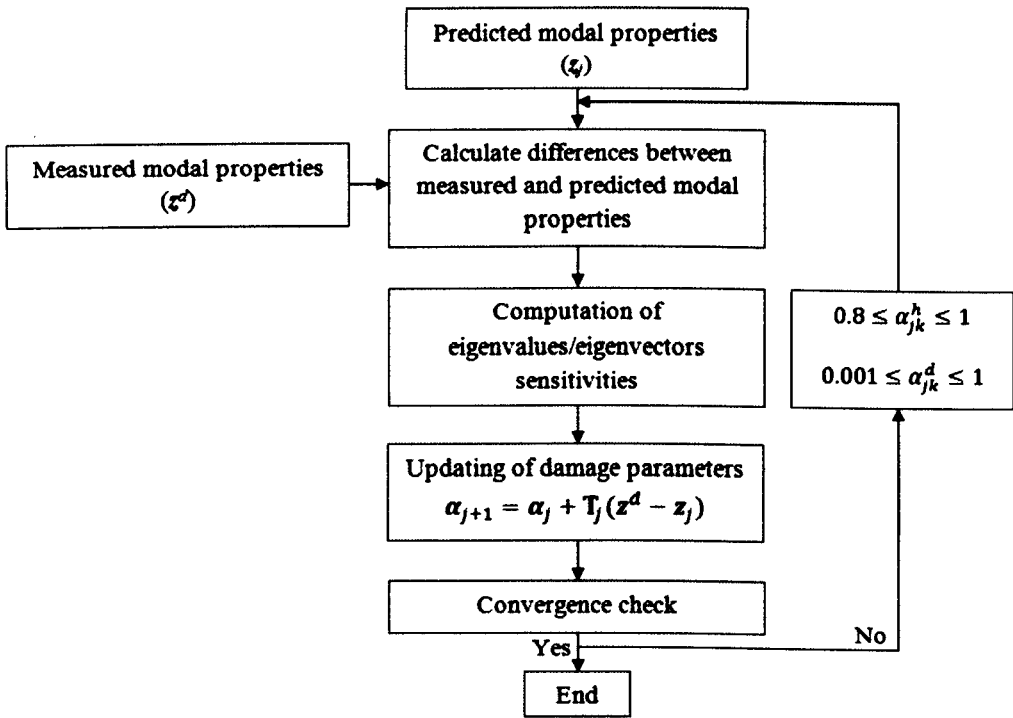


Figure 7.7: FE model updating for damage identification

An objective function of

$$J = \sum_{i=1}^n w_i^\lambda \left( \frac{\lambda_i^{\text{damage}}}{\lambda_i^{\text{damageexp}}} - 1 \right)^2 + \sum_{i=1}^n \sum_{k=1}^{20} w_{ik}^\phi \left( \frac{\phi_{ik}^{\text{damage}}}{\phi_{ik}^{\text{damageexp}}} - 1 \right)^2 \quad (7.8)$$

is considered in the identification work, where  $w_i^\lambda$  and  $w_{ik}^\phi$  are weighting coefficients assigned to the objective function (Eq. (7.8)) to give more weight to certain output data that may need greater accuracy than the others (i.e., modes with lower level of confidence).

The identification procedure is performed using a combination of MATLAB and SOL200 of NASTRAN to update the initial (i.e. the benchmark) FE model until the computed natural frequencies and mode shapes match those from the damaged experimental data. The FE model updating procedure is conducted based on the first five natural frequencies and the first mode shape of the damaged structure. Furthermore, all frequencies and mode shapes data at those twenty DOFs are given the same confidence level. Hence,  $w_i^\lambda = w_{ik}^\phi = 1$ . Consequently, Eq. (7.8) reduces to

$$J = \sum_{i=1}^5 \left( \frac{\lambda_i^{\text{damage}}}{\lambda_i^{\text{damageexp}}} - 1 \right)^2 + \sum_{k=1}^{20} \left( \frac{\phi_{1k}^{\text{damage}}}{\phi_{1k}^{\text{damageexp}}} - 1 \right)^2 \quad (7.9)$$

As mentioned earlier, changes in the Young's modulus of the patch for the twenty spot welds are observed to indicate the loss of stiffness at those twenty spot weld locations. These changes are represented by the coefficient as defined in Eqs. (7.5) to (7.7). Coefficients that belong to the five spot welds in the damaged region are treated as potential damage, while the rest of the coefficients are assumed to be healthy.

The initial natural frequencies from the benchmark FE model are given in Table 7.10 (Column II), while the initial MAC values are given in Table 7.11. It can be seen that the natural frequencies of the first five modes show errors of up to approximately 9%, while the MAC values show good correlation only for the first and fifth modes. The MAC values for modes 2, 3 and 4 highlight the mode swapping problem between the undamaged and damaged experimental mode shapes (see Table 7.9). In order to improve the correlation between the modes and to reduce the discrepancies of the initial FE model against the experimental data of the damaged structure, the FE model updating is performed to identify and quantify the damaged parameters.

The damage identification procedure converges after fifteen iterations and the identified damage coefficients are tabulated in Table 7.12 and illustrated in Fig. 7.8. It can be seen that the damage has been successfully located and quantified at spot weld 13. However, the supposedly healthy spot welds are also affected by the procedure with the biggest error of approximately 50% at the adjacent spot welds (i.e., spot welds 12 and 14), which is believed to be due to the spillover effect of FE model updating.

Using these identified parameters, the updated natural frequencies are computed as shown in Table 7.10 (Column III). Although the error for the fundamental natural frequency is increased, the errors for the other frequencies are reduced significantly. The total error of the natural frequencies is also decreased to approximately 6%, as compared with its initial error of about 24%. The updated MAC values are calculated

as in Table 7.13. It can be observed that the correlation has improved for all the modes, which means that the identification procedure has successfully match the FE model to the damaged measured data. It should also be noted that the correlation between the measured and analytical modes is checked by calculating the MAC values before and after the updating procedure. However, a better procedure may be employed by conducting cross-orthogonality check (available in NASTRAN - see Ref. [129]) in order to assess the degree of correlation between the measured and numerical mode shapes during the updating loop.

Table 7.10: Experimental and FE results (in Hz) of the damaged structure

Mode	I Experiment	II Initial		III Updated	
		FE	Error (%)	Updated FE	Error (%)
1	510.40	508.39	0.39	501.41	1.76
2	532.10	580.89	9.17	523.00	1.71
3	545.70	624.47	14.43	548.15	0.45
4	572.60	557.71	2.60	575.12	0.44
5	609.00	631.63	3.72	618.88	1.62
Total error			30.31		5.98

Table 7.11: Initial MAC values of the damaged structures

FE modes	Experimental modes				
	1	2	3	4	5
1	<b>0.82</b>	0.05	0.00	0.00	0.02
2	0.00	0.00	<b>0.53</b>	0.04	0.01
3	0.00	0.01	0.08	<b>0.84</b>	0.01
4	0.09	<b>0.55</b>	0.08	0.00	0.01
5	0.01	0.08	0.12	0.14	<b>0.89</b>

Table 7.12: Damage coefficients for spot weld 11 to 15

Parameter	Initial value	Identified value
$\alpha_{11}$	1	0.9032
$\alpha_{12}$	1	0.5421
$\alpha_{13}$	1	0.0017
$\alpha_{14}$	1	0.4363
$\alpha_{15}$	1	0.8764

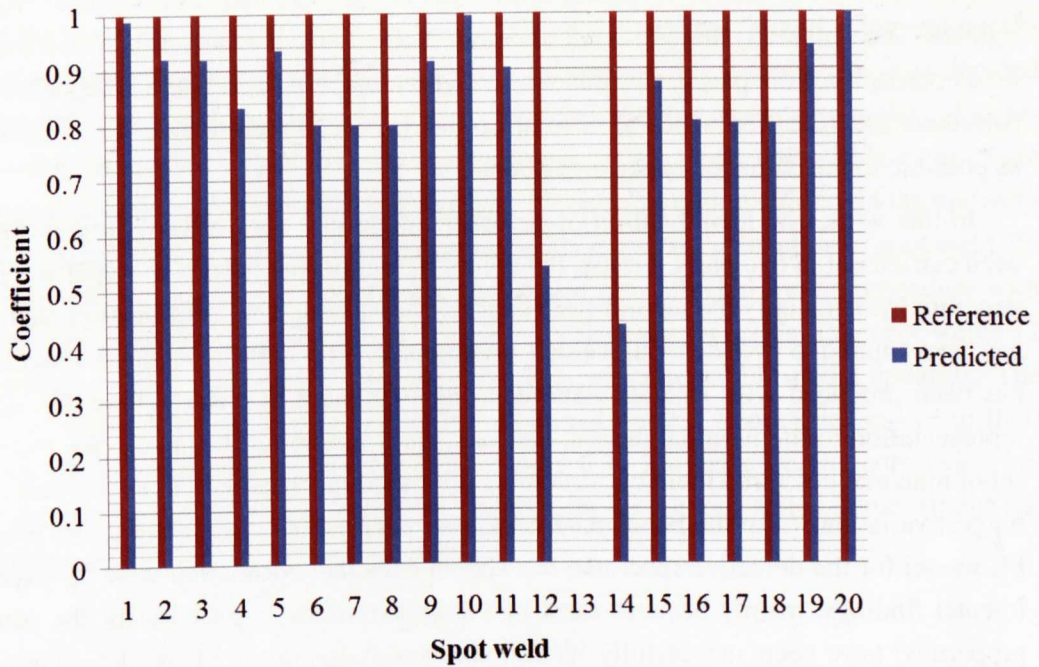


Figure 7.8: Identified parameters

Table 7.13: Updated MAC values of the damaged structures

FE modes	Experimental modes				
	1	2	3	4	5
1	<b>0.87</b>	0.17	0.00	0.00	0.02
2	0.20	<b>0.93</b>	0.00	0.06	0.04
3	0.00	0.01	<b>0.55</b>	0.09	0.02
4	0.02	0.01	0.05	<b>0.89</b>	0.37
5	0.02	0.01	0.16	0.23	<b>0.92</b>

## 7.5 Conclusions

This chapter has presented a brief overview of vibration- or frequency-based damage identification using inverse methods, with some advantages and disadvantages highlighted. The sensitivity-based model updating methods have been selected as a practical approach for the purpose of this work, and the updating procedure is regarded as parameter identification which aims to bring the numerical prediction to be as closely as possible to the damaged experimental data.

In this work, the identification of defects/damage in a spot welded structure has been carried out in two parts. Firstly, the ability of identifying defects in a spot welded structure by using only the natural frequencies is presented. The identification method has been applied to two identical welded structures; one (i.e., the benchmark structure) has been produced with smaller manufacturing tolerances to ensure closer physical representation to the nominal design, and another structure has been selected from a set of nine manufactured identical structures presented in Chapter 4. The latter has the biggest variations from the benchmark data, thus is classified as defective. The initial FE model for the defective specimen has shown excellent correlation with the experimental findings, mainly because most of the uncertainties (especially for the patch properties) have been successfully identified when updating the FE model, firstly in Chapter 5 and secondly when updating the benchmark structure. Furthermore, the predicted natural frequencies from the updated defective model agree with the measured defective data and the identified defect parameters are found to be reasonable and in agreement with the findings from the visual inspection. The total error of the identified defective model is around 1.5%, in comparison with the initial total error of approximately 5.5%. The diameter of the ‘oversized’ welds ( $d_{\text{big}}$ ) is increased by approximately 9% from the initial value and the ‘undersized’ weld ( $d_{\text{small}}$ ) is reduced by approximately 25%. It should also be noted that the mesh size used in the model is fixed to 20% of the nominal diameter. Hence, increased value of  $E_{\text{bigpatch}}$  indicates not only increased rigidity at the patch area, but may also demonstrates affected area that is bigger than the size of the mesh used for the patch. Conversely, reduced value of  $E_{\text{smallpatch}}$  demonstrates reduced rigidity that consequently indicates smaller patch area. If the updated values are believed to reflect the reality, both sets of welds may be classified as defects, hence support the findings from the earlier visual inspection made to detect physical inconsistencies in the welds.

In the second part of the chapter, damage was introduced to the benchmark structure used in the first part by drilling out spot weld 13. Then, the developed FE model of the benchmark structure is updated to match the measured data of the damaged structure to localise and quantify the damage. The identification procedure is conducted based on the first five natural frequencies and the first mode shape of the damaged

structure, and damage is characterised by the reductions in Young's modulus of the patches surrounding the twenty spot welds to indicate the loss of material/stiffness at the damage region. Due to the symmetrical nature of the welded structure, more information is required to assist the identification process. The experimental mode shapes of the damaged structure are observed and it is acknowledged that the damage occurs only at one quarter of the welded structure. Based on this information, it is decided that only one quarter of the structure would be considered as damage region, thus reducing the number of possible damage locations. In this work, spot welds 11 to 15 are regarded as possible damaged spot welds in the damage region. Based on the updating results, it can be concluded that damage certainly exists at the location of spot weld 13. However, the supposedly healthy spot welds are also affected by the procedure with the biggest error of approximately 50% at the adjacent spot welds (i.e., spot welds 12 and 14), which is believed to be due to the spillover effect of FE model updating. The identification procedure also brings the predicted natural frequencies closer to their measured counterparts, with total error of only 6%. Furthermore, the correlation between the numerical and experimental modes are very good, which demonstrates the success of the identification procedure.





# Chapter 8

## Conclusions and Future Work

### 8.1 Conclusions of the thesis

A set of nominally identical structures that comprise two substructures connected together by a number of laser weld joints have been produced in this research. Deterministic FE modelling and model updating procedure have been conducted in two stages: (1) the FE modelling and model updating of the substructures, and (2) the FE modelling and model updating of the welded structures. In the first stage, experimental modal analysis is performed on each of the substructures by using fixed hammer and measurement points so the modal data of the substructures can be determined. The hammer point is chosen with care to ensure all the modes can be excited, while the measurement points are selected at locations that can provide most information of the mode shapes. The experimental data have been used to validate the FE models of both substructures and the updated deterministic models have been employed in modelling the welded structures. In doing so, the modelling uncertainties from the substructures' FE models are removed prior to modelling the welded structures; hence the uncertainties in the developed FE model are attributed only to the weld modelling. Similarly to the substructures, experimental modal analysis with fixed hammer and measurement points is conducted on the laser welded structures. However, due to the complexity of the welded structures, an additional test is carried out with 80-point roving hammer points and four fixed measurement points in order to capture the actual mode shapes of the structures. These detailed experimental data have been employed in validating the developed model of the welded structures.

In order to represent the laser weld joints in the FE model of the welded structures, three different types of most commonly used spot weld models (i.e., beam, brick and CWELD elements) have been investigated. The findings show that the natural frequencies are significantly underestimated and the mode shapes are not predicted accurately when single beam element is employed. The problems are solved when using the brick element but due to the use of solid brick element and congruent mesh, the

computational penalty is so significant. In the end, the CWELD element is selected to represent the laser weld joint as it can provide reasonable modal data estimations of the welded structures, although initially the capability of the elements to represent the laser spot welds was uncertain and its potential in producing reasonably accurate values of natural frequencies was questionable. It is also found that the CWELD parameters (i.e., diameter and Young's modulus) alone cannot improve the results of the initial model even after updating. Further investigation reveals that when a patch parameter is included in the updating, the results improve significantly. Most importantly, it is essential to have an appropriate mesh in the FE model since it will influence the size of the patch used in the FE model. The CWELD element simulates the force transfer between the two patches accurately for  $d_{\text{weld}}/S \leq 1$ . The stiffness of the connection may be underestimated by the CWELD element if the diameter is larger than the surface patch. In this work, the size of the patches is set to be 20% bigger than the nominal diameter of the spot weld joints (consequently gives  $d_{\text{weld}}/S = 0.83$ ), while the Young's modulus of the patch should be approximately three times the value of the Young's modulus of the weld. These values are recommended as starting points for dynamic analysis of structures of similar constructions with many laser spot welds when the CWELD element is used. Nevertheless, users may need to make appropriate modifications to fit the requirements of their structures.

Better information on the manufacturing variability that exists in the welded structures can be observed due to the availability of individually-measured data, hence non-deterministic (or stochastic) model updating is conducted in this research. Firstly, two case studies on parameter selection in the stochastic model updating procedure have been conducted using two very different sets of structures: simple plates and complicated hat-shaped shells. Different sets of parameters (i.e., geometrical and material properties) are investigated and the findings in the case studies are used as a guideline in selecting the updating parameters for quantifying variability in the dynamics of the laser welded structures. It has been demonstrated that the selection of parameters should be made by choosing the most sensitive parameters that affect the outputs of the system. This can be easily achieved by carrying out a simple sensitivity analysis. The selection of parameters should also be made so that the mean outputs are closer to the measured outputs, and convergence between the scatter plots of the predicted and measured outputs can be obtained. This can be achieved by including both geometrical and material properties in the updating procedure, rather than choosing a number of geometrical properties alone. For example, although variation of thickness across the plate is incorporated into the FE model, good convergence could not be reached; indicating that certain modes (for example, torsional modes) could not be improved by solely having the thickness variation. When using material properties as updating parameters, the problematic modes are better represented. For instance, updated shear

modulus value improves the torsional modes representation.

The stochastic model updating problem for the welded structures is solved by employing the perturbation method using two approaches of parameter weighting matrices. The first approach considers only the main uncertain parameters, hence equal weighting has been employed when estimating the means and covariances of the parameters. On the other hand, more parameters are accounted for in the second approach by incorporating the uncertainties associated with the laser spot weld joints (i.e.,  $d$ ,  $E_{\text{weld}}$  and  $E_{\text{patch}}$ ) and also the uncertainties associated with the substructures (i.e.,  $E$  and  $G$  of the flat plates, and  $T_1$ ,  $T_2$  and  $E$  of the hat-shaped shells) due to the deformation following the welding process. Consequently, two different weightings have to be introduced, one for each step of updating. The second approach has significantly improved the results over the first approach. Scatter clouds of the measured and predicted outputs are generated by the Monte Carlo simulation following the Gaussian distribution to show convergence of the stochastic updating procedure, and it is found that the predicted space has converged upon the measured space very well. Additionally, the number of samples (i.e., five hundred) used in plotting the scatter clouds are clearly enough to give an accurate estimate of the parameter variability using the perturbation method. This is achieved by employing a combination of both geometrical and material properties in the updating procedure, rather than using a number of similar type of parameters.

Identification of defects in a spot welded structure by using only the natural frequencies information is also presented in this thesis. FE model updating has been carried out for predicting the extent of the defects, and the procedure is regarded as parameter identification that aims to bring the numerical prediction to be as closely as possible to the measured counterpart of the defective structure. The method has been applied to two identical welded structures: (1) the benchmark structure, and (2) the defective structure. The initial FE model for the defective specimen has shown excellent correlation with the experimental findings, mainly because most of the uncertainties (especially for the patch properties) have been successfully identified when updating the FE model, firstly in Chapter 5 and secondly when updating the benchmark structure. Furthermore, the predicted natural frequencies from the updated defective model agree with the measured defective data and the identified defect parameters are found to be reasonable and in agreement with the findings from the visual inspection. The total error of the identified defective model is around 1.5%, in comparison with the initial total error of approximately 5.5%. The diameter of the ‘oversized’ welds ( $d_{\text{big}}$ ) is increased by approximately 9% from the initial value and the ‘undersized’ weld ( $d_{\text{small}}$ ) is reduced by approximately 25%. It should also be noted that the mesh size used in the model is fixed to 20% of the nominal diameter. Hence, increased value of  $E_{\text{bigpatch}}$  indicates not only increased rigidity at the patch area, but may also demonstrates affected

area that is actually bigger than the size of the mesh used for the patch. Conversely, reduced value of  $E_{\text{smallpatch}}$  demonstrates reduced rigidity that consequently indicates smaller patch area. If the updated values are believed to reflect the reality, both sets of welds may be classified as defects, hence support the findings from the earlier visual inspection made to detect physical inconsistencies in the welds.

The benchmark structure used in the defects identification is deliberately damaged by removing one of the laser spot welds (i.e., spot weld 13). Then, damage identification is performed by FE model updating using not only the natural frequencies, but also the mode shape information of the damaged structure. More modal parameters are used in this work as natural frequencies alone are not enough for damage localisation and quantification. The identification procedure is conducted based on the first five natural frequencies and the first mode shape of the damaged structure, and damage is characterised by the reductions in Young's modulus of the patches surrounding the twenty spot welds to indicate the loss of material/stiffness at the damage region. In order to assist the identification process further, more information have to be considered due to the symmetrical nature of the damaged structure. The experimental mode shapes of the damaged structure are observed and it is acknowledged that the damage occurs only at one quarter of the welded structure. Based on this information, it is decided that only one quarter of the structure would be considered as damage region, thus reducing the number of possible damage locations. In this work, spot welds 11 to 15 are regarded as possible damaged spot welds in the damage region. Based on the updating results, it can be concluded that damage certainly exists at the location of spot weld 13. However, the supposedly healthy spot welds are also affected by the procedure with the biggest error of approximately 50% at the adjacent spot welds (i.e., spot welds 12 and 14), which is believed to be due to the spillover effect of FE model updating. The identification procedure also brings the predicted natural frequencies closer to their measured counterparts, with total error of only 6%. Furthermore, the correlation between the numerical and experimental modes are very good, which demonstrates the success of the identification procedure. In general, the identification procedure has successfully identified, localised and quantified the damage spot weld.

In conclusion, the laser weld joints have been modelled reasonably well by using the CWELD elements by NASTRAN. The deterministic FE model updating procedure has successfully brought the numerical model closer to the experimental data, that results in a reliable FE model of the laser welded structures to be used in further analysis. The developed deterministic model is then employed in the non-deterministic (or stochastic) model updating and the updated results are very well correlated with their experimental counterparts. Moreover, the deterministic model is used in the defects and damage identification work and good results are obtained. These findings therefore certify the applicability of the combined use of CWELD and the design sensitiv-

ity and optimisation solution (SOL 200) by NASTRAN in modelling the laser welded structures for wider applications.

## **8.2 Recommendations for future work**

The study undertaken in this thesis has covered the application of FE model updating using SOL 200 in NASTRAN for developing a reliable FE model of the laser welded structures, with some encouraging results in the deterministic analysis, stochastic analysis and the identification of defects/damage exercise. Although the method is successfully implemented in this research, some improvements can be made in order to ensure better predictions in the future. From the findings presented in this thesis, some general recommendations for future work in the area of model updating are outlined below.

1. The structures used in this research are the simplified version of the substructures commonly used in the automotive industry. Future investigations can be considered for real structures (such as the door panel, floor or roof from an actual BIW). It is interesting to see if the results outlined in this thesis are in agreement with those achieved from these more complex structures. Moreover, the feasibility of using the developed model to represent different configurations of laser weld joints (for instance, the continuous welds) can also be considered in the future.
2. The structures used in this research are modelled as linear systems. However, some nonlinearities due to geometrical, material and boundary conditions may exist in the structures. Therefore, it is interesting to investigate how these uncertainties can be incorporated into the FE model.
3. The stochastic model updating for estimation of variability in welded structures has been carried out by using the perturbation method. However, it is interesting to investigate other methods (for example, the interval method) so comparisons can be made with the perturbation method presented in this thesis.
4. The damage identification work presented in this thesis is the traditional vibration-based identification method using the natural frequencies and mode shape data of the damaged structure. It is also recognised that more damage information can be gathered using the FRF information. Thus, future work for structural damage detection is proposed by employing the FRFs when constructing the damage identification algorithm. In addition, modern damage detection methods (for example, wavelet analysis) may also be employed for identifying damage in the welded structures.



# Appendices



**PAGE  
MISSING  
IN  
ORIGINAL**

# Appendix A: Welding Procedure Specification

## Welding Procedure Specifications

**WPS identification** : Spot Weld Configuration – Hatplate A1:A3, B2:B3, C1:C3

**Manufacturer** : Laser Lab, Department of Engineering, University of Liverpool  
(Mr. Andy Snaylam)

### Equipment identification:

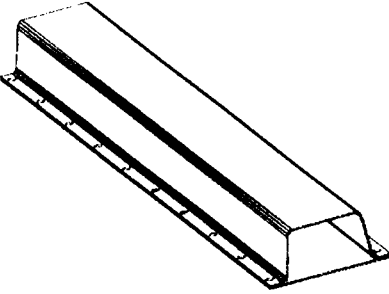
- laser welding machine : Ferranti Photonics AF8 8 kW CO<sub>2</sub> Laser
- beam quality (K, M2 or BPP value) - beam polarisation:  
M<sub>2</sub> = 4.0 - Linear Polarisation
- beam delivery system : Gold coated reflective mirrors
- beam focusing system : Zinc Selenide (ZnSe) 190 mm focal length lens
- shielding gas system : 6 mm pipe feed to nozzle

**Parent material specification:** 1: cold rolled mild steel  
2: cold rolled mild steel

- material thickness (mm): 1: 1.5 mm  
2: 1.5 mm

**Joint type:**

- sheet or plate
- cylindrical
- axial
- radial
- other

Joint design	Welding technique
	<p>Sample is placed in jig and clamped in place. Licom CAD/CAM program written to produce 10 equally spaced laser welds on each side of clamped sample using CNC table. Program includes all laser commands to turn shroud gas, laser beam on/off, etc., so each weld is produced in the same time frame. Finished sample removed from clamps and jig.</p>

Jigs, fixtures and tooling : Yes  No

Mechanically fixed : Clamps

Tack weld; process : On corners of complete sample

Back support: Yes  No

<b>Preparation :</b> Samples are cleaned, jigs are produced prior to welding			
<b>Procedure :</b>			
	<b>Tacking pass</b>	<b>Welding pass</b>	<b>Cosmetic pass</b>
<b>Welding position</b>			
<b>Welding technique</b>		- as before-	
<b>Beam power at workpiece</b> - continuous (W)		4000	
<b>Beam orientation angle</b> - longitudinal - transverse - position		90 degrees 90 degrees 6 mm from the edges	
<b>Travel speed (m/min)</b>		-	

<b>Laser duration (sec)</b>		1	
<b>Shielding gas</b> - classification and type - flow rate (L/min)		Helium 30	
<b>Working distance (mm)</b>		72	
<b>Shielding gas nozzle</b> - location (mm) - diameter (mm) - orientation:		10 6	

Name : Andy Snaylam

Date : March 2008



# Appendix B: NASTRAN input files

## Appendix B1: NASTRAN input file (.bdf) for Normal Modes analysis (SOL 103) of flat plates

```
$ Direct Text Input for Nastran System Cell Section
$ Direct Text Input for File Management Section

$ Normal Modes Analysis, Database
SOL 103

$ Direct Text Input for Executive Control
CEND
TITLE = FLAT PLATE
ECHO = NONE

$ Direct Text Input for Global Case Control Data
.
.
.

$ Direct Text Input for this Subcase
.
.
.

$ Direct Text Input for Bulk Data

$ Elements and Element Properties for region : plate_prop
PSHELL 1 1 1.45 1 1

$ Pset: "plate_prop" will be imported as: "pshell.1"
CQUAD4 1 1 1 2 13 12
.
.
.
CQUAD4 300 1 329 330 341 340
```

\$ Referenced Material Records  
\$ Material Record : plate\_mat

MAT1	1	2.1+8	8.1+7	7.86-6
------	---	-------	-------	--------

\$ Nodes of the Entire Model

GRID	1		0.	0.	0.
------	---	--	----	----	----

.

.

GRID	341		110.	564.	0.
------	-----	--	------	------	----

ENDDATA



## Appendix B2: Optimisation code for updating of flat plates

```

$ ...DESIGN VARIABLE DEFINITION

$ Plate_E
DESVAR 1 E 1. .88 1.05 .001

$ Plate_G
DESVAR 2 G 1. .99 1.04 .001

$ ...DEFINITION OF DESIGN VARIABLE TO ANALYSIS MODEL PARAMETER RELATIONS

DVMREL1 1 MAT1 1 E
1 2.1+8

DVMREL1 2 MAT1 1 G
2 8.1+7

$ ...STRUCTURAL RESPONSE IDENTIFICATION

DRESP1,1 ,FREQ_1 ,FREQ , , ,1
DRESP1,2 ,FREQ_2 ,FREQ , , ,2
DRESP1,3 ,FREQ_3 ,FREQ , , ,3
DRESP1,4 ,FREQ_4 ,FREQ , , ,4
DRESP1,5 ,FREQ_5 ,FREQ , , ,5

DRESP2,60 ,SUU ,70
DRESP1 1 2 3 4 5

DEQATN 70 SUU(F1,F2,F3,F4,F5)=
(F1/24.12-1.)**2+(F2/66.92-1.)**2+
(F3/77.65-1.)**2+(F4/131.97-1.)**2+
(F5/158.80-1.)**2

$ ...OPTIMIZATION CONTROL
DOPTPRM DESMAX 50 FSDMAX 0 P1 0 P2 1
METHOD 1 OPTCOD MSCADS CONV1 .001 CONV2 1.-20
CONVDV .001 CONVPR .01 DELP .2 DELX .5
DPHIN .01 DXMIN .05 CT -.03 GMAX .005
CTMIN .003

```

# Appendix B3:

## NASTRAN input file (.bdf) for Normal Modes analysis (SOL 103) of hat-shaped shells

```

$ Direct Text Input for Nastran System Cell Section
$ Direct Text Input for File Management Section

$ Normal Modes Analysis, Database
SOL 103

$ Direct Text Input for Executive Control
CEND
TITLE = HAT
ECHO = NONE

$ Direct Text Input for Global Case Control Data

.
.
.

$ Direct Text Input for this Subcase

.
.
.

$ Direct Text Input for Bulk Data

$ Elements and Element Properties for region : fold
PSHELL 1 1 1.45 1 1
$ Pset: "fold" will be imported as: "pshell.1"
CQUAD4 189 1 286 287 290 289

.
.
.

CQUAD4 1598 1 2276 2277 2280 2279

$ Elements and Element Properties for region : flat
PSHELL 2 1 1.45 1 1
$ Pset: "flat" will be imported as: "pshell.2"
CQUAD4 1 2 1 2 5 4

.
.
.

CQUAD4 3008 2 3883 2275 2278 3894

```

\$ Referenced Material Records  
\$ Material Record : MS

MAT1	1	2.1+8	0.3	7.86-6
------	---	-------	-----	--------

\$ Nodes of the Entire Model

GRID	1	0.	0.	1.5
------	---	----	----	-----

.  
.  
.

GRID	3894	79.4	564.	40.
------	------	------	------	-----

ENDDATA

# Appendix B4:

## Optimisation code for updating of hat-shaped shells

```

$ ...DESIGN VARIABLE DEFINITION

$ folds thickness
DESVAR 1    fold_t  1.    0.85  1.1  .001

$ flats thickness
DESVAR 2    flat_t  1.    0.85  1.1  .001

$ E
DESVAR 3    E      1.    0.85  1.05 .001

$ ...DEFINITION OF DESIGN VARIABLE TO ANALYSIS MODEL PARAMETER RELATIONS

DVPREL1 1    PSHELL 1    T
        1    1.45

DVPREL1 2    PSHELL 2    T
        2    1.45

DVMREL1 3    MAT1  1    E
        3    2.1+8

$ ...STRUCTURAL RESPONSE IDENTIFICATION

DRESP1,1    ,FREQ_1 ,FREQ ,    ,    ,1
DRESP1,2    ,FREQ_2 ,FREQ ,    ,    ,2
DRESP1,3    ,FREQ_3 ,FREQ ,    ,    ,3
DRESP1,4    ,FREQ_4 ,FREQ ,    ,    ,4
DRESP1,5    ,FREQ_5 ,FREQ ,    ,    ,5

DRESP2,60    ,SUU    ,70
    DRESP1    1    2    3    4    5

DEQATN 70    SUU(F1,F2,F3,F4,F5)=
    (F1/70.11-1.)**2+(F2/273.70-1.)**2+
    (F3/287.92-1.)**2+(F4/334.73-1.)**2+
    (F5/395.43-1.)**2

$ ...OPTIMIZATION CONTROL
DOPTPRM DESMAX 50    FSDMAX 0    P1    0    P2    1
    METHOD 1    OPTCOD MSCADS CONV1 .001 CONV2 1.-20
    CONVDV .001    CONVPR .01    DELP .2    DELX .5
    DPMIN .01    DXMIN .05    CT    -.03    GMAX .005
    CTMIN .003

$ Referenced Coordinate Frames
ENDDATA

```

# Appendix B5:

## NASTRAN input file (.bdf) for Normal Modes analysis (SOL 103) of flat plates with refined mesh

```

$ Direct Text Input for Nastran System Cell Section
$ Direct Text Input for File Management Section

$ Normal Modes Analysis, Database
SOL 103

$ Direct Text Input for Executive Control
CEND
TITLE = PLATE WITH REFINED MESH
ECHO = NONE

$ Direct Text Input for Global Case Control Data
.
.
.

$ Direct Text Input for this Subcase
.
.
.

$ Direct Text Input for Bulk Data

$ Elements and Element Properties for region : plate
PSHELL 1 1 1.45 1 1

$ Pset: "plate" will be imported as: "pshell.1"
CQUAD4 1 1 1 2 25 24

.
.
.

CQUAD4 2068 1 2161 2162 2185 2184

$ Referenced Material Records
$ Material Record : MS

MAT1 1 2.0886+88.26+7 7.86-6

$ Nodes of the Entire Model
GRID 1 0. 0. 0.

.
.
.

GRID 2185 110. 564. 0.

ENDDATA

```

# Appendix B6:

## NASTRAN input file (.bdf) for Normal Modes analysis (SOL 103) of welded structures with CBAR elements

```

$ Direct Text Input for Nastran System Cell Section
$ Direct Text Input for File Management Section

$ Normal Modes Analysis, Database
SOL 103

$ Direct Text Input for Executive Control
CEND
TITLE = WELDED STRUCTURES WITH CBAR ELEMENTS
ECHO = NONE

$ Direct Text Input for Global Case Control Data

.
.
.

$ Direct Text Input for this Subcase

.
.
.

$ Direct Text Input for Bulk Data

$ Elements and Element Properties for region : fold
PSHELL 1 1 1.31 1 1

$ Pset: "fold" will be imported as: "pshell.1"
CQUAD4 2257 1 2471 2472 2475 2474

.
.
.

CQUAD4 3666 1 4461 4462 4465 4464

$ Elements and Element Properties for region : flat
PSHELL 2 1 1.53 1 1

$ Pset: "flat" will be imported as: "pshell.2"
CQUAD4 2069 2 2186 2187 2190 2189

.
.
.

CQUAD4 5076 2 6068 4460 4463 6079

$ Elements and Element Properties for region : plate
PSHELL 3 2 1.45 2 2

```

\$ Pset: "plate" will be imported as: "pshell.3"

CQUAD4	1	3	1	2	25	24
.						
.						
.						
CQUAD4	2068	3	2161	2162	2185	2184

\$ Elements and Element Properties for region : weld

PBARL	4	3		ROD
	2.5			

\$ Pset: "weld" will be imported as: "pbarl.4"

CBAR	10001	4	3618	68	1.	1.	0.
CBAR	10002	4	3648	298	1.	1.	0.
CBAR	10003	4	3678	528	1.	1.	0.
CBAR	10004	4	3708	758	1.	1.	0.
CBAR	10005	4	3738	988	1.	1.	0.
CBAR	10006	4	3768	1218	1.	1.	0.
CBAR	10007	4	3798	1448	1.	1.	0.
CBAR	10008	4	3828	1678	1.	1.	0.
CBAR	10009	4	3858	1908	1.	1.	0.
CBAR	10010	4	3888	2138	1.	1.	0.
CBAR	10011	4	2193	48	1.	1.	0.
CBAR	10012	4	2223	278	1.	1.	0.
CBAR	10013	4	2253	508	1.	1.	0.
CBAR	10014	4	2283	738	1.	1.	0.
CBAR	10015	4	2313	968	1.	1.	0.
CBAR	10016	4	2343	1198	1.	1.	0.
CBAR	10017	4	2373	1428	1.	1.	0.
CBAR	10018	4	2403	1658	1.	1.	0.
CBAR	10019	4	2433	1888	1.	1.	0.
CBAR	10020	4	2463	2118	1.	1.	0.

\$ Referenced Material Records  
 \$ Material Record : plate

MAT1	2	2.0886+88.26+7		7.86-6
------	---	----------------	--	--------

\$ Material Record : hat

MAT1	1	2.1422+8	.3	7.86-6
------	---	----------	----	--------

\$ Material Record : weld

MAT1	3	2.1+8	.3	7.86-6
------	---	-------	----	--------

\$ Nodes of the Entire Model

GRID	1	0.	0.	0.
------	---	----	----	----

.

.

.

GRID	6079	79.4	564.	40.
------	------	------	------	-----

ENDDATA

# Appendix B7:

## NASTRAN input file (.bdf) for Normal Modes analysis (SOL 103) of welded structures with CHEXA elements

```

$ Direct Text Input for Nastran System Cell Section
$ Direct Text Input for File Management Section

$ Normal Modes Analysis, Database
SOL 103

$ Direct Text Input for Executive Control
CEND
TITLE = WELDED STRUCTURES WITH CHEXA ELEMENTS
ECHO = NONE

$ Direct Text Input for Global Case Control Data

.
.
.

$ Direct Text Input for this Subcase

.
.
.

$ Direct Text Input for Bulk Data

$ Elements and Element Properties for region : plate
PSHELL 1 1 1.45 1 1

$ Pset: "plate" will be imported as: "pshell.1"
CQUAD4 8949 1 10736 10737 10742 10741

.
.
.

CQUAD4 17972 1 20332 12616 12621 20373

$ Elements and Element Properties for region : fold
PSHELL 2 2 1.31 2 2

$ Pset: "fold" will be imported as: "pshell.2"
CQUAD4 1053 2 1287 1288 1292 1291

.
.
.

CQUAD4 5376 2 6762 6763 6767 6766

$ Elements and Element Properties for region : weld
PSOLID 3 3 0

```



\$ Pset: "weld" will be imported as: "psolid.3"

CHEXA 20001 3 363 364 359 358 10757 10758  
10753 10752

.  
.  
.

CHEXA 20080 3 1269 1270 1265 1264 11663 11664  
11659 11658

\$ Elements and Element Properties for region : flat

PSHELL 4 2 1.53 2 2

\$ Pset: "flat" will be imported as: "pshell.4"

CQUAD4 301 4 342 343 348 347

.  
.  
.

CQUAD4 8948 4 10722 6760 6764 10735

\$ Referenced Material Records

\$ Material Record : plate

MAT1 1 2.0886+88.26+7 7.86-6

\$ Material Record : hat

MAT1 2 2.1422+8 .3 7.86-6

\$ Material Record : weld

MAT1 3 2.1+8 .3 7.86-6

\$ Nodes of the Entire Model

GRID 1 0. 0. 0.

.  
.  
.

GRID 6079 79.4 564. 40.

ENDDATA

# Appendix B8:

## NASTRAN input file (.bdf) for Normal Modes analysis (SOL 103) of welded structures using CWELD elements with PARTPAT format

```

$ Direct Text Input for Nastran System Cell Section
$ Direct Text Input for File Management Section

$ Normal Modes Analysis, Database
SOL 103

$ Direct Text Input for Executive Control
CEND
TITLE = WELDED STRUCTURES WITH CWELD ELEMENTS (PARTPAT FORMAT)
ECHO = NONE

$ Direct Text Input for Global Case Control Data
.
.
.

$ Direct Text Input for this Subcase
.
.
.

$ Direct Text Input for Bulk Data

$ Elements and Element Properties for region : fold
PSHELL 1 1 1.305 1 1

$ Pset: "fold" will be imported as: "pshell.1"
CQUAD4 2257 1 2471 2472 2475 2474
.
.
.
CQUAD4 3666 1 4461 4462 4465 4464

$ Elements and Element Properties for region : flat
PSHELL 2 1 1.53 1 1

$ Pset: "flat" will be imported as: "pshell.2"
CQUAD4 2069 2 2186 2187 2190 2189
.
.
.
CQUAD4 5076 2 6068 4460 4463 6079

$ Elements and Element Properties for region : plate
PSHELL 3 2 1.45 2 2

```

\$ Pset: "plate" will be imported as: "pshell.3"

CQUAD4 5077 3 6080 6081 6092 6091

.  
.  
.

CQUAD4 5376 3 6408 6409 6420 6419

\$ Connector elements and properties for region : weld

\$ Pset: "weld" will be imported as: "pweld.4"

PWELD 4 3 5. OFF SPOT

CWELD 10001 4 3618 PARTPAT 3618 6421

2 3

CWELD 10002 4 3648 PARTPAT 3648 6422

2 3

CWELD 10003 4 3678 PARTPAT 3678 6423

2 3

CWELD 10004 4 3708 PARTPAT 3708 6424

2 3

CWELD 10005 4 3738 PARTPAT 3738 6425

2 3

CWELD 10006 4 3768 PARTPAT 3768 6426

2 3

CWELD 10007 4 3798 PARTPAT 3798 6427

2 3

CWELD 10008 4 3828 PARTPAT 3828 6428

2 3

CWELD 10009 4 3858 PARTPAT 3858 6429

2 3

CWELD 10010 4 3888 PARTPAT 3888 6430

2 3

CWELD 10011 4 2193 PARTPAT 2193 6431

2 3

CWELD 10012 4 2223 PARTPAT 2223 6432

2 3

CWELD 10013 4 2253 PARTPAT 2253 6433

2 3

CWELD 10014 4 2283 PARTPAT 2283 6434

2 3

CWELD 10015 4 2313 PARTPAT 2313 6435

2 3

CWELD 10016 4 2343 PARTPAT 2343 6436

2 3

CWELD 10017 4 2373 PARTPAT 2373 6437

2 3

CWELD 10018 4 2403 PARTPAT 2403 6438

2 3

CWELD 10019 4 2433 PARTPAT 2433 6439

2 3

CWELD 10020 4 2463 PARTPAT 2463 6440

2 3

\$ Referenced Material Records

\$ Material Record : plate

MAT1 2 2.0886+88.26+7 7.86-6

\$ Material Record : hat

MAT1 1 2.1422+8 .3 7.86-6

\$ Material Record : weld

MAT1 3 2.1+8 .3 7.86-6

\$ Nodes of the Entire Model

GRID 2186 0. 0. 1.5

.  
.  
.

GRID 6440 5. 552. 0.

ENDDATA 862897a1

# Appendix B9:

## Optimisation code for updating of welded structures using CWELD elements with PARTPAT format

```

$ ...DESIGN VARIABLE DEFINITION

$ diameter
DESVAR 1 D 1. 0.7 1.1 .01

$ E_weld
DESVAR 2 E_weld 1. 0.9 1.04 .01

$ ...DEFINITION OF DESIGN VARIABLE TO ANALYSIS MODEL PARAMETER RELATIONS
DVPREL1 1 PWELD 4 D
1 5.

DVMREL1 2 MAT1 3 E
2 2.1+8

$ ...STRUCTURAL RESPONSE IDENTIFICATION
DRESP1,1 ,FREQ_1 ,FREQ , , ,1
DRESP1,2 ,FREQ_2 ,FREQ , , ,2
DRESP1,3 ,FREQ_3 ,FREQ , , ,3
DRESP1,4 ,FREQ_4 ,FREQ , , ,4
DRESP1,5 ,FREQ_5 ,FREQ , , ,5

DRESP2,60 ,SUU ,70
DRESP1 1 2 3 4 5

DEQATN 70 SUU(F1,F2,F3,F4,F5)=
(F1/508.12-1.)**2+(F2/553.69-1.)**2+
(F3/575.39-1.)**2+(F4/627.45-1.)**2+
(F5/643.66-1.)**2

$ ...OPTIMIZATION CONTROL
DOPTPRM DESMAX 50 FSDMAX 0 P1 0 P2 1
METHOD 1 OPTCOD MSCADS CONV1 .001 CONV2 1.-20
CONVDV .001 CONVPR .01 DELP .2 DELX .5
DPMIN .01 DXMIN .05 CT -.03 GMAX .005
CTMIN .003

```

# Appendix B10:

## NASTRAN input file (.bdf) for Normal Modes analysis (SOL 103) of welded structures using CWELD elements with ALIGN format

```

$ Direct Text Input for Nastran System Cell Section
$ Direct Text Input for File Management Section

$ Normal Modes Analysis, Database
SOL 103

$ Direct Text Input for Executive Control
CEND
TITLE = WELDED STRUCTURES WITH CWELD ELEMENTS (ALIGN FORMAT)
ECHO = NONE

$ Direct Text Input for Global Case Control Data
.
.
.

$ Direct Text Input for this Subcase
.
.
.

$ Direct Text Input for Bulk Data

$ Elements and Element Properties for region : fold
PSHELL 1 1 1.305 1 1

$ Pset: "fold" will be imported as: "pshell.1"
CQUAD4 2257 1 2471 2472 2475 2474
.
.
.
CQUAD4 3666 1 4461 4462 4465 4464

$ Elements and Element Properties for region : flat
PSHELL 2 1 1.53 1 1

$ Pset: "flat" will be imported as: "pshell.2"
CQUAD4 2069 2 2186 2187 2190 2189
.
.
.
CQUAD4 5076 2 6068 4460 4463 6079

$ Elements and Element Properties for region : plate
PSHELL 3 2 1.45 2 2

```

\$ Pset: "plate" will be imported as: "pshell.3"

CQUAD4 1 3 1 2 25 24

.  
.  
.

CQUAD4 2068 3 2161 2162 2185 2184

\$ Elements and Element Properties for region : patch

PSHELL 4 3 1.53 3 3

\$ Pset: "patch" will be imported as: "pshell.4"

CQUAD4 23 4 24 25 48 47

.  
.  
.

CQUAD4 3288 4 3888 3889 3892 3891

\$ Connector elements and properties for region : weld

\$ Pset: "weld" will be imported as: "pweld.5"

PWELD 5 4 5.47 OFF SPOT

CWELD	10001	5		ALIGN	68	3618
CWELD	10002	5		ALIGN	298	3648
CWELD	10003	5		ALIGN	528	3678
CWELD	10004	5		ALIGN	758	3708
CWELD	10005	5		ALIGN	988	3738
CWELD	10006	5		ALIGN	1218	3768
CWELD	10007	5		ALIGN	1448	3798
CWELD	10008	5		ALIGN	1678	3828
CWELD	10009	5		ALIGN	1908	3858
CWELD	10010	5		ALIGN	2138	3888
CWELD	10011	5		ALIGN	48	2193
CWELD	10012	5		ALIGN	278	2223
CWELD	10013	5		ALIGN	508	2253
CWELD	10014	5		ALIGN	738	2283
CWELD	10015	5		ALIGN	968	2313
CWELD	10016	5		ALIGN	1198	2343
CWELD	10017	5		ALIGN	1428	2373
CWELD	10018	5		ALIGN	1658	2403
CWELD	10019	5		ALIGN	1888	2433
CWELD	10020	5		ALIGN	2118	2463

\$ Referenced Material Records

\$ Material Record : plate

MAT1 2 2.0886+88.26+7 7.86-6

\$ Material Record : hat

MAT1 1 2.1422+8 .3 7.86-6

\$ Material Record : weld

MAT1 4 2.1+8 .3 7.86-6

\$ Material Record : patch

MAT1 3 3.5+8 .3 7.86-6

\$ Nodes of the Entire Model

GRID 1 0. 0. 0.

.  
.  
.

GRID 6079 79.4 564. 40.

ENDDATA



# Appendix B11:

## Optimisation code for updating of welded structures using CWELD elements with ALIGN format

```

$ ...DESIGN VARIABLE DEFINITION

$ diameter
DESVAR  1      D      1.      0.7      1.1      .01

$ E_weld
DESVAR  2      E_weld 1.      0.9      1.04     .01

$ E_patch
DESVAR  3      E_patch 1.      0.1      10.      .01

$ ...DEFINITION OF DESIGN VARIABLE TO ANALYSIS MODEL PARAMETER RELATIONS
DVPREL1 1      PWELD  5      D
        1      5.

DVMREL1 2      MAT1   4      E
        2      2.1+8

DVMREL1 3      MAT1   3      E
        3      3.5+8

$ ...STRUCTURAL RESPONSE IDENTIFICATION
DRESP1,1      ,FREQ_1 ,FREQ  ,      ,      ,1
DRESP1,2      ,FREQ_2 ,FREQ  ,      ,      ,2
DRESP1,3      ,FREQ_3 ,FREQ  ,      ,      ,3
DRESP1,4      ,FREQ_4 ,FREQ  ,      ,      ,4
DRESP1,5      ,FREQ_5 ,FREQ  ,      ,      ,5

DRESP2,60     ,SUU     ,70
DRESP1      1      2      3      4      5

DEQATN 70     SUU(F1,F2,F3,F4,F5)=
              (F1/508.12-1.)**2+(F2/553.69-1.)**2+
              (F3/575.39-1.)**2+(F4/627.45-1.)**2+
              (F5/643.66-1.)**2

$ ...OPTIMIZATION CONTROL
DOPTPRM DESMAX 50      FSDMAX 0      P1      0      P2      1
        METHOD  1      OPTCOD MSCADS CONV1 .001  CONV2 1.-20
        CONVDV .001   CONVPR .01    DELP   .2    DELX   .5
        DPMIN  .01    DXMIN  .05    CT     -.03  GMAX   .005
        CTMIN  .003

```



## Appendix C: Example of calculation for covariance matrix of parameters

The parameter covariance matrix equation (Eq. (6.19)) is given as follows.

$$\mathbf{C}_{\theta\theta_{j+1}} = \mathbf{C}_{\theta\theta_j} - \mathbf{C}_{\theta z_j} \hat{\mathbf{T}}_j^T + \hat{\mathbf{T}}_j \mathbf{C}_{EE} \hat{\mathbf{T}}_j^T - \hat{\mathbf{T}}_j \mathbf{C}_{z\theta_j} + \hat{\mathbf{T}}_j \mathbf{C}_{ZZ_j} \hat{\mathbf{T}}_j^T$$

The covariance matrix of measurement is given as,

$$\mathbf{C}_{EE} = \text{cov}(\Delta z_m, \Delta z_m) = \begin{bmatrix} 0.0126 & 0.0275 & 0.0513 & 0.0451 & 0.0875 \\ 0.0275 & 0.0632 & 0.1053 & 0.1053 & 0.1889 \\ 0.0513 & 0.1053 & 0.3248 & 0.1683 & 0.5434 \\ 0.0451 & 0.1053 & 0.1683 & 0.1796 & 0.3073 \\ 0.0875 & 0.1889 & 0.5434 & 0.3073 & 0.9490 \end{bmatrix}$$

and prior estimates of the other covariance matrices used in the equation are:

$$\mathbf{C}_{\theta\theta_j} = \text{cov}(\Delta\theta_j, \Delta\theta_j) = \begin{bmatrix} 0.0001 & 0 & 0 \\ 0 & 0.0001 & 0 \\ 0 & 0 & 0.0001 \end{bmatrix}$$

$$\begin{aligned} \mathbf{C}_{\theta z_j} &= \mathbf{C}_{\theta\theta_j} \times \mathbf{S}_j^T = \mathbf{C}_{\theta\theta_j} \times \begin{bmatrix} 1.1843 & 21.9064 & 1.1843 \\ 22.4784 & 22.3718 & 22.4784 \\ 4.6171 & 65.8456 & 4.6171 \\ 47.5645 & 37.5525 & 47.5645 \\ 69.4971 & 15.1519 & 69.4971 \end{bmatrix}^T \\ &= \begin{bmatrix} 0.0001 & 0.0022 & 0.0005 & 0.0048 & 0.0069 \\ 0.0022 & 0.0022 & 0.0066 & 0.0038 & 0.0015 \\ 0.0001 & 0.0022 & 0.0005 & 0.0048 & 0.0069 \end{bmatrix} \end{aligned}$$

$$\begin{aligned} \mathbf{C}_{Z\theta_j} &= \mathbf{S}_j \times \mathbf{C}_{\theta\theta_j} = \begin{bmatrix} 1.1843 & 21.9064 & 1.1843 \\ 22.4784 & 22.3718 & 22.4784 \\ 4.6171 & 65.8456 & 4.6171 \\ 47.5645 & 37.5525 & 47.5645 \\ 69.4971 & 15.1519 & 69.4971 \end{bmatrix} \times \mathbf{C}_{\theta\theta_j} \\ &= \begin{bmatrix} 0.0001 & 0.0022 & 0.0001 \\ 0.0022 & 0.0022 & 0.0022 \\ 0.0005 & 0.0066 & 0.0005 \\ 0.0048 & 0.0038 & 0.0048 \\ 0.0069 & 0.0015 & 0.0069 \end{bmatrix} \end{aligned}$$

$$\mathbf{C}_{ZZ_j} = \mathbf{S}_j \times \mathbf{C}_{\theta\theta_j} \times \mathbf{S}_j^T = \begin{bmatrix} 0.0483 & 0.0543 & 0.1453 & 0.0935 & 0.0497 \\ 0.0543 & 0.1511 & 0.1681 & 0.2978 & 0.3463 \\ 0.1453 & 0.1681 & 0.4378 & 0.2912 & 0.1639 \\ 0.0935 & 0.2978 & 0.2912 & 0.5935 & 0.7180 \\ 0.0497 & 0.3463 & 0.1639 & 0.7180 & 0.9889 \end{bmatrix}$$

By taking appropriate values for weighting matrices  $\mathbf{W}_{\epsilon\epsilon}$  and  $\mathbf{W}_{\theta\theta}$ , the transformation matrix  $\mathbf{T}_j$  is given as:

$$\begin{aligned} \mathbf{T}_j &= (\mathbf{S}_j^T \mathbf{W}_{\epsilon\epsilon} \mathbf{S}_j + \mathbf{W}_{\theta\theta})^{-1} \mathbf{S}_j^T \mathbf{W}_{\epsilon\epsilon} \\ &= \begin{bmatrix} -0.0009 & 0.0009 & -0.0027 & 0.0024 & 0.0054 \\ 0.0041 & 0.0022 & 0.0123 & 0.0028 & -0.0035 \\ -0.0009 & 0.0009 & -0.0027 & 0.0024 & 0.0054 \end{bmatrix} \end{aligned}$$

By using the given input matrices, the new estimate of the parameter covariance matrix can be computed as:

$$\mathbf{C}_{\theta\theta_{j+1}} = \begin{bmatrix} 0.0007 & 0.0002 & -0.0003 \\ 0.0002 & 0.0003 & 0.0002 \\ -0.0003 & 0.0002 & 0.0007 \end{bmatrix}$$

# References

- [1] R. J. Allemang. The modal assurance criterion twenty years of use and abuse. *Sound and Vibration*, pages 14–21, August 2003.
- [2] D. J. Ewins. *Modal testing: theory, practice and application*. Research Studies Press Ltd., Hertfordshire, England, 2nd edition, 2000.
- [3] N. M. M. Maia and J. M. M. Silva. *Theoretical and experimental modal analysis*. Research Studies Press Ltd., Somerset, England, 1997.
- [4] M. I. Friswell and J. E. Mottershead. *Finite element model updating in structural dynamics*. Kluwer Academic Publishers, Dordrecht, The Netherlands, 1995.
- [5] A. Berman and W. G. Flannelly. Theory of incomplete models of dynamic structures. *AIAA Journal*, 9:1481–1487, 1971.
- [6] J. D. Collins, G. C. Hart, T. K. Hasselman, and B. Kennedy. Statistical identification of structures. *AIAA Journal*, 12:185–190, 1974.
- [7] R. M. Lin, H. Du, and J. H. Ong. Sensitivity based method for structural dynamic model improvement. *Computers and Structures*, 47:349–369, 1993.
- [8] Y. Xia, H. Hao, J. M. W Brownjohn, and P-Q. Xia. Damage identification of structures with uncertain frequency and mode shape data. *Earthquake Engng Struct. Dyn.*, 31:1053–1066, 2002.
- [9] C. Mares, J. E. Mottershead, and M. I. Friswell. Stochastic model updating: part 1 - theory and simulated example. *Mechanical Systems and Signal Processing*, 20:1674–1695, 2006.
- [10] J. E. Mottershead, C. Mares, S. James, and M. I. Friswell. Stochastic model updating: part 2 - application to a set of physical structures. *Mechanical Systems and Signal Processing*, 20:2171–2185, 2006.
- [11] H. Haddad Khodaparast, J. E. Mottershead, and M. I. Friswell. Perturbation methods for the estimation of parameter variability in stochastic model updating. *Mechanical Systems and Signal Processing*, 22:1751–1773, 2008.

- [12] H. C. Frey and D. E. Burmaster. Methods for characterizing variability and uncertainty: comparison of bootstrap simulation and likelihood-based approaches. *Risk Analysis*, 19:109–130, 1999.
- [13] W. L. Oberkampf, S. M. DeLand, B. M. Rutherford, K. V. Diegert, and K. F. Alvin. Error and uncertainty in modeling and simulation. *Reliability Engineering and System Safety*, 75:333–357, 2002.
- [14] W. L. Oberkampf, T. G. Trucano, and C. Hirsch. Verification, validation, and predictive capability in computational engineering and physics. *Appl Mech Rev*, 57:345–384, 2004.
- [15] S.W. Doebling, C. R. Farrar, and M. B. Prime. A summary review of vibration-based damage identification methods. *The Shock and Vibration Digest*, 30:91–105, 1998.
- [16] S.W. Doebling, C. R. Farrar, M. B. Prime, and D. W. Shevitz. Damage identification and health monitoring of structural and mechanical systems from changes in their vibration characteristics: a literature review. Technical report, Los Alamos National Laboratory, New Mexico, 1996.
- [17] M.O. Abdalla, K. M. Grigoriadis, and D. C. Zimmerman. Enhanced structural damage detection using alternating projection methods. *AIAA Journal*, 36:1305–1311, 1998.
- [18] M. Baruch. Damage detection based on reduced measurements. *Mechanical Systems and Signal Processing*, 12:23–46, 1998.
- [19] Y. Zou, L. Tong, and G. P. Steven. Vibration-based model-dependent damage (delamination) identification and health monitoring for composite structures - a review. *Journal of Sound and Vibration*, 230:357–378, 2000.
- [20] Y. J. Yan, L. Cheng, Z. Y. Wu, and L. H. Yam. Development in vibration-based structural damage detection technique. *Mechanical Systems and Signal Processing*, 21:2198–2211, 2007.
- [21] M. Palmonella, M. I. Friswell, J. E. Mottershead, and A. W. Lees. Finite element models of spot welds in structural dynamics: review and updating. *Computers and Structures*, 83:648–661, 2005.
- [22] M. Palmonella, M. I. Friswell, J. E. Mottershead, and A. W. Lees. Guidelines for the implementation of the cweld and acm2 spot weld models in structural dynamics. *Finite Elements in Analysis and Design*, 41:193–210, 2004.

- [23] M. Palmonella, M. I. Friswell, C. Mares, and J. E. Mottershead. Improving spot weld models in structural dynamics. In *Proceeding of DETC '03*, Illinois, USA, 2003.
- [24] J. E. Mottershead and M. I. Friswell. Model updating in structural dynamics: A survey. *Journal of Sound and Vibration*, 167:347–375, 1993.
- [25] X.G. Hua, Y. Q. Ni, Z. Q. Chen, and J. M. Ko. An improved perturbation method for stochastic finite element model updating. *Int. J. Numer. Meth. Engng*, 73:1845–1864, 2008.
- [26] Y. J. Yan, H. N. Hao, and L. H. Yam. Vibration-based construction and extraction of structural damage feature index. *International Journal of Solids and Structures*, 41:6661–6676, 2004.
- [27] C.P. Fritzen, D. Jennewein, and T. Kiefer. Damage detection based on model updating methods. *Mechanical Systems and Signal Processing*, 12:163–186, 1998.
- [28] R. O. De Alba, N. S. Ferguson, and B. R. Mace. A multipoint constraint model for the vibration of spot welded structures. Technical report, Institute of Sound and Vibration Research, University of Southampton, 2009.
- [29] Y. Cho, S.J. Hu, and W. Li. Resistance spot welding of aluminium and steel: a comparative experimental study. *Journal of Engineering Manufacture*, 217:1355–1363, 2003.
- [30] S. Donders, M. Brughmans, L. Hermans, C. Liefoghe, H. Van der Auweraer, and W. Desmet. The robustness of dynamic vehicle performance to spot weld failures. *Finite Elements in Analysis and Design*, 42:670–682, 2006.
- [31] S. Xu and X. Deng. An evaluation of simplified finite element models for spot-welded joints. *Finite Elements in Analysis and Design*, 40:1175–1194, 2004.
- [32] X. Deng, W. Chen, and G. Shi. Three-dimensional finite element analysis of the mechanical behavior of spot welds. *Finite Elements in Analysis and Design*, 35:17–39, 2000.
- [33] A. De, S. K. Maiti, C. A. Walsh, and H. K. D. H. Bhadeshia. Finite element simulation of laser spot welding. *Science and Technology of Welding and Joining*, 8:377–384, 2003.
- [34] Z.B. Dong and Y. H. Wei. Three dimensional modelling weld solidification cracks in multipass welding. *Theoretical and Applied Fracture Mechanics*, 46:156–165, 2006.

- [35] S.A. Tsirkas, P. Papanikos, and Th. Kermanidis. Numerical simulation of the laser welding process in butt-joint specimens. *Journal of Materials Processing Technology*, 134:59–69, 2003.
- [36] S.K. Cho, Y. S. Yang, K. J. Son, and J. Y. Kim. Fatigue strength in laser welding of the lap joint. *Finite Elements in Analysis and Design*, 40:1059–1070, 2004.
- [37] The American Welding Society, Miami, FL. *Welding Handbook: Volume 1 Welding Technology*, 8th edition, 1987.
- [38] Y. Cho, I. Chang, and H. Lee. Single-sided resistance spot welding for auto body assembly. *Welding Journal*, pages 26–29, August 2006.
- [39] J. L. Dohner. White paper: on the development of methodologies for constructing predictive models of structures with joints and interfaces. Technical report, Sandia National Laboratories, Albuquerque, 2001.
- [40] L. Gaul and J. Lenz. Nonlinear dynamics of structures assembled by bolted joints. *Acta Mechanica*, 125:169–181, 1997.
- [41] L. Gaul and R. Nitsche. The role of friction in mechanical joints. *Applied Mechanics Review*, 54:93–106, 2001.
- [42] M. Oldfield, H. Ouyang, and J. E. Mottershead. Simplified models of bolted joints under harmonic loading. *Computers and Structures*, 84:25–33, 2005.
- [43] R.A. Ibrahim and C. L. Pettit. Uncertainties and dynamic problems of bolted joints and other fasteners. *Journal of Sound and Vibration*, 279:857–936, 2005.
- [44] J. Kim, J-C. Yoon, and B-S. Kang. Finite element analysis and modelling of structure with bolted joints. *Applied Mathematical Modelling*, 31:895–911, 2007.
- [45] H. Ouyang, M. J. Oldfield, and J. E. Mottershead. Experimental and theoretical studies of a bolted joint excited by a torsional dynamic load. *International Journal of Mechanical Sciences*, 48:1447–1455, 2006.
- [46] W. Chen and X. Deng. Performance of shell elements in modelling spot-welded joints. *Finite Elements in Analysis and Design*, 35:41–57, 2000.
- [47] D. Heiserer, M. Chargin, and J. Sielaff. High performance, process oriented, weld spot approach. In *1st MSC Worldwide Automotive User*, Munich, Germany, 1999.



- [48] P. Salvini, F. Vivio, and V. Vullo. A spot weld finite element for structural modelling. *International Journal of Fatigue*, 22:645–656, 2000.
- [49] J. Fang, C. Hoff, B. Holman, F. Mueller, and D. Wallerstein. Weld modelling with msc.nastran. In *Proceeding of 2nd MSC Worldwide Automotive Conference*, Dearborn, Michigan, 2000.
- [50] M. Palmonella. *Improving finite element models of spot welds in structural dynamics*. PhD thesis, University of Wales, Swansea, 2003.
- [51] B. Chang, Y. Shi, and S. Dong. Comparative studies on stresses in weld-bonded, spot-welded and adhesive-bonded joints. *Journal of Materials Processing Technology*, 87:230–236, 1999.
- [52] B. Chang, Y. Shi, and S. Dong. Studies on a computational model and the stress weld characteristics of weld-bonded joints for a car body steel sheet. *Journal of Materials Processing Technology*, 100:171–178, 2000.
- [53] D. Radaj and S. Zhang. Geometrically nonlinear behaviour of spot welded joints in tensile and compressive shear loading. *Engineering Fracture Mechanics*, 51:281–294, 1995.
- [54] G. Zhang and B. Richter. A new approach to the numerical fatigue-life prediction of spot-welded structures. *Fatigue Fract Engng Mater Struct*, 23:499508, 2000.
- [55] F. Vivio, G. Ferrari, P. Salvini, and V. Vullo. Enforcing of an analytical solution of spot welds into finite elements analysis for fatigue life estimation. *International Journal of Computer Applications in Technology*, 15:218–219, 2002.
- [56] The MSC.Software Corporation. *MSC.NASTRAN 2005 - Quick Reference Guide*, 2004.
- [57] J. Montalvo-Urquizo, Z. Akbay, and A. Schmidt. Adaptive finite element models applied to the laser welding problem. *Computational Materials Science*, 46:245254, 2009.
- [58] W. Christian. Finite element simulation of crash testing of self-piercing rivet joints, peel specimen. Master's thesis, Lund University, Lund, 2002.
- [59] B. Langrand, E. Deletombe, E. Markiewicz, and Drazetic. Riveted joint modeling for numerical analysis of airframe crashworthiness. *Finite Elements in Analysis and Design*, 38:21–44, 2001.

- [60] B. Kelly and C. Costello. Fea modelling of setting and mechanical testing of aluminium blind rivets. *Journal of Materials Processing Technology*, 153154:7479, 2004.
- [61] K. Iyer, S. J. Hu, F. L. Brittman, P. C. Wang, D. B. Hayden, and S. P. Marin. Fatigue of single- and double-rivet self-piercing riveted lap joints. *Fatigue Fract Engng Mater Struct*, 28:9971007, 2005.
- [62] G. Beer. An isoparametric joint/interface element for finite element analysis. *International Journal for Numerical Methods in Engineering*, 21:585–600, 1985.
- [63] H. Ahmadian, M. Ebrahimi, J. E. Mottershead, and M. I. Friswell. Identification of bolted-joint interface models. In *27th International Seminar on Modal Analysis*, Katholieke Universiteit Leuven, 2002.
- [64] H. Ahmadian, J. E. Mottershead, S. James, M. I. Friswell, and C. A. Reece. Modelling and updating of large surface-to-surface joints in the awe-mace structure. *Mechanical Systems and Signal Processing*, 20:868–880, 2006.
- [65] M. H. Mayer and L. Gaul. Segment-to-segment contact elements for modelling joint interfaces in finite element analysis. *Mechanical Systems and Signal Processing*, 21:724–734, 2007.
- [66] A. M. Brown and R. M. Seugling. Using plate finite elements for modeling fillets in global response analysis. *Finite Elements in Analysis and Design*, 40:1963–1975, 2004.
- [67] K. He and W. D. Zhu. Modeling of fillets in thin-walled beams using shell/plate and beam finite elements. *Journal of Vibration and Acoustics*, 131, 2009.
- [68] D. J. Ewins. Basics and state-of-the-art of modal testing. *Sadhana*, 25:207–220, 2000.
- [69] J.E. Mottershead, C. Mares, M. I. Friswell, and S. James. Selection and updating of parameters for an aluminium space-frame model. *Mechanical Systems and Signal Processing*, 14:923–944, 2000.
- [70] R. Kenigsbuch and Y. Halevi. Model updating in structural dynamics: a generalised reference basis approach. *Mechanical Systems and Signal Processing*, 12:75–90, 1998.
- [71] C.P. Fritzen and S. Zhu. Updating of finite element models by means of measured information. *Computers & Structures*, 40:475–486, 1991.

- [72] J. E. Mottershead. On the zeros of structural frequency response functions and their sensitivities. *Mechanical Systems and Signal Processing*, 12:591–597, 1998.
- [73] W. D’Ambrogio and A. Fregolent. The use of antiresonances for robust model updating. *Journal of Sound and Vibration*, 236:227–243, 2000.
- [74] O. C. Zienkiewicz, Taylor R. L., and J. Z. Zhu. *The finite element method: its basis and fundamentals*. Elsevier/Butterworth-Heinemann, Oxford, England, 2005.
- [75] The MacNeal-Schwendler Corporation, Los Angeles, CA. *User’s Guide: MSC/NASTRAN Basic Dynamic Analysis*, 1993.
- [76] T. R. Kim and S. M. Wu. Identification of joint parameters for a taper joint. *Transaction of the ASME*, 111:282–287, 1989.
- [77] J. R. F. Arruda and J. M. C. Santos. Mechanical joint parameter estimation using frequency response functions and component mode synthesis. *Mechanical Systems and Signal Processing*, 7:493–508, 1993.
- [78] X. G. Hua, Y. Q. Ni, and J. M. Ko. Adaptive regularization parameter optimization in output-error-based finite element model updating. *Mechanical Systems and Signal Processing*, 23:563–579, 2009.
- [79] R. L. Fox and M. P. Kapoor. Rates of change of eigenvalues and eigenvectors. *AIAA Journal*, 6:2426–2429, 1968.
- [80] H. Ahmadian, J. E. Mottershead, and M. I. Friswell. Regularisation methods for finite element model updating. *Mechanical Systems and Signal Processing*, 12:47–64, 1998.
- [81] J. E. Mottershead, M. I. Friswell, G. H. T. Ng, and J. A. Brandon. Geometric parameters for finite element model updating of joints and constraints. *Mechanical Systems and Signal Processing*, 10:171–182, 1996.
- [82] G.H. Kim and Y.S. Park. An improved updating parameter selection method and finite element model update using multiobjective optimisation technique. *Mechanical Systems and Signal Processing*, 18:59–78, 2004.
- [83] G.M.L. Gladwell and H. Ahmadian. Generic element matrices suitable for finite element model updating. *Mechanical Systems and Signal Processing*, 9:601–614, 1995.

- [84] H. Ahmadian, G. M. L. Gladwell, and F. Ismail. Parameter selection strategies in finite element model updating. *ASME Journal of Vibration and Acoustics*, 119:37–45, 1997.
- [85] C. Mares, M. I. Friswell, and J. E. Mottershead. Model updating using robust estimation. *Mechanical Systems and Signal Processing*, 16:169–183, 2002.
- [86] The MacNeal-Schwendler Corporation, Los Angeles, CA. *User's Guide: MSC/NASTRAN Design Sensitivity and Optimization*, 1993.
- [87] S. S. Rao. *Optimization: theory and applications*. Wiley Eastern Limited, New Delhi, India, 1979.
- [88] B. R. Mace, K. Worden, and G. Manson. Uncertainty in structural dynamics. *Journal of Sound and Vibration*, 288:423–429, 2005.
- [89] W. L. Oberkampf, J. C. Helton, C. A. Joslyn, S. F. Wojtkiewicz, and S. Ferson. Challenge problems: uncertainty in system response given uncertain parameters. *Reliability Engineering and System Safety*, 85:11–19, 2004.
- [90] J. R. Fonseca, M. I. Friswell, J. E. Mottershead, and A. W. Lees. Uncertainty identification by the maximum likelihood method. *Journal of Sound and Vibration*, 288:587–599, 2005.
- [91] R. Y. Rubinstein and D. P. Kroese. *Simulation and the Monte Carlo Method*. John Wiley & Sons, Inc., New Jersey, 2008.
- [92] K. Binder and D. W. Heermann. *Monte Carlo simulation in statistical physics: an introduction*. Springer, Germany, 2002.
- [93] R. H. Myers, D. C. Montgomery, and C. M. Anderson-Cook. *Response surface methodology: process and product optimization using designed experiments*. John Wiley & Sons, Inc., New Jersey, 2009.
- [94] Y. Ben-Haim. Convex models of uncertainty: applications and implications. *Erkenntnis*, 41:139–156, 1994.
- [95] Y. Ben-Haim and I. Elishakoff. *Convex models of uncertainty in applied mechanics*. Elsevier, Amsterdam, 1990.
- [96] S. Adhikari and M. I. Friswell. Random matrix eigenvalue problems in structural dynamics. *Int. J. Numer. Meth. Engrg.*, 69:562–591, 2007.
- [97] G. Stefanou. The stochastic finite element method: past, present and future. *Comput. Methods Appl. Mech. Engrg.*, 198:1031–1051, 2009.

- [98] M.I. Friswell. The adjustment of structural parameters using a minimum variance estimator. *Mechanical Systems and Signal Processing*, 3:143–155, 1989.
- [99] H. Haddad Khodaparast and J. E. Mottershead. Efficient methods in stochastic model updating. In *Proceeding of ISMA 2008*, Leuven, Belgium, 2008.
- [100] Y. Govers and M. Link. Stochastic model updating - covariance matrix adjustment from uncertain experimental modal data. *Mechanical Systems and Signal Processing*, 24:696–706, 2010.
- [101] A. Teughels and G. De Roeck. Structural damage identification of the highway bridge z24 by fe model updating. *Journal of Sound and Vibration*, 278:589–610, 2004.
- [102] R. Pascual, I. Trendafilova, J. C. Golinval, and W. Heylen. Damage detection using model updating and identification techniques. In *Identification in Engineering Systems: Proceedings of the Second International Conference*, Swansea, UK, 1999.
- [103] M.I. Friswell, J. E. T. Penny, and S. D. Garvey. Parameter subset selection in damage location. *Inverse Problems in Engineering*, 5:189–215, 1997.
- [104] C. R. Farrar and S. W. Doebling. Damage detection ii: field applications to large structures. Technical report, Los Alamos National Laboratory, New Mexico, 1998.
- [105] J. Sinha, M. I Friswell, and S. Edwards. Simplified models for the location of cracks in beam structures using measured vibration data. *Journal of Sound and Vibration*, 251:13–38, 2002.
- [106] M. K. Yoon, D. Heider, J. W. Gillespie, C. P. Ratcliffe, and R. M. Crane. Local damage detection using the two-dimensional gapped smoothing method. *Journal of Sound and Vibration*, 279:119–139, 2005.
- [107] E. P. Carden and P. Fanning. Vibration based condition monitoring: a review. *Structural Health Monitoring*, 3:355–377, 2004.
- [108] H. Van der Auweraer and B. Peeters. International research projects on structural health monitoring: an overview. *Structural Health Monitoring*, 2:341–358, 2003.
- [109] P. Hajela and F. J. Soeiro. Recent developments in damage detection based on system identification methods. *Structural Optimization*, 2:1–10, 1990.

- [110] H. G. Natke and C. Cempel. Fault detection and localisation in structures: a discussion. *Mechanical Systems and Signal Processing*, 5:345–356, 1991.
- [111] H. Sohn, C. R. Farrar, F. M. Hemez, D. D. Shunk, D. W. Stinemates, B. R. Nadler, and J. J. Czarnecki. A review of structural health monitoring literature: 1996–2001. Technical report, Los Alamos National Laboratory, New Mexico, 2004.
- [112] O. S. Salawu. Detection of structural damage through changes in frequency: a review. *Engineering Structures*, 19:718–723, 1997.
- [113] P. Cawley and R. D. Adams. The locations of defects in structures from measurements of natural frequencies. *Journal of Strain Analysis*, 14:49–57, 1979.
- [114] T. Y. Kam and T. Y. Lee. Detection of cracks in structures using modal test data. *Engineering Fracture Mechanics*, 42:381–387, 1992.
- [115] M. Kaouk and D. C. Zimmerman. Structural damage assessment using a generalized minimum rank perturbation theory. *AIAA Journal*, 32:836–842, 1994.
- [116] J. M. Ricles and J. B. Kosmatka. Damage detection in elastic structures using vibratory residual forces and weighted sensitivity. *AIAA Journal*, 30:2310–2316, 1992.
- [117] A. K. Pandey, M. Biswas, and M. M. Samman. Damage detection from changes in curvature mode shapes. *Journal of Sound and Vibration*, 145:321–332, 1991.
- [118] G. H. James III. Development of structural health monitoring techniques using dynamics testing. Technical report, Sandia National Laboratories, Albuquerque, 1996.
- [119] H. T. Banks, D. J. Inman, D. J. Leo, and Y. Wang. An experimentally validated damage detection theory in smart structures. *Journal of Sound and Vibration*, 191:859–880, 1996.
- [120] C. R. Farrar and D. A. Jauregui. Comparative study of damage identification algorithms applied to a bridge: 1. experiment. *Smart Mater. Struct.*, 7:704–719, 1998.
- [121] Y-S. Lee and M-J. Chung. A study on crack detection using eigenfrequency test data. *Computers and Structures*, 77:327–342, 2000.
- [122] W-X. Ren and G. De Roeck. Structural damage identification using modal data. i: simulation verification. *Journal of Structural Engineering*, 128:87–95, 2002.

- [123] R. Perera and A. Ruiz. A multistage fe updating procedure for damage identification in large-scale structures based on multiobjective evolutionary optimization. *Mechanical Systems and Signal Processing*, 22:970–991, 2008.
- [124] U. Lee and J. Shin. A frequency response function-based structural damage identification method. *Computers and Structures*, 80:117–132, 2002.
- [125] Z. Wang, R.M. Lin, and M.K. Lim. Structural damage detection using measured frf data. *Comput. Methods Appl. Mech. Engrg.*, 147:187–197, 1997.
- [126] R. P. C. Sampaio, N. M. M. Maia, and J. M. M. Silva. Damage detection using the frequency-response-function curvature method. *Journal of Sound and Vibration*, 226:1029–1042, 1999.
- [127] S. K. Thyagarajan, M. J. Schulz, and P. F. Pai. Detecting structural damage using frequency response functions. *Journal of Sound and Vibration*, 210:162–170, 1998.
- [128] L. M. Khoo, P. R. Mantena, and P. Jadhav. Structural damage assessment using vibration modal analysis. *Structural Health Monitoring*, 3:177–194, 2004.
- [129] Y. T. Chung. Model reduction and model correlation using msc/nastran. In *Proceeding of World Users' Conference*, 1995.